INFORMATION TO USERS

This manuscript has been reproduced from the microfilm master. UMI films the text directly from the original or copy submitted. Thus, some thesis and dissertation copies are in typewriter face, while others may be from any type of computer printer.

The quality of this reproduction is dependent upon the quality of the copy submitted. Broken or indistinct print, colored or poor quality illustrations and photographs, print bleedthrough, substandard margins, and improper alignment can adversely affect reproduction.

In the unlikely event that the author did not send UMI a complete manuscript and there are missing pages, these will be noted. Also, if unauthorized copyright material had to be removed, a note will indicate the deletion.

Oversize materials (e.g., maps, drawings, charts) are reproduced by sectioning the original, beginning at the upper left-hand corner and continuing from left to right in equal sections with small overlaps. Each original is also photographed in one exposure and is included in reduced form at the back of the book.

Photographs included in the original manuscript have been reproduced xerographically in this copy. Higher quality 6" x 9" black and white photographic prints are available for any photographs or illustrations appearing in this copy for an additional charge. Contact UMI directly to order.

UMI®

ABSTRACT

Title of Dissertation: PERSISTENCE OF THE DEEP-INELASTIC REACTION MECHANISM INTO THE INTERMEDIATE ENERGY REGIME

Daniel Edward Russ, Doctor of Philosophy, 1998

Dissertation directed by: Professor Alice C. Mignerey

Department of Chemistry and Biochemistry

Projectile-like fragments produced in the reaction ^{129}Xe + ^{nat}Cu and ^{nat}Sc at E/A = 30, 40, 50, and 60 MeV were detected using a new forward array, the Maryland Forward Array, for the Michigan State University 4π array. The charge, energy and position of the fragments were measured. Inclusive energy, charge and velocity distributions, as well as mean charge and charge width as a function of energy, and mean velocity as a function of charge, were generated. In addition, the deflection functions for the systems were measured over the range of the detector.

The data are compared to the results of Tassan-Got's stochastic nucleon exchange model to see if a deep-inelastic process can produce the fragments seen in these reactions. In addition, a dynamic model, BUU, is used to see its predictions for peripheral collision reproduce the trends seen in the data.

At E/A = 30 and 40 MeV, a comparison of the data with Tassan-Got model calculations and an orbiting pattern in the deflection function suggest that the deep-inelastic reaction mechanism is occurring for both the Xe + Cu and Sc systems. At E/A = 50 MeV, the grazing angle for the Xe + Sc system falls inside the detector's inner radius, so no conclusion, based on the deflection function, about deep-inelastic

process is made, however for the Xe + Cu system, the mean charge, charge width and mean velocity plots support the presence of deep-inelastic reaction. At E/A = 60 MeV, the grazing angle falls inside the detector's inner radius for both systems. However, the differences in the data suggests that the deep-inelastic process may no longer be occurring.

PERSISTENCE OF THE DEEP-INELASTIC REACTION MECHANISM INTO

THE INTERMEDIATE ENERGY REGIME

by

Daniel E. Russ

Dissertation submitted to the Faculty of the Graduate School of the
University of Maryland, College Park in partial fulfillment
of the requirements for the degree of
Doctor of Philosophy
1998

Advisory Committee

Professor Alice Mignerey, Chair/Advisor
Professor William Walters
Professor Thomas O'Haver
Professor Samuel Grim
Professor Phil Roos

UMI Number: 9939666

UMI

300 North Zeeb Road
Ann Arbor, MI 48103

ACKNOWLEDGMENTS

I would like to thank my advisor, Dr. Alice Mignerey, for her support and guidance throughout my years in graduate school and during my senior year as an undergraduate at the University of Maryland. She gave me the opportunity to work on a variety of interesting projects. I tested (played) and set up state of the art electronics, computers, and detector systems.

I would also like to thank my parents, Gerald and Lana Russ. Never in my mind was there a question as to what I would do after high school. When I was finished at Maryland as an undergraduate, the question was not "Should I go to graduate school?" but "Which graduate school should I go to?". They inspired me to be inquisitive and gave me a zest for learning.

In addition, I would like to thank all my friends and family who helped me get through my years at Maryland.

Finally, a very special thank you to the one person who waited not so patiently for me to finish, my wife Lauren. She has been my excuse for going into the office on rainy days, and staying up late writing. I met her as I started graduate school, and I married her just before finishing. Thank you Lauren.

ii

TABLE OF CONTENTS

iv

LIST OF TABLES

LIST OF FIGURES

ix

x

xiii

xvi

Chapter I Introduction

The study of nuclear reactions goes back to Geiger and Marsden's gold foil experiment. Alpha particles were elastically scattered off gold and other heavy targets. Elastic scattering was the only reaction possible because the alpha particles did not have enough energy to make it past the Coulomb barrier.

Then, with the advent of cyclotrons, projectiles with sufficient energy to induce nuclear reactions became feasible. A major goal of studying nuclear reactions is to understand the different reaction mechanisms by which nuclei interact. Currently, no one theory can describe globally nuclear reactions. But different theories are applicable for particular energy and centrality regions.

Heavy-ion (A > 4) reaction mechanisms can be categorized by the bombarding energy and impact parameter. Reactions with beam energy (E_{Beam}) less than around 20 MeV/A are considered low energy reactions, while reaction with 100 MeV/A < E_{beam} < 1000 MeV/A are considered high energy. Higher beam energies are considered relativistic and ultrarelativistic. The impact parameter (b) can be described as the distance between two point particles when they pass by each other in the absence of any force acting between them [WON90]. Because of Coulomb repulsion, the projectile scatters in an approximately hyperbolic path, as shown in Fig. I.1. Therefore, the distance of closest approach is larger than the impact parameter. For reactions with a small impact parameter, the nuclei collide "head on" in a central collision; for reactions with impact parameters around the sum of the projectile and target radii ($R_p + R_t$), the nuclei barely collide in a very peripheral collision.

In low energy central collisions, projectile and target nuclei can fuse forming a compound nucleus. The compound nucleus remains intact long enough for the system to reach thermal equilibrium. This allows a decoupling of the entrance and exit channels. Statistical models of evaporation and fission can well reproduce data

1

Figure I.1 An example of (a) a grazing collision and (b) a central collision. The solid line represents the path the projectile travels, and the dashed line is the path the projectile would travel if there were no interaction with the target.

2

$b_{grazing}$

$b_{grazing} < r_p + r_t$

Projectile

$b = 0$

r_p

r_t

Target

3
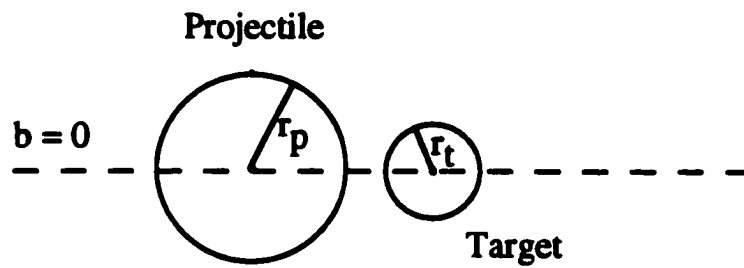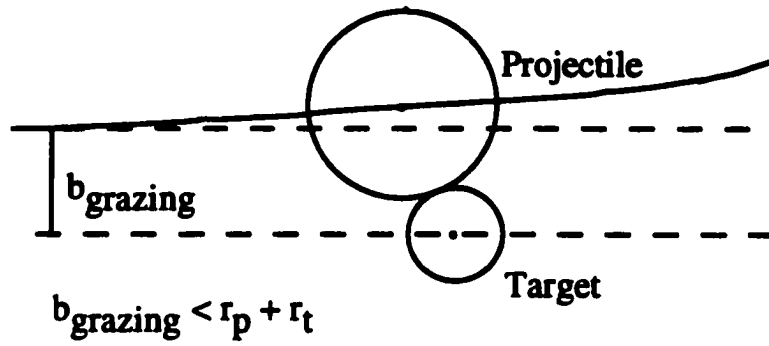
from low energy central collisions. In more peripheral collisions, deep-inelastic reactions that form projectile-like fragments (PLF) and target-like fragments (TLF) retain a memory of the incoming channel. Stochastic nucleon exchange models, along with statistical decay models, are used to predict experimental results and have met with a good deal of success. These low energy collisions are fairly well understood, and are controlled to a large part by the mean-field effects of the nuclear potential.

In high-energy the system is viewed as a collection of nucleons. The reactions can be viewed as geometric in nature, such as in a participant-spectator scenario [Day86]. Nucleons that are in the region of overlap between the projectile and target are considered participants in the reaction, whereas the other nucleons are considered spectators. The participant nucleons can be sheared off the projectile leaving the spectator nucleons whizzing off at beam velocity. These reactions are dominated by the hard scattering of participant nucleons. Between these two energy regimes is the intermediate energy region (20 MeV$< E_{beam}$/A $<$100 MeV). Both mean field and hard scattering considerations need to be accounted for. This interplay between the mean field and hard scattering makes theoretical description of these reactions difficult.

The intermediate energy region has stimulated a wide array of research interests. In the low energy scenario, the moderately excited compound nucleus survives long enough for the system to reach thermal equilibrium before decaying via a chain of particle emissions and fission. Entering into the intermediate energy, the excitation energy of the system increases and the time between successive emissions decreases. When the time between successive decays becomes small enough, the system can no longer reach thermal equilibrium. Eventually, with enough excitation, the system may explode in one multifragment decay. It is not known at what excitation energy multifragmentation becomes the dominant decay mode. The method by which the system breaks apart is also unclear. Some multifragmentation models

4

assume that the nucleus undergoes a liquid-gas transition, and recently "caloric curves" have been measured for several systems [LEE97] showing a plateau in temperature with increasing excitation energy. The plateau is analogous to the plateau in the temperature with increasing energy in water as it boils. Other models assume a statistical break-up of the compound system after some degree of equilibration. Dynamic models, which calculate the phase space coordinates of individual nucleons, predict the formation of "neck regions" and other non-spherical geometries where particles are emitted from nonequilibrated systems.

Studies of a the systems, ^{124,136}Xe + ^{112,124}Sn at E/A = 55 MeV [Sob97] and Xe + Sn at E/A=50 MeV [Luk97] have claimed that dynamic effects different than the deep-inelastic mechanism are occurring and intermediate mass fragments ($2 < Z < Z_{beam}/2$) may be the result of emission of particles from the neck region. However, orbiting patterns in the deflections functions from ^{136}Xe + ^{209}Bi at E/A=28 MeV [Bal95] show strong evidence of deep-inelastic reactions.

I.A Deep-Inelastic Reactions

Deep-inelastic or damped reactions have been extensively studied with low energy heavy-ion reactions [SCH84, TOK92] and bridge the gap between direct reactions (pickup/stripping of a nucleon) and compound nucleus formation. Deep-inelastic reactions occur for collisions with impact parameters larger that the impact parameter associated with the critical angular momentum (ℓ_{crit}) for fusion and smaller than the grazing impact parameter (b_{gr}). The value of ℓ_{crit} is the maximum angular momentum that the system can have and still fuse. The value of b_{gr} corresponds to the impact parameter where the distance of closest approach of the projectile and target is the equal to the sum of the projectile and target radii.

Deep-inelastic reactions occur when the projectile and target overlap to form a dinuclear system. A window for nucleon exchange opens, and nucleons pass through

5

it carrying angular momentum and kinetic energy with them. Large amounts of excitation energy can be generated in the dinuclear system. The amount of excitation energy in the system is a function of the number of nucleons exchanged. As the projectile and target overlap, the dinuclear system rotates and then separates, forming a projectile-like fragment (PLF) and a target-like fragment (TLF). The system rotates while the nuclei are in contact due to conservation of angular momentum. The larger the angular momentum, the faster the system rotates, but the shorter the system stays in contact. The smaller the angular momentum, the slower the system rotates, but the longer the system stays in contact. This effect leads to focusing of the PLF around the grazing angle. In addition the longer the system is intact, the more nucleons are exchanged, and the system becomes more excited.

I.B Signatures of Deep-Inelastic Reactions

The double differential cross section, $\partial^2\sigma/\partial E\partial\theta$, or deflection function as this E and θ dependence is commonly called, is used as a signature of rotation in a deep-inelastic reaction. In deep-inelastic reactions, the PLF is focused toward the grazing angle. However, as the impact parameter decreases, the system rotates and the PLF goes to smaller angles, as seen in Fig. I.2. The rotation will eventually pass through zero degrees and enter into negative angles. As the amount of rotation increases, the PLF scattering angle is larger and the kinetic energy decreases. The double differential cross-section for potassium isotopes in an ^{40}Ar + ^{232}Th reaction at 388 MeV is shown in Fig I.3 [SIW76]. A large peak corresponding to quasi-elastic events is seen. The ridge of products with lower energy and smaller angles are events where the dinuclear system rotates longer and more kinetic energy is converted into excitation energy. As the system passes through zero degrees, a second ridge is seen where the products continue to lose energy, except the scattering angle increases.

6

Figure I.2 A schematic showing the scatter angles arising from the different classical trajectories.

energy decreases

deflection angle

$R_p + R_t$

ℓ_{crit} ℓ_{max}

ℓ

8
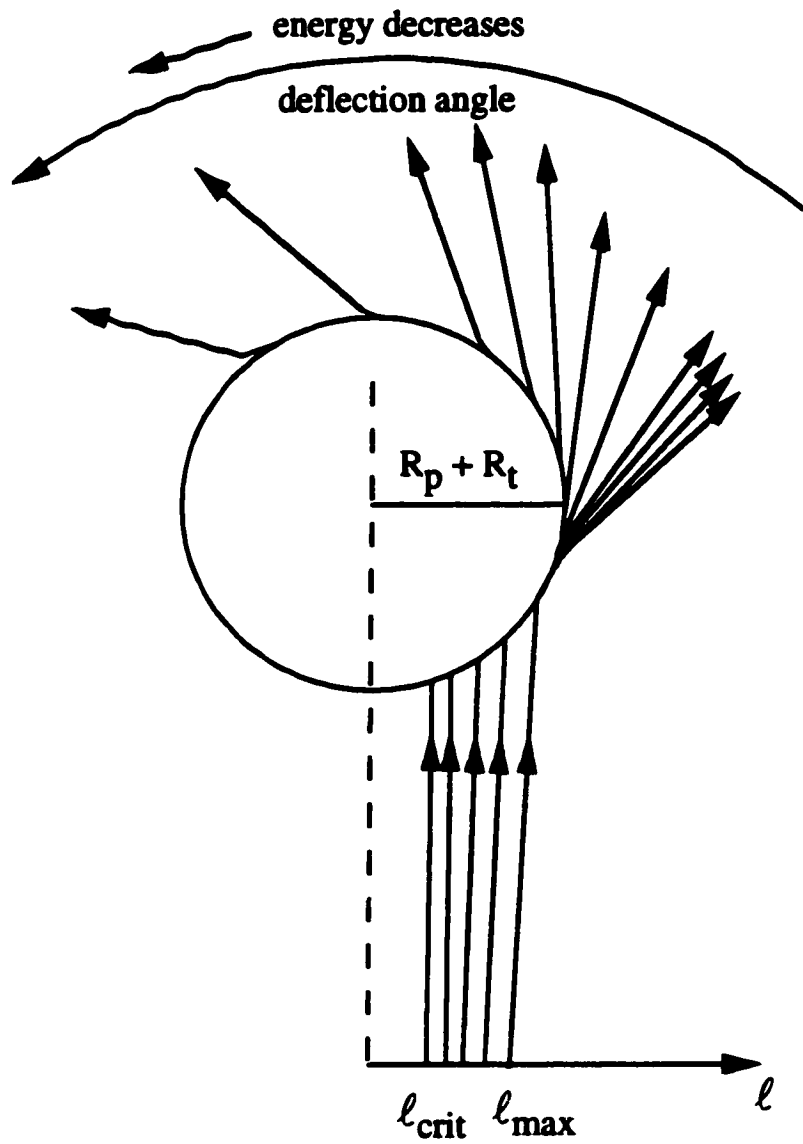
Figure I.3 The deflection function for potassium ions for the reaction ^{232}Th + ^{40}Ar at

388 MeV. The circles are calculations for angular momentum values ranging from ℓ =

180$\hbar$ to ℓ = 250$\hbar$ [SIW76].

9

$^{232}Th(^{40}Ar, K)Ac$

10
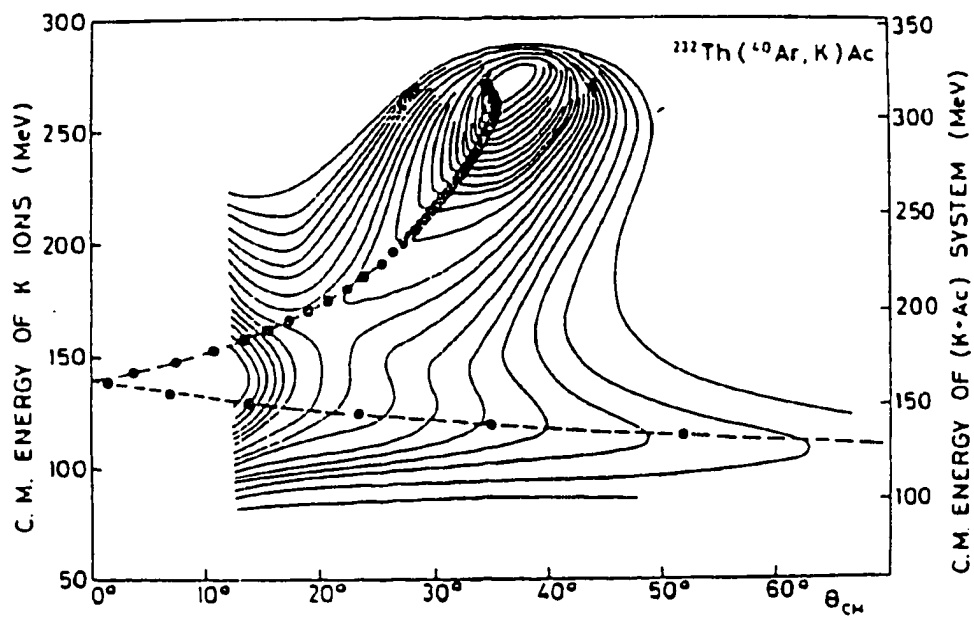
This is the negative angle scattering ridge. The dots on the figure represent a model calculation performed with $\ell = 180\,\hbar$ to $\ell = 250\,\hbar$ [SIW76].

Another signature of the deep-inelastic reaction is the broadening of mass and charge distributions with increasing total kinetic energy loss (TKEL). This is viewed as an indication of the nucleonic exchange process. A deep-inelastic reaction will have a smooth mean charge with increasing TKEL. The mean charge and charge widths as a function of the TKEL for ^{56}Fe + ^{165}Ho at E/A = 12 MeV [Mad95] are shown in Fig. I.4 (a) and (b), respectively. The arrow is the value of the TKEL associated with the entrance channel Coulomb barrier.

I.C Signatures of Other Mechanisms

If a participant-spectator mechanism is occurring, then the signatures of the reaction would be different than those for a deep-inelastic reaction. The size of the projectile spectator is a measure of the impact parameter. A large projectile spectator means that there was very little overlap of the system (peripheral collision), and a small projectile spectator indicates a more central collision [WES76]. The velocity of the projectile spectator is very nearly beam velocity, so the mean velocity should not change with the Z of the projectile spectator. In addition, the width of the charge distribution should not change much with increasing energy loss and be very small. The mean of the velocity distributions should be near the beam velocity for all Z's.

I.D Research Goals

The goal of this research project is to examine the extent to which the deep-inelastic mechanism is responsible for the production of PLF's in E/A = 30, 40, 50, and 60 MeV ^{129}Xe + ^{nat}Cu and ^{nat}Sc reactions. In order to study PLF's, a detector with the ability to identify a large range of products over a large range of energies was built. Since PLF's from deep-inelastic reactions are focused towards the grazing angle, which goes from 1.0" in the Xe + Sc at E/A = 60 MeV system to 2.8" in the Xe

11

Figure I.4 The (a) mean charges and (b) charge widths as a function of TKEL for the system ^{56}Fe + ^{165}Ho at E/A=12 MeV [Mad95]. The arrow in the figure is the value of the TKEL associated with the entrance channel Coulomb barrier.

12

13
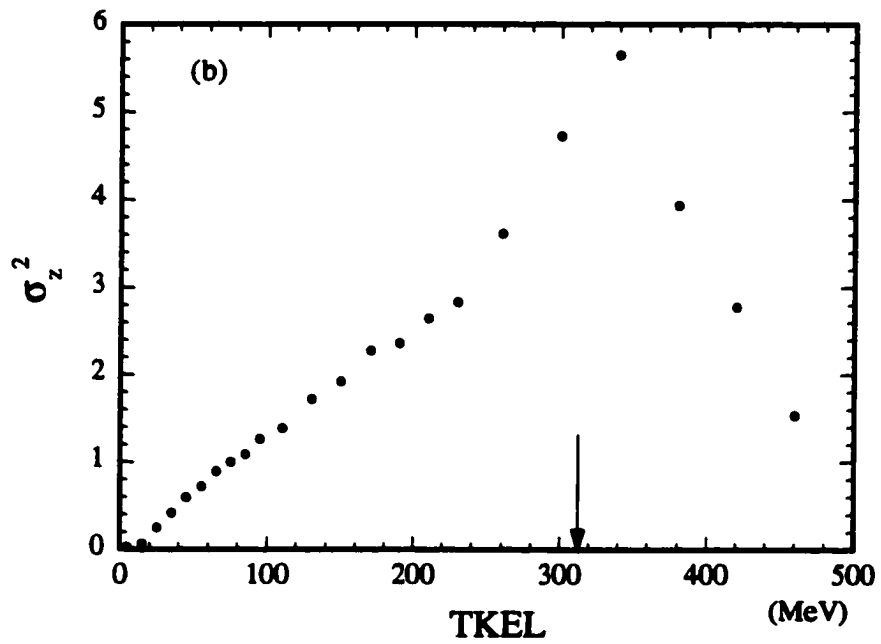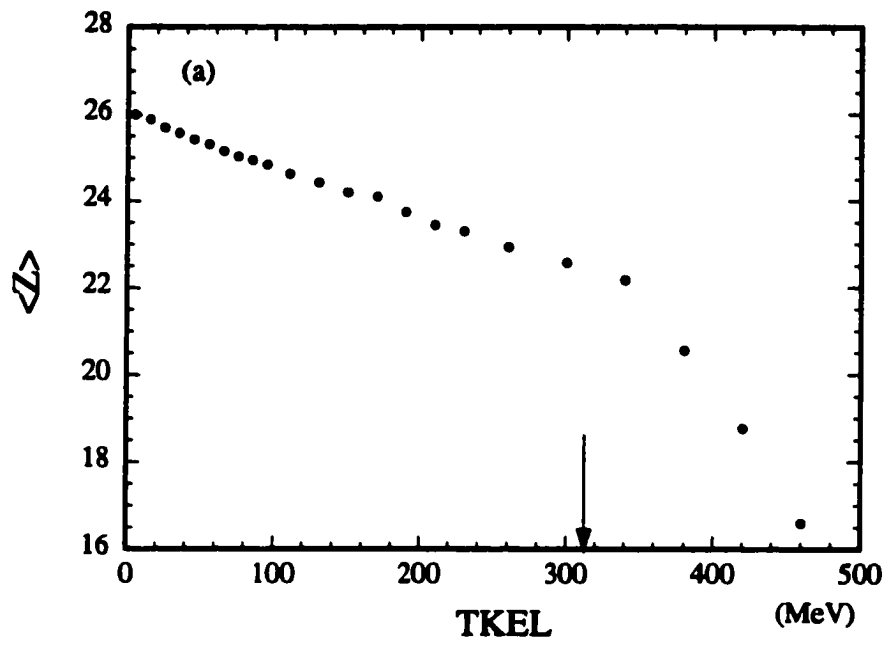
+ Cu at E/A = 30 MeV system, the new detector sits at very forward angles. The detector needs to be fast and durable since it receives a large number of events. The new detector, the Maryland forward array (MFA), is a segmented silicon-plastic-plastic detector telescope.

The data from the MFA will be compared to Tassan-Got's stochastic nucleon exchange model [TAS91] to see if a deep-inelastic model can predict the experimental results. In addition, the data will also be compared to a BUU model which will see if a microscopic model can predict the experimental results.

The experimental technique and equipment used in the experiment are described in Chapter II. Chapter III describes the results of the experiment. Descriptions of Tassan-Got and BUU models and the results of the model calculations are presented in Chapter IV. A comparison of the models and experimental results can be found in Chapter V. Finally a summary of the results for each system and concluding remarks are in Chapter VI.

14

Chapter II Experimental Details

The experiment was performed at the National Superconducting Cyclotron Laboratory (NSCL) on the campus of Michigan State University (MSU) as experiment 93046. A beam of ^{129}Xe at E/A = 30, 40, 50 and 60 MeV was extracted from the K1200 cyclotron. In addition, beams of ^{4}He, ^{12}C, ^{16}O, ^{40}Ar, and ^{84}Kr at E/A = 40 MeV and 60 MeV were extracted as calibration beams. Reaction parameters for the Xe + ^{nat}Cu calculated using the systematics of the Atomic Data and Nuclear Data Tables [WIL80] are listed in Table II.1 for a natural Cu (A = 63.546) target.

Table II.1 Reaction Parameters for ^{129}Xe + ^{nat}Cu and (^{nat}Sc)

	30 MeV/A	40 MeV/A	50 MeV/A	60 MeV/A
R_{int} (fm)	12.94	12.94	12.94	12.94
	(12.46)	(12.46)	(12.46)	(12.46)
V_{coul} (MeV)	174.33	174.33	174.33	174.33
	(131.03)	(131.03)	(131.03)	(131.03)
E_{cm} (MeV)	1277.22	1702.96	2128.70	2554.70
	(1000.13)	(1333.51)	(1666.89)	(2000.27)
$\theta_{graz,Lab}$ (deg)	2.77	2.04	1.61	1.31
	(2.08)	(1.53)	(1.21)	(1.00)
$\theta_{graz,cm}$ (deg)	8.40	6.18	4.89	4.05
	(8.04)	(5.92)	(4.69)	(3.88)
ℓ_{crit} ($\hbar$)	115.96	115.96	115.96	115.96
	(108.00)	(108.00)	(108.00)	(108.00)
ℓ_{max} ($\hbar$)	613.00	721.69	816.02	900.53
	(463.94)	(545.71)	(616.74)	(680.39)

15

II.A Experiment Setup

The beam was directed into the N2 vault at the NSCL which contains the MSU 4π array [WES85], a 32 element truncated icosahedron (soccer ball) with 20 regular hexagonal sides and 12 regular pentagonal sides, with an approximate outer radius of 1 meter. The front and back pentagons were removed for the beam entrance and a forward array. The beam current was measured using a faraday cup at the end of the beam line. The 4π array was augmented with a new far forward array, the Maryland Forward Array (MFA) [RUS97], which fits inside the forward array of the 4π. The targets were 1.3-mg/cm^2 thick copper, 1.0-mg/cm^2 thick scandium and 0.4-mg/cm^2 thick gold. The current analysis of this experiment is limited to the study of the projectile-like fragments measured by the MFA.

II.B Maryland Forward Array

The MFA is an array of 16 silicon-phoswich detectors forming a circle centered on the beam axis, as shown in Fig. II.1. The inner and outer diameters of the MFA are 2.4 cm and 4.8 cm, respectively. Mounted inside the MSU 4π array, the MFA sits 96 cm from the target. The active region covers between 1.4° to 2.9° in the laboratory. The active area of one of the MFA segments is 3.39 cm^2 or a solid angle of 0.368 msr. The total active area is 54.29 cm^2 or 5.89 msr.

Phoswich detectors are commonly used to measure the intermediate mass fragments produced in intermediate energy heavy-ion reactions. They consist of a fast and slow plastic element sharing a single photomultiplier tube (PMT). The thin piece of fast scintillating plastic, the ΔE detector, is optically coupled to a thick piece of slow scintillating plastic, the E detector. The fast and slow plastics have different response times. The PMT signal, which is the sum of the ΔE and E signals, can be separated into the ΔE and E components by splitting the PMT signal and sending each

16

Figure II.1 A schematic of the Maryland forward array showing the different parts of the array

17

Silicon

Fast plastic

Slow plastic

Light guide

Photomultiplier tube

Beam

18
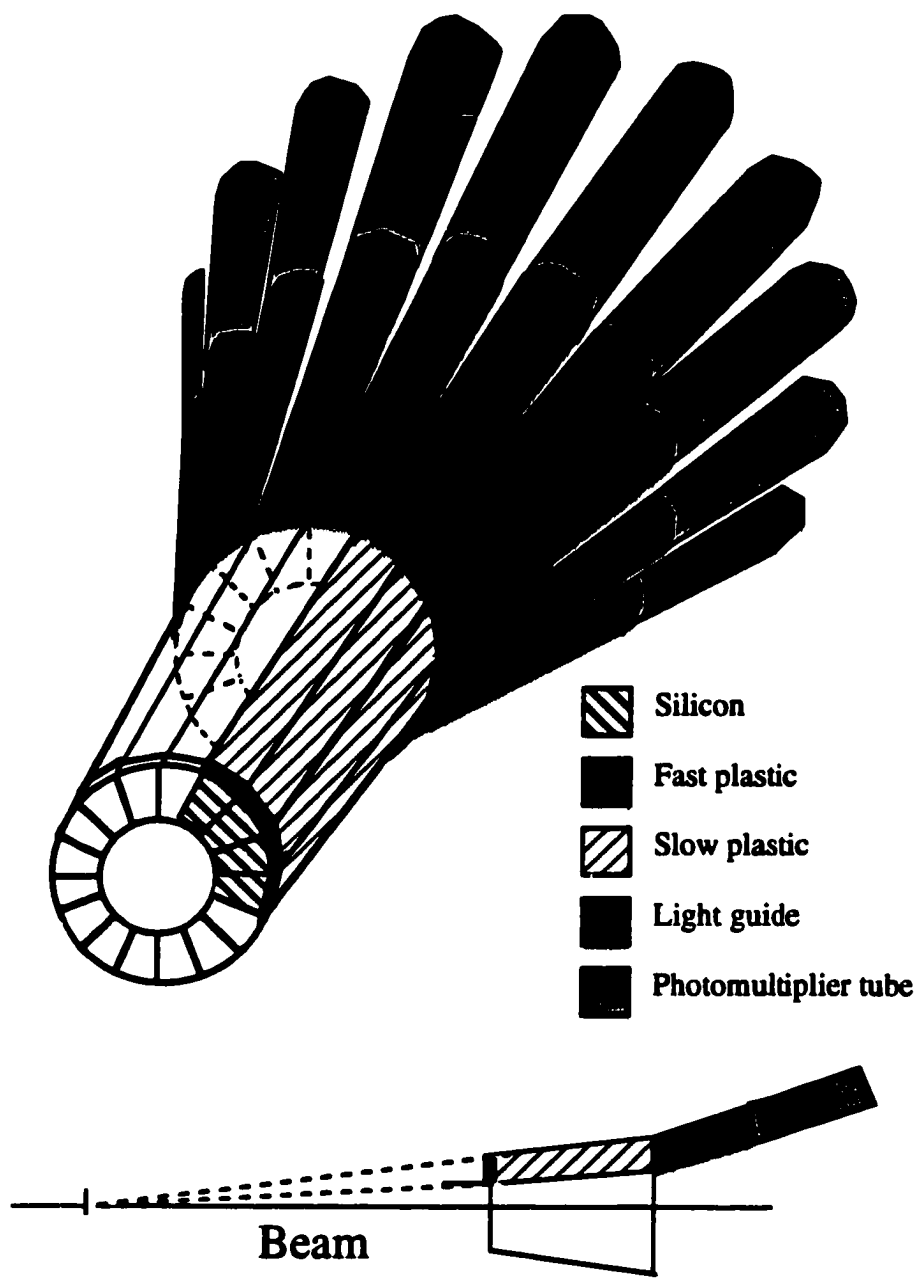
of the split signals into charge integrating analog to digital converters (QDC's). The two QDC's have different time gates over which they are integrated. The first QDC time gate is set corresponding to a peak in the ΔE signal. The second QDC time gate is set corresponding to a later time when the ΔE signal has decayed away. The integrated values are proportional to the light output of the plastic detectors, which in turn is related to the energy deposited.

The ΔE detector used by the MFA consists of 1.0 mm of BC400 fast plastic. The fast plastic has a characteristic rise time of 0.9 ns and a decay time of 2.4 ns. The E detector consists of 10. cm of BC444 slow plastic. The rise time of the slow plastic is 19.5 ns, and the decay time is 179.7 ns. Physical properties of the fast and slow plastics are shown in Table II.2. The phoswich is optically coupled to a Hammumatsu R1924 PMT via a BC800 light guide.

Table II.2 Technical Specifications for the Scintillating Plastic

	Fast Plastic	Slow Plastic
Material	BC400	BC444
Light Output	65 % Anthracene	45 % Anthracene
Rise Time	0.9 ns	19.5 ns
Decay Time	2.4 ns	179.7 ns
Density	1.032 g/cm^3	1.032 g/cm^3

The voltages on the PMT's are set with a LeCroy 1440 HV power supply. Using the LeCroy 1440, voltages can be set and monitored remotely using a computer outside the vault. The voltages were set around -900 V, and were checked throughout the experiment.

19

Figure II.2 A schematic of the front and back of the silicon detector used with the

Maryland forward array.

20

front (cm)

back (cm)

21
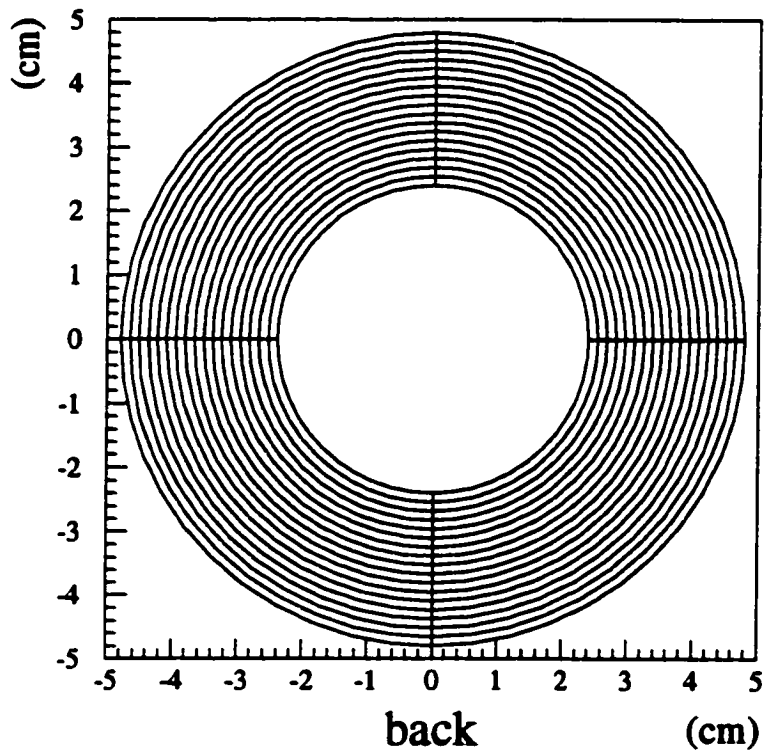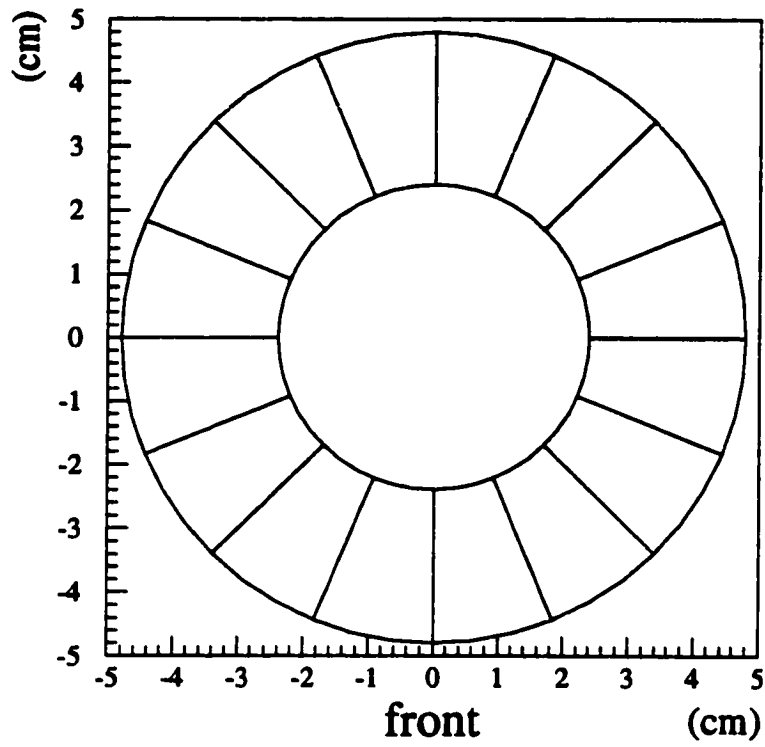
A schematic of the silicon detector is shown in Fig. II.2. The silicon element of the MFA is a Micron Semiconductor design S (Heildelberg) annular silicon detector. This commercially available detector is a 2-sided 300.-μm thick silicon wafer. The detector is fully depleted at 20.5 V. On the front face the detector is segmented into 16 equal arcs of 22.5°. On the back are 16 concentric rings broken into quadrants for a total of 64 strips.

II.C Maryland Forward Array Electronics

The electronics for the phoswich element of the MFA were designed to match the electronics for the MSU 4π array, the intention being that, for data acquisition purposes, the MFA would look like the rest of the MSU 4π. An electronics diagram for the MFA is shown in Fig. II.3. A complete description of the 4π array electronics can be found in MSU 4π LUsers guide [CEB89], along with a complete description of each of the modules used in the setup.

A signal from the MFA's PMT was amplified and split into 3 similar signals using a passive splitter box specially designed for the MSU 4π [CEB89]. Each splitter module had 16 BNC inputs and 48 (3 groups of 16) ECL outputs. One set was delayed by 300 ns and placed in the ΔE Fast Encoding Readout ADC (FERA) to be read into the computer. The second set was delayed by 150 ns and placed in the E FERA. The FERA integrated the signal it received from the PMT while a gate was opened. The ΔE and E FERA's had different time gates so that they would integrate different parts of the PMT signal. The FERA's in this experiment were set in zero suppression mode, meaning that if, after pedestal subtraction, there was a zero value in an ADC channel, then no data word was written into the data stream. The third set of signals was placed into a 16 channel Phillips discriminator and used to set the trigger logic and ADC gates.

22

Figure II.3 Diagram of the electronics for the MFA used in experiment 93046.

23

24
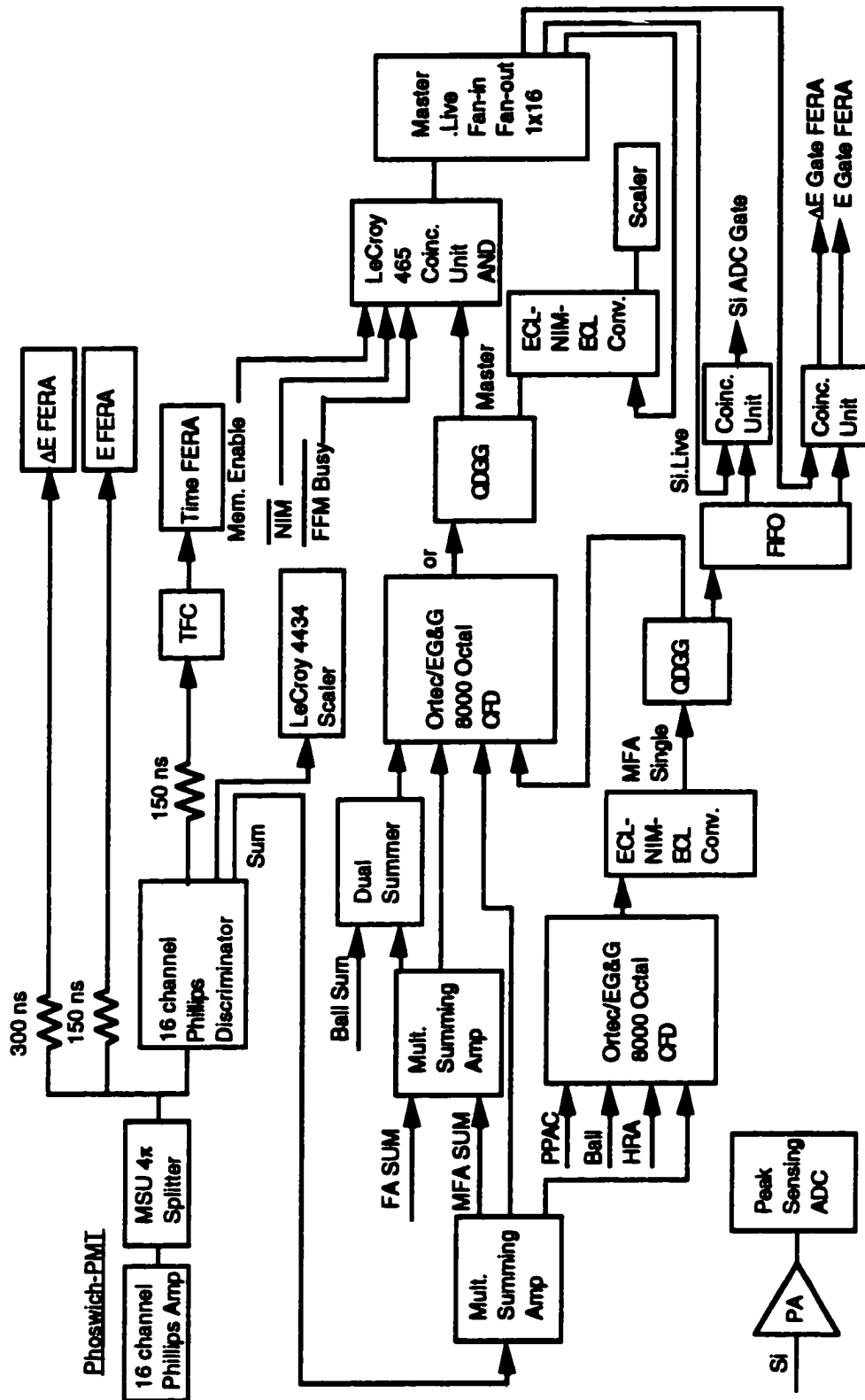
The signals from the silicon detectors were pre-amplified with NSCL quint preamplifiers and then shaped using NSCL shaping amplifiers. The shaped pulse height was proportional to the energy deposited in the silicon detector. Gates for the peak sensing ADC's were created by the MFA signal.

II.D Calibration of the Maryland Forward Array

The MFA was designed to identify the charge and measure the kinetic energy of a fragment. The method used to calibrate the MFA has undergone many iterations. It has spanned the range from simple to highly complex before settling in on the method described here. The general philosophy behind the calibration is to decide if the fragment stops in the fast plastic, slow plastic, or neither. If a fragment stops in the fast plastic, then the silicon and fast plastic detectors are used to identify the fragment. If the fragment stops in the slow plastic, then the fast and slow plastic detectors are used. If neither of these situations occur, then the MFA cannot identify the fragment and the fragment is discarded.

II.D.1 Energy Calibration of the Silicon Element of the MFA

The energy calibration for the silicon detector was performed using the centroids of elastic peaks of several calibration beams. The pulse height of the silicon signal responds linearly with the amount of energy deposited. Energy loss calculations were performed using *MFA_ELOSS*, a FORTRAN computer code based on Zieglar systematics [BIR89,ZIE80]. No pulse height defect corrections were attempted because the particles that are identifiable do not stop in the silicon detector [KEH92, MOU78]. The calibration results for one of the 16 silicon segments are shown in Fig. II.4.

25

Figure II.4 The raw silicon detector ADC value versus the elastic energy of the beam.

26

y-axis: E_{Si} (MeV)

x-axis: Si channels

— linear fit
y = 608.06 + 1.6155 x
R = 0.99998

27
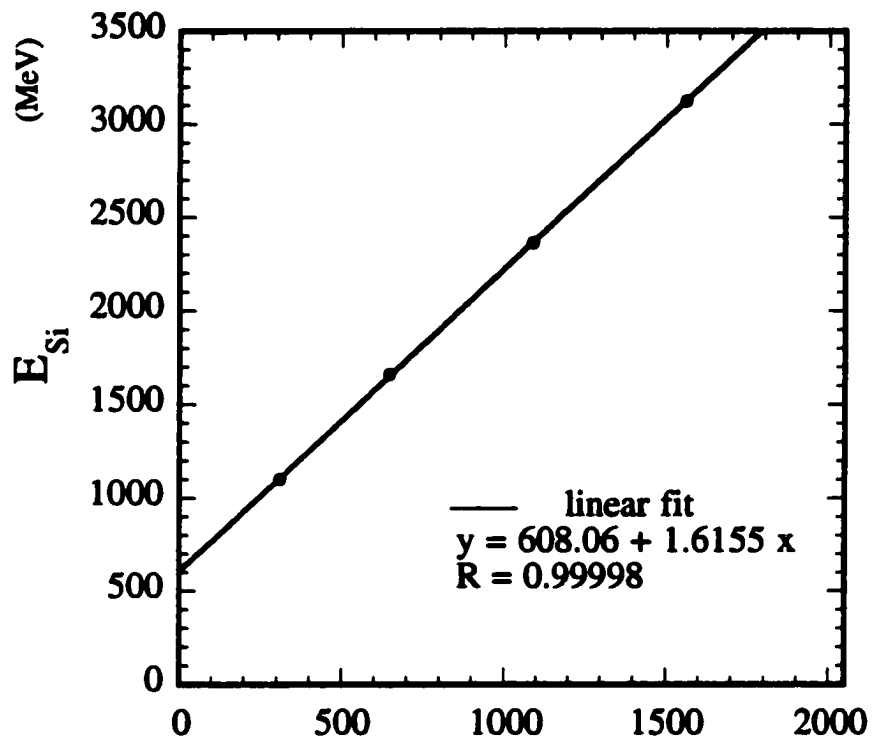
II.D.2 Light Output of the Scintillating Plastic Detectors

The light output from scintillating plastic detectors is inherently non-linear. Over the range of Z and E in this experiment, the light output has a strong non-linear Z and E dependence. This makes particle identification and energy calibration difficult. Also, since the fast and slow plastics share a single PMT, some of the light from the fast plastic will be digitized in the slow gate and some of the light from the slow plastic will be digitized in the fast gate. It is necessary to decompose the signals from the raw *fast* and raw *slow* QDC values into values that are a function of the light output from only the ΔE detector, the ΔL value, and a value that is a function of the light from only the E detector, the L value. A 2-dimensional *fast* versus *slow* histogram for the MFA is shown in Fig. II.5. The data fall between 2 lines. The first, the punch-in line, is a collection of particles that stop in the fast plastic. These particles deposit no energy in the slow plastic. All the light is from the fast plastic and the points should fall on the y-axis (L = 0). The other line, the neutral line, consists of neutral particles and cosmic rays which leave little to no energy in the fast plastic. The neutral line should fall along the x-axis (ΔL = 0). The decomposition into ΔL and L is equivalent to pulling the neutral line and punch-in lines onto the x and y axes, respectively. Typically, a linear mapping is performed [CEB92], however for the MFA a linear mapping cannot be used because the punch-in "line" is a curve.

The method used to decomposed the signals is similar to a linear mapping. Two functions, $f(slow)$ and $g^{-1}(fast)$, are subtracted from the *fast* and *slow* values, respectively, to take into account the light from slow and fast plastics. The mapping is done using the following equations:

$$\Delta L = (fast - Y_0) - f(slow),$$ (II-1)

$$L = (slow - X_0) - g^{-1}(fast).$$ (II-2)

28

Figure II.5 Scatter plot of the raw *fast* versus *slow* ADC values.

29
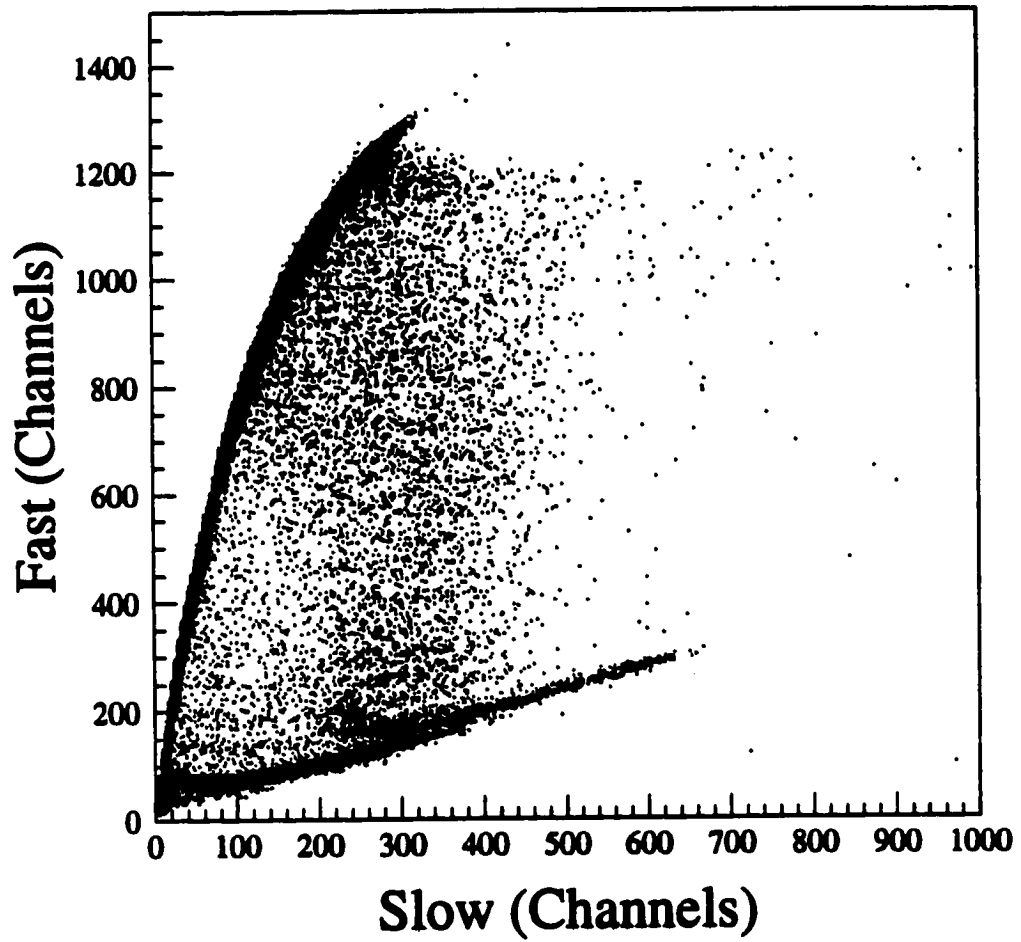
In the linear case [CEB92], $f(slow) = k_n(slow - X_0)$, and $g^{-1}(fast) = (fast - Y_0)/k_p$, where k_n and k_p are the slopes of the neutral line and the punch-in lines, respectively. The intersection of the punch-in and neutral lines is the point (X_0, Y_0), and is a measure of the offset in the QDC. In principle, the punch-in curve can be fit to a function of the *slow* signal. However, inverse functions can be difficult to calculate depending on the function chosen. In order to simplify the procedure, data are plotted as a *slow* versus *fast* 2-dimensional histogram. Fitting the function in this manner gives the inverse function $g^{-1}(fast)$ directly. The punch-in curve is fit to a linear + exponential function

$$g^{-1}(fast) = e^{(a+b\,fast)} + c + d\,fast, \tag{II-3}$$

where a, b, c and d are fitted parameters. The linear + exponential function has the property of being approximately linear for small values of the raw *fast* signal. This being the case, the point (X_0, Y_0) can be calculated assuming 2 straight lines. The first line is the neutral line, the second line is the line tangent to the punch-in curve at *fast* = 0. This line should approximate the punch-in curve for small raw *fast* values. The slope of this line is given by $g^{-1}(0)$, and the intercept is $g(0)$. For the linear + exponential function,

$$\text{slope} = g'(0) = \frac{1}{g'^{-1}(0)} = \frac{1}{be^a + d} \tag{II-4}$$

and

$$\text{intercept} = g(0) = \frac{g^{-1}(0)}{g'^{-1}(0)} = \frac{e^a + c}{be^a + d}. \tag{II-5}$$

The linear approximation can be interpreted in another way. It is an ideal response for the detector. Under this assumption, for every value of the raw *fast* signal, there is a *fast'* signal which is the ideal response of the detector. The *fast'* value is a linear extrapolation of the low energy response of the scintillating plastic for

31

all points, including those not on the punch-in curve. It should be noted that this method does not include any contribution to the non-linearity caused by the slow plastic, or by a mixed *fast-slow* term. The *fast* value is given by

$$fast' = \frac{e^{(a+b\,fast)} + c + d\,fast - e^a - c}{b\,e^a + d},$$ (II-6)

where a, b, c, and d are the same parameters as in Eq. II-3. A *fast* vs. *slow* distribution is shown in Fig. II.6. The *fast* vs. *slow* distribution is linearly mapped using Eqs. II.4 and II.5 to put the punch-in curve on the ΔL axis and the neutral curve on the L axis. The L and ΔL values are used to identify the fragment, and calculate the fragment's kinetic energy.

II.D.3 Particle Identification of Fragments

In order to identify the fragments, the detector that the particles stops in must be known. A threshold value is set on the L value to discriminate whether or not a particle made it into the slow plastic. For particles to be identified, it is also required to have a ΔL value. As seen in Table II.3, a flag is set on these conditions specifying the set of detectors to use for particle identification.

Table II.3 PID Flags and their Meaning

Condition	Description	Value
$\Delta L{>}0$ AND L<20	Particle is identified with the silicon and fast plastic detectors	flag = 1
$\Delta L{>}0$ AND L<20	Particle is identified with the fast and slow plastic detectors	flag = 2
Else ($\Delta L{\leq}0$)	Particle cannot be identified	flag = -3

32

Figure II.6 Scatter plot of the *fast* versus the *slow* ADC values.

33

34
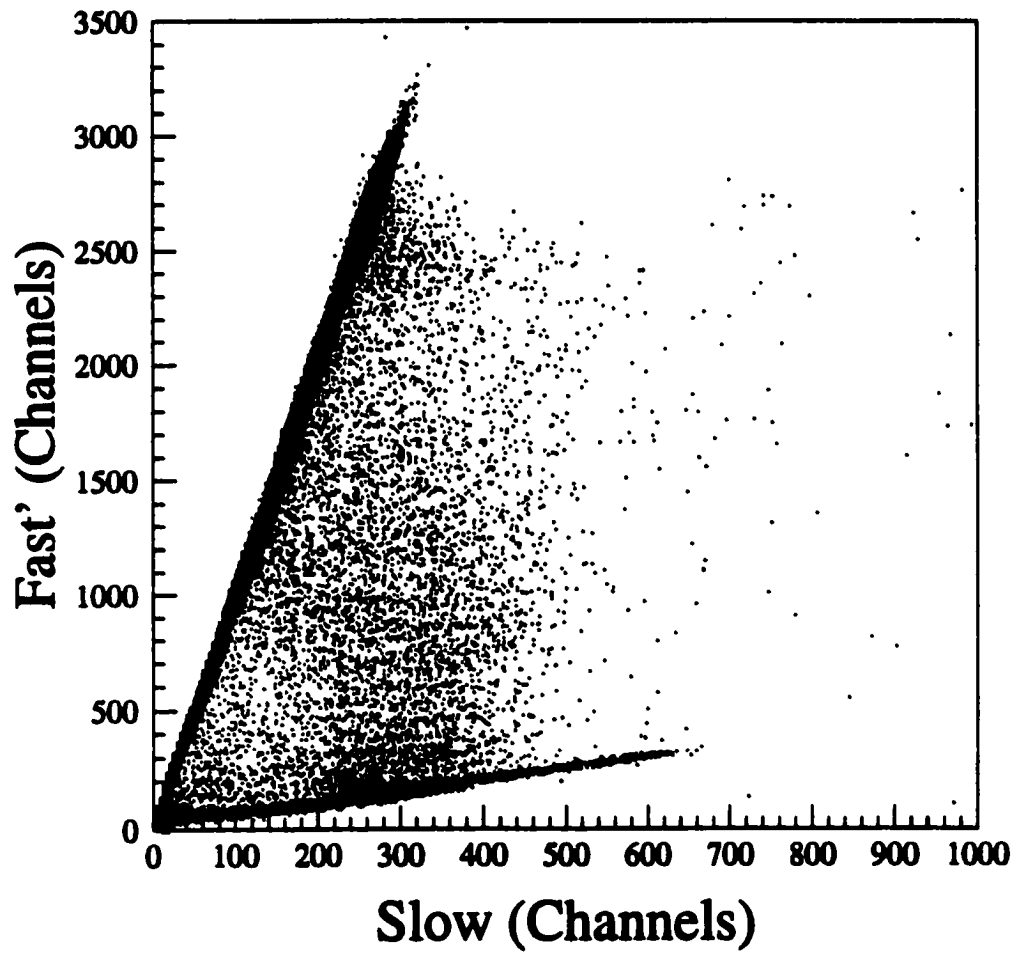
For the plastic detectors, the centroids of the elastic peaks for the calibration beams were calibrated using,

$$\Delta L = a_1 \Delta E^{b_1} Z^{c_1} \qquad \text{(II-7)}$$

and

$$L = a_2 E^{b_2} Z^{c_2}, \qquad \text{(II-8)}$$

where a_1, a_2, b_1, b_2, c_1 and c_2 are constant for a given detector and ΔE and E are the energy deposited in the fast and slow plastic detectors, respectively. The values of a_1, a_2, b_1, b_2, c_1 and c_2 are given in Table A.1.

Using Eqs. II-7 and II-8, an energy loss computer code can be modified to calculate ΔL and L values. Energy loss calculations for each Z from 2 to 54 over an energy range from 2 to 70 MeV/A were performed. The energy loss calculations for Z = 6 and Z = 8 are shown in Fig. II.7. The dots represent the calculated points, and the x's are the data from the calibration runs. The function $\Delta L(L)$ was fit for each Z using the equation

$$\Delta L(L) = \frac{s_1}{s_2 + L} \qquad \text{(II-9)}$$

for points where the particle stopped in the slow plastic, with fitting parameters s_1 and s_2. The solid line in the Fig. II.7 is a fit using Eq. II-9. Since this is a calculation based on energy loss, the detector in which the particle stops is not ambiguous. The values of s_1 and s_2 are parameterized in terms of Z using a second order polynomial,

$$s_1(Z) = s_{10} + s_{11}Z + s_{12}Z^2 \qquad \text{(II-10)}$$

and

$$s_2(Z) = s_{20} + s_{21}Z + s_{22}Z^2. \qquad \text{(II-11)}$$

One problem that arises from the parameterization of $s_1(Z)$ is that it creates a region in the ΔL-L plot where there is no solution. A power-fit would be a better parameterization; however, upon substitution into Eq. II-9, it cannot be solved

35

Figure II.7 The calculated ΔL and L values for Z = 6 and 8. The dots represent calculated values for fragments with Z = 6 or 8 and E/A = 10 to 70 MeV. Points with L = 0 are removed. The x's are the ΔL and L values from the ^{12}C and ^{16}O beams at E/A = 40 and 60 MeV.

36

37
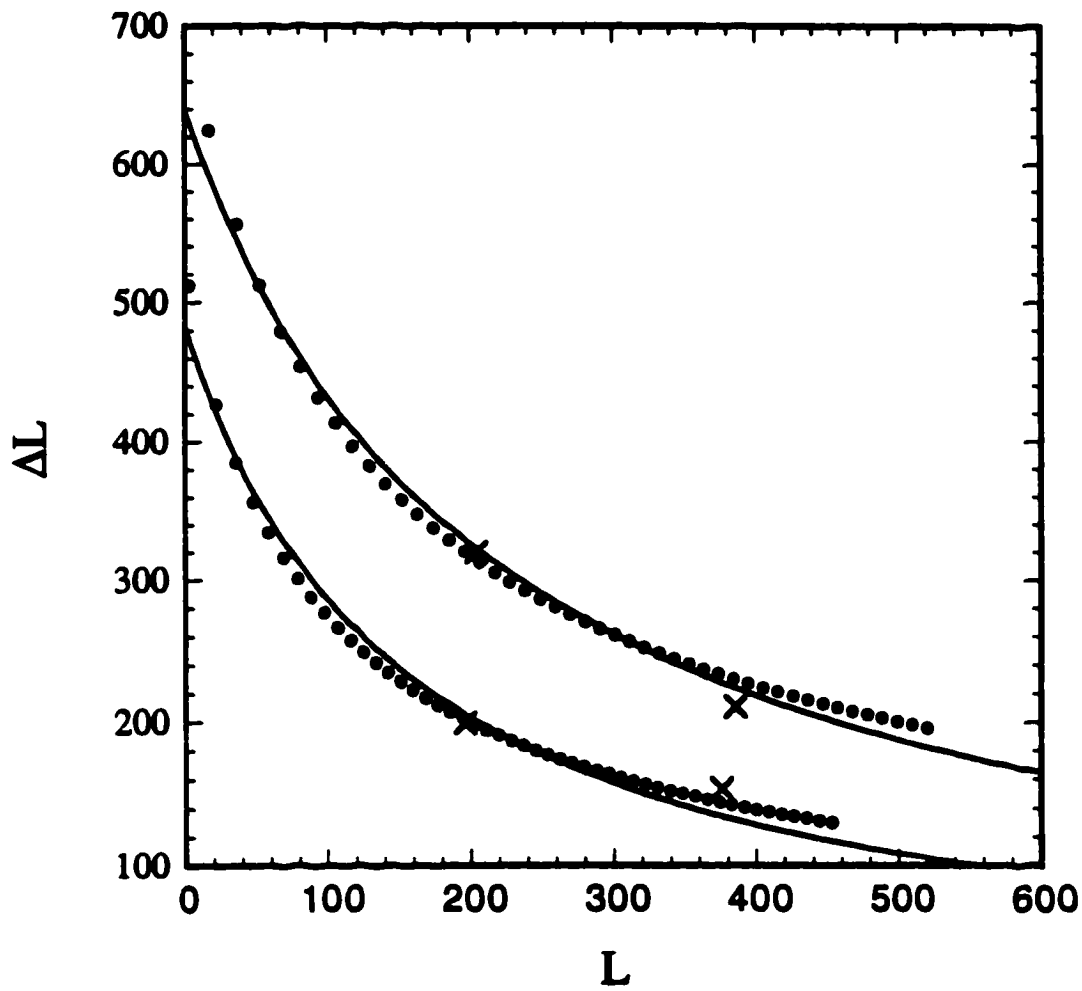
analytically. In order to minimize the size of the region where there is no solution, s_1 is refit using points for $Z < 20$. The values of s_{10}, s_{11}, s_{12}, s_{20}, s_{21}, and s_{22} are given in Table A.2. The second order fits are shown in Fig. II.8 for s_1, and s_2.

Substituting this parameterization into Eq. II-9 and collecting terms yields

$$(s_{22} - s_{12}) Z^2 + (s_{21} - s_{11}) Z + (s_{20} - s_{10} + \Delta L \; L) = 0, \qquad (II\text{-}12)$$

which has a quadratic form and can be solved analytically.

For particles that stop in the fast plastic, an analogous method is used. The function Si(ΔL) is fit to energy loss calculations using the equation

$$Si(\Delta L) = \frac{f_1}{f_2 + \Delta L}, \qquad (II\text{-}13)$$

where f_1, and f_2 are parameterized in terms of Z using a second order polynomial,

$$f_1(Z) = f_{10} + f_{11}Z + f_{12}Z^2 \qquad (II\text{-}14)$$

and

$$f_2(Z) = f_{20} + f_{21}Z + f_{22}Z^2. \qquad (II\text{-}15)$$

Substituting this parameterization into Eq. II-13 and collecting terms yields a form analogous to Eq. II-12,

$$(f_{22} - f_{12}) Z^2 + (f_{21} - f_{11}) Z + (f_{20} - f_{10} + Si \; \Delta L) = 0. \qquad (II\text{-}16)$$

The values of f_{10}, f_{11}, f_{12}, f_{20}, f_{21}, and f_{22} are given in Table A.3. The second order fits are shown in Fig. II.9 for f_1, and f_2.

II.D.4 Kinetic Energy of the Fragments

The kinetic energy of a fragment is calculated using the value from the stopping detector and the results of the energy loss calculations. The elements in front of the stopping detector are used as a degrader. The energy is Z dependent, so the particle identification must be done first. The function KE(ΔL) or KE(L) is fit to a polynomial; KE(ΔL) is used when the fragment stops in the fast plastic, and KE(L) is

38

Figure II.8 Polynomial fits to the parameters s_1 and s_2 used in Eq. 9.

a)

b)

40
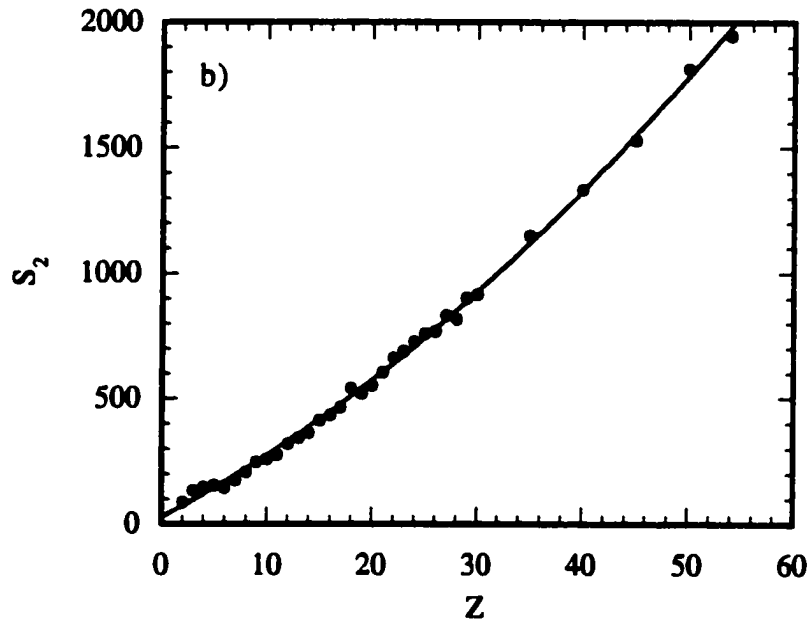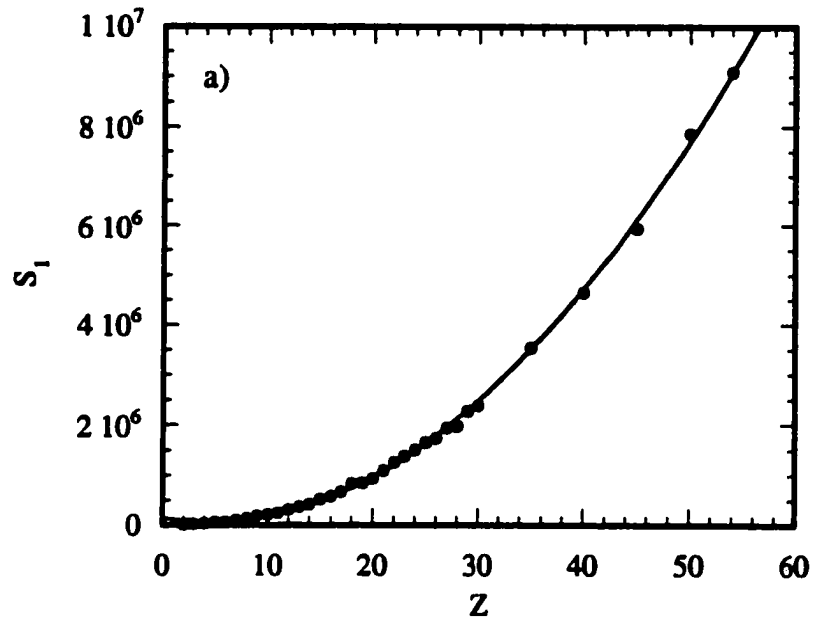
Figure II.9 Polynomial fits to the parameters f_1 and f_2 used in Eq. 13.

41

a)

b)

42
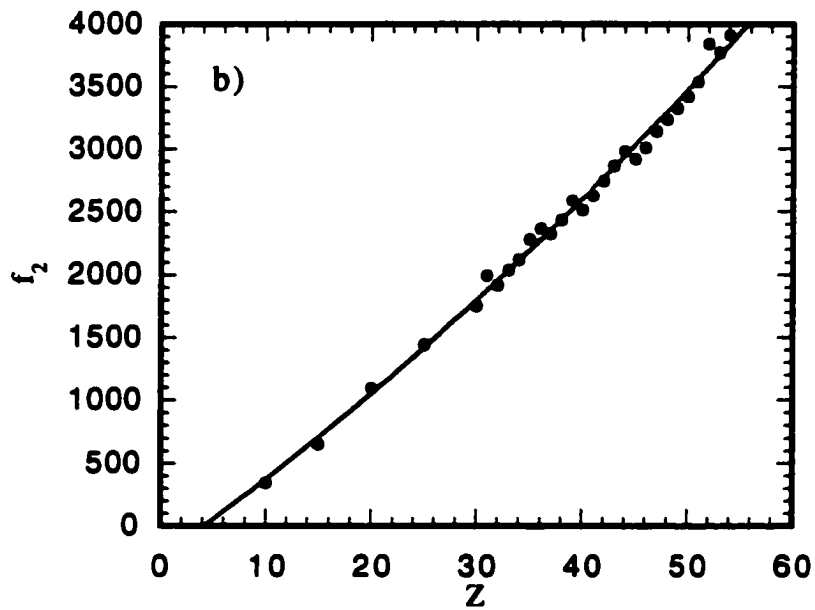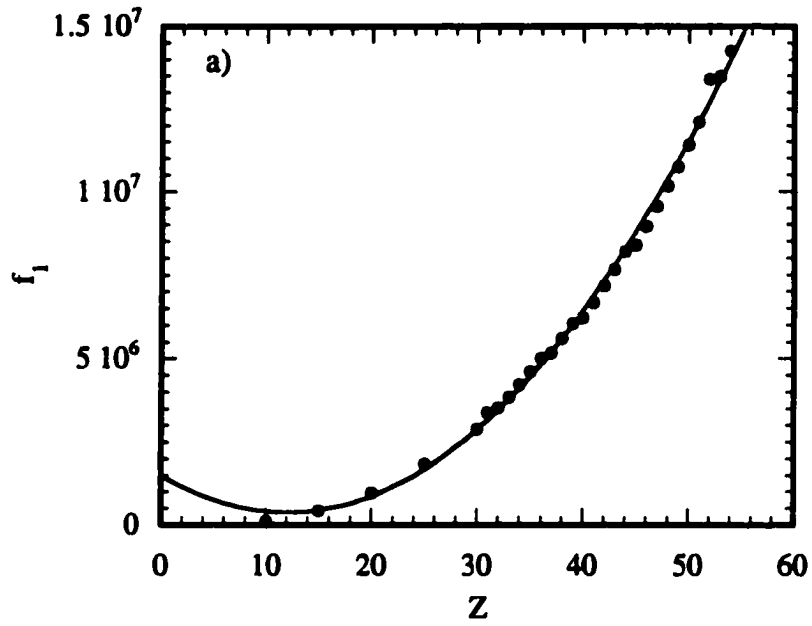
used when the fragment stops in the slow plastic. The function is parameterized in terms of a second order polynomial giving

$$KE(L) = m_2 L^2 + m_1 L + m_0 \qquad \text{(II-17)}$$

and

$$KE(\Delta L) = n_2 \Delta L^2 + n_1 \Delta L + n_0, \qquad \text{(II-18)}$$

where m_0, m_1, m_2, n_0, n_1, and n_2 are functions of Z. Each parameter is fit to a 2$^{\text{nd}}$ or higher order polynomial in terms of Z for each of the 16 detectors. Once the Z is identified using the method in Sec. II.D.3, the energy can be calculated from the ΔL or L using Eqs. II-7 or II-8. The fitting functions and their parameters for m_0, m_1, m_2, n_0, n_1, and n_2 are given in Tables A.4 and Table A.5.

After the energy and charge calibration, the data are compared to Eloss calculations for punching into and out of the detector, as shown in Fig. II.10 for a E/A = 50 MeV Xe+Cu system. The three solid lines are the detector energy threshold (labelled threshold w/Si), the energy where fragments enter the slow plastic (labelled punch into slow plastic), and the energy where the fragments punch out of the detector. The dashed line in is the detector threshold when the silicon detector is not used. There is no low Z data identified with the silicon - fast due to an offset in the Si ADC's.

II.D.5 Angular Identification

The position of a particle is measured by correlating which silicon strip and segment fired. The distance away from the center of the detector is measured by the strip that is hit. The strip number is converted to a distance in centimeters by using

$$d = 2.4 + \frac{2.4(17 - \text{strip})}{16}. \qquad \text{(II-19)}$$

The strip number is defined in this experiment as an integer from 1 to 16 with the outermost strip being defined as one, and the innermost strip as 16. Subtracting

43

Figure II.10 Calibrated charge vs. energy distribution for Xe + Cu at E/A = 50 MeV. The solid lines are an Eloss calculation showing the threshold of the MFA with the silicon detector, the energy required to punch into the slow plastic for each Z, and the energy required to punch out of the detector. The dashed line is the MFA threshold without the silicon detector.

44

Particle Kinetic Energy (MeV)

45
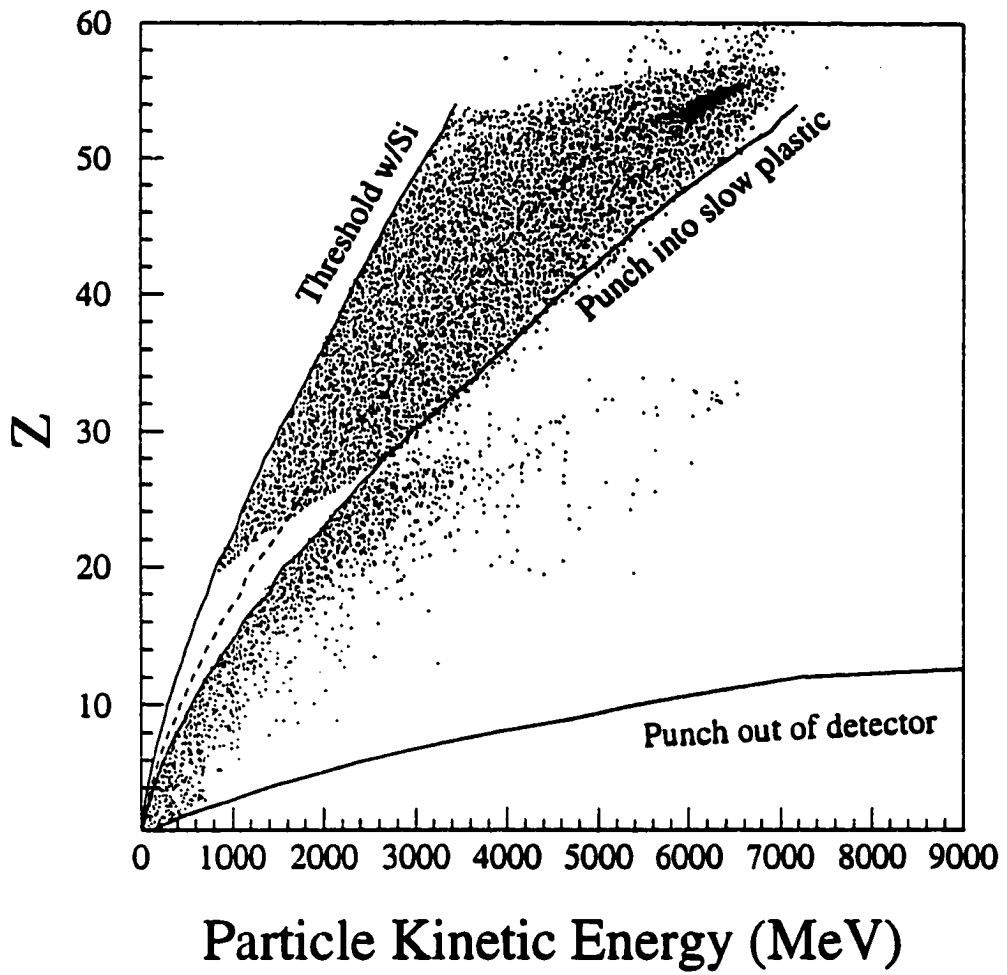
from 17 reverses the order in which the strips are defined. The constant 2.4 is the inner radius of the silicon detector, and the 2.4 in the numerator is the difference between the inner and outer radii. Figure II.11, shows the hit pattern on the silicon detector for one experimental run. If the beam was centered on the detector, the number of counts at a distance away from the center of the detector would be constant with respect to ϕ, with ϕ given by the segment,

$$\phi = 78.75 - 22.5 \ (\text{segment-1}), \tag{II-20}$$

where segment is an integer from one to 16. The numbering scheme for the segments starts at one, centered on 78.75°, and goes around the detector clockwise until it reaches 16, centered on 348.75°. As seen in Fig. II.11, the beam is not centered on the silicon detector. Since the silicon detector has fine angular resolution, it is necessary to correct for the beam position.

In order to calculate the beam position, a circle is with equal number of counts is created. The center of the circle is the beam position. A histogram of the distance away from the center of the MFA for one Si segment is shown in Fig. II.12. As seen in the figure, farther away from beam corresponds to less counts. The distribution for each Si segment is fit to a power law. By choosing one value for the number of counts, 16 distances can be calculated using the different power fits. These 16 distances, along with the ϕ value of the Si segment, are converted from polar coordinates (d, ϕ) to rectangular coordinates (X,Y). The origin of both of these systems is the center of the detector. These 16 points should lie in a circle centered on the beam position. The value for the number of counts should be chosen so that the 16 points that form the circle are within the detector. This is not a requirement, but since a power fit was used to calculate the distance, it is best not to extrapolate beyond the experimental data.

Figure II.11 Contour plot showing the hit pattern on the silicon detector . The data is smoothed by adding a random value to spread the data across the face of a detector segement.

47

48
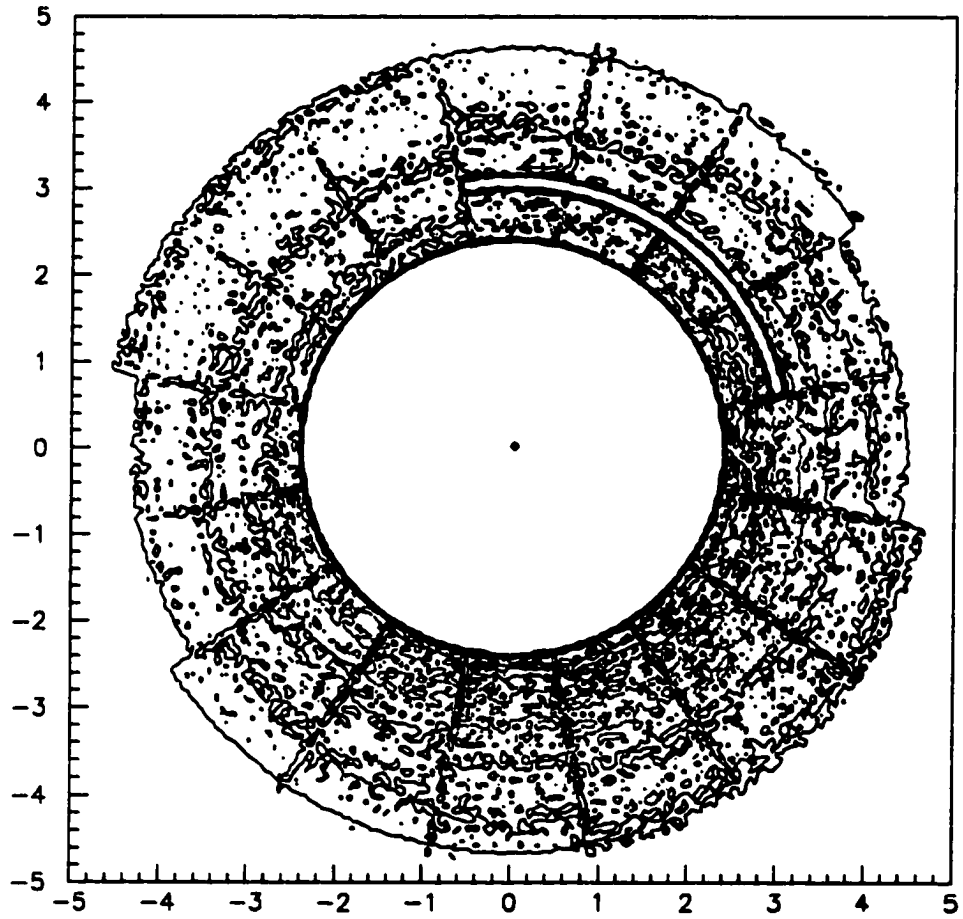
Figure II.12 An example of a fit to the histograms of distances away from the center of the detector.

50
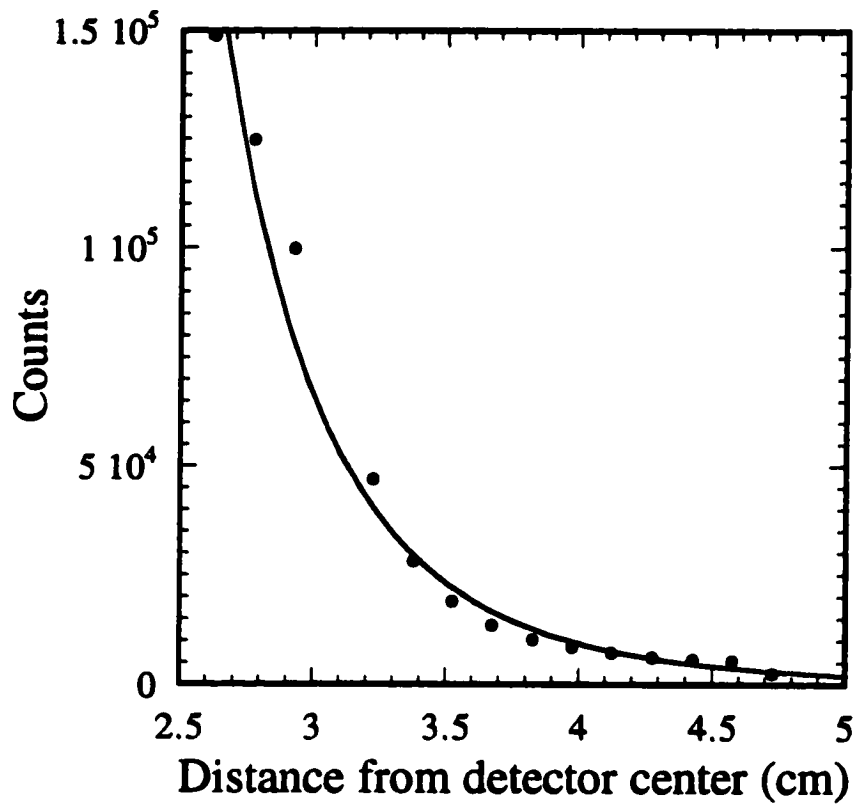
The method used to find the beam center is illustrated in Fig. II.13. Three non-colinear points are required to define a circle. Three points (X_1,Y_1), (X_2,Y_2), and (X_3,Y_3) are chosen from the 16 points. The set of all points equidistant to points (X_1,Y_1) and (X_2,Y_2) is the line L_1, which is perpendicular to a line that runs between the points. The slope of line L_1 is

$$m_{L1} = \frac{X_1 - X_2}{Y_1 - Y_2}. \qquad \text{(II-21)}$$

As denoted by the stars in Fig. II.13, the line also runs through the midpoint of the two points, $((X_1+X_2)/2, (Y_1+Y_2)/2)$. The slope and any point on the line completely define L_1. Line L_2 is the set of points equidistant to the points (X_1,Y_1) and (X_3,Y_3). The slope and midpoint for line L_2 are calculated in the same manner as was done for L_1, except that X_3 and Y_3 are substituted for X_2 and Y_2. The two lines L_1 and L_2 intersect at the center of the circle, which is the position of the beam, (X_c, Y_c). The method is repeated for all combinations of the 16 points taken 3 at a time. The center is the average X and Y of the 560 different combinations possible. The beam center for each run is shown in Fig. II.14. The dots represent the mean X or Y position of the beam when the data trigger is one particle in the MFA. The x's represent the mean X or Y position of the beam when the data trigger is two particles in the main ball of the MSU 4π.

For every hit in the silicon detector, a silicon segment and a strip measure the position. The segment and strip are converted to polar coordinates (d,ϕ). Since the detector has only 16 strips/segment and only 16 segments, the data are spread out over the region covered by the strip and segment by adding a random number from -11.5 to +11.5 to the ϕ, and adding a random number from -0.75 to +0.75 to the d. The value of 11.5 and 0.75 correspond to half the ϕ coverage of the segment and half the distance between strips, respectively. The spreading smoothes the data so that angular distributions can be made. After spreading, the data are converted to

51

rectangular coordinates (X,Y). This spreading technique was also employed in producing the hit pattern shown in Fig. II.11.

For each hit, the average beam center for a run is subtracted from the position based on the segment number and strip number to give the fragment position in the coordinate system centered on the beam. The new position is converted into spherical coordinates (r, θ, ϕ) and used for further analysis.

Figure II.13 A schematic describing the method used to calculate the position of the beam. The points (X_1,Y_1), (X_2,Y_2), and (X_3,Y_3) are 3 non-linear points. The dashed lines are the lines connecting the points, and the solid lines are the all the point equidistant from (X_1,Y_1) and (X_2,Y_2) (labeled L1) or (X_1,Y_1) and (X_3,Y_3) (labeled L2). The stars indicate the midpoint between points (X_1,Y_1) and (X_2,Y_2) and the midpoint between points (X_1,Y_1) and (X_3,Y_3).

53

(X_1,Y_1)

L_1

(X_c,Y_c)

(X_2,Y_2)

L_2

(X_3,Y_3)

54
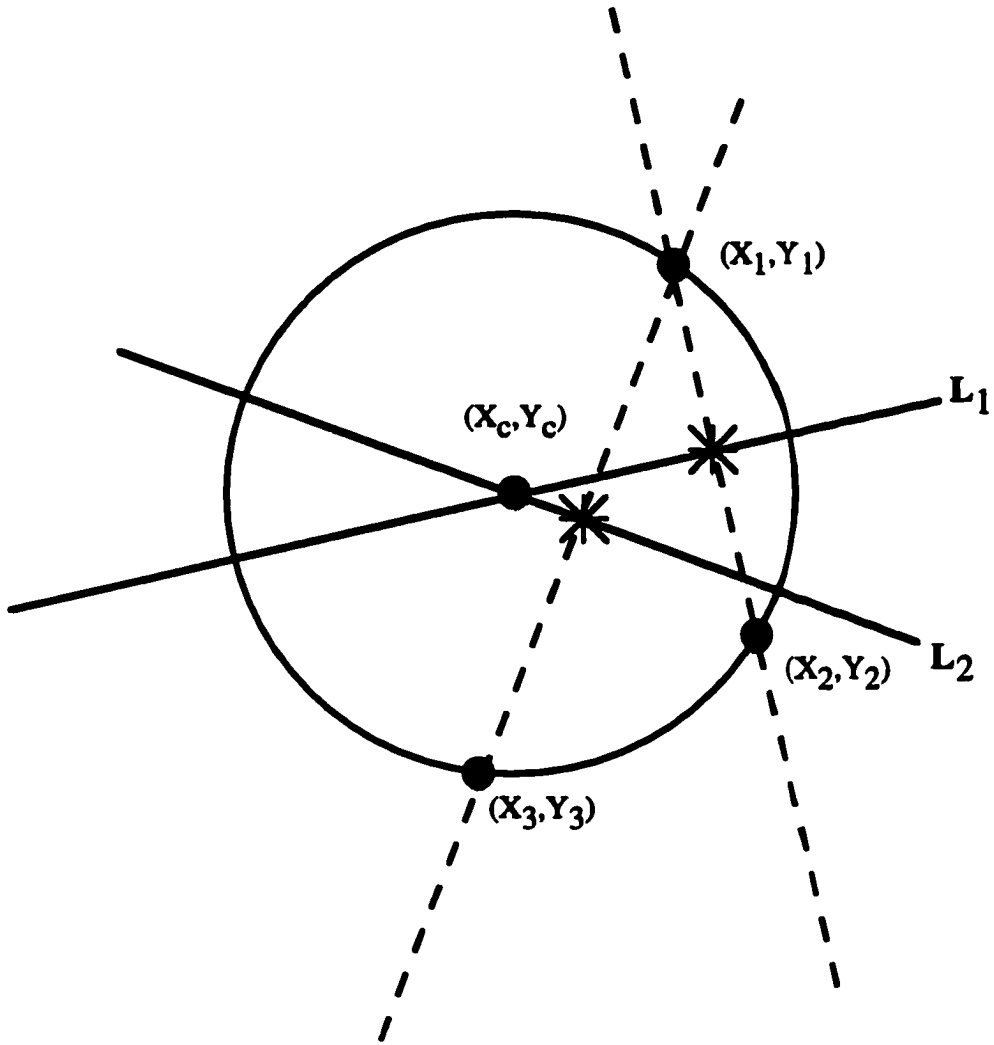
Figure II.14 The beam position for each run. The dots represent the mean value of the X and Y position of the beam for an MFA1 trigger, and the x's are the mean values of the X and Y position of the beam for a BALL2 trigger. The error bars are one standard deviation above and below the mean.

56
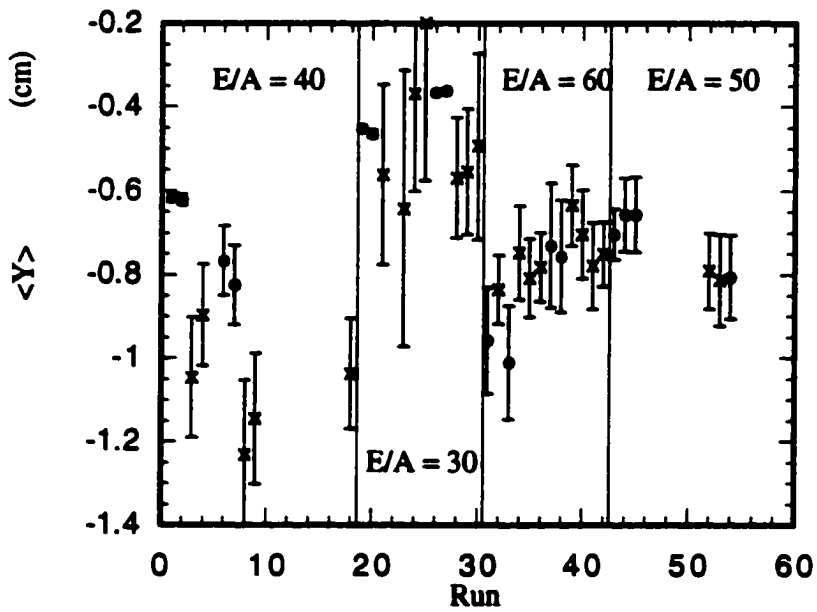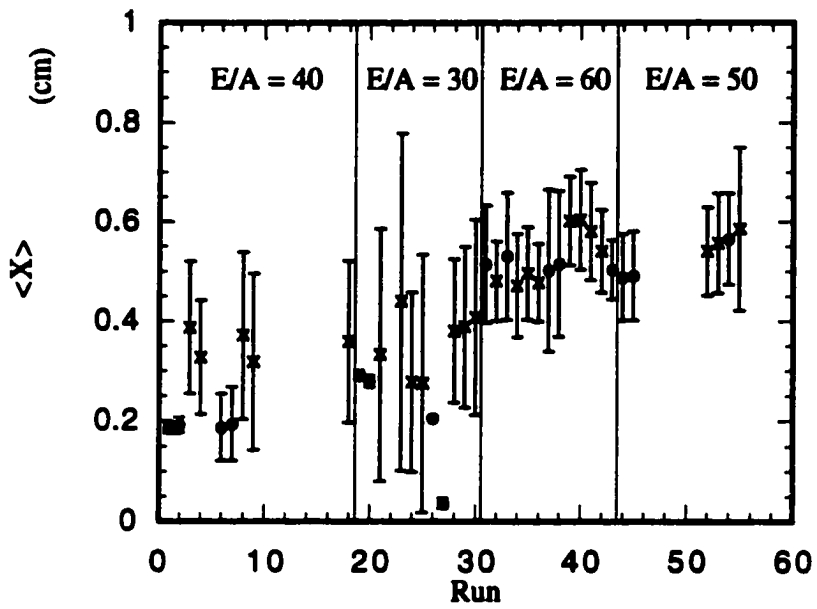
Chapter III   Results

The results presented here are from NSCL experiment 93046, a ^{129}Xe beam at E/A = 30, 40, 50, and 60 MeV on targets of ^{nat}Cu and ^{nat}Sc. In Sec. III.A charge and energy distributions are shown for the Xe + Cu and Sc at all beam energies. Section III.B presents the means and widths of the charge distributions gated on PLF laboratory energy. In Sec. III.C the mean energy distributions as a function of Z for all systems in the study are shown. Velocity distributions as a function Z, are also presented in this section. The deflection functions or "Wilcynski-type" plots are shown in Sec III.D. The data are normalized by setting the area under the elastic peak, scaled by the beam current, equal to the Rutherford cross section.

III.A   Charge and Energy Distributions

The charge and energy distributions show what type of fragments are formed in a reaction. The charge vs. laboratory kinetic energy 2-dimensional histograms for Xe + Cu are shown in Fig. III.1 (a)-(d). At E/A = 30 MeV, Fig. III.1(a), there are numerous fragments in the elastic region, and a ridge of fragments with decreasing charge and energy. Most of the fragments formed are $35 \leq Z \leq 56$, however there are some fragments with $Z < 35$ not seen in the figure because their yields falls below the lowest contour. Increasing in energy to E/A = 40 MeV, Fig III.1 (b), the same shape to the distribution is seen, but a larger fraction of the fragments are outside the elastic region. One reason for this is that the grazing angle decreases with increasing beam energy, and the elastic cross section decreases dramatically outside the grazing angle. At E/A = 50 MeV and E/A = 60 MeV, the trend towards forming smaller, less energetic fragments increases with increasing beam energy. The same trends are seen for the Xe + Sc system, as shown in Fig III.2 (a)-(d).

57

Figure III.1 Log Contour plot of the Z vs. kinetic energy of the fragments for Xe +
Cu at (a) E/A = 30 MeV, (b) E/A = 40 MeV, (c) E/A = 50 MeV, and (d) E/A = 60
MeV

58

Axis labels: Z (vertical), E_{lab} (horizontal). Panels (a), (b), (c), (d).

59
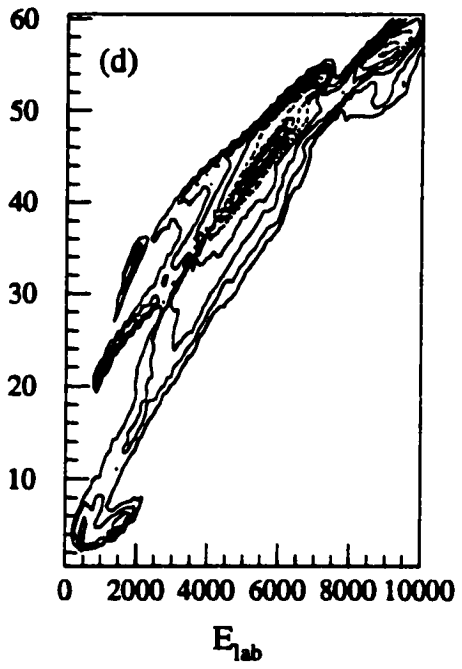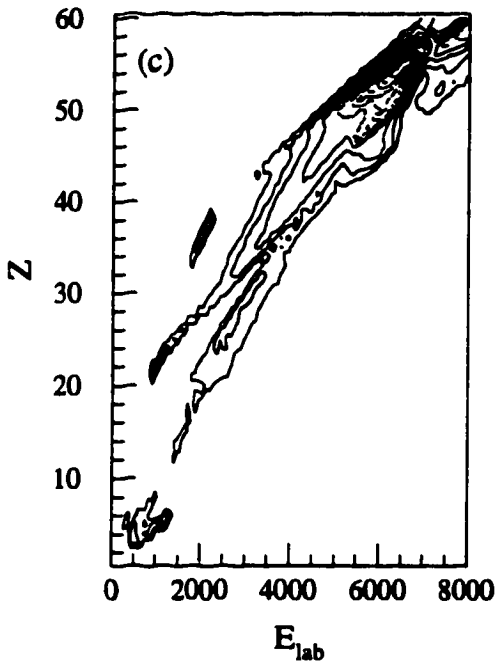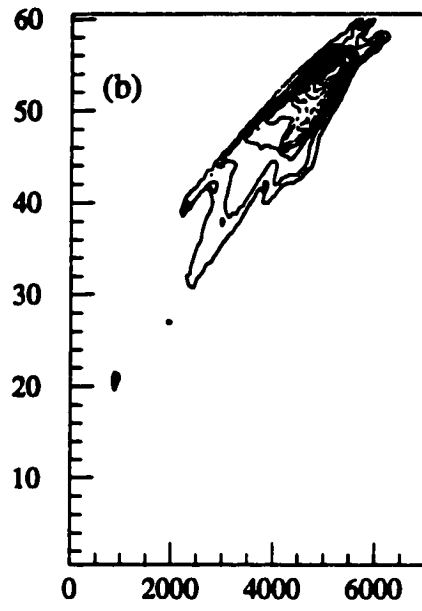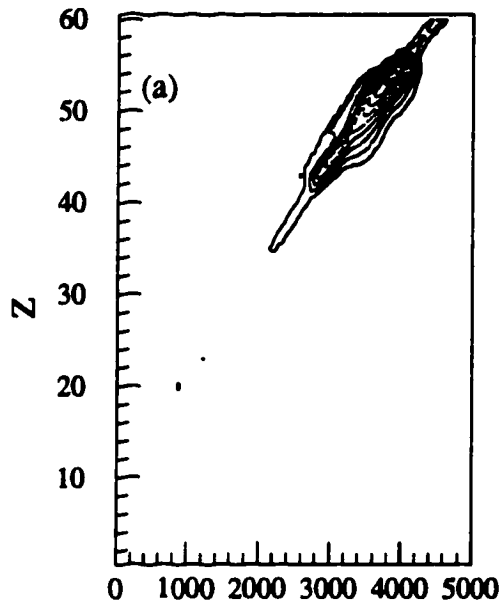
Figure III.2 Log Contour plot of the Z vs. kinetic energy of the fragments for Xe + Sc

at (a) E/A = 30 MeV, (b) E/A = 40 MeV, (c) E/A = 50 MeV, and (d) E/A = 60 MeV

60

61
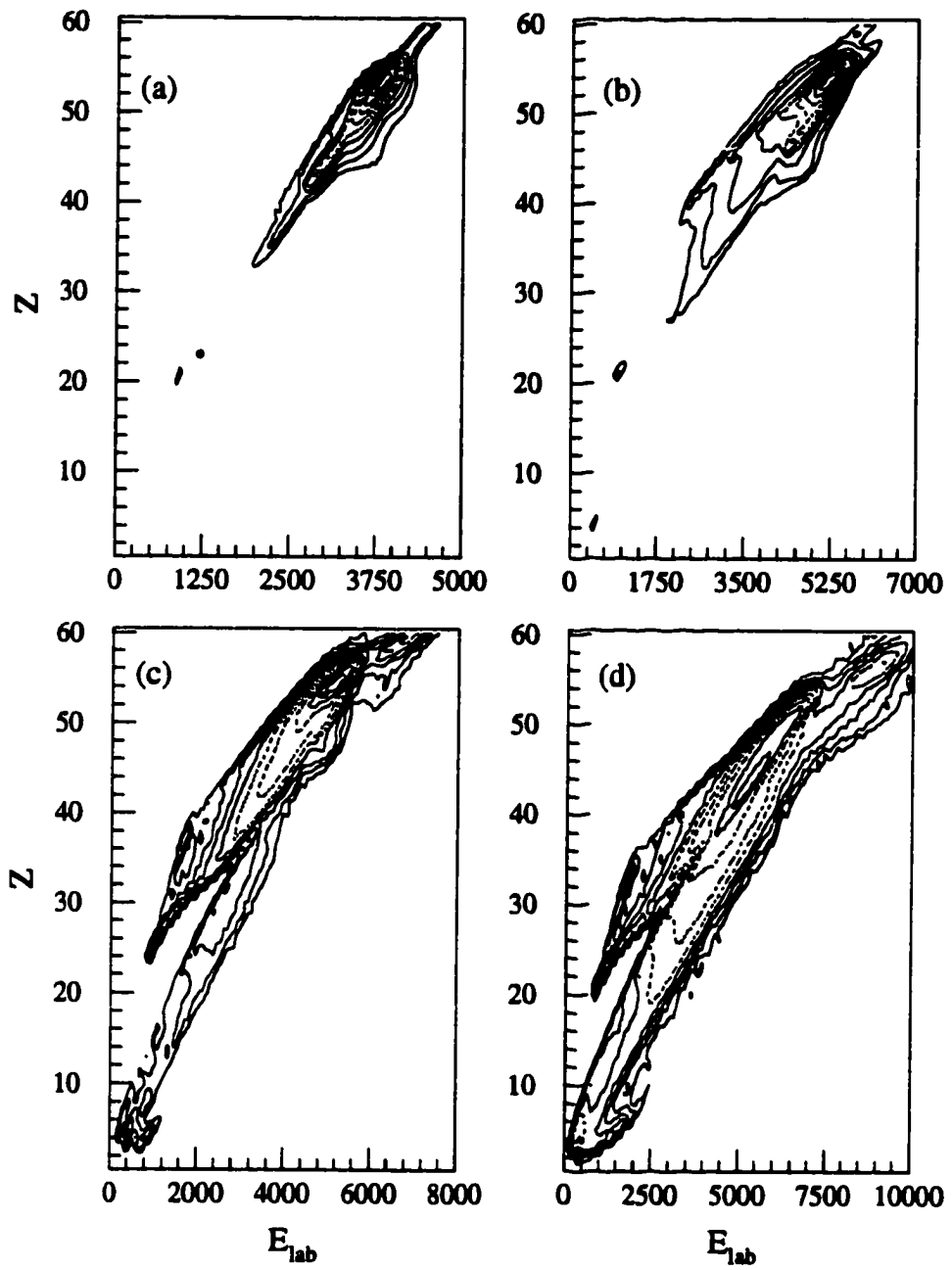
The charge distributions integrated over kinetic energy for Xe + Cu at E/A = 30, 40, 50, and 60 MeV are shown in Fig. III.3 (a)-(d). For E/A = 30, 40, and 50 MeV, the elastic peak at Z = 54 is easily seen. Along with the elastic peak is a tail of lower Z fragments that increases in magnitude with beam energy. However, in the E/A = 60 MeV system the elastic peak is not noticeable. This is because the grazing angle falls inside the inner radius of the MFA. The charge distributions for the Xe + Sc system at E/A = 30, 40, 50 and 60 MeV are shown in Fig. III.4 (a)-(d). Since Sc has a smaller nuclear charge (Z_{Sc}=21, Z_{Cu}=29) than Cu, the grazing angle becomes smaller. The elastic peak is visible at E/A = 30 and 40 MeV, but it is not visible at E/A = 50 and 60 MeV. This leads to a difference in the shape of the charge distributions. The hole in the Z distribution around Z = 17 is caused by a negative offset in the Si ADC. Fragments in the hole should be identified using the Si and Fast plastic, however these fragments do not drop enough energy in the Si to overcome the offset. Since they have a zero value in the Si, the fragment is removed from the data stream. The charge distributions at E/A = 40 MeV are similar to those at E/A = 30 MeV, with the noticeable exception that the total cross section for the data is less than the cross section at the other energies. This may be caused by the position of the beam. Because the elastic cross section is very sensitive to the angle, if the calculated beam center is off by 0.1 mm, it will cause a noticeable difference in the cross-section. However, the shape of the distribution should not change if the beam center is off.

The laboratory kinetic energy distributions for the Xe + Cu system at E/A = 30, 40, 50 and 60 MeV are shown in Fig. III.5 (a)-(d). A peak in the energy distribution is seen around the beam energy at E/A = 30, 40, and 50 MeV. As with the charge distributions, the number of lower energy fragments formed from the reactions increase with beam energy when compared to the elastic peak. The energy

62

distributions for the Xe + Sc system at E/A = 30, 40, 50, and 60 MeV are shown in Fig. III.6 (a)-(d). The energy distributions for the Xe + Cu and Sc are very similar for the E/A= 30 and 40 MeV systems, however the grazing angle for the Xe + Sc at E/A = 50 MeV falls inside the inner radius of the MFA, whereas it does not in the Xe + Cu at E/A = 50 MeV. This causes differences in the shapes of the energy distributions.

III.B Mean Charge and Charge Width Distributions

How the mean charge varies with laboratory kinetic energy is often interesting when studying reaction mechanisms. Laboratory kinetic energy was chosen instead of the more standard total kinetic energy loss (TKEL) used at lower energies to avoid assuming 2-body kinematics. The charge centroids and widths are measured two ways. In both cases, charge distributions are created with laboratory kinetic energy bins 200-MeV wide. Each distribution this then fit to a Gaussian distribution

$$y = \frac{A}{\sigma}\exp\left[-\frac{1}{2}\left(\frac{Z-\langle Z\rangle}{\sigma}\right)^2\right],$$ (III.1)

where y is the number of counts with nuclear charge Z (or the probability of having nuclear charge Z when the distribution is normalized to one), $\langle Z\rangle$ is the mean of the charge distribution, σ is the standard deviation of the charge distribution, and A is a normalization constant. A moment analysis is also performed, where the first moment, or the mean, is given by

$$<Z>=\frac{1}{n}\sum_{i=1}^{n}Z_i,$$ (III.2)

and the second moment, or the variance, is given by

$$\sigma_Z^2 = \frac{1}{n-1}\sum_{i=1}^{n}(Z_i - \langle Z\rangle)^2,$$ (III.3)

63

where Z_i is the nuclear charge of one fragment in the histogram, $<Z>$ is the mean nuclear charge of the distribution, σ_Z^2 is the variance of the distribution, and n is the number of fragments in the histogram.

The mean charges for Xe + Cu at E/A = 30, 40, 50 and 60 MeV are shown in Fig. III.7 (a)-(d). There is very little difference between the two methods when the distributions are fairly Gaussian in shape. However, when there is outlying data, the Gaussian fitting is done excluding the outlying data; the moment analysis is always done over the entire distribution. For all the Xe + Cu systems, a smooth decrease in mean charge is seen with decreasing energy. The results for the Xe + Sc system at E/A = 30, 40, 50, and 60 MeV, shown in Fig. III.8 (a)-(d), are very similar to their Xe + Cu analogues.

The charge widths for Xe + Cu and Xe + Sc at E/A = 30, 40, 50 and 60 MeV are seen in Fig. III.9 (a)-(d) and Fig. III.10 (a)-(d), respectively. There is a more significant difference between the Gaussian fitting and the moment analysis, particularly in the higher energy bins. This is primarily due to non-Gaussian tails in the distributions that increase the width in the moment analysis. Since the Gaussian fits excludes these regions, the methods yield different results. In both the Xe + Cu and Sc systems at E/A = 30 and 40, the trend shows an increase in the width of the charge distribution with decreasing laboratory energy (or an increase in TKEL). However, at E/A = 50 and 60 MeV, there is a flat region in the highest kinetic energy bins, where the width does not change. For lower kinetic energy bins, the widths increase with decreasing kinetic energy.

III.C Mean Velocity

Instead of comparing the mean energy, the mean velocity can also be used. This removes the trivial mass dependence from the energy. Since the MFA can

Figure III.3 Inclusive charge distributions for the data from the reaction Xe + Cu at (a) E/A = 30 MeV, (b) E/A = 40 MeV, (c) E/A = 50 MeV, and (d) E/A = 60 MeV. The charge distributions are integrated over the detector's coverage.

65

Xe+Cu

66
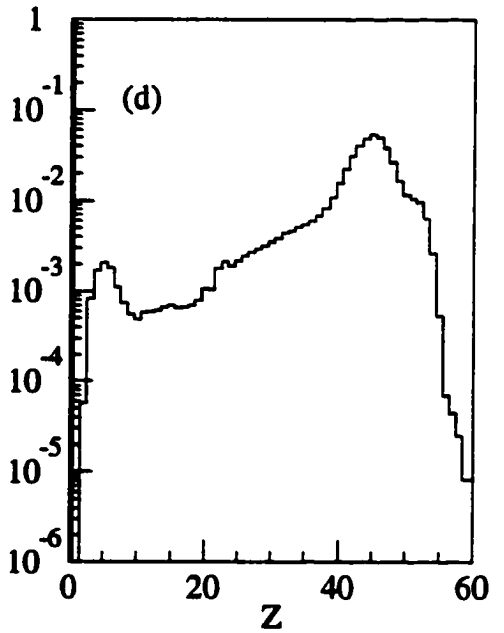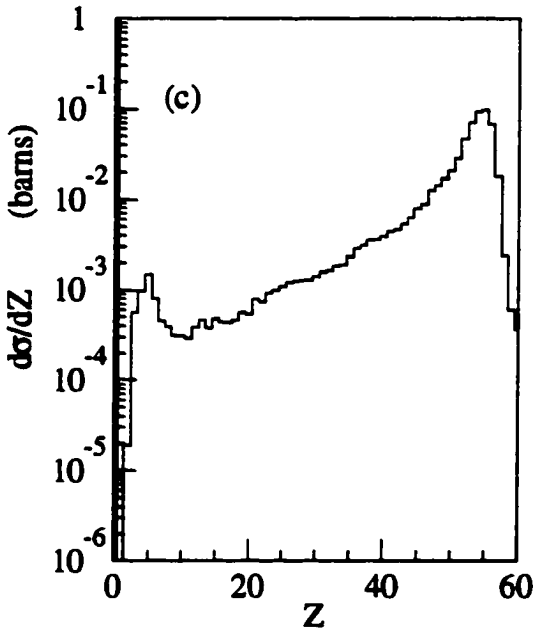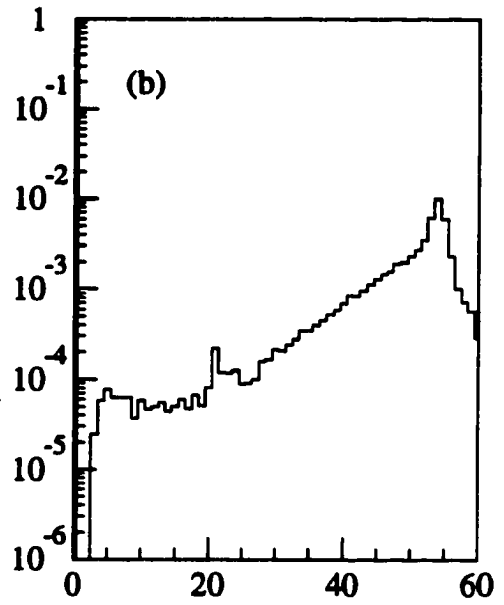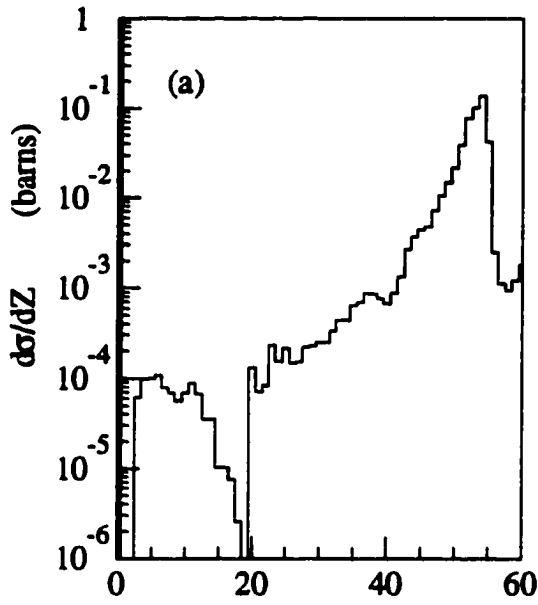
Figure III.4 Inclusive charge distributions for the data from the reaction Xe + Sc at (a) E/A = 30 MeV, (b) E/A = 40 MeV, (c) E/A = 50 MeV, and (d) E/A = 60 MeV. The charge distributions are integrated over the detector's coverage.

67

68
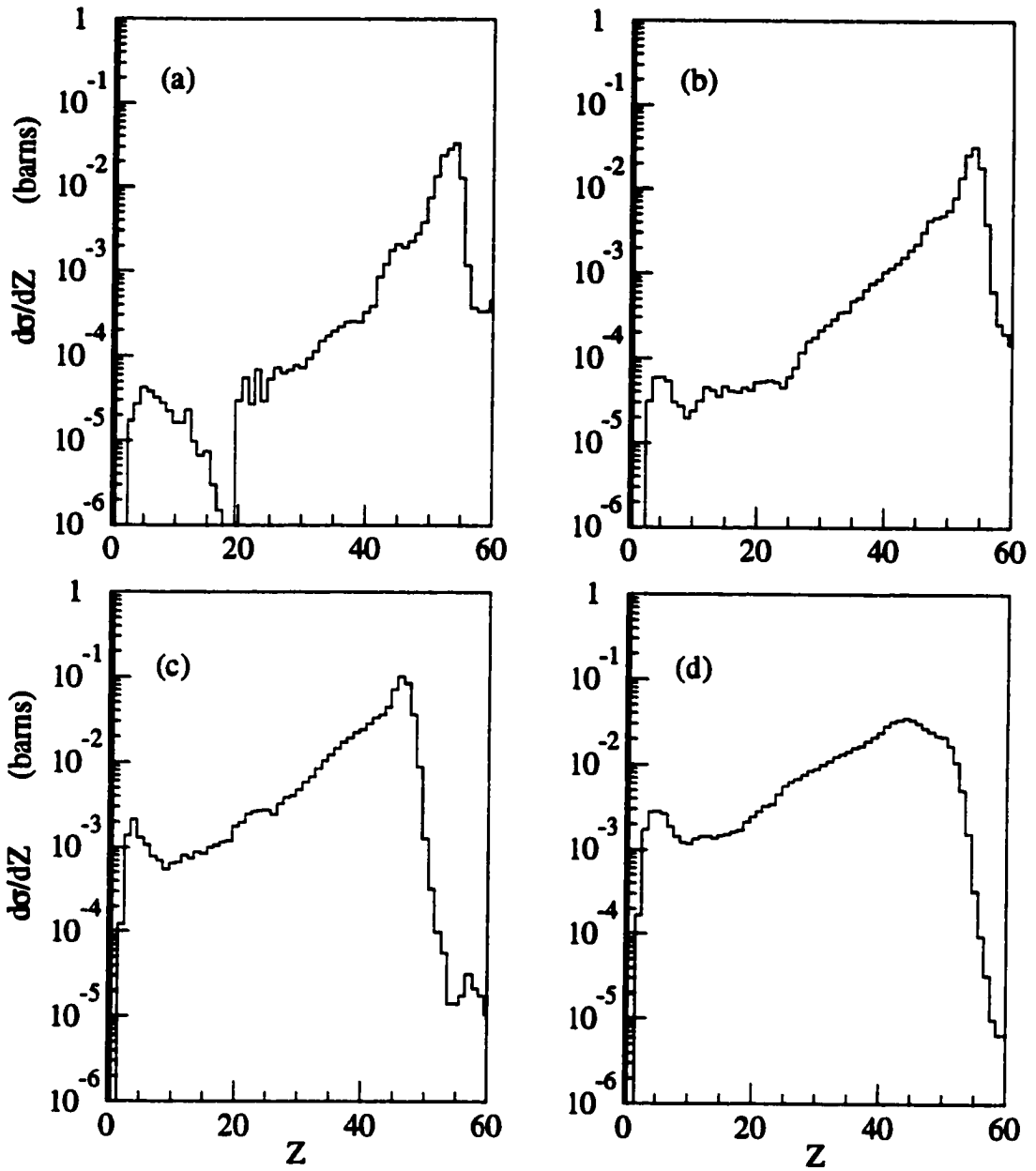
Figure III.5 Inclusive energy distributions for the data from the reaction Xe + Cu at

(a) E/A = 30 MeV, (b) E/A = 40 MeV, (c) E/A = 50 MeV, and (d) E/A = 60 MeV.

The charge distributions are integrated over the detector's coverage.

69

70
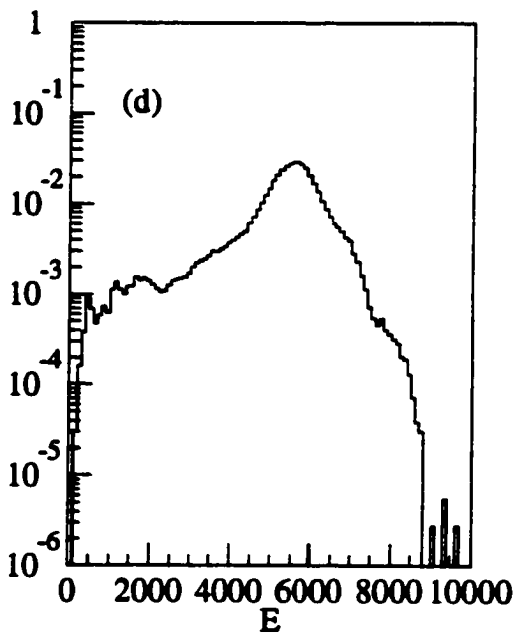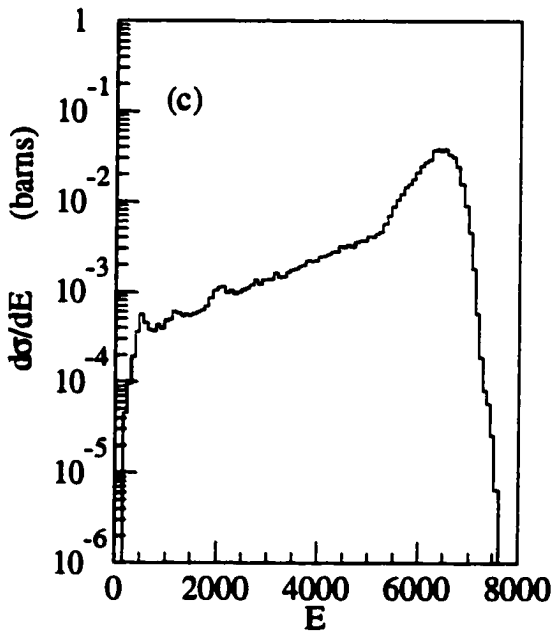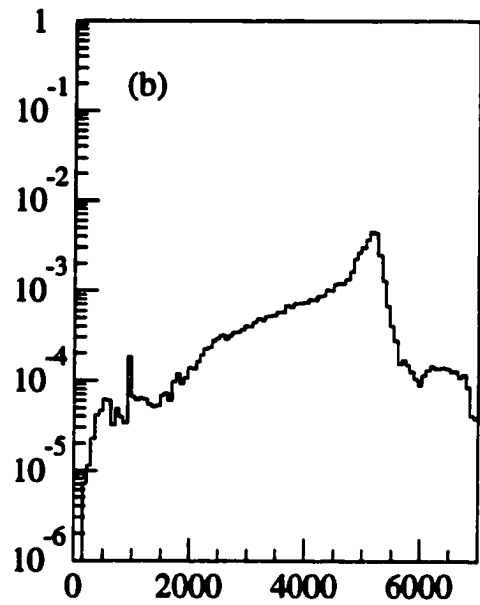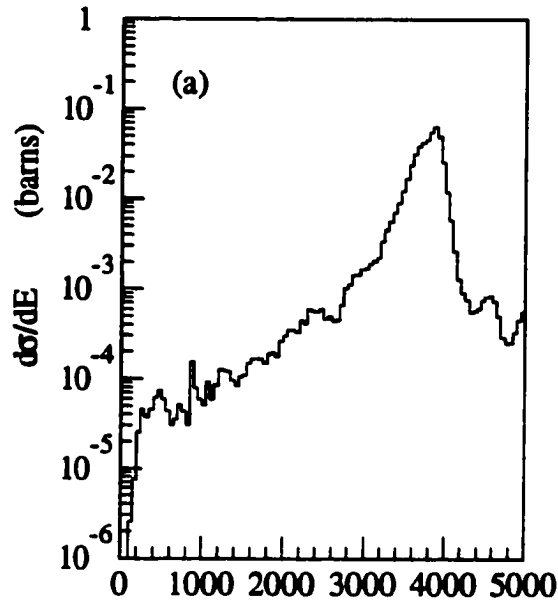
Figure III.6 Inclusive energy distributions for the data from the reaction Xe + Sc at (a) E/A = 30 MeV, (b) E/A = 40 MeV, (c) E/A = 50 MeV, and (d) E/A = 60 MeV. The charge distributions are integrated over the detector's coverage.

71

72
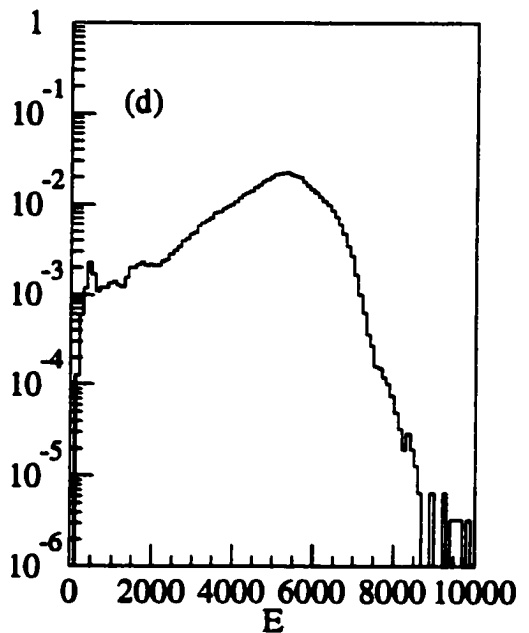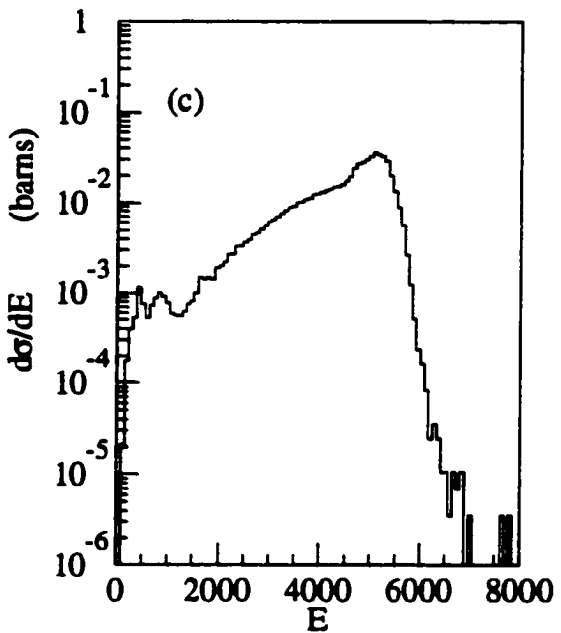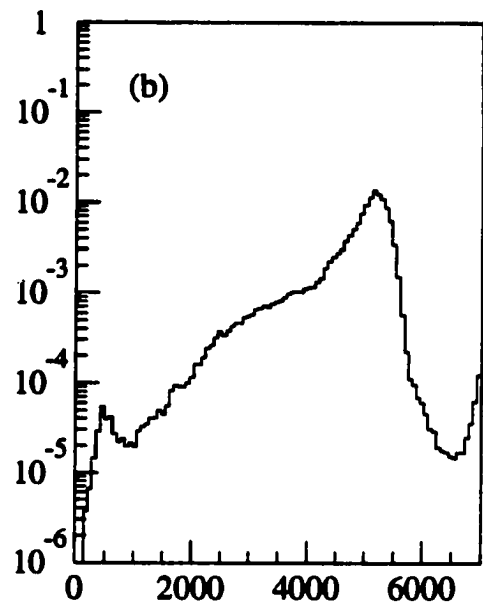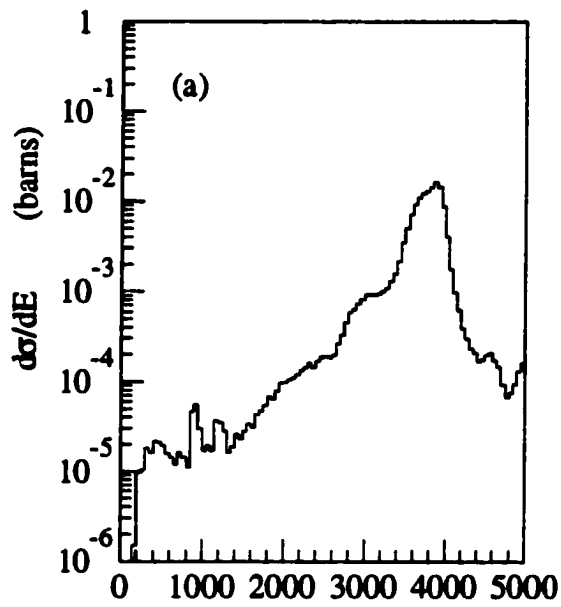
Figure III.7 Energy dependence of the mean charge for the reaction Xe + Cu at (a)

E/A = 30 MeV, (b) E/A = 40 MeV, (c) E/A = 50 MeV, and (d) E/A = 60 MeV. The

dots represent Gaussian fits to the charge distributions and the X's represent the first

moment from a moment analysis.

73

74
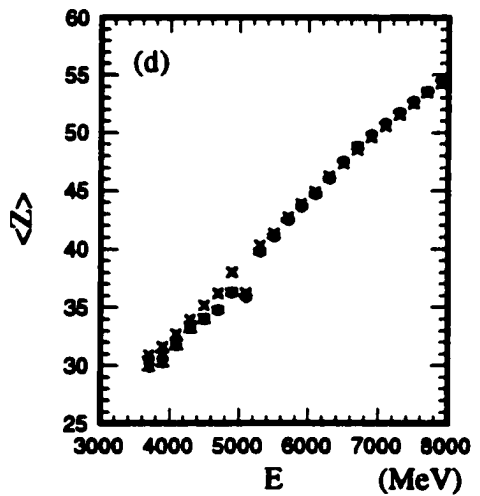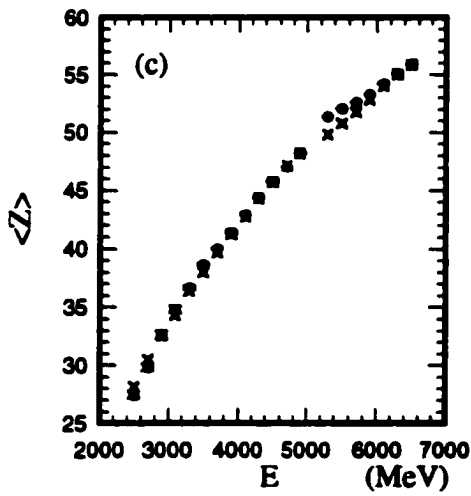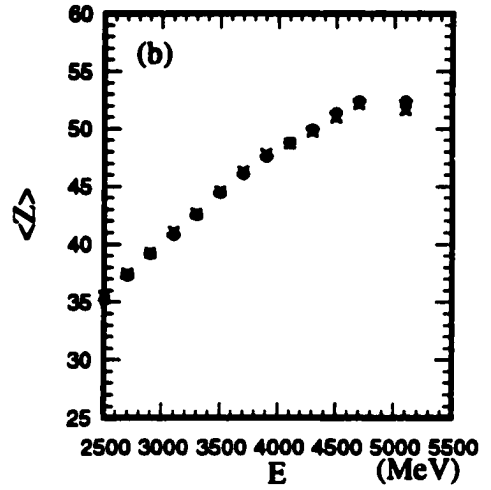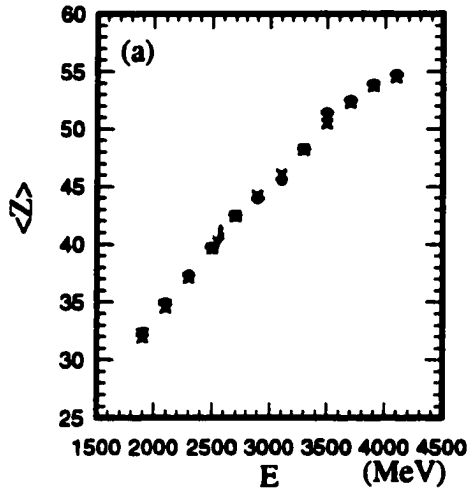
Figure III.8 Energy dependence of the mean charge for the reaction for the reaction Xe + Sc at (a) E/A = 30 MeV, (b) E/A = 40 MeV, (c) E/A = 50 MeV, and (d) E/A = 60 MeV. The dots represent Gaussian fits to the charge distributions and the X's represent the first moment from a moment analysis.

76
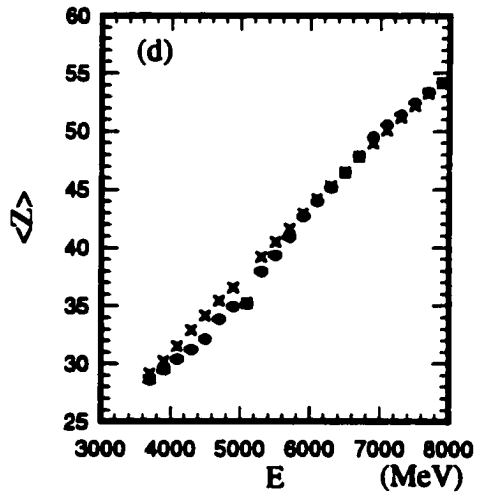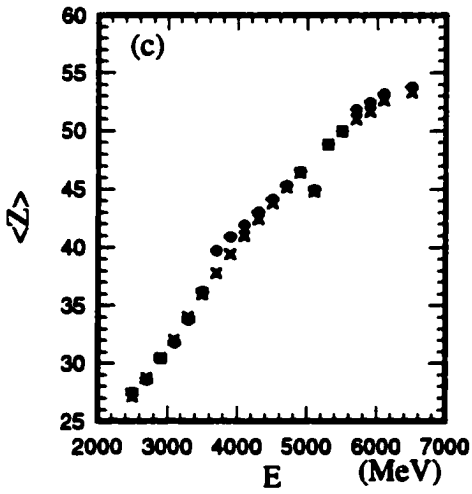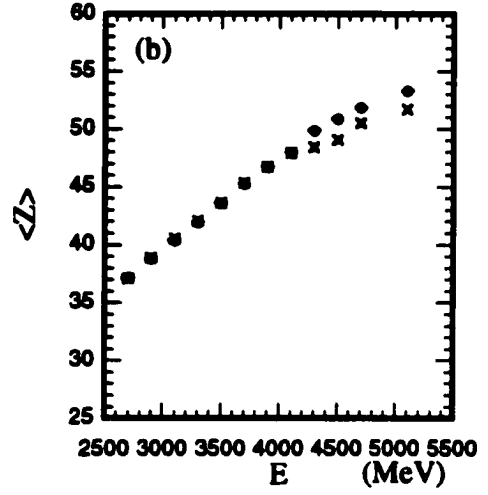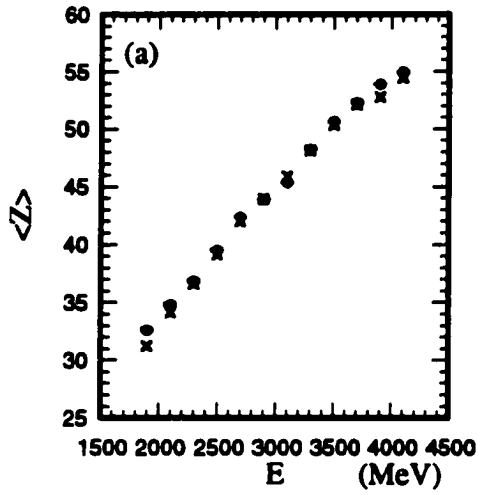
Figure III.9 Energy dependence of the widths of the charge distributions for the reaction for the reaction Xe + Cu at (a) E/A = 30 MeV, (b) E/A = 40 MeV, (c) E/A = 50 MeV, and (d) E/A = 60 MeV. The dots represent Gaussian fits to the charge distributions and the X's represent the second moment from a moment analysis.

77

78
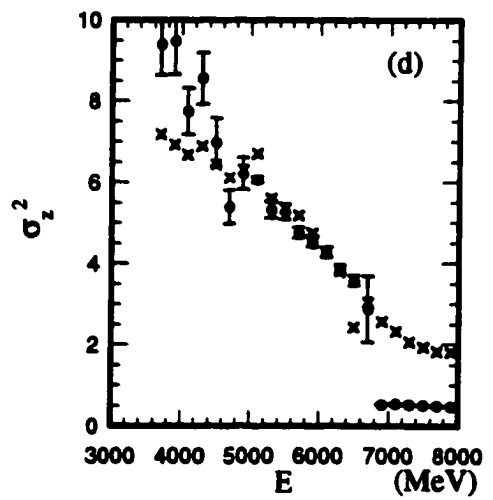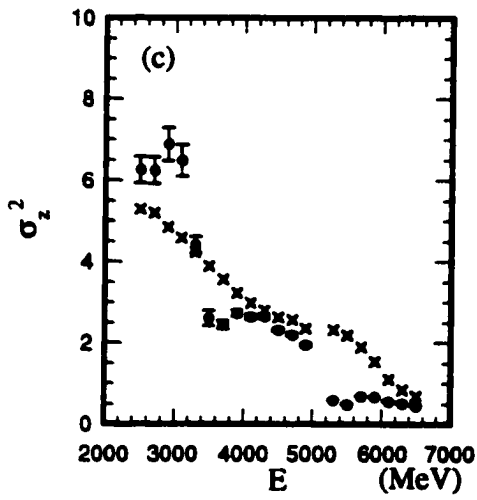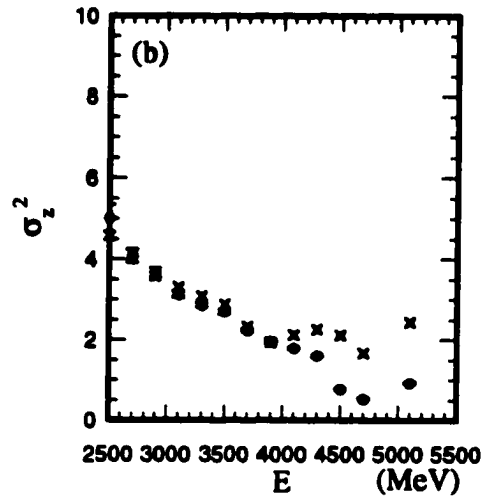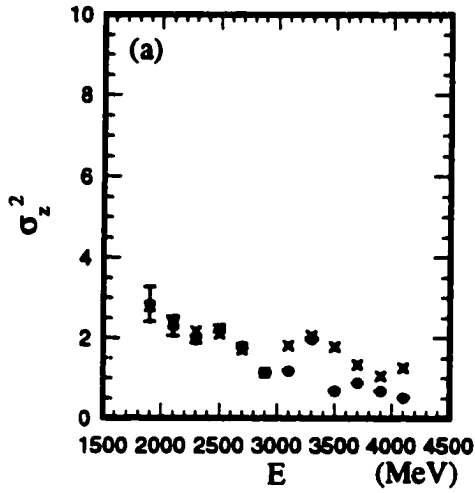
Figure III.10 Energy dependence of the widths of the charge distributions for the reaction for the reaction Xe + Sc at (a) E/A = 30 MeV, (b) E/A = 40 MeV, (c) E/A = 50 MeV, and (d) E/A = 60 MeV. The dots represent Gaussian fits to the charge distributions and the X's represent the second moment from a moment analysis.

79
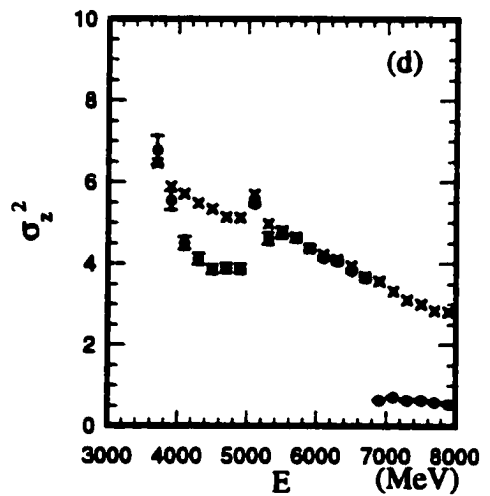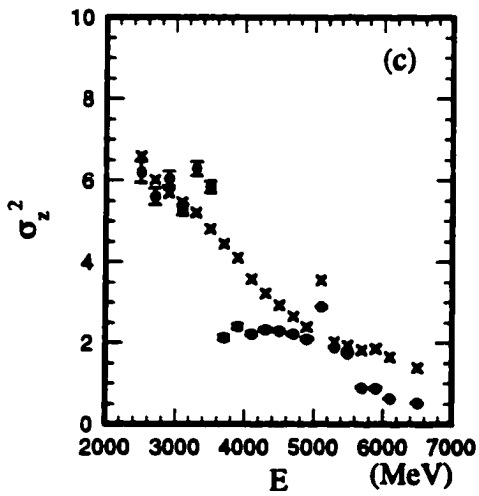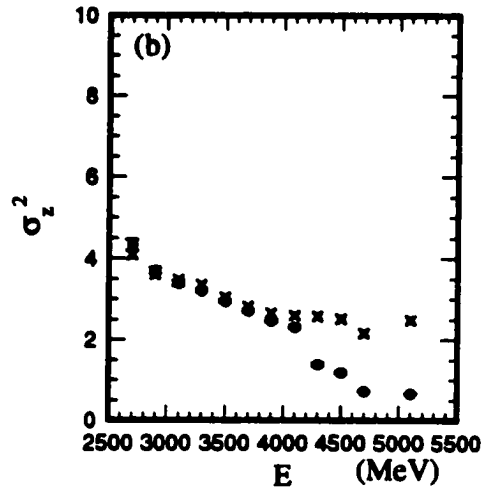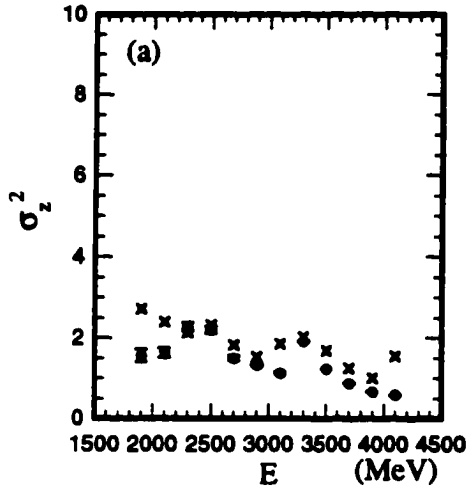
measure charge and not mass, the mass is parameterized by using [BOW91]

$$A = 2.08Z + 0.0029Z^2, \tag{III.4}$$

where Z is the atomic number and A is the mass number. The velocity of the particle is calculated by

$$Vel = \sqrt{2E/A}, \tag{III.5}$$

where E is the laboratory kinetic energy of the fragment. The velocity is then divided by the beam velocity so that the systems with different beam energies can be compared directly. Velocity distributions are gated on the Z of the fragment to show the mean velocity as a function of the Z. The mean velocity plots for Xe + Cu and Sc at E/A = 30, 40, 50, and 60 MeV are shown in Figs. III.11 and III.12 (a) - (d), respectively. At E/A = 30, 40, and 50 MeV, the velocity decreases with decreasing Z until around Z = 20, 25, and 30 for E/A = 30, 40, and 50 MeV, respectively. After this initial decrease in the velocity, the velocity increases for light fragments. In the E/A =60 MeV systems, the velocity remains around the beam velocity, except for the smallest Z values.

III.D Deflection Functions

The double differential cross section $\partial^2\sigma/\partial E\partial\theta$, which will be referred to as the deflection function, can provide evidence for rotation in the dinuclear system. The deflection functions for the Xe + Cu and Sc systems at E/A = 30, 40, 50 and 60 MeV are shown in Fig III.13 to III.20. At E/A = 30 MeV, there is a ridge of products located at the elastic energy and within the grazing angle. A second extends off it and goes to smaller energies and angles. A third ridge observed at even lower energies, goes to higher angles with decreasing energy. This is the typical "orbiting pattern" seen when a system rotates, with the excitation energy of the system related to the amount of time the system rotates. The third ridge is the mirror of the rotation past zero degrees (see Fig I.3). This orbiting pattern is also seen the Xe + Cu and Sc

81

systems at E/A = 30 and 40 MeV. At E/A = 50 MeV, the Xe + Cu possibly shows an orbiting pattern, however in the Xe + Sc system since the elastic peak falls inside the inner radius of the detector, only the low energy negative angle scattering branch is seen. For the Xe + Cu and Sc systems at E/A = 60 MeV, both cases fall outside the grazing angle, and no orbiting is observed.

Figure III.11 Charge dependence of the means of the velocity distributions for the reaction Xe + Cu at (a) E/A = 30 MeV, (b) E/A = 40 MeV, (c) E/A = 50 MeV, and (d) E/A = 60 MeV. The dots represent Gaussian fits to the charge distributions and the X's represent the second moment from a moment analysis.

83

84
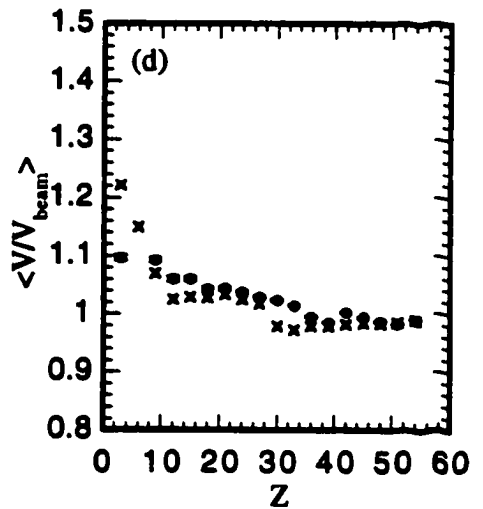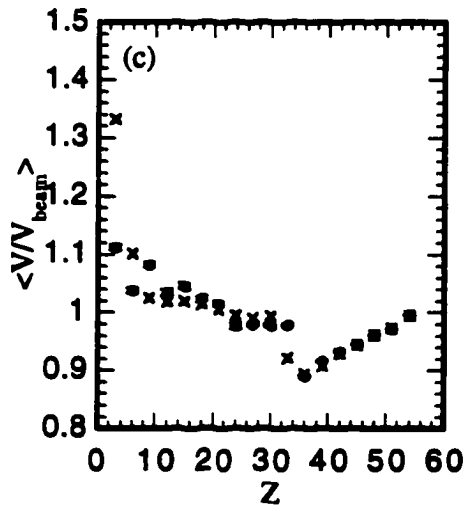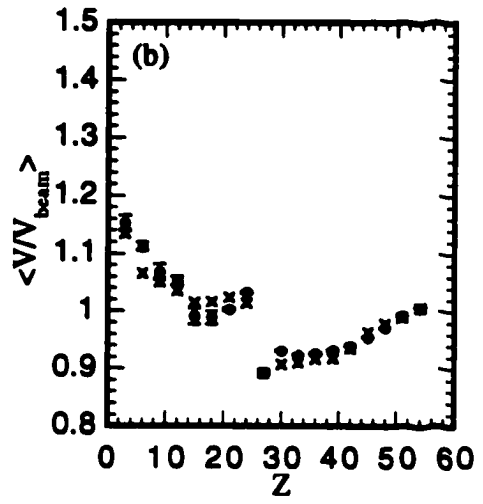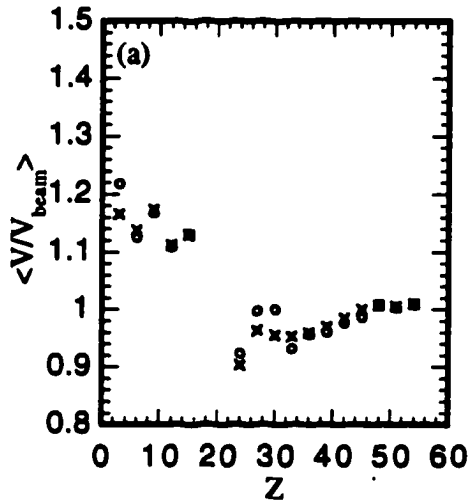
Figure III.12 Charge dependence of the means of the velocity distributions for the reaction Xe + Sc at (a) E/A = 30 MeV, (b) E/A = 40 MeV, (c) E/A = 50 MeV, and (d) E/A = 60 MeV. The dots represent Gaussian fits to the charge distributions and the X's represent the second moment from a moment analysis.

85
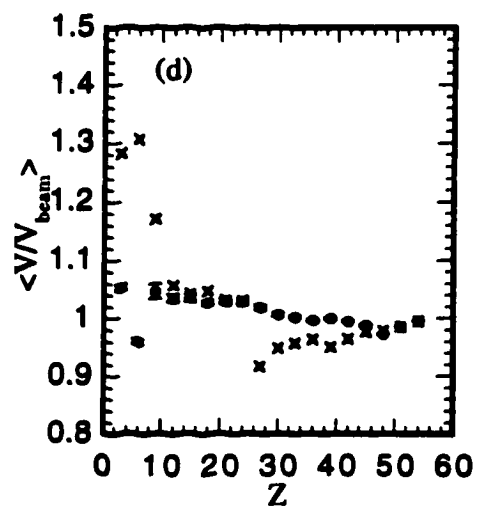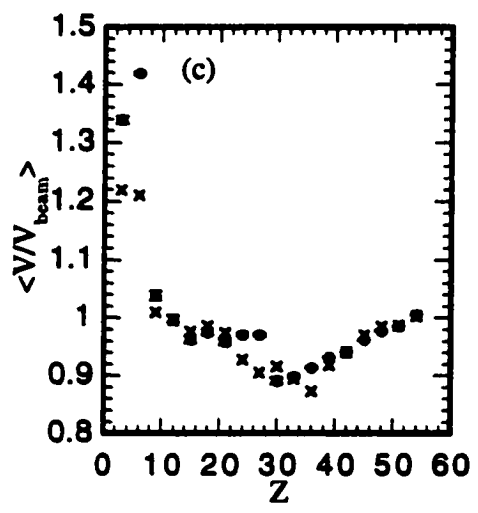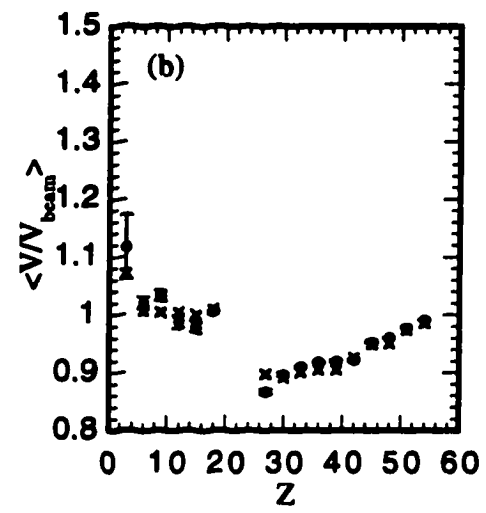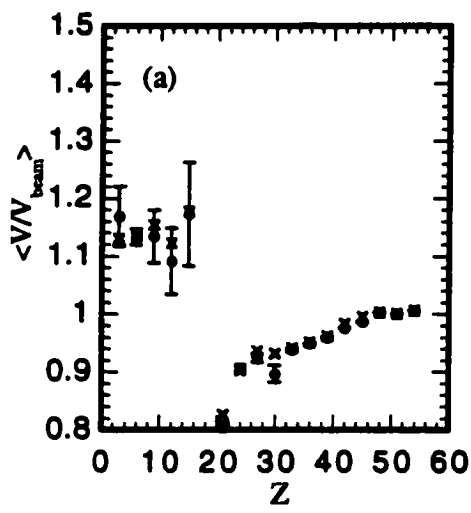
Figure III.13 Deflection function showing the double differential cross section $\frac{\partial^2\sigma}{\partial E\partial\theta}$ for Xe + Cu at E/A = 30 MeV on a log scale.

88
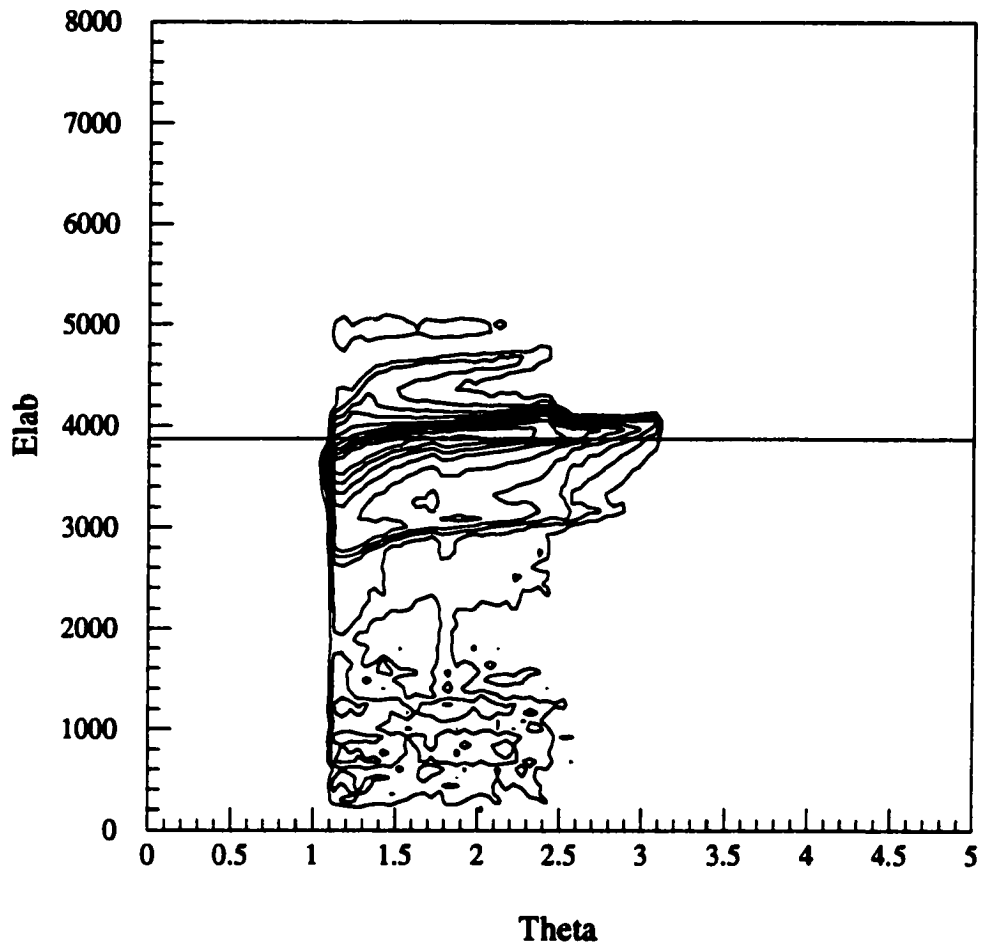
Figure III.14 Deflection function showing the double differential cross section $\frac{\partial^2 \sigma}{\partial E \partial \theta}$ for Xe + Cu at E/A = 40 MeV on a log scale.

90
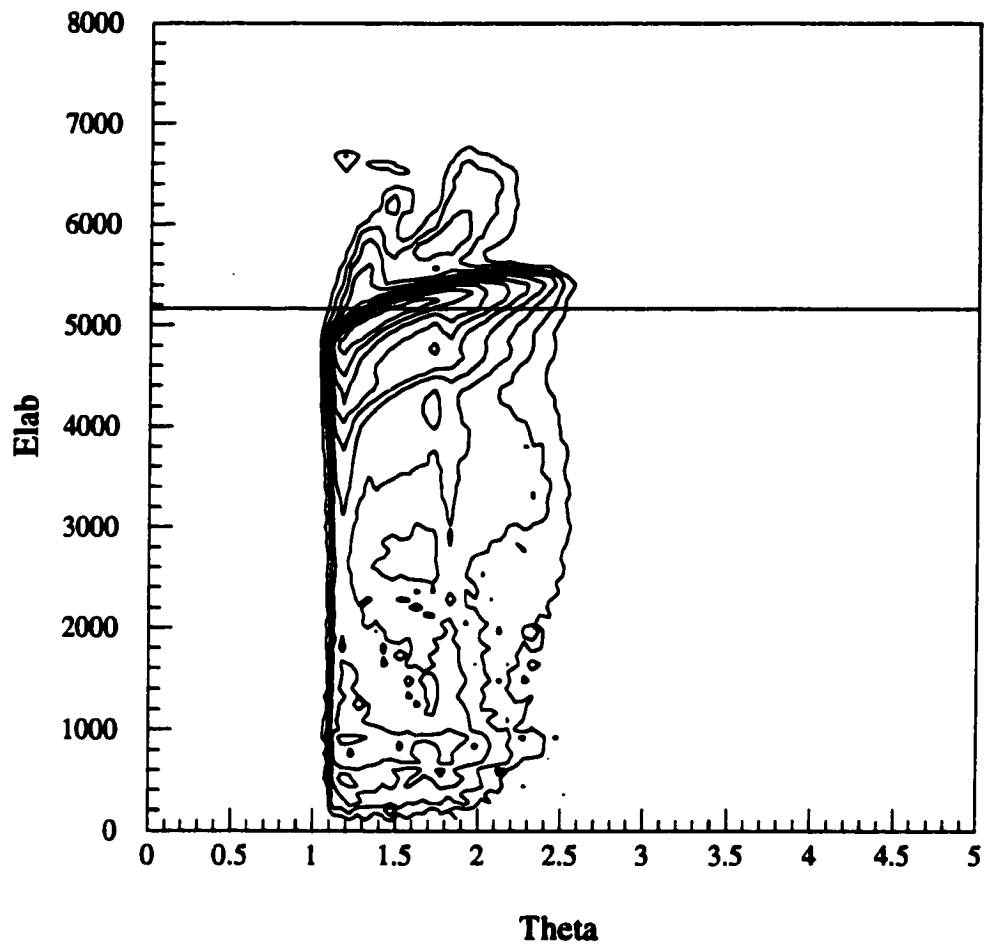
Figure III.15 Deflection function showing the double differential cross section $\frac{\partial^2\sigma}{\partial E \partial \theta}$ for Xe + Cu at E/A = 50 MeV on a log scale.

92
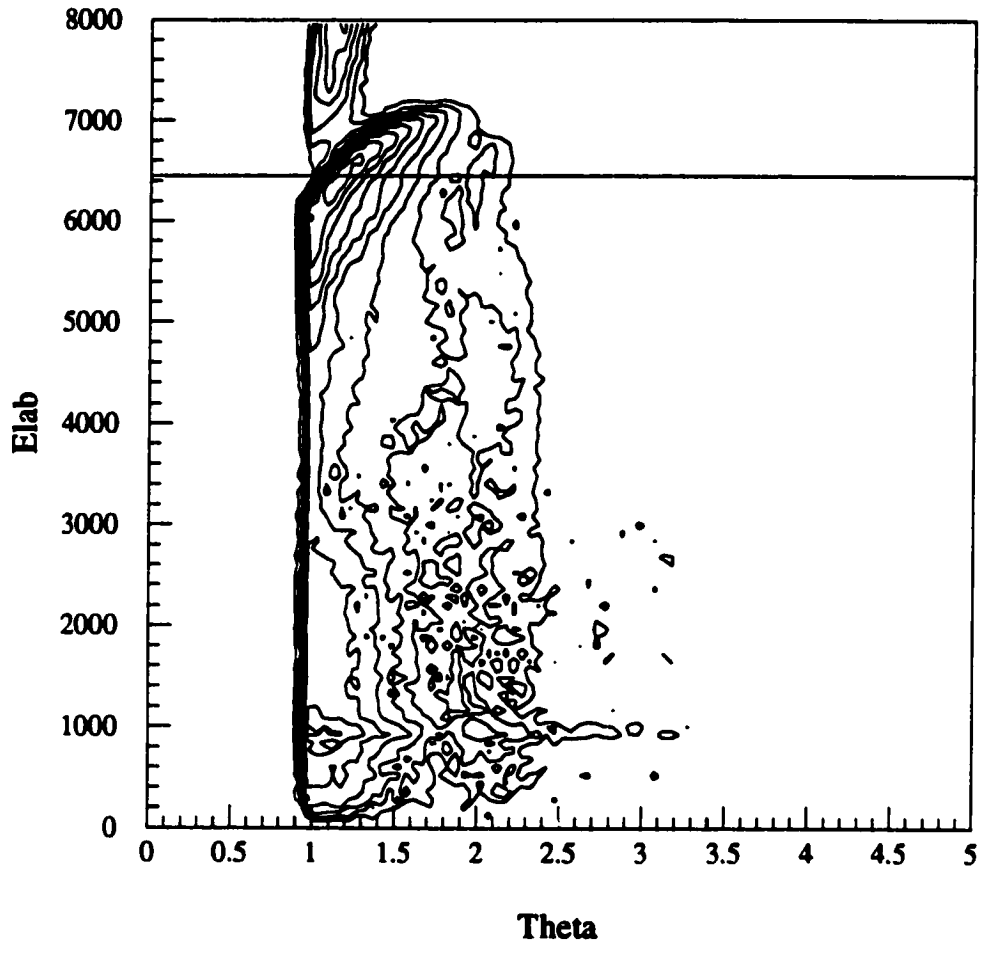
Figure III.16 Deflection function showing the double differential cross section $\frac{\partial^2 \sigma}{\partial E \partial \theta}$

for Xe + Cu at E/A = 60 MeV on a log scale.

93

94
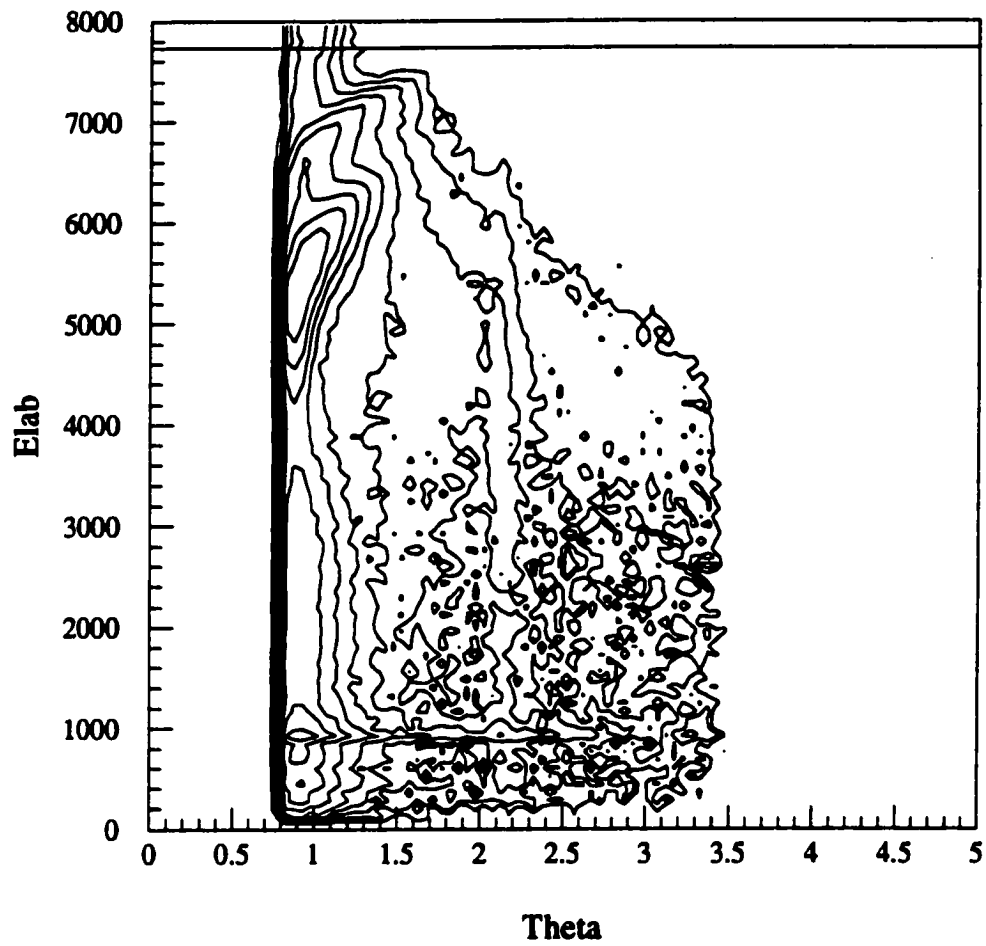
Figure III.17 Deflection function showing the double differential cross section $\frac{\partial^2\sigma}{\partial E\partial\theta}$ for Xe + Sc at E/A = 30 MeV on a log scale.

95

96
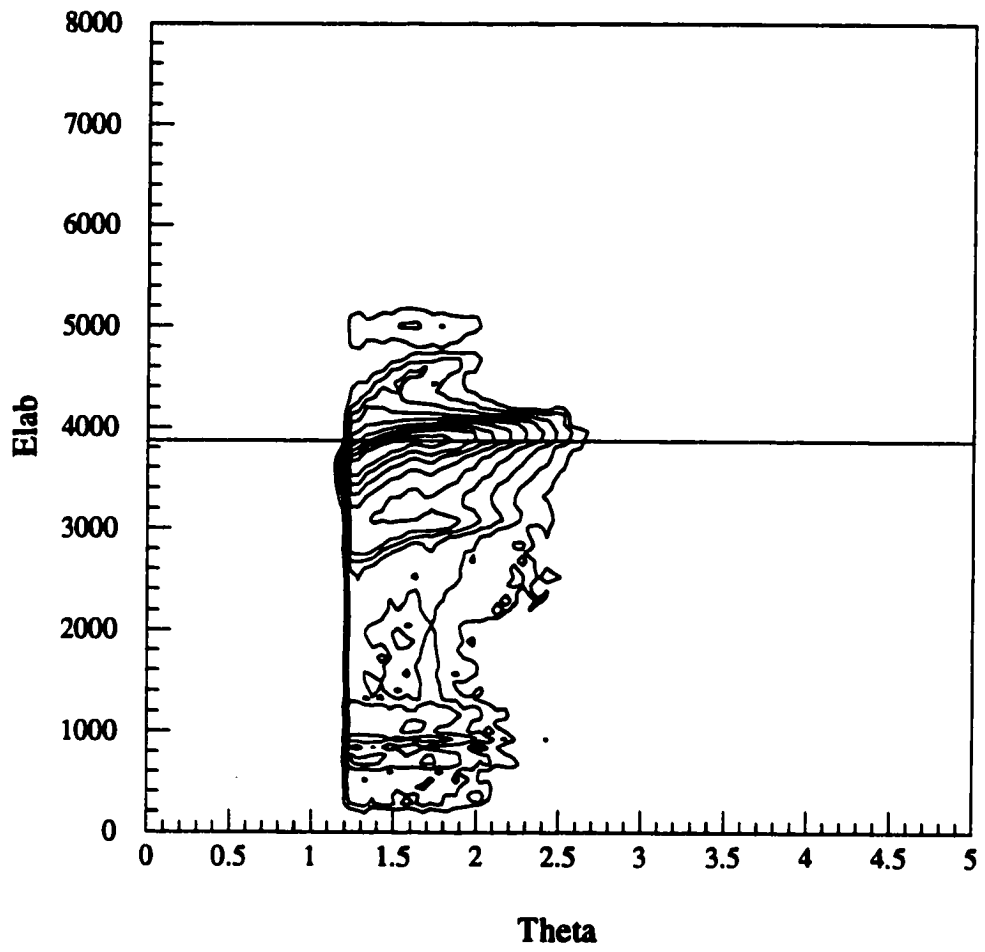
Figure III.18 Deflection function showing the double differential cross section $\frac{\partial^2 \sigma}{\partial E \partial \theta}$

for Xe + Sc at E/A = 40 MeV on a log scale.

97

98
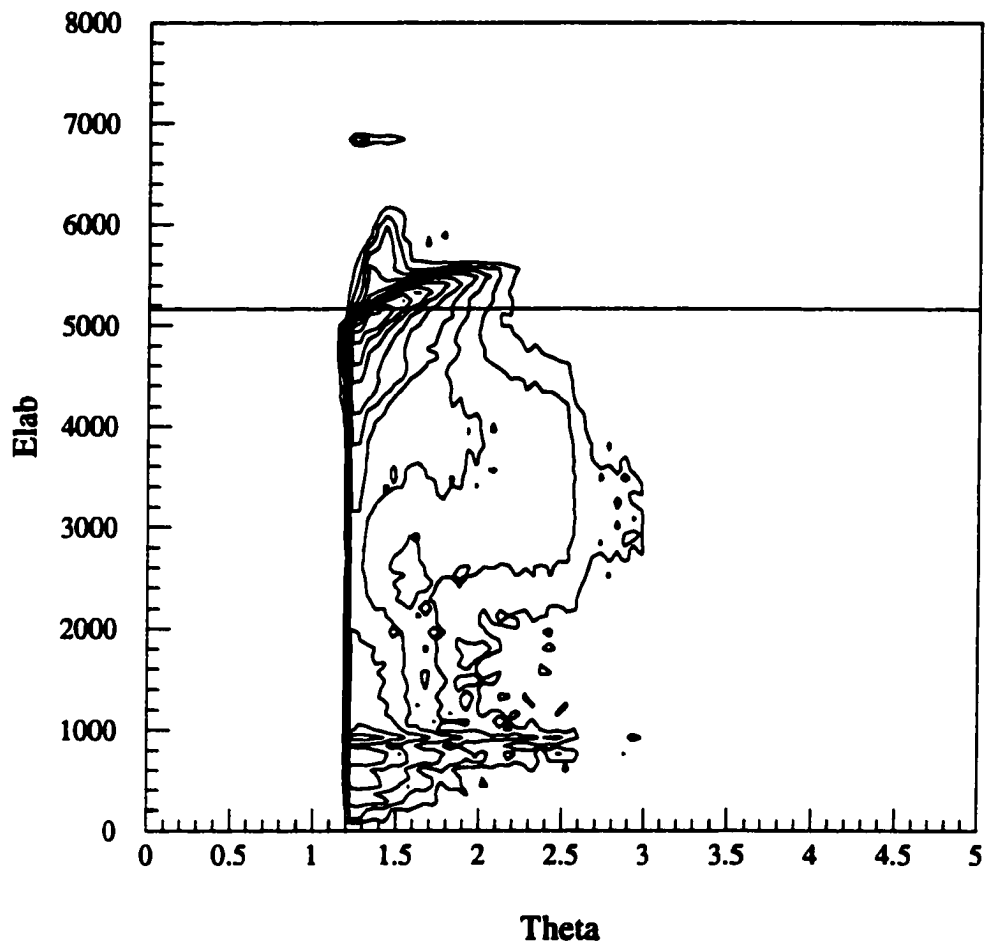
Figure III.19 Deflection function showing the double differential cross section $\frac{\partial^2\sigma}{\partial E\partial\theta}$

for Xe + Sc at E/A = 50 MeV on a log scale.

100
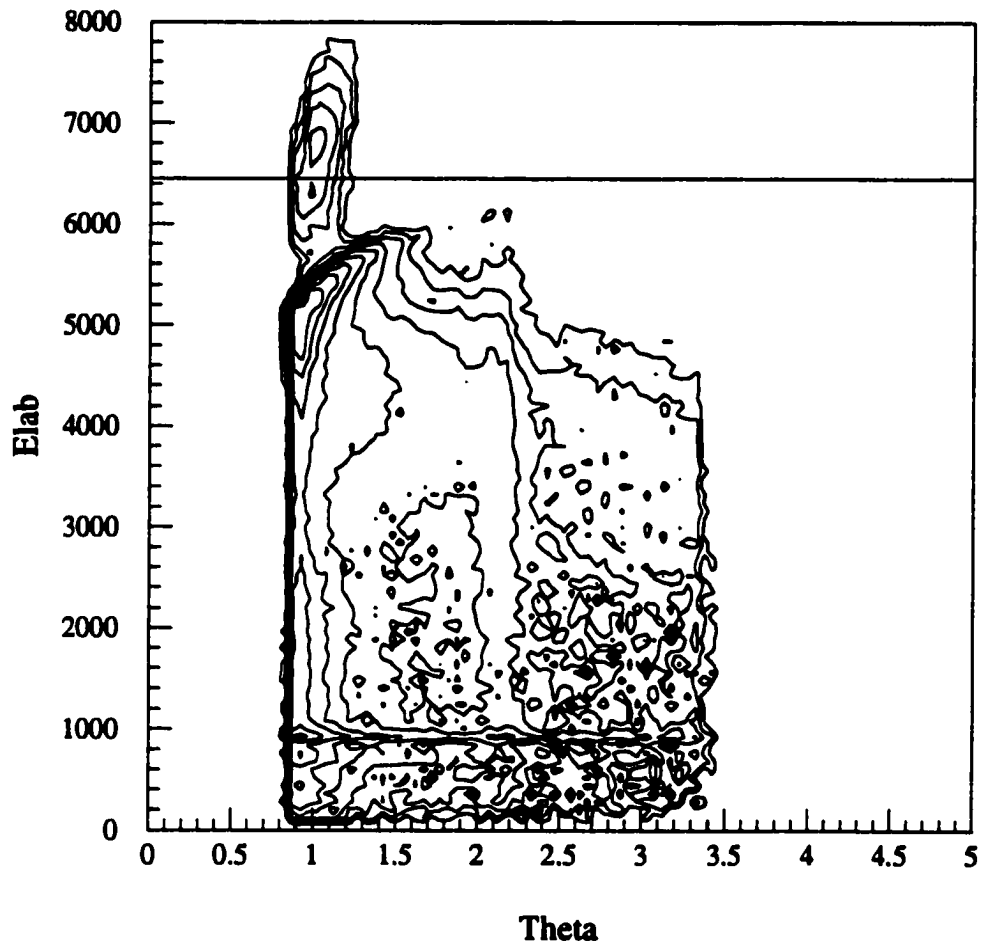
Figure III.20 Deflection function showing the double differential cross section $\frac{\partial^2\sigma}{\partial E\partial\theta}$

for Xe + Sc at E/A = 60 MeV on a log scale.

101

102
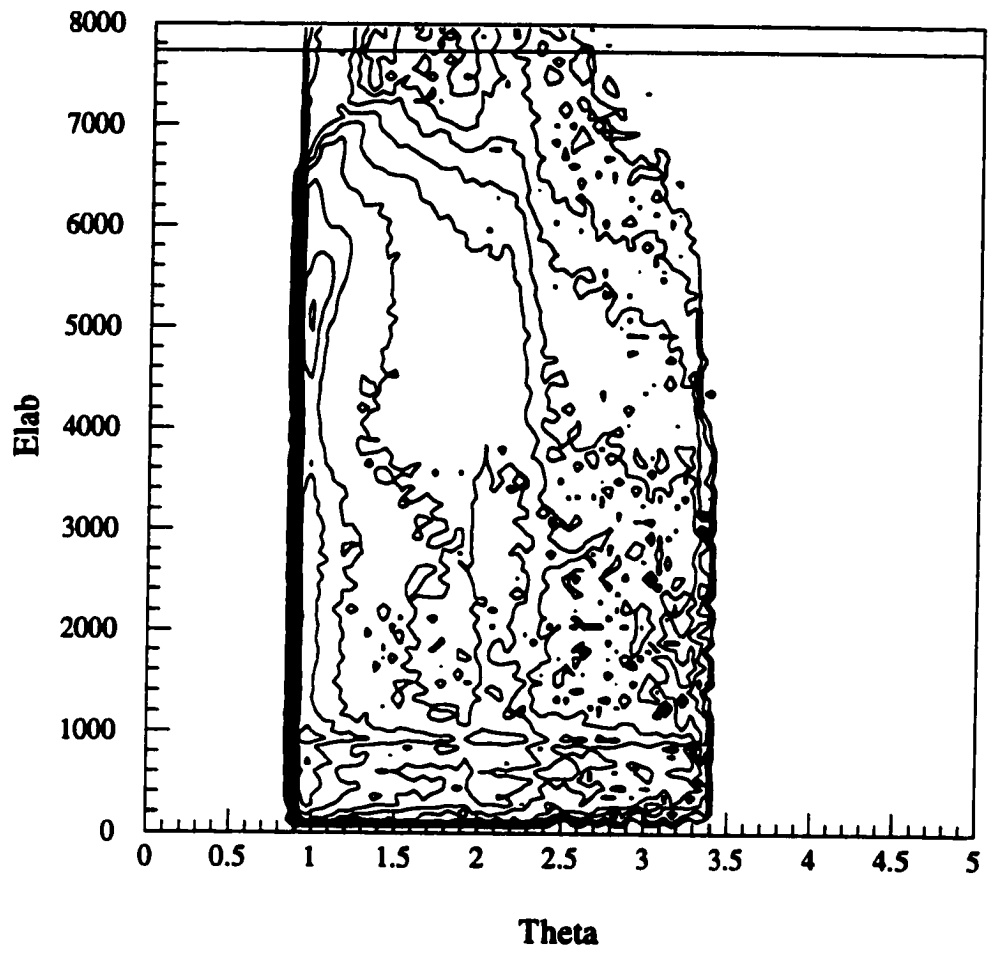
Chapter IV Model Calculations

Model predictions serve as a guide to help understand the signatures of reaction mechanisms. In this study the data are compared to two models. One of the models, the Tassan-Got (TG) model [TAS91], is a stochastic nucleon exchange model which is used to describe deep-inelastic reactions. The other model solves the Boltzmann-Uehling-Uhlenbeck [BER88] (BUU) equation and is a fully microscopic model which tracks nucleons as they interact with each other under the influence of a mean field.

The cooling of hot nuclei, with temperatures above a few MeV, is not a well understood phenomena. Both TG and BUU form excited primary fragments. Before the results can be compared to experimental data, the primary fragments must be allowed to de-excite. After the models are run, the calculated hot fragments are then allowed to cool using two different "afterburners". The sequential binary decay code GEMINI [CHA88,CHA90] is the standard decay model used for nuclear systems with low to moderate excitation energy. The simultaneous multifragmentation model SMM[BON85a, BON85b, BAR87] is often used for hot systems formed in intermediate energy heavy-ion collisions. These two models use very different assumptions. Whether hot nuclei break apart in a series of sequential 2-body steps or in one multfragment step is still under debate.

The results of the models are normalized to the geometric cross section as a function of the ℓ-value for the primary calculations.

IV.A Tassan-Got's Stochastic Nucleon Exchange Model

Tassan-Got's model assumes that energy dissipation occurs through a stochastic exchange of nucleons. As the projectile and target touch, a window opens for nucleon exchange, as seen in the shaded region in Fig. IV.1 [TAS91]. As

103

Figure IV.1 A schematic diagram showing the geometry assumed in the TG model. The x, y, and z axes are defined in (a). The point O is the origin of the coordinate system, and C_1 and C_2 are the centers of the donor and acceptor nuclei, respectively. The window of overlap is shown in (b). The values of ρ and θ define the position in the window of the transferred nucleon.

105
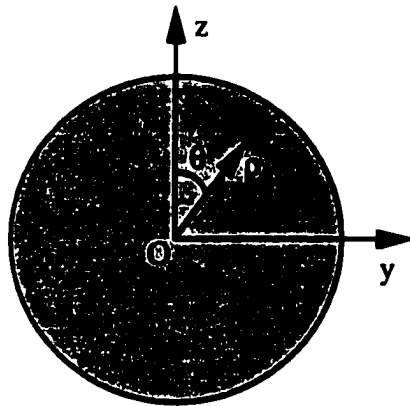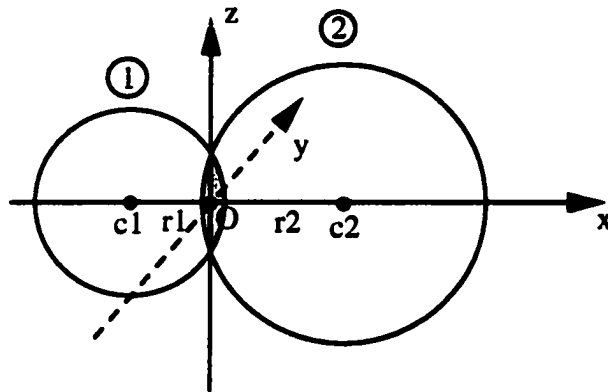
nucleons transfer from the donor to the acceptor, they bring relative kinetic energy with them.

The transfer process is parameterized by 5 parameters, $\sigma(p_{1x}, p_{1y}, p_{1z}, \rho, \theta)$. The first 3 parameters are the x, y, and z components of the momentum of the transferred nucleon. The last 2 parameters, ρ and θ, define the position of the transferred particle in the window, as shown in Fig. IV.1. The origin of the reference frame is in the center of the overlapping region, labeled O in the figure, and ρ and θ are defined in the y-z plane. Only transfers that occur in the appropriate direction are allowed. The probability for a transfer to occur is given by

$$P = \int \Phi T n_1 (1 - n_2) d^5\sigma, \qquad \text{(IV-1)}$$

where Φ is the one way phase space flux and T is the barrier penetrability calculated using a sum of two Woods-Saxon potentials. The variables n_1 and n_2 are the occupation probabilities.

A random drawing decides the type, proton or neutron, and the direction of the transfer. Energy conservation is maintained by requiring

$$\Delta\delta_1 + \Delta\delta_2 + \Delta E_1^* + \Delta E_2^* + \Delta K + \Delta U = 0, \qquad \text{(IV-2)}$$

where $\Delta\delta_1$ and $\Delta\delta_2$ are the changes in the mass excess after the removal of a nucleon from nucleus 1 and the addition of a nucleon to nucleus 2. The ΔK term is the relative kinetic energy of the nucleon, and ΔU is the difference in the potential well depth of the donor and acceptor nuclei, as shown in Fig IV.2 [TAS91]. The values ΔE_1^* and ΔE_2^* are differences in the excitation energy over the ground state due to differences in the Fermi energies of the donor and acceptor nuclei,

$$\Delta E_1^* = \varepsilon_{F1} - \varepsilon_1 \qquad \text{(IV-3)}$$

and

$$\Delta E_2^* = \varepsilon_2 - \varepsilon_{F2}. \qquad \text{(IV-4)}$$

106

Figure IV.2 Potential wells for the donor and acceptor nuclei. The energies ε_{F1} and ε_{F2} are the Fermi energies, U_1 and U_2 are the depths of the potential wells, and $\varepsilon1$ and $\varepsilon2$ are the different energies of the transferred nucleon over the Fermi energies for the donor and acceptor nuclei, respectively.

107

108
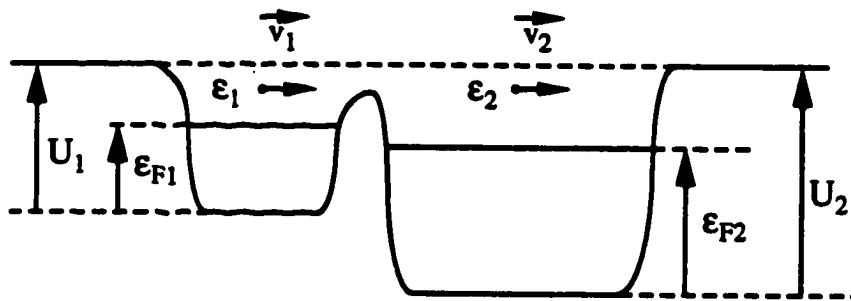
After a transfer occurs, new values for A, Z, and E* are calculated and the process starts again.

IV.B Boltzmann-Uehling-Uhlenbeck Equation (BUU)

The BUU equation is a combination of the cascade model and the Vlasov equation [BER88]. In the cascade model, the nucleus is considered a spherical collection of point particles. The nucleus is then boosted to beam velocity and given a particular impact parameter with respect to the target. The projectile and target nucleons are allowed to scatter off each other and are followed throughout the reaction. The cascade model treats only the hard scattering of the nucleons and ignores mean-field effects. The Vlasov equation is an approximation of time dependent Hartree-Fock theory. The BUU equation is

$$\frac{\partial f}{\partial t} + v \cdot \nabla_r f - \nabla_r U \cdot \nabla_p f = \bar{I}|f|, \qquad \text{(IV-5)}$$

where $\bar{I}|f|$ is the average rate of change of the particle distribution f. This is numerically solved using the cascade model. The left side of the equation, when set to zero, is the Vlasov equation. The mean-field potential U used in the BUU equation is a density dependent Skyrme potential

$$U(\rho) = A\left(\frac{\rho}{\rho_0}\right) + B\left(\frac{\rho}{\rho_0}\right)^{\sigma}, \qquad \text{(IV-6)}$$

where the A term is attractive, the B term is repulsive, $\sigma > 1$, ρ is the density, and ρ_0 is the normal nuclear density ($\sim 0.15 \text{ fm}^{-3}$).

The solution to the BUU equation is a particle distribution function; it does not produce individual fragments. A clustering routine is necessary to create fragments out of the particle distributions. Garcia-Solis' [GAR96] clustering routine was used in this study. The routine looks for fragment seeds by breaking up coordinate space into cubes with sides $2r_b$. The cube is considered "interior" if the nuclear density at

109

the center of each face of the cube is greater than normal nuclear density. In this case, the nucleons in the center are surrounded by nuclear matter. A nucleon is an "exterior nucleon" that is part of the cluster if its momentum and position are within the Fermi momentum and r_b, the cube size of the seed. The value of r_b was set to 9 fm.

In addition, when in time during the collision to start the clustering is important. Typically, a freeze-out time is chosen at the time when the overall density and energy are at a minimum [GAR96]. The time dependence of the density and energy are shown in Fig. IV.3. After the first minimum, the system will continue to oscillate in density and energy. The first minimum was chosen as the freeze-out time at around $t = 90$ fm/c. At this point the BUU is stopped [BER88], and clusters are created from the resultant nucleon distribution in phase space.

IV.C GEMINI

The sequential decay code GEMINI follows the decay chain of a hot compound nucleus. It steps though binary decays until the fragments no longer have enough energy to decay. For $Z \leq 2$, GEMINI uses Hauser-Feschbach formalism to calculate the decay widths for evaporation of light particles (Z_1,A_1) from the hot system (Z_0,A_0), leaving the residual nucleus (Z_2,A_2). The decay width Γ is given by

$$\Gamma(Z_1,A_1,Z_2,A_2) = \frac{2J_1+1}{2\pi\rho_0} \sum_{\ell=|J_0-J_2|}^{J_0+J_2} \int_0^{E^*-B-\epsilon_{rot}} T_\ell(\epsilon)\rho_2(U_2,J_2)d\epsilon, \qquad (IV-7)$$

where ℓ and ϵ are the angular momentum and the kinetic energy for the emitted fragment. The transmission coefficient T_ℓ is taken from the sharp-cut off model,

$$T_\ell(\epsilon) = \begin{cases} 0 & \epsilon < \epsilon_{coul} + \dfrac{\hbar^2\ell(\ell+1)}{2\mu R^2} \\ 1 & \epsilon \geq \epsilon_{coul} + \dfrac{\hbar^2\ell(\ell+1)}{2\mu R^2} \end{cases}, \qquad (IV-8)$$

110

Figure IV.3 Time dependence of the overall density and energy calculated by the BUU model.

111
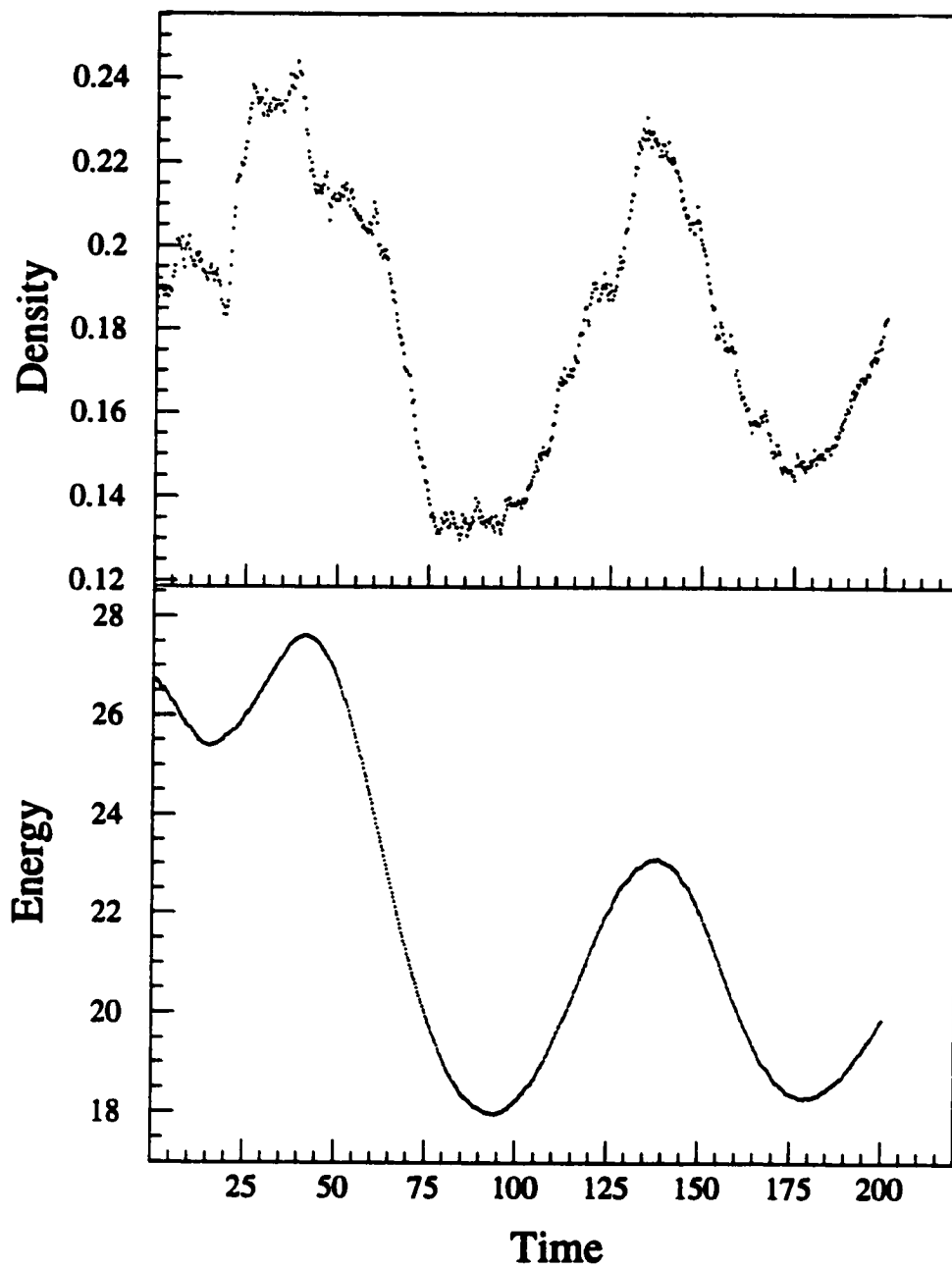
where μ is the reduced mass and ε_{coul} is the Coulomb barrier. The absorptive radius R is calculated using

$$R = \begin{cases} 1.16A_2^{1/3} + 2.6\,\text{fm} & \text{for proton and neutron emission} \\ 1.16A_2^{1/3} + 3.7\,\text{fm} & \text{for alpha emission} \end{cases} \qquad \text{(IV-9)}$$

The level density of the residual nucleus $\rho(U_2, J_2)$ is calculated using the Fermi-gas model with the Lestone [LES95] temperature dependent level density parameter.

For Z > 2, the transition state formalism of Moretto is used to calculate the decay widths. The decay width is given by

$$\Gamma(Z_1, A_1, Z_2, A_2) = \frac{1}{2\pi\rho_0} \int_0^{E^* - E_{sad}(J_0)} \rho_2(U_{sad}, J_0)d\varepsilon, \qquad \text{(IV-10)}$$

where ρ_{sad} is the level density of the conditional saddle point configuration, ε is the kinetic energy, T_r is the transmission coefficient, and U_{sad} is the thermal energy of the saddle point, given by

$$U_{sad} = E^* - E_{sad}(J_0) - \varepsilon. \qquad \text{(IV-11)}$$

The deformational plus rotational energy of the saddle point $E_{sad}(J_0)$ is given by

$$E_{sad}(J_0) = E_{sad}^{RFRM}(J_0) - M_{Y+e}(Z_1, A_1) + M_{exp}(Z_1, A_1), \qquad \text{(IV-12)}$$

where $E_{sad}^{RFRM}(J_0)$ is the saddle point energy from the rotating finite range model, M_{y+e} is the mass calculated from the Yukawa+exponential model, and M_{exp} is the experimental mass.

After the hot system breaks up, the resulting fragments are treated as new excited systems which can decay if they have sufficient excitation energy. The decay chain is followed until all the fragments are cool.

113

IV.D Simultaneous Multifragmentation Model

The simultaneous multifragmentation model SMM [BON85a, BON85b, BAR87] starts with an excited compressed system characterized by mass A_0, charge Z_0, and total energy E_0. The system goes through three stages. First, during formation of the hot system, cracks form in the system. Second, the system expands and fragments form. Last, light particles evaporate removing the last of the excitation energy. Before the system expands through a break-up volume, thermal equilibrium is reached and the system attains an average composition of protons and neutrons. After the break-up the system is in a final state partition. The partition consists of all the fragments that the system broke into. The probability that the final state is in partition {F} is given by

$$\Delta \Gamma_F = \exp S_F(A_0, Z_0, E_0), \qquad \text{(IV-13)}$$

where S_F is the final state entropy. The final states are constrained by

$$\sum_{A,Z} N_{A,Z} A = A_0, \qquad \text{(IV-15)}$$

$$\sum_{A,Z} N_{A,Z} Z = Z_0 \qquad \text{(IV-16)}$$

and

$$E_{tot} = \frac{3}{5} \frac{Z_0^2 e^2}{R} + \sum_{A,Z} N_{A,Z} E_{A,Z} = E_0^{ground} + E_0^* = E_0, \qquad \text{(IV-17)}$$

where $N_{A,Z}$ is the multiplicity of fragments with mass A and charge Z, and E_0^* is the excitation energy above the ground state E_0^{ground}. The total energy E_{tot} is the sum of the Coulomb energy of a homogeneous charged sphere of radius R and the contribution of the individual fragments. The energy $E_{A,Z}$ for each fragment with mass A and charge Z is approximated using the liquid drop model as the sum of the bulk, surface, clustering, Coulomb, and translational energies

114

$$E_{A,Z} = E_{A,Z}^B + E_{A,Z}^S + E_{A,Z}^{sym} + E_{A,Z}^C + E_{A,Z}^T. \qquad \text{(IV-18)}.$$

IV.E Primary Distributions

The primary Z vs. E* distributions calculated by the TG model for the Xe +

Sc and Cu systems at E/A = 30 MeV are shown in Fig. IV.4 (a) and (b), respectively.

For both systems, the TG model predicts formation of an excited PLF. The TG

model tends to drive the primary system toward greater mass asymmetry, as seen in

lower energy reactions with similar mass asymmetries [MAD92, MAD95].

Increasing the beam energy has little effect on the primary Z vs. E* distribution

calculated with the TG model, other than to make the system slightly more excited.

The calculated primary Z vs. E* distributions for Xe + Sc and Cu systems at E/A =

30, 40, 50, and 60 MeV are shown in Fig. IV.4 - IV.7 (a) and (b), respectively. The

TLF is not shown because it typically does not have enough energy to be identified by

the MFA and is mostly at angles covered by other detectors. Neglecting the TLF

saves CPU time, which can be considerable for the afterburners. Excited products

from more central collisions are not seen in the TG results because the TG model

restricts the angular momentum range from ℓ_{crit} to ℓ_{max}. By definition, fusion cannot

occur over ℓ_{crit}.

The primary Z vs. E* distributions calculated by the BUU model for the Xe +

Sc and Cu systems at E/A = 30 MeV are shown in Fig. IV.4 (c) and (d), respectively.

The solid lines mark $Z_{projectile}$ = 54 and Z_{target} = 21 and 29. Unlike the TG model

results, BUU predicts the formation of many light charged particles. The BUU model

also tends to create systems with more excitation energy than systems from the TG

model, since the BUU calculation includes reactions over all impact parameters, not

just peripheral collisions. Unlike the TG model, BUU predicts a very different

primary distribution for the Xe + Sc and Xe + Cu systems. In the Sc system, it

115

Figure IV.4 Primary charge vs. excitation energy at E/A = 30 MeV from the (a) Xe +

Sc TG, (b) Xe + Cu TG, (c) Xe + Sc BUU, and (d) Xe + Cu BUU model

calculations.

116

Sc   Cu

(a)   (b)

(c)   (d)

E*   (MeV)   E*   (MeV)

117
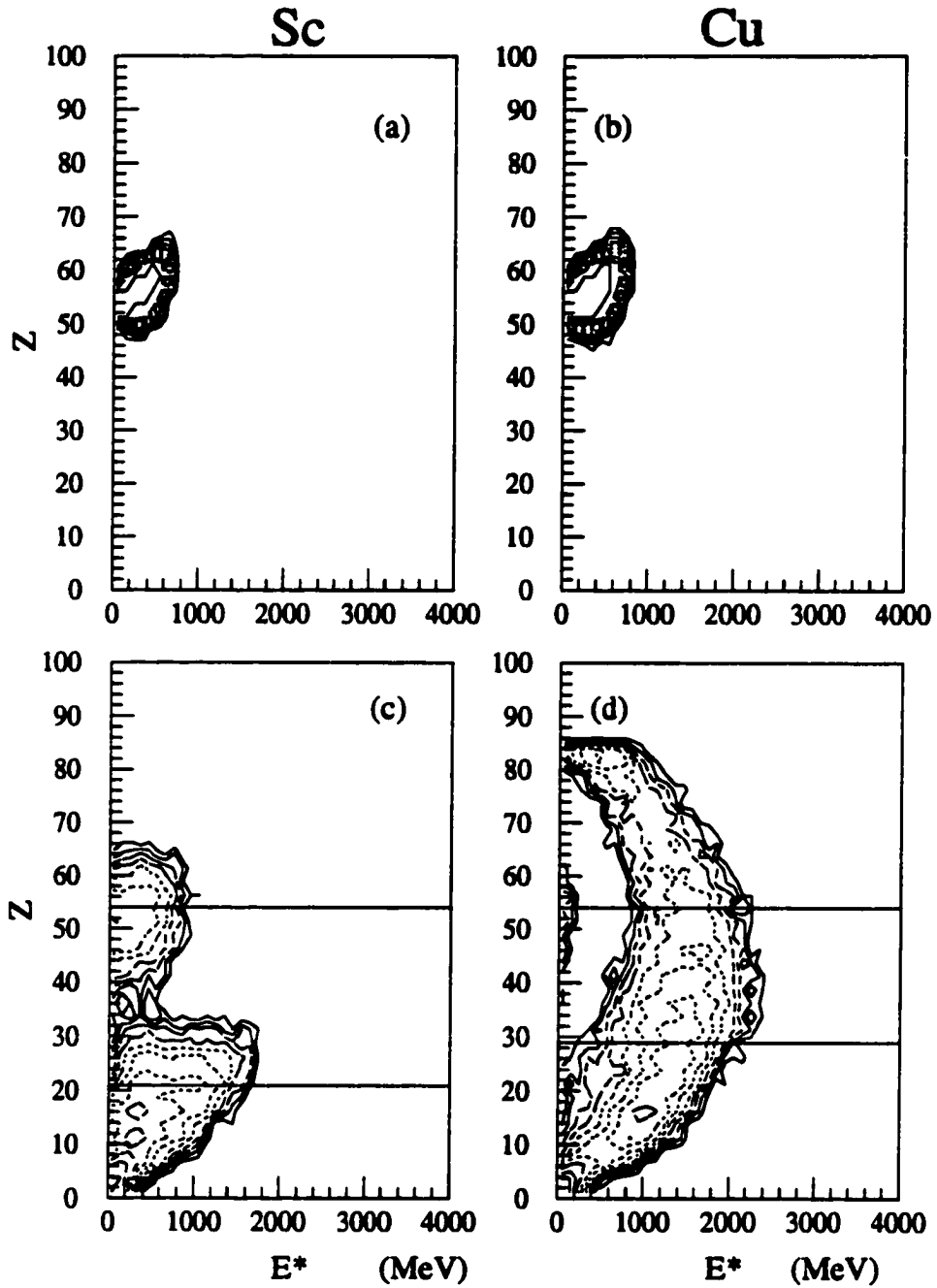
appears that a PLF is present with excitation energy similar to the TG result. However, in the Xe + Cu system the PLF cross section is very small and the PLF has very low excitation energy. Instead, a significant fusion-like component exists in the Xe + Cu system, along with copious production of IMF's.

The BUU generated primary Z vs. E* distributions for E/A = 40 MeV are shown in Fig. IV.5 (c) and (d). Again, the primary fragments are very different in the two systems. For the Xe + Sc system, no longer can a clear PLF be seen. Fragments from near Z = 54 down to IMF's are produced, and the system has greater excitation energy than at E/A = 30 MeV. For the Xe + Cu case, the system no longer completely fuses. A highly excited system forms when the projectile tears off a chunk of the target. Increasing the beam energy to E/A = 50 MeV, shown in Fig. IV.6 (c) and (d), causes a dramatic difference in the Z vs. E* distribution between the Xe + Sc and Xe + Cu systems. A projectile spectator, with Z around 54 and low excitation energy, and a hot target-like fragment are seen in the Cu distribution. Thus, the BUU model predicts a participant-spectator reaction in the Xe + Cu system, but not in the Xe + Sc system. At E/A = 60 MeV, shown in Fig. IV.7 (c) and (d), an excited PLF and TLF are formed in the Xe + Cu system, however it's not seen in the Xe + Sc system. The incomplete fusion-like component of the Xe + Sc resembles the Xe + Cu at E/A = 40 MeV.

The primary deflection functions calculated using the TG model for Xe + Sc and Cu at E/A = 30, 40, 50, and 60 MeV are shown in Figs. IV.8 - IV.11 (a) and (b). The deflection functions calculated by the TG model for the Xe + Sc system are very similar to the deflection functions for the Xe + Cu system. This is not true for the BUU calculations shown in Figs. IV.8 - IV.11 (c) and (d). The BUU calculations have a much smaller cross section for the higher energy fragments at small angles for the Xe + Sc system than for the Xe + Cu system. Since the MFA sits at small angles,

118

Figure IV.5 Primary charge vs. excitation energy at E/A = 40 MeV from the (a) Xe +

Sc TG, (b) Xe + Cu TG, (c) Xe + Sc BUU, and (d) Xe + Cu BUU model

calculations.

119

Sc   Cu

(a)   (b)

(c)   (d)

E*   (MeV)   E*   (MeV)

120
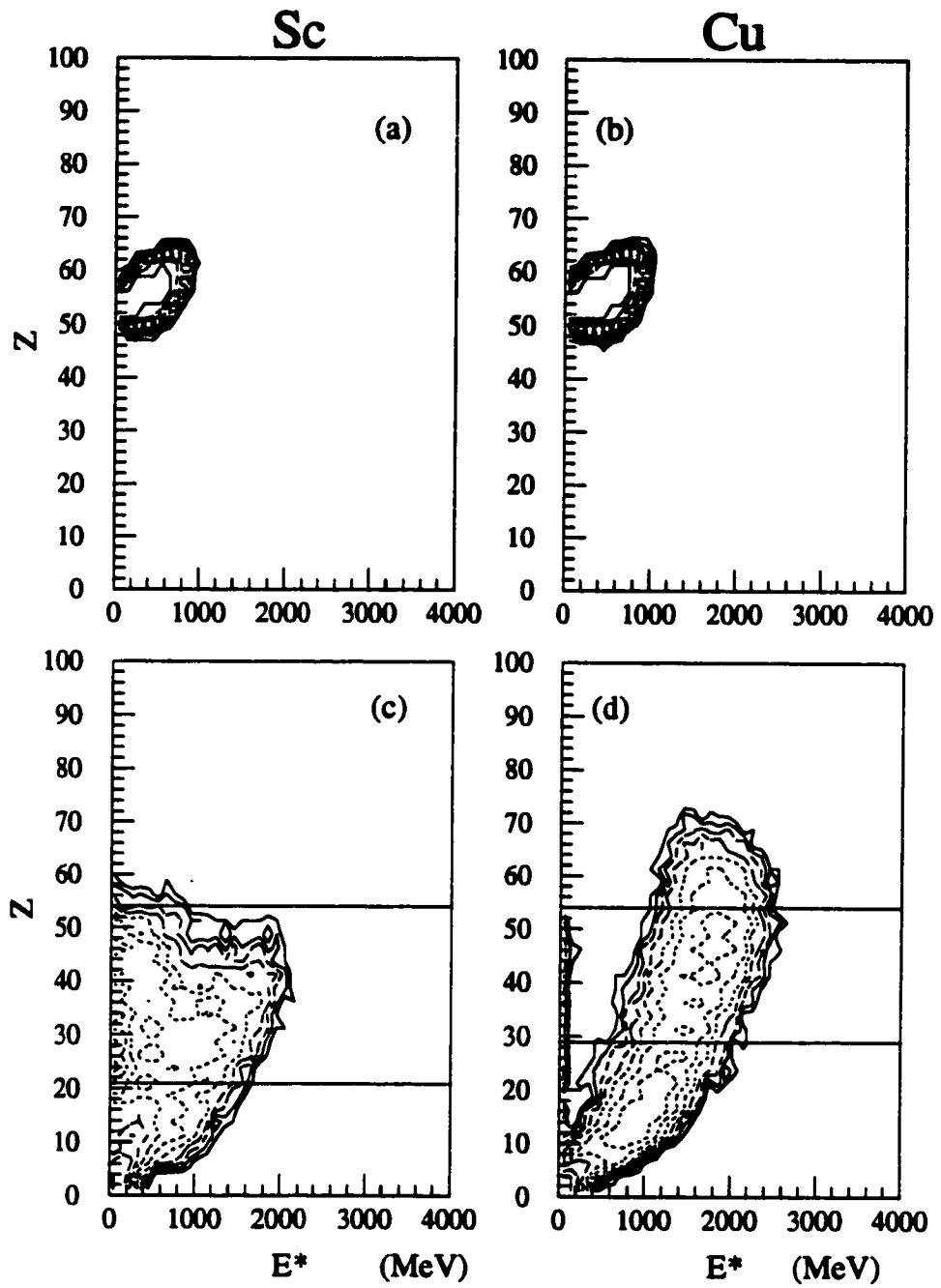
Figure IV.6 Primary charge vs. excitation energy at E/A = 50 MeV from the (a) Xe +

Sc TG, (b) Xe + Cu TG, (c) Xe + Sc BUU, and (d) Xe + Cu BUU model

calculations.

121

122
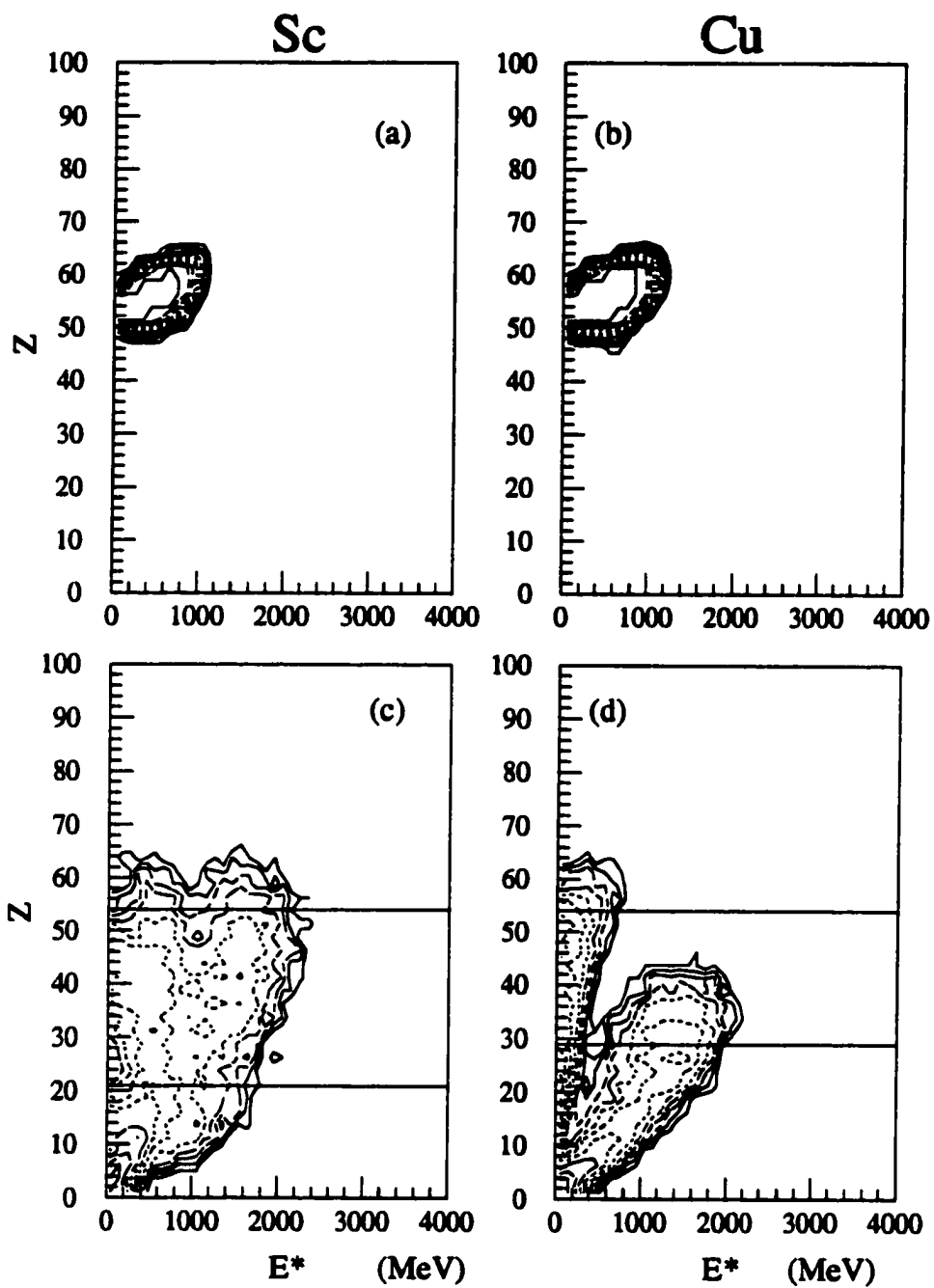
Figure IV.7 Primary charge vs. excitation energy at E/A = 60 MeV from the (a) Xe +

Sc TG, (b) Xe + Cu TG, (c) Xe + Sc BUU, and (d) Xe + Cu BUU model

calculations.

124
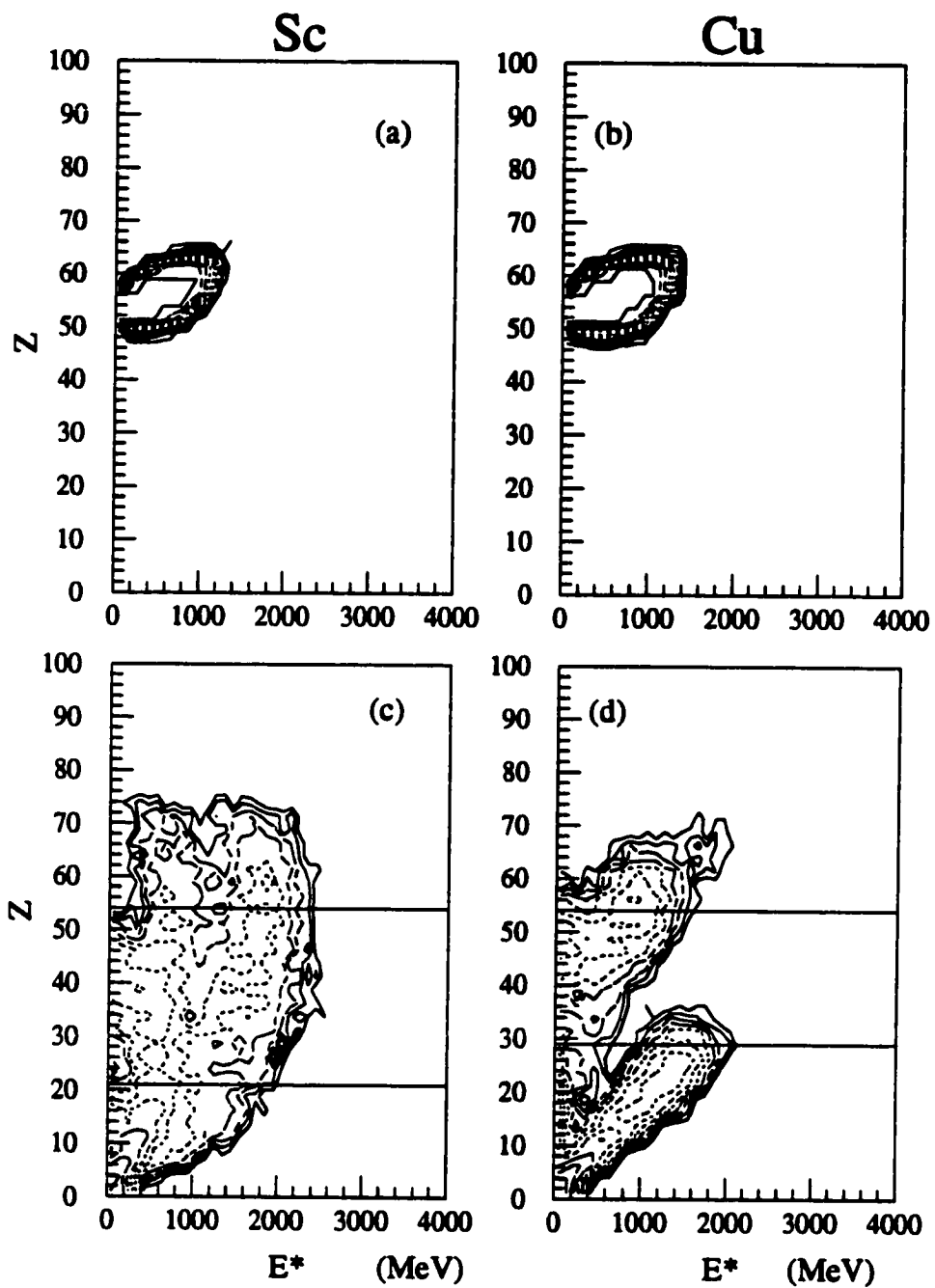
Figure IV.8 Kinetic energy of the primary fragments vs. scattering angle at E/A = 30 MeV from the (a) Xe + Sc TG, (b) Xe + Cu TG, (c) Xe + Sc BUU, and (d) Xe + Cu BUU model calculations.

126
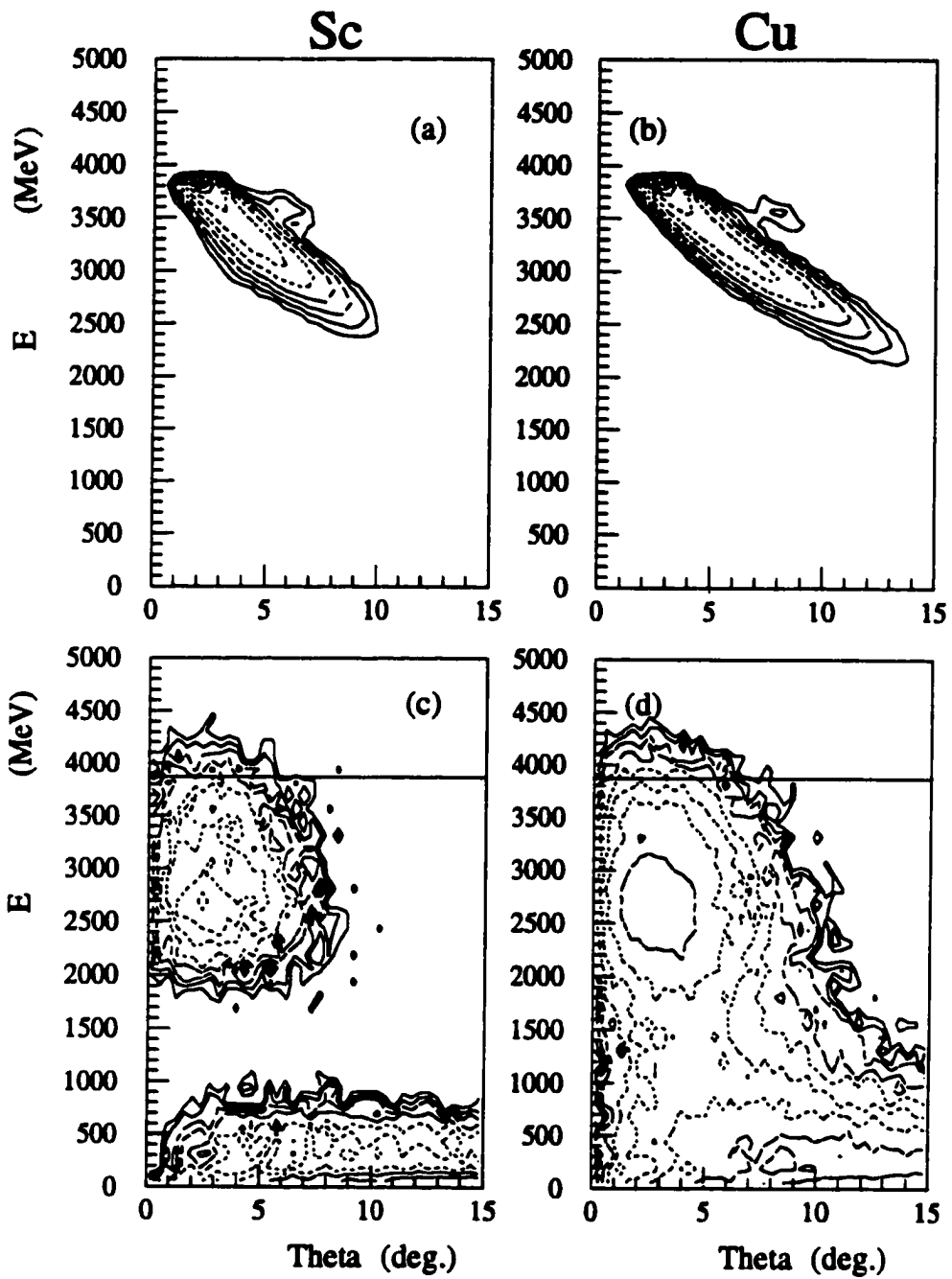
Figure IV.9 Kinetic energy of the primary fragments vs. scattering angle at E/A = 40 MeV from the (a) Xe + Sc TG, (b) Xe + Cu TG, (c) Xe + Sc BUU, and (d) Xe + Cu BUU model calculations.

128
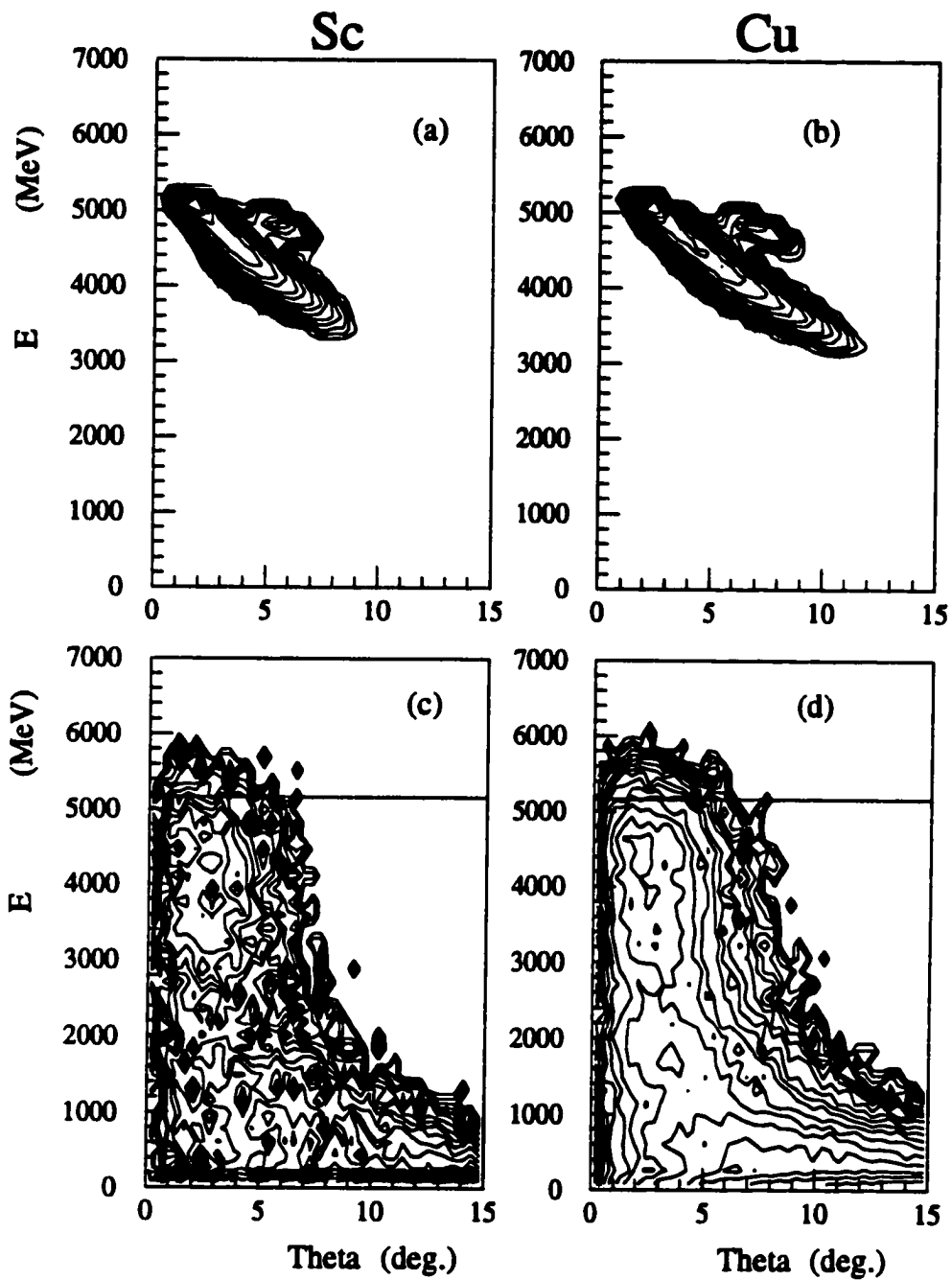
Figure IV.10 Kinetic energy of the primary fragments vs. scattering angle at E/A = 50 MeV from the (a) Xe + Sc TG, (b) Xe + Cu TG, (c) Xe + Sc BUU, and (d) Xe + Cu BUU model calculations.

130
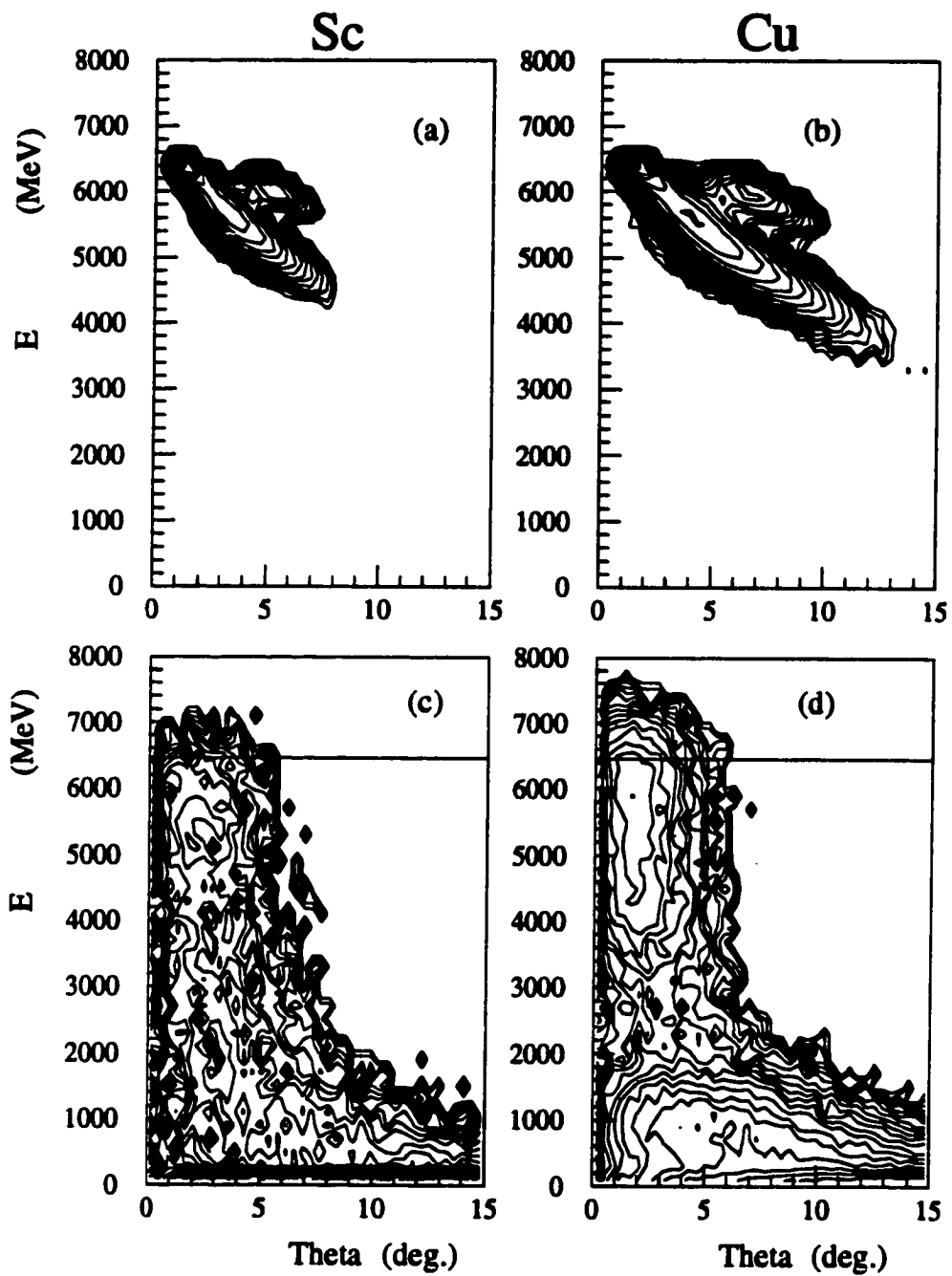
Figure IV.11 Kinetic energy of the primary fragments vs. scattering angle at E/A = 60 MeV from the (a) Xe + Sc TG, (b) Xe + Cu TG, (c) Xe + Sc BUU, and (d) Xe + Cu BUU model calculations.

131

Sc   Cu

(a)   (b)

(c)   (d)

Theta (deg.)   Theta (deg.)

132
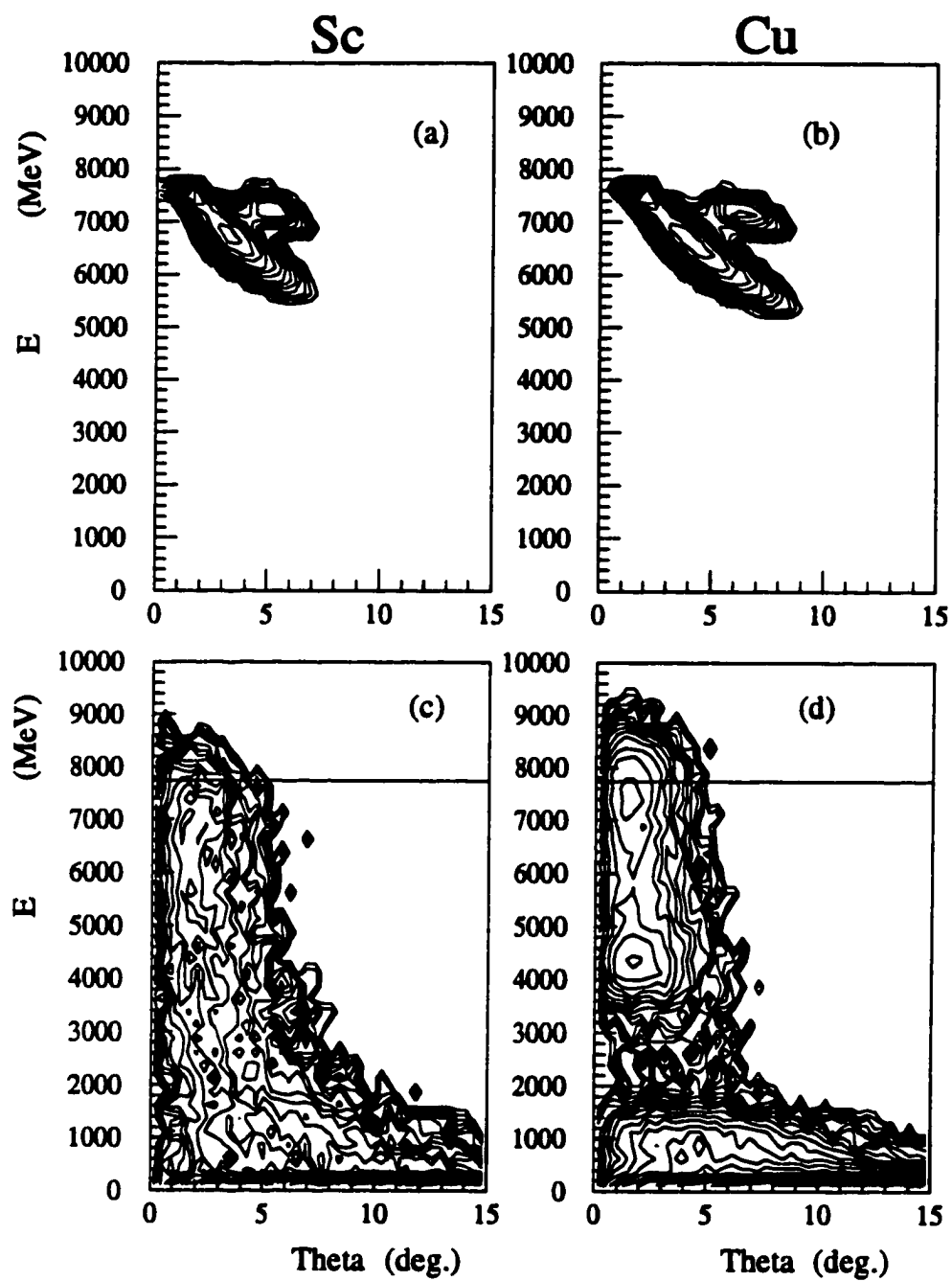
the BUU calculated cross sections are expected to be smaller for the Xe + Sc system than in the Xe + Cu system.

The Z vs. theta distributions calculated by the TG model for Xe + Sc and Cu at E/A = 30, 40, 50, and 60 shown in Figs. IV.12 - IV.15 (a) and (b) are very similar for the two targets. This is in contrast to the Z vs. theta distributions calculated by the BUU model for Xe + Sc and Cu at E/A = 30, 40, 50, and 60 MeV, shown in Figs. IV.12 - IV.15 (c) and (d), which are very different. For the E/A = 30 MeV systems, the Xe + Sc has a clear PLF focused at forward angles, and a TLF that is spread out to larger angles. In the Xe + Cu system, no PLF/TLF distinction exists. There is a peak at Z around 46, possibly due to incomplete fusion where a chunk of the projectile was removed by the target. Increasing to E/A = 40 MeV, the PLF and TLF are no longer seen in the Xe + Sc system. The Xe + Cu system forms fragments extending to much larger Z values than does the Xe + Sc system (ΔZ_{Cu-Sc} = 8) although forward focused peaks around Z = 46 are seen fro both systems. At E/A = 50 MeV, there is a large contribution from incomplete fusion in the Xe + Sc system. In the Xe + Cu system, a participant spectator peak exists along with many light charged particles. At E/A = 60 MeV, large systems are formed in the Xe + Sc calculation resembling the Xe + Cu at E/A = 40 MeV, while the Xe + Cu still contains the projectile spectator peak seen at E/A = 50 MeV. The Z around 46 peak persists . for the Xe + Sc even at E/A = 60 MeV.

IV.F MFA Filter

Since the MFA has such a small angular coverage, the geometric, as well as the energy, filter has a significant effect on the final distributions. The filter rejects fragments that have too little energy to punch into the fast plastic, and rejects fragments that have enough energy to punch out of the slow plastic, since in either case the MFA cannot identify the fragment. The filter also rejects fragments that fall

Figure IV.12 Primary charge vs. scattering angle at E/A = 30 MeV from the (a) Xe + Sc TG, (b) Xe + Cu TG, (c) Xe + Sc BUU, and (d) Xe + Cu BUU model calculations.

134

Sc   Cu

(a) (b)

(c) (d)

Theta (deg.)   Theta (deg.)

135
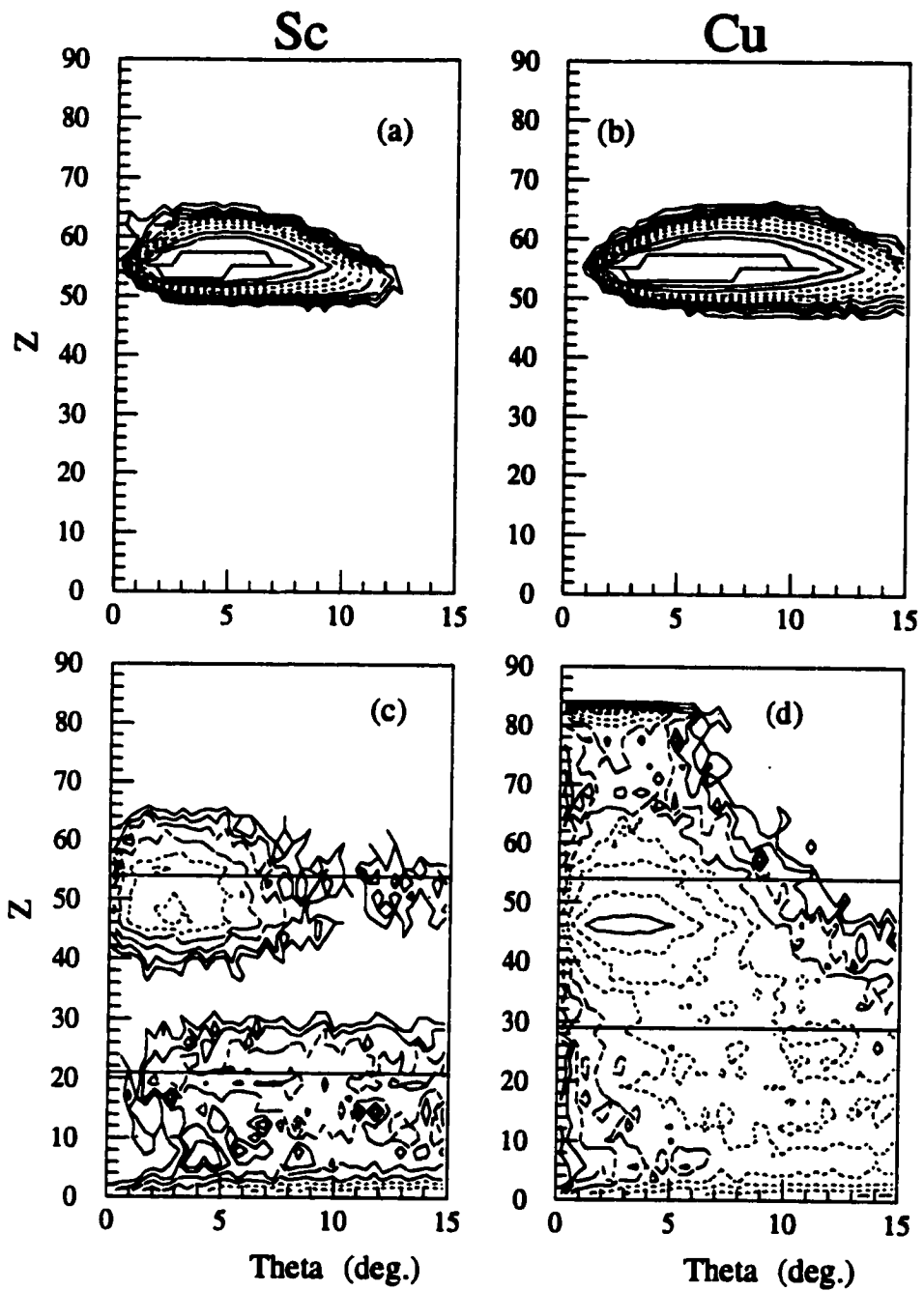
Figure IV.13 Primary charge vs. scattering angle at $E/A = 40$ MeV from the (a) Xe + Sc TG, (b) Xe + Cu TG, (c) Xe + Sc BUU, and (d) Xe + Cu BUU model calculations.

.

136

137
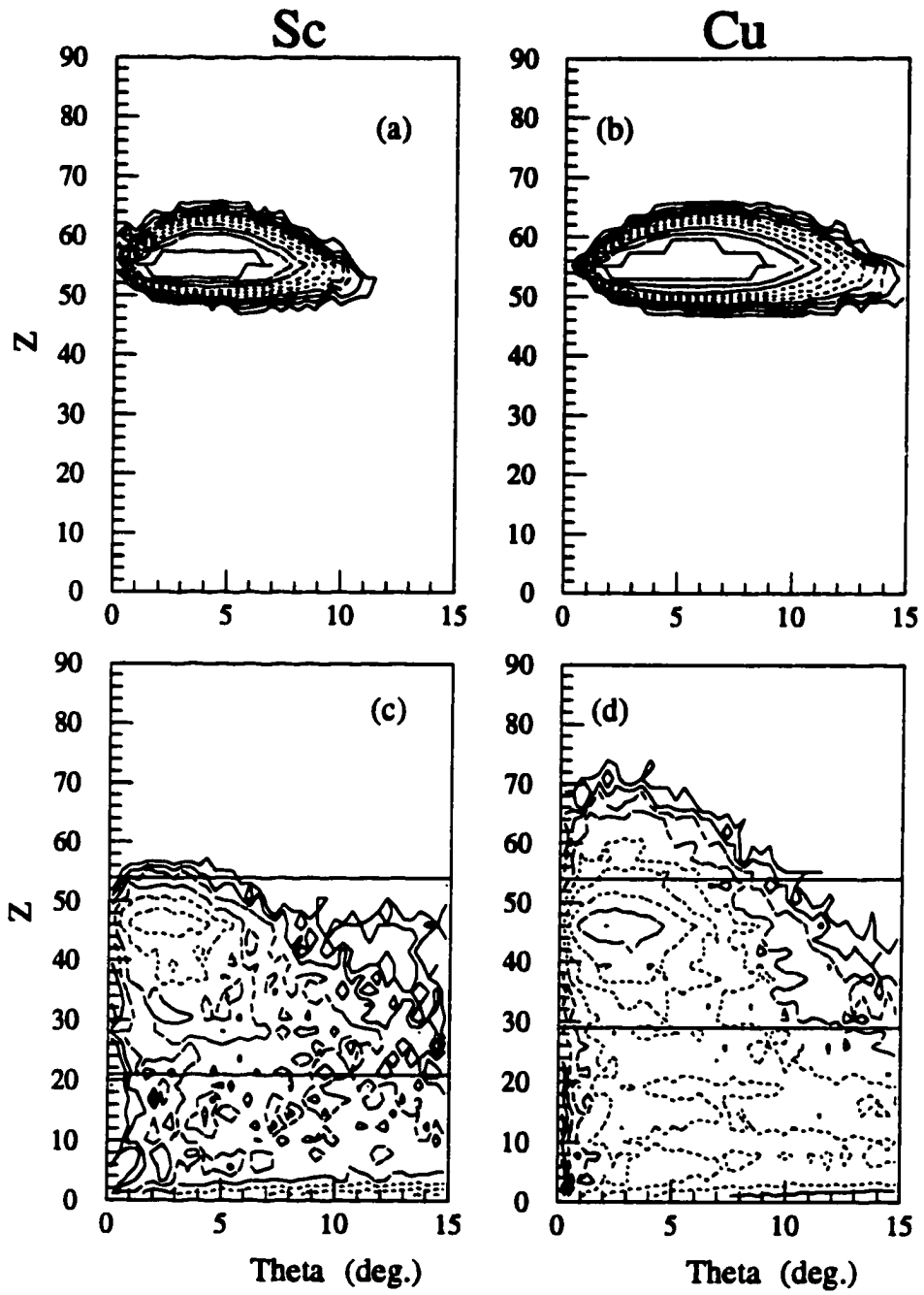
Figure IV.14 Primary charge vs. scattering angle at E/A = 50 MeV from the (a) Xe + Sc TG, (b) Xe + Cu TG, (c) Xe + Sc BUU, and (d) Xe + Cu BUU model calculations.

138

139
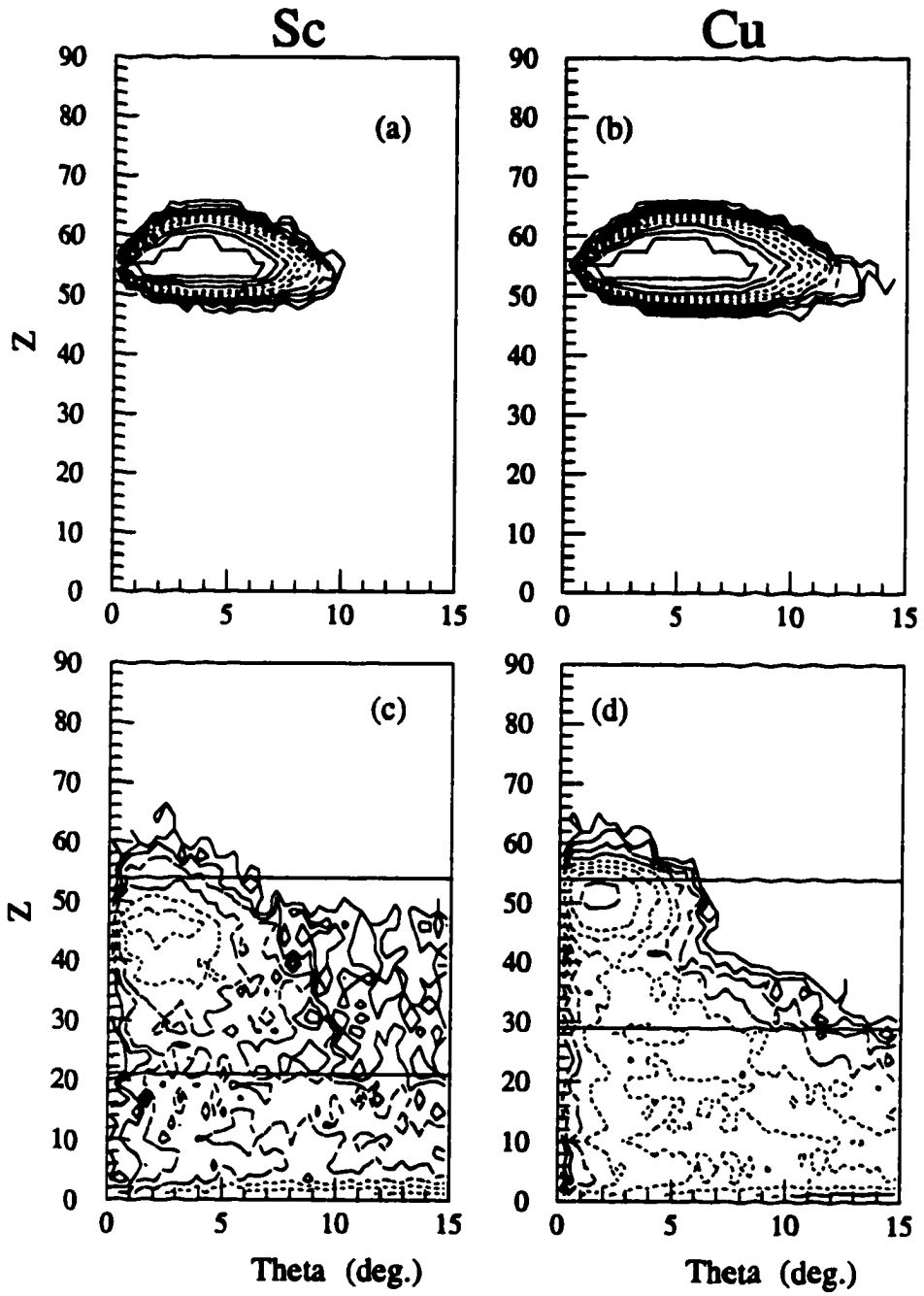
Figure IV.15 Primary charge vs. scattering angle at E/A = 60 MeV from the (a) Xe + Sc TG, (b) Xe + Cu TG, (c) Xe + Sc BUU, and (d) Xe + Cu BUU model calculations.

141
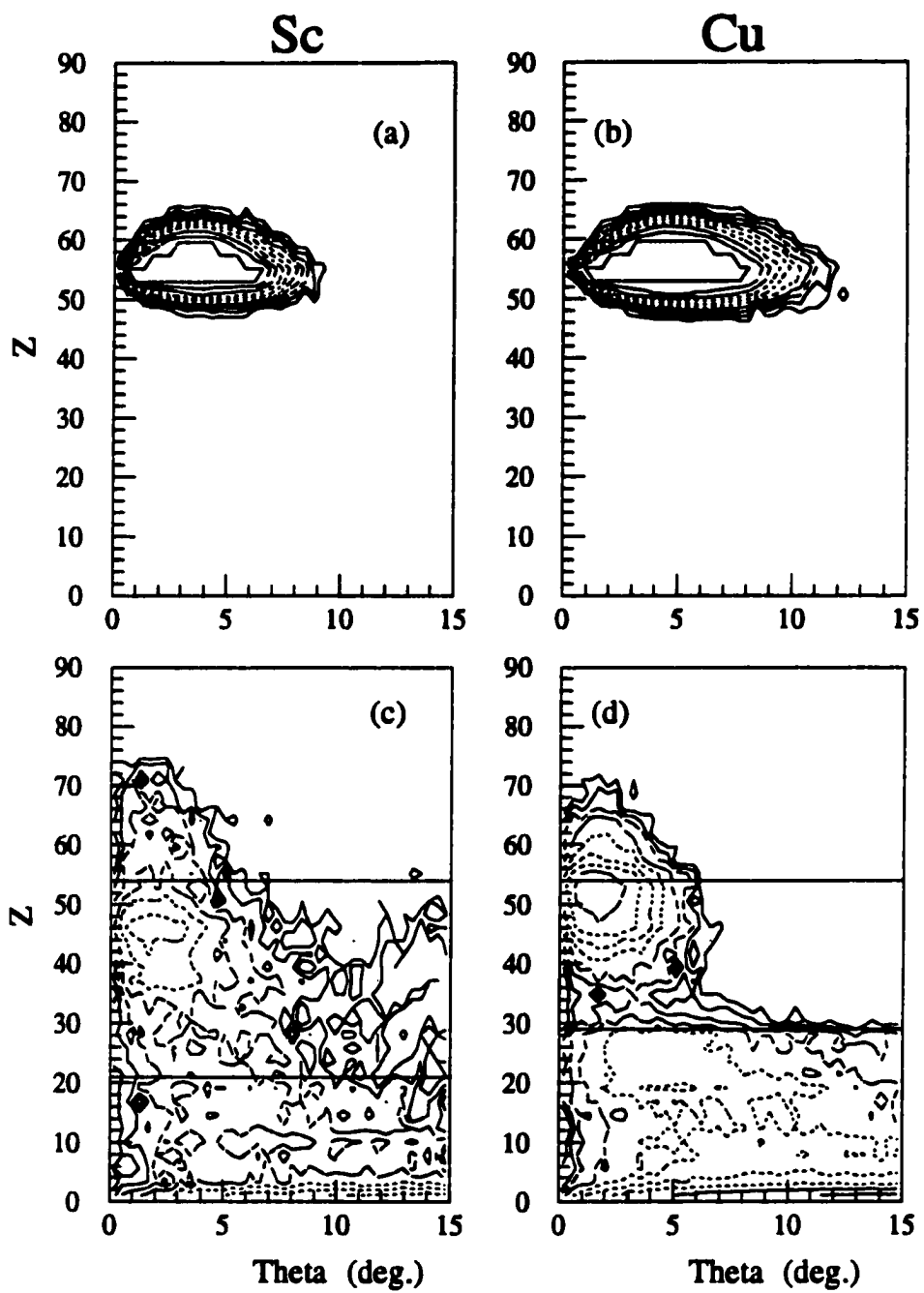
outside the angular coverage of the MFA. Since the beam was not centered, the position of the fragment was shifted by the measured mean center for each energy and target combination. After the GEMINI and SMM afterburners were run, the calculated results were filtered with the MFA filtering routine. The effect of the filter can be seen in Fig. IV.16 (a) and (b). The solid lines are the unfiltered TG calculated (a) charge and (b) energy distributions with a GEMINI afterburner. The dotted lines are the same distributions after going through the MFA filter. The dashed lines are the results for the filtered TG calculation with an SMM afterburner.

IV.G Secondary distributions

The secondary charge distributions calculated by the TG model for Xe + Cu at E/A = 30, 40, 50, and 60 MeV are shown in Fig. IV.17 (a) - (d). The solid and dashed lines are the results from the TG model with the GEMINI afterburner or with the SMM afterburner, respectively. The similarity between the results of the two afterburners at the higher energies is interesting considering they have such radically different assumptions. One difference that stands out is the presence of a symmetric fission peak around Z = 30 in the TG+GEM results. The energy distributions calculated by TG+GEM and TG+SMM for the Xe + Cu at E/A = 30, 40, 50 and 60 MeV are shown in Fig. IV.18 (a)-(d). The fission peak located just below E = 0.5 E_{beam} is evident in the TG+GEM results. The velocity distributions for the Xe + Cu system at 30, 40, 50 and 60 MeV are shown in Fig. IV.19 (a)-(d). There is a predominance of fragments near the beam velocity, regardless of the secondary decay mode. The TG results for the Xe + Sc system are not shown because they are very similar to TG results for the Xe + Cu system as noted in the primary distributions.

As with the TG model results, there is little difference between the SMM and GEMINI afterburners in the BUU secondary distributions. The BUU secondary charge distributions are shown in Fig. IV.20 (a)-(d) for the Xe + Cu system

142

Figure IV.16 Effect of the MFA geometric and energy filter on the TG model results. The solid line is the unfiltered TG+GEM results. The dotted and dashed lines are the filtered results from the TG+GEM and TG+SMM models, respectively.

143

144
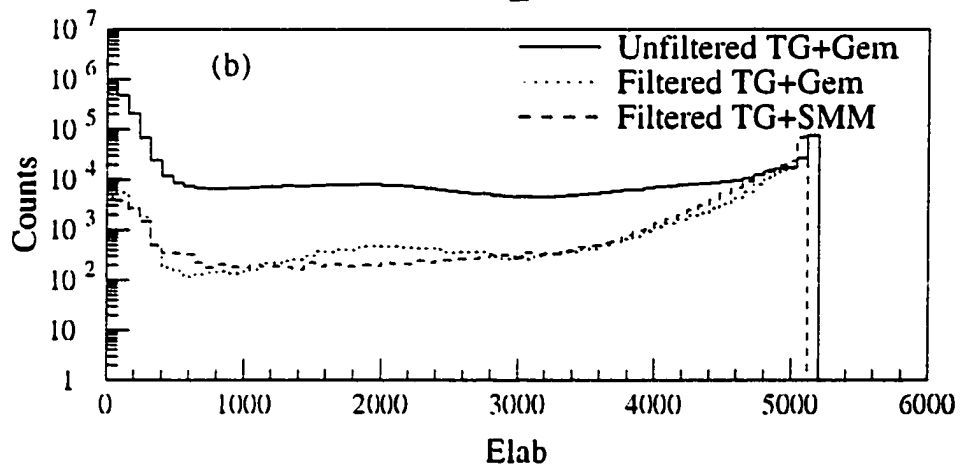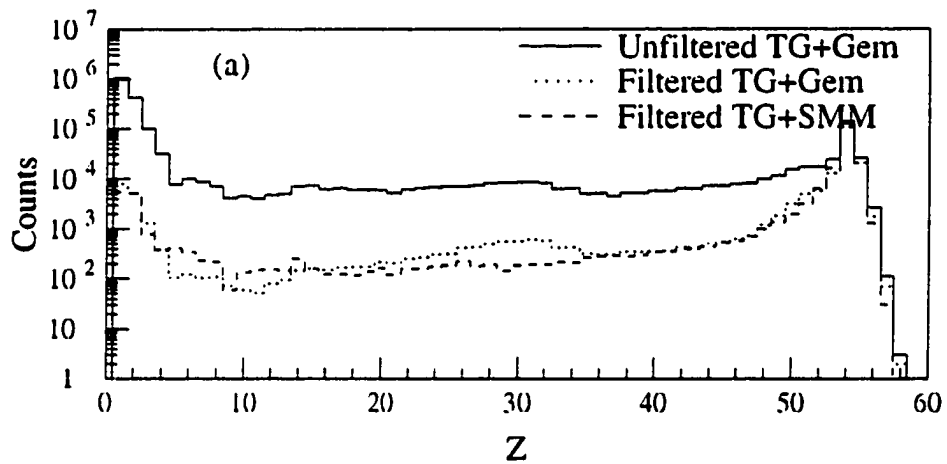
Figure IV.17 The calculated secondary charge distributions for the TG+GEM and

TG+SMM models for Xe + Cu at (a) E/A = 30 MeV, (b) E/A = 40 MeV (c) E/A = 50

MeV, and (d) E/A = 60 MeV. The solid and dashed lines represent the TG+GEM and

TG+SMM results, respectively.

145

146
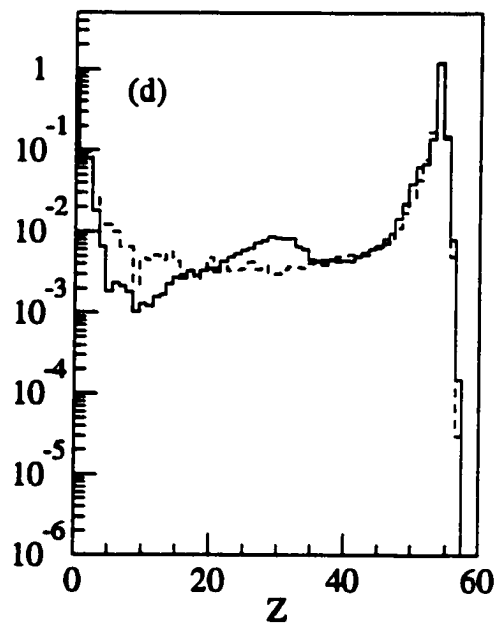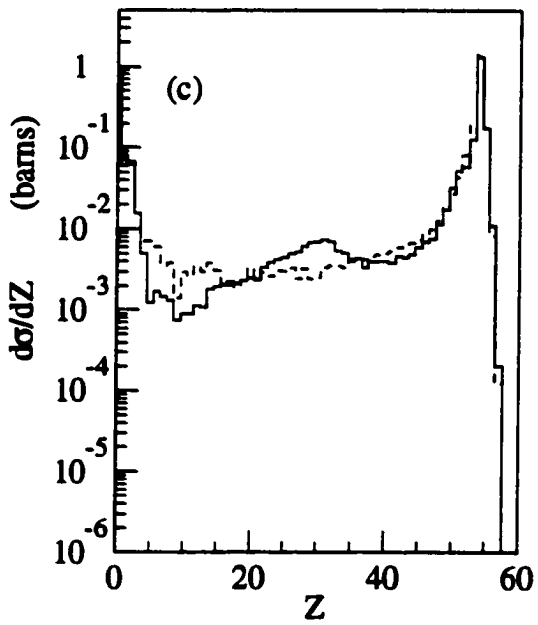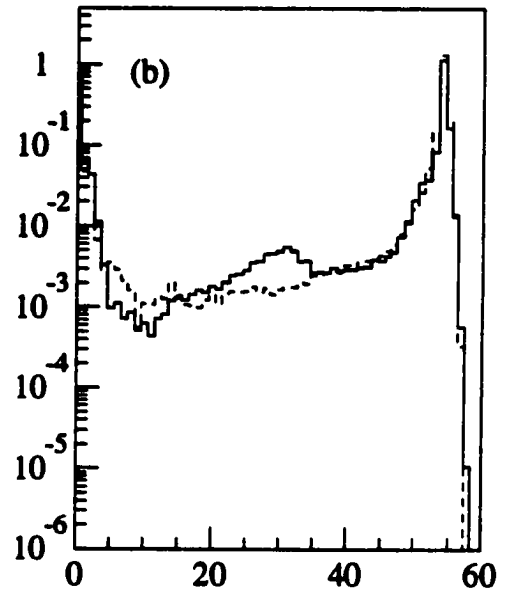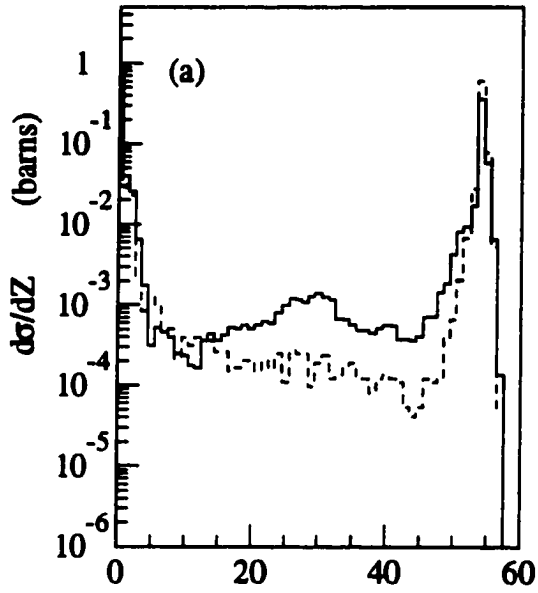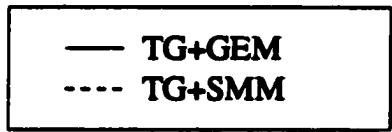
Figure IV.18 The calculated secondary energy distributions for the TG+GEM and TG+SMM models for Xe + Cu at (a) E/A = 30 MeV, (b) E/A = 40 MeV (c) E/A = 50 MeV, and (d) E/A = 60 MeV. The solid and dashed lines represent the TG+GEM and TG+SMM results, respectively

147

148
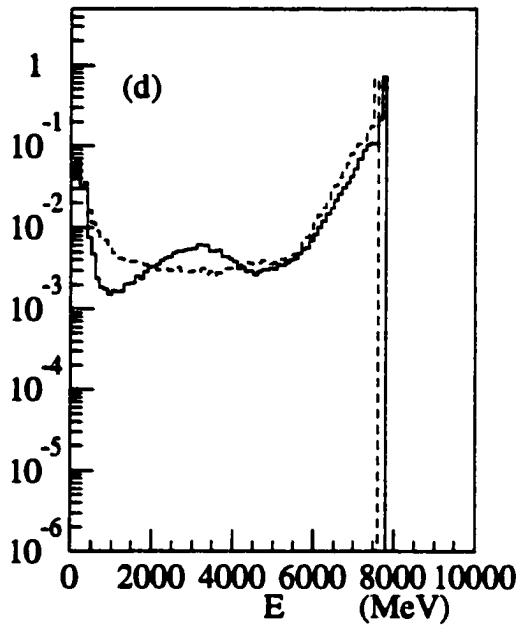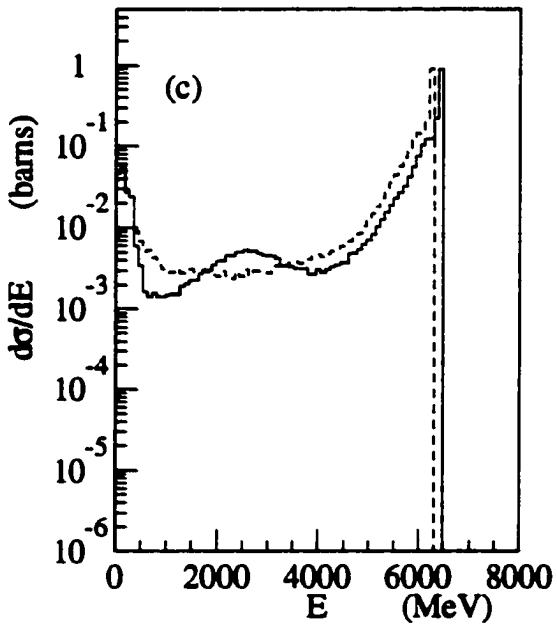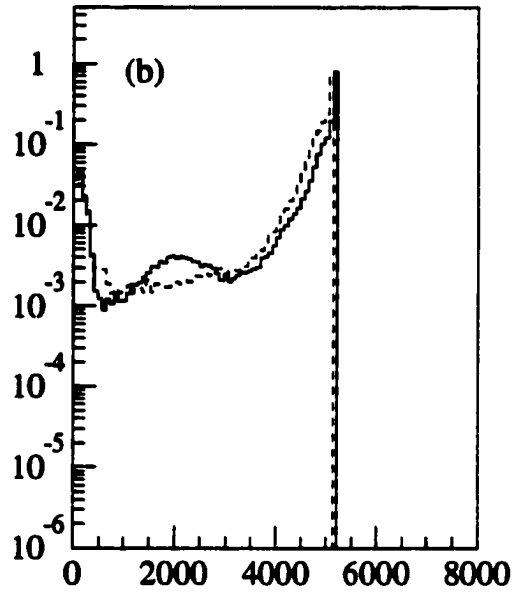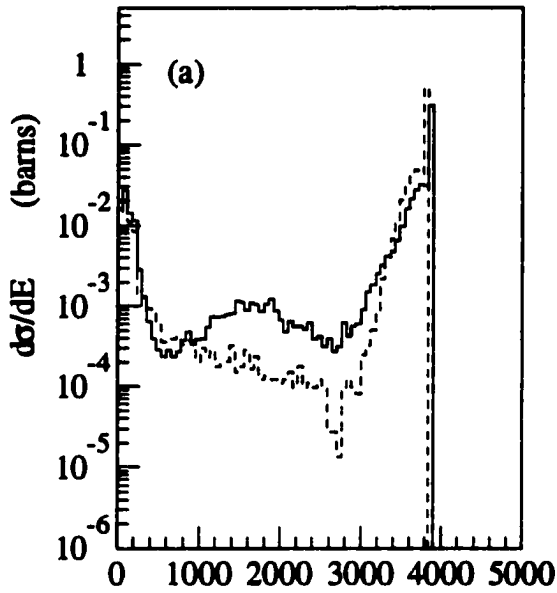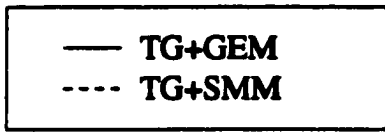
Figure IV.19 The calculated secondary velocity distributions for the TG+GEM and TG+SMM models for Xe + Cu at (a) E/A = 30 MeV, (b) E/A = 40 MeV (c) E/A = 50 MeV, and (d) E/A = 60 MeV. The solid and dashed lines represent the TG+GEM and TG+SMM results, respectively.

150
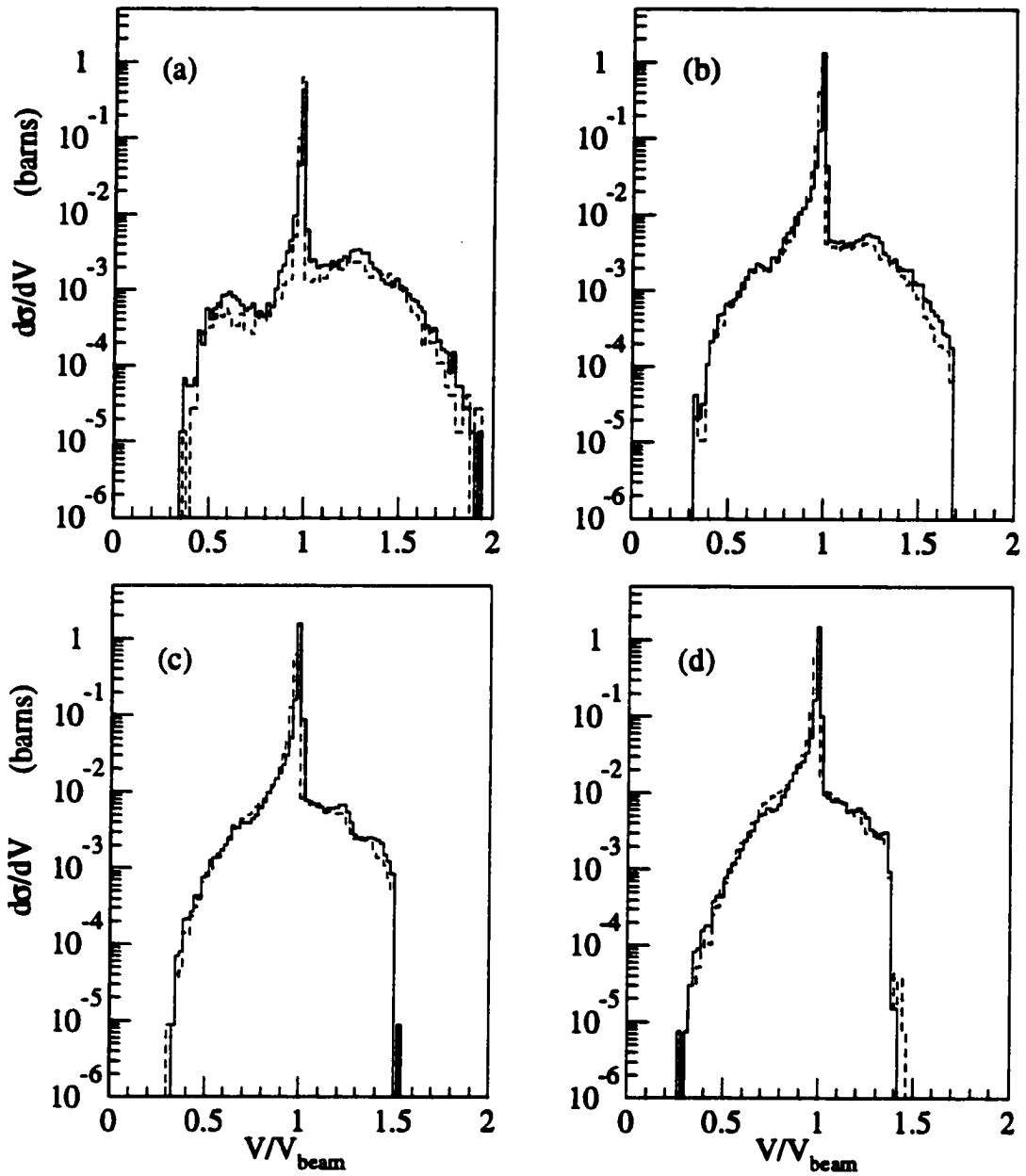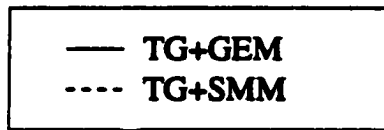
Figure IV.20 The calculated secondary charge distributions for the BUU+GEM and BUU+SMM models for Xe + Cu at (a) E/A = 30 MeV, (b) E/A = 40 MeV (c) E/A = 50 MeV, and (d) E/A = 60 MeV. The solid and dashed lines represent the BUU+GEM and BUU+SMM results, respectively.

151

152
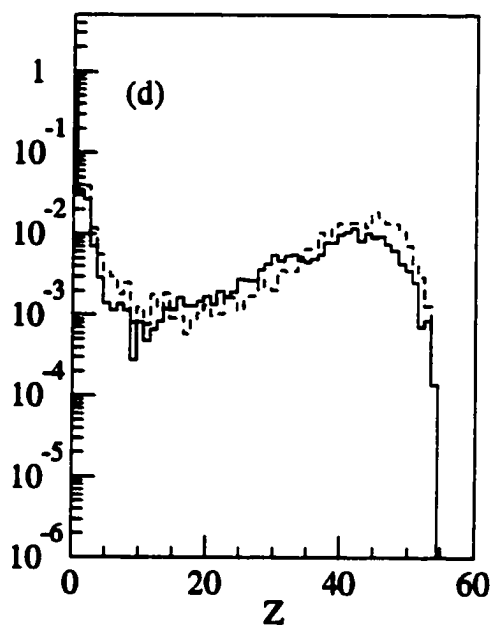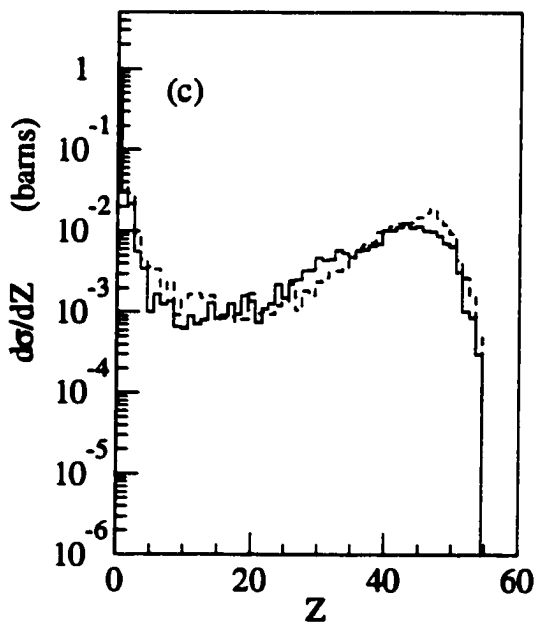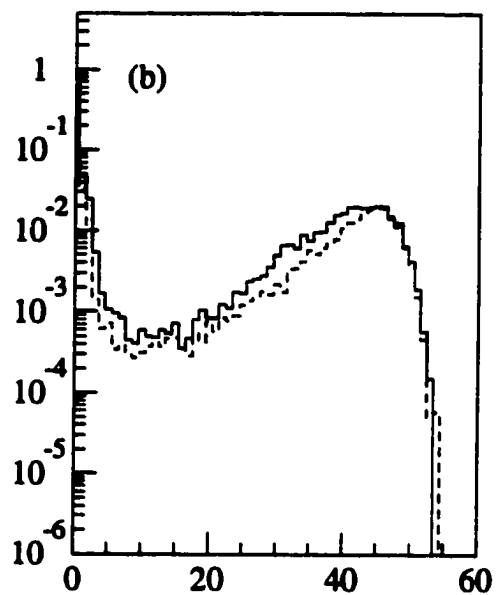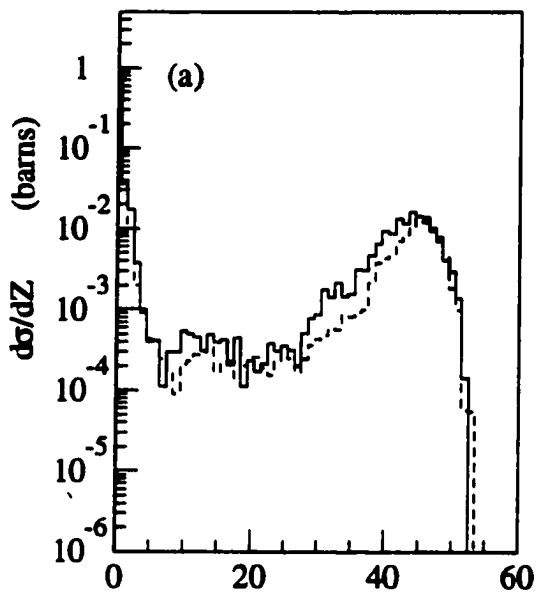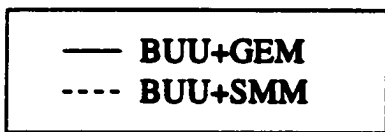
at E/A = 30, 40, 50, and 60 MeV and in Fig IV.21 (a)-(d) for Xe + Sc system. Notice that there are few products with Z near the beam. As shown in Figs. IV.4 - IV.7, the BUU model fails to produce many primary fragments in this region. Also, there is no peak associated with symmetric fission in the BUU+GEM calculation. The situation is the same for the calculated energy distributions for the Xe + Cu system at E/A = 30, 40, 50, and 60 MeV, shown in Fig IV. 22 (a)-(d), and for the Xe + Sc system at E/A = 30, 40, 50, and 60 MeV, shown in Fig. IV.23 (a)-(d).

A comparison between the charge distributions of Xe + Sc and Cu at E/A = 30, 40, 50 and 60 MeV calculated using BUU+GEM is shown in Fig. IV.24 (a)-(d). The solid line is the Xe + Cu system and the dashed line is the Xe + Sc system. There is about a factor of 10 difference in the cross section for these two systems at E/A = 30 and 40 MeV. As the energy increases, this discrepancy becomes smaller. As seen in the BUU primary distributions, the Xe + Sc system does not produced as many forward moving PLF's as in the Xe + Cu system. A comparison between the energy distributions of Xe + Sc and Cu at E/A = 30, 40, 50 and 60 MeV calculated using BUU+GEM, Fig. IV.25 (a)-(d), shows the same effect.

The velocity distributions calculated with BUU+GEM and BUU+SMM for the Xe + Cu system at E/A = 30, 40, 50, and 60 MeV are shown in Fig. IV-26 (a)-(d). For all the distributions, the two afterburners look similar.

153

Figure IV.21 The calculated secondary charge distributions for the BUU+GEM and

BUU+SMM models for Xe + Sc at (a) E/A = 30 MeV, (b) E/A = 40 MeV (c) E/A =

50 MeV, and (d) E/A = 60 MeV. The solid and dashed lines represent the

BUU+GEM and BUU+SMM results, respectively.

154

155
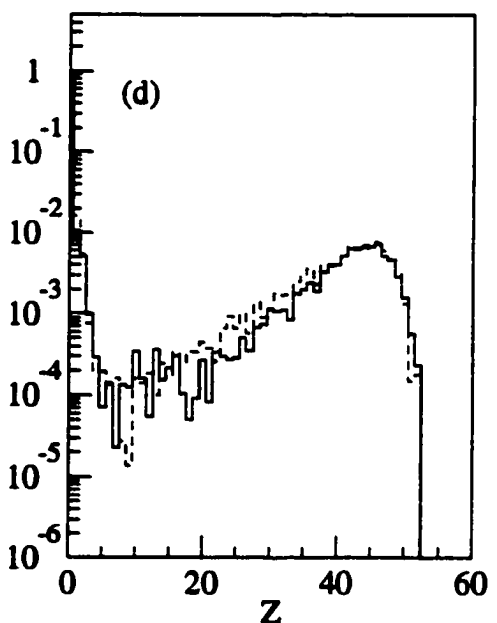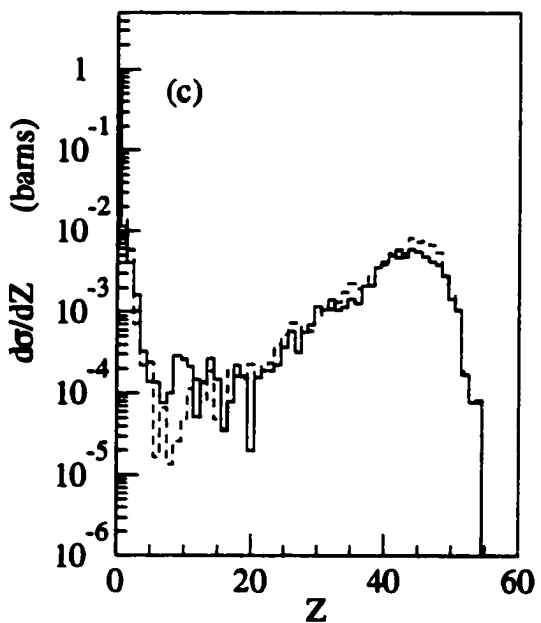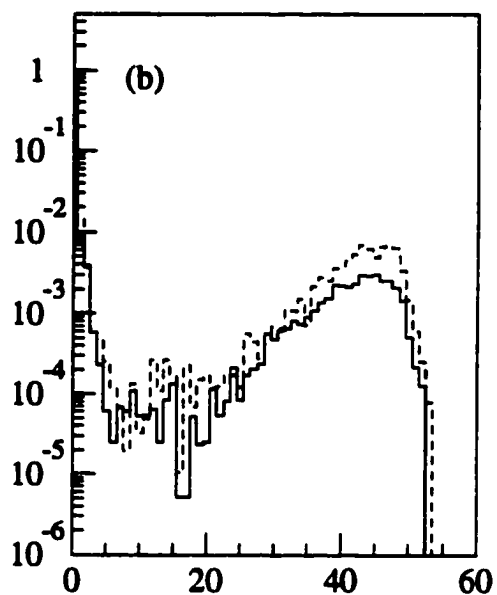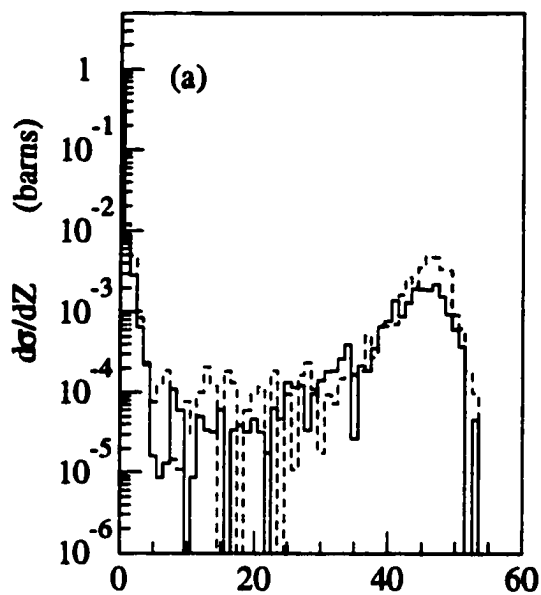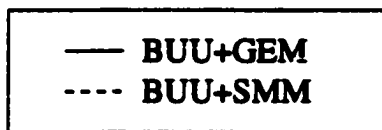
Figure IV.22 The calculated secondary energy distributions for the BUU+GEM and

BUU+SMM models for Xe + Cu at (a) E/A = 30 MeV, (b) E/A = 40 MeV (c) E/A =

50 MeV, and (d) E/A = 60 MeV. The solid and dashed lines represent the

BUU+GEM and BUU+SMM results, respectively.

156

Legend:
- BUU+GEM (solid line)
- BUU+SMM (dashed line)

(a) (b) (c) (d)

y-axis: $d\sigma/dE$ (barns)

x-axis: E (MeV)

157
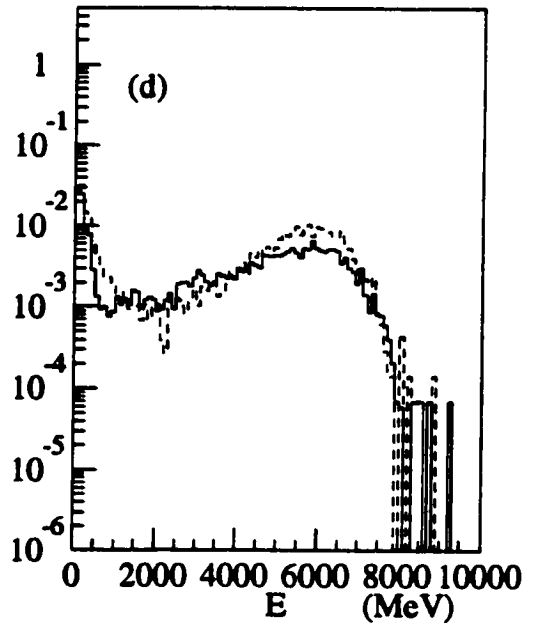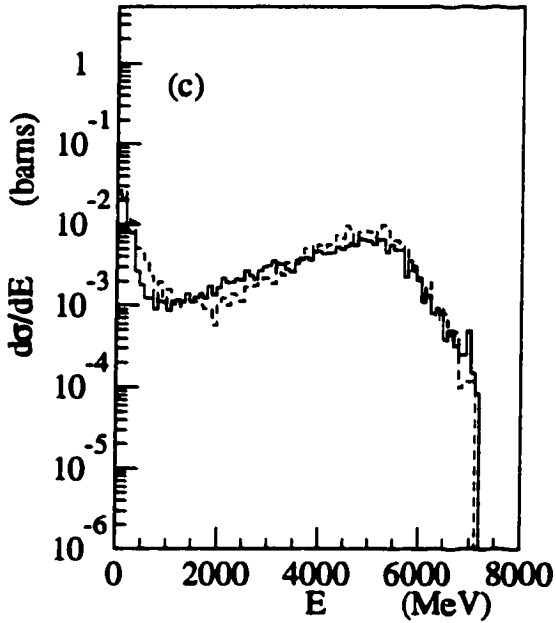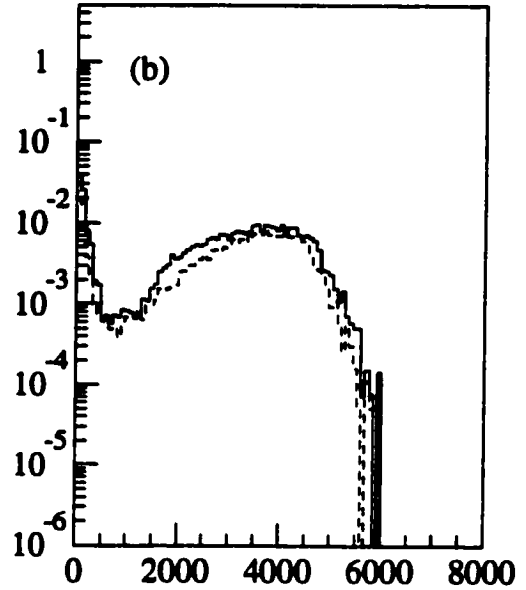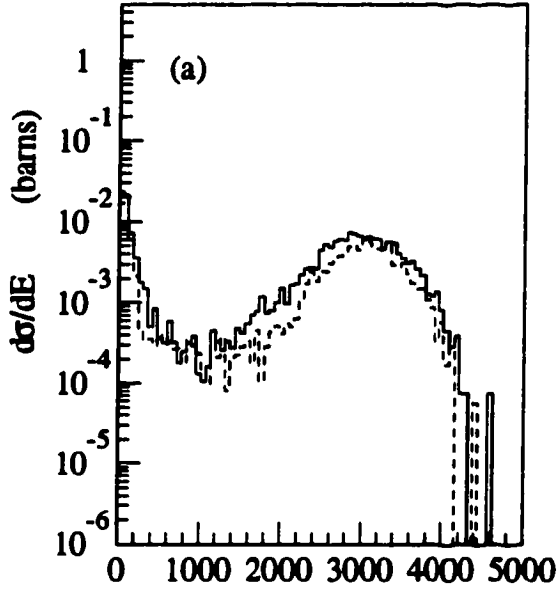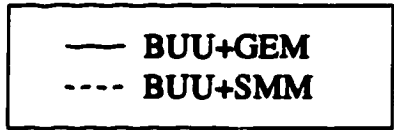
Figure IV.23 The calculated secondary energy distributions for the BUU+GEM and

BUU+SMM models for Xe + Sc at (a) E/A = 30 MeV, (b) E/A = 40 MeV (c) E/A =

50 MeV, and (d) E/A = 60 MeV. The solid and dashed lines represent the

BUU+GEM and BUU+SMM results, respectively.

158

159
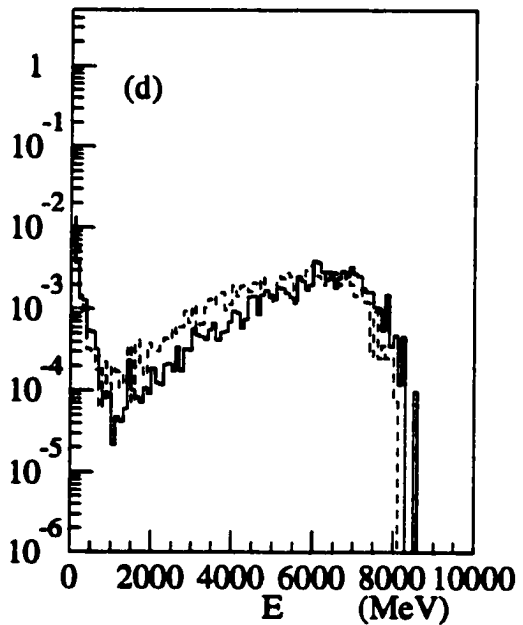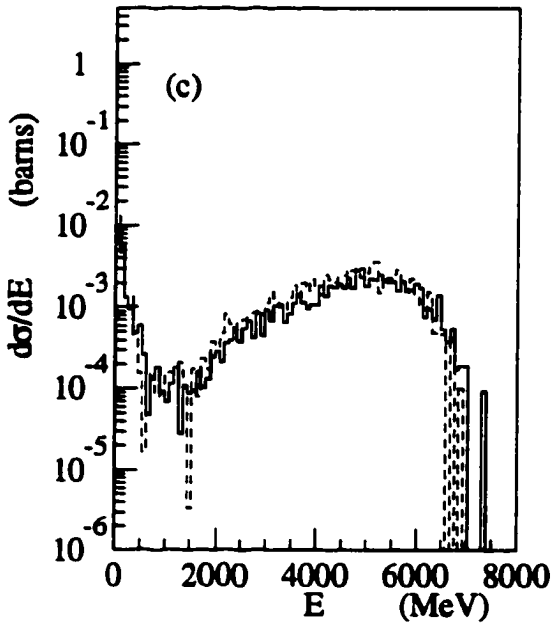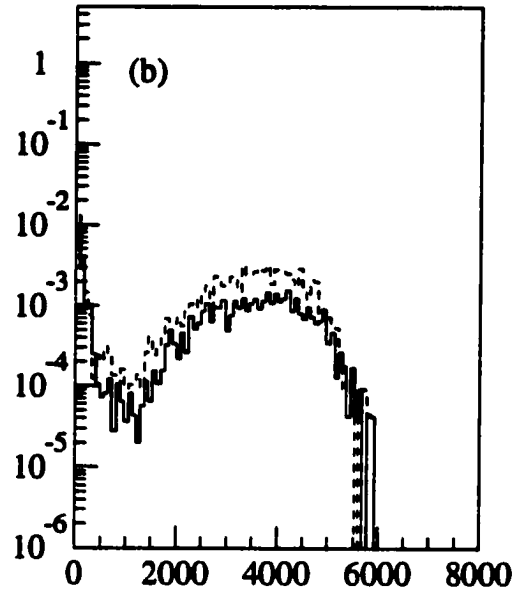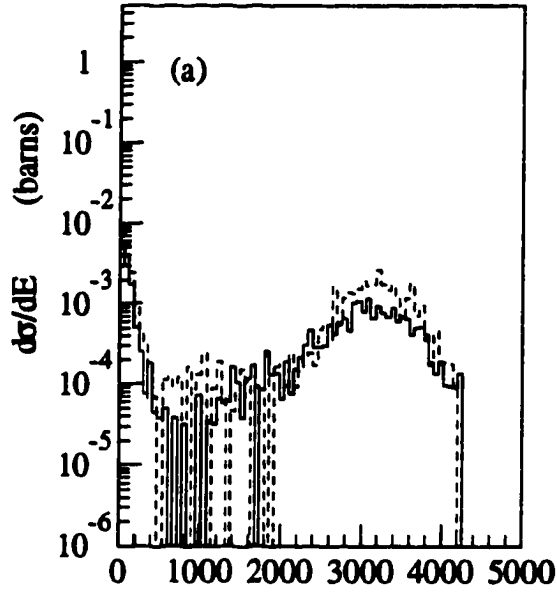
Figure IV.24 A comparison between the BUU+GEM charge distributions for the Xe + Cu and Sc systems at (a) E/A = 30 MeV, (b) E/A = 40 MeV (c) E/A = 50 MeV, and (d) E/A = 60 MeV. The solid and dashed lines represent the Xe + Cu and Xe + Sc systems, respectively.

160

Figure legend:
— BUU+GEM (Xe+Cu)
---- BUU+GEM (Xe+Sc)

Plots (a), (b), (c), (d): $d\sigma/dZ$ (barns) versus Z
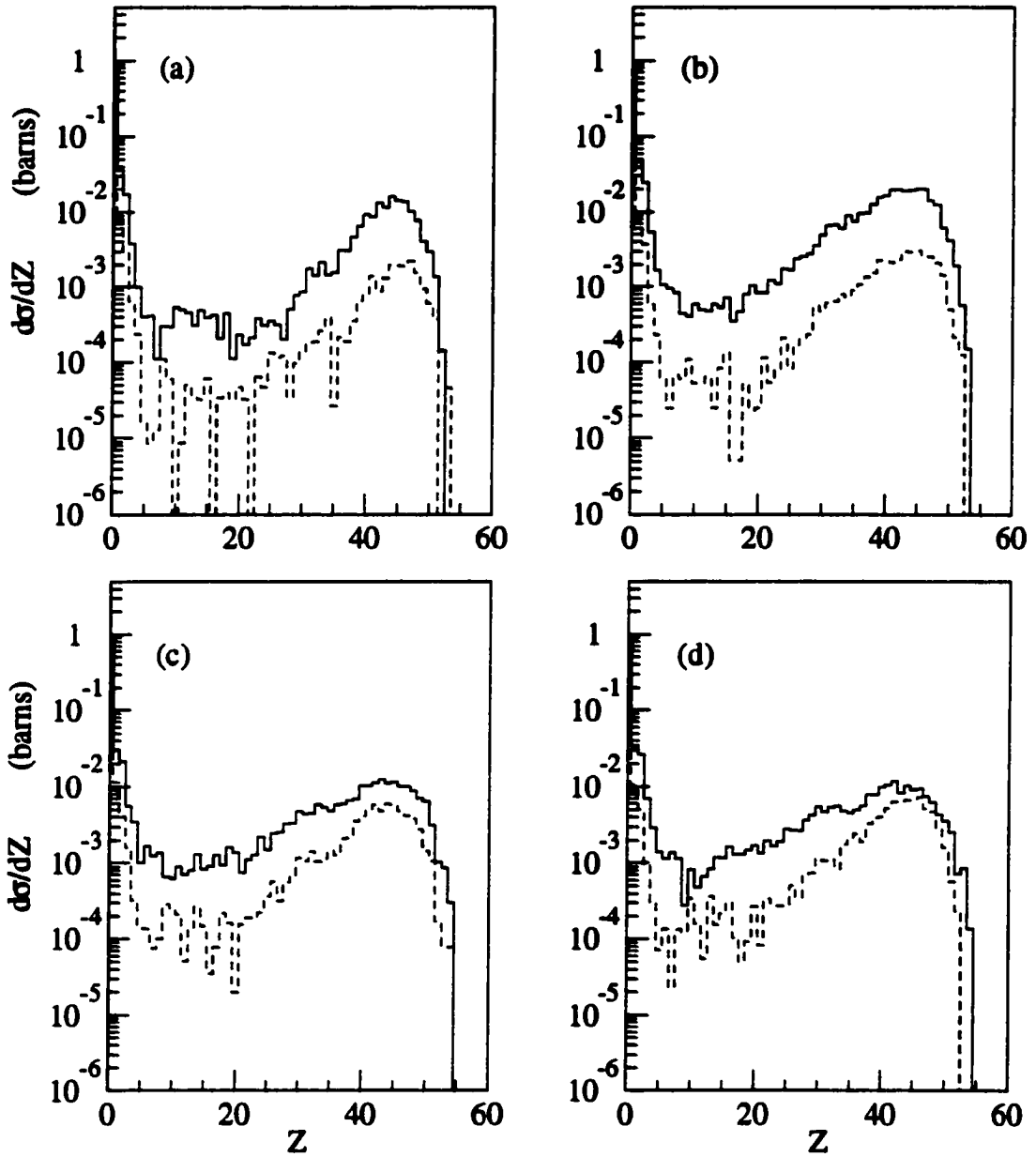
Figure IV.25 A comparison between the BUU+GEM energy distributions for the Xe + Cu and Sc systems at (a) E/A = 30 MeV, (b) E/A = 40 MeV (c) E/A = 50 MeV, and (d) E/A = 60 MeV. The solid and dashed lines represent the Xe + Cu and Xe + Sc systems, respectively.

162

163
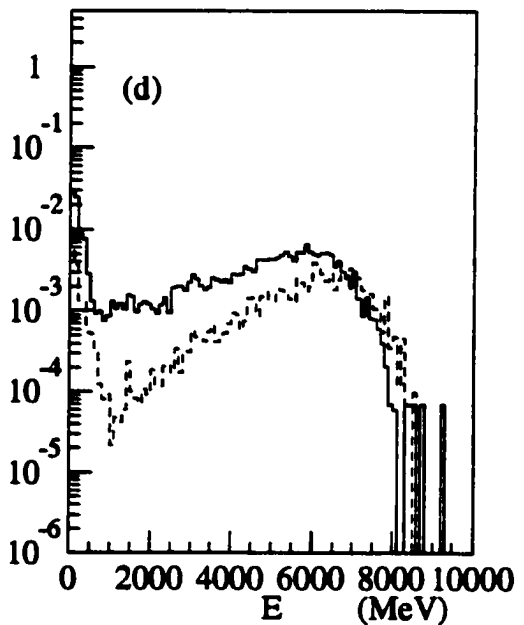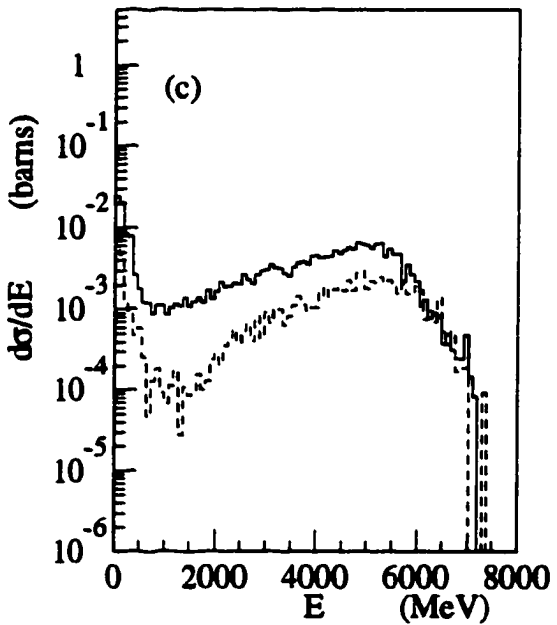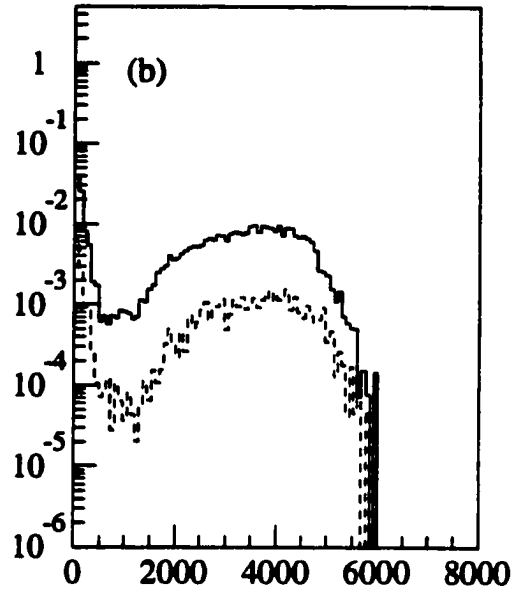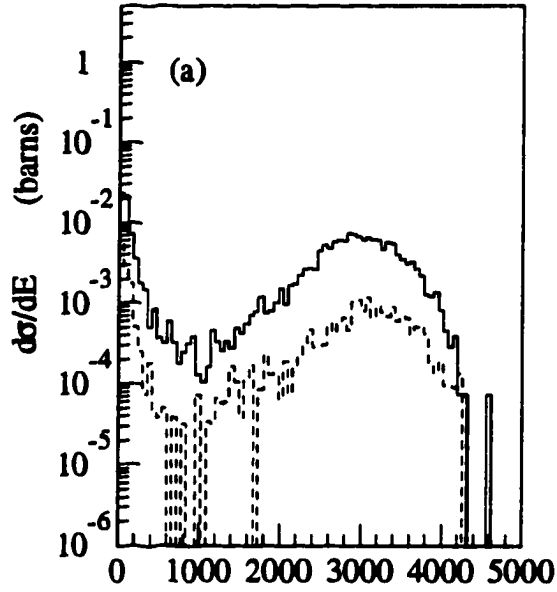
Figure IV.26 The calculated secondary velocity distributions for the BUU+GEM and BUU+SMM models for Xe + Cu at (a) E/A = 30 MeV, (b) E/A = 40 MeV (c) E/A = 50 MeV, and (d) E/A = 60 MeV. The solid and dashed lines represent the BUU+GEM and BUU+SMM results, respectively.

164

Legend:
— BUU+GEM
---- BUU+SMM

165

Chapter V Discussion

As mentioned in Chap. I, the goal of the research project is to see to what extent the deep-inelastic mechanism is responsible for the production of PLF's in Xe + Cu and Sc reactions at E/A = 30, 40, 50 and 60 MeV. In order to do this, data are compared to model predictions. In this study, the charge, mean charge, charge width, energy, velocity and mean velocity distributions are compared with model predictions.

V.A Inclusive Distributions

V.A.1 Inclusive Charge Distributions

A comparison of the inclusive charge distributions for the Xe + Cu system at E/A = 30, 40, 50, and 60 MeV with the TG+GEM and BUU+GEM calculated distributions is shown in Fig. V.1(a)-(d). A comparison of the data with the TG+SMM and BUU+SMM is shown in Fig. V.2(a)-(d). The dots represent the data, and the solid and dashed lines represent the TG and BUU model distributions with the appropriate afterburners, respectively. At E/A = 30 MeV, the TG+GEM predicts a narrower quasi-elastic peak than seen in the data and has a pronounced fission peak at around Z = 30, not seen in the data. The data have a smooth decrease in the cross section with Z. With the SMM afterburner, the quasi-elastic peak is even narrower than with the GEM afterburner. The BUU+GEM and BUU+SMM do not have quasi-elastic peaks because the primary BUU mechanism does not produce many PLF's.

At E/A = 40 MeV, the TG+GEM and TG+SMM overpredict the cross section, and predict a narrower quasi-elastic peak than seen in the data. The BUU fails to produce a quasi-elastic peak. At E/A = 50 MeV, the TG model fits the data remarkably well from the quasi-elastic region to around Z = 35. Again, BUU fails to

166

Chapter V Discussion

As mentioned in Chap. I, the goal of the research project is to see to what extent the deep-inelastic mechanism is responsible for the production of PLF's in Xe + Cu and Sc reactions at E/A = 30, 40, 50 and 60 MeV. In order to do this, data are compared to model predictions. In this study, the charge, mean charge, charge width, energy, velocity and mean velocity distributions are compared with model predictions.

V.A Inclusive Distributions

V.A.1 Inclusive Charge Distributions

A comparison of the inclusive charge distributions for the Xe + Cu system at E/A = 30, 40, 50, and 60 MeV with the TG+GEM and BUU+GEM calculated distributions is shown in Fig. V.1(a)-(d). A comparison of the data with the TG+SMM and BUU+SMM is shown in Fig. V.2(a)-(d). The dots represent the data, and the solid and dashed lines represent the TG and BUU model distributions with the appropriate afterburners, respectively. At E/A = 30 MeV, the TG+GEM predicts a narrower quasi-elastic peak than seen in the data and has a pronounced fission peak at around Z = 30, not seen in the data. The data have a smooth decrease in the cross section with Z. With the SMM afterburner, the quasi-elastic peak is even narrower than with the GEM afterburner. The BUU+GEM and BUU+SMM do not have quasi-elastic peaks because the primary BUU mechanism does not produce many PLF's.

At E/A = 40 MeV, the TG+GEM and TG+SMM overpredict the cross section, and predict a narrower quasi-elastic peak than seen in the data. The BUU fails to produce a quasi-elastic peak. At E/A = 50 MeV, the TG model fits the data remarkably well from the quasi-elastic region to around Z = 35. Again, BUU fails to

166

Figure V.1 A comparison of the inclusive charge distributions for the data (dots) and

TG+GEM (solid lines) and BUU+GEM (dashed lines) model calculations for the Xe

+ Cu system at (a) E/A = 30 MeV, (b) E/A = 40 MeV (c) E/A = 50 MeV, and (d) E/A

= 60 MeV.

167

168
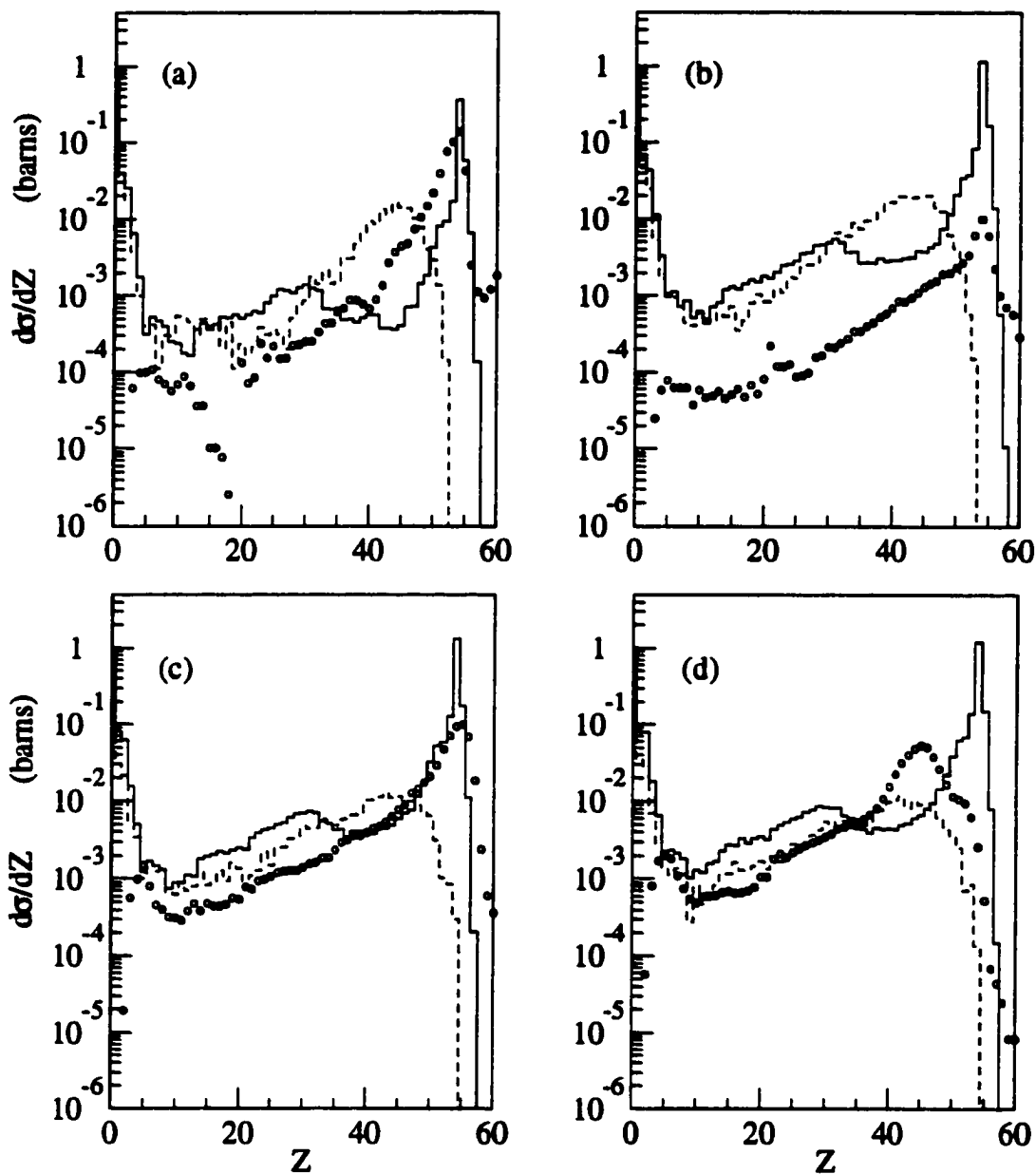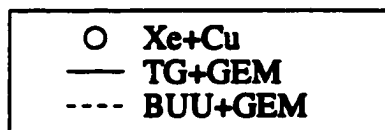
Figure V.2 A comparison of the inclusive charge distributions for the data (dots) and

TG+SMM (solid lines) and BUU+SMM (dashed lines) model calculations for the Xe

+ Cu system at (a) E/A = 30 MeV, (b) E/A = 40 MeV (c) E/A = 50 MeV, and (d) E/A

= 60 MeV.

169

170
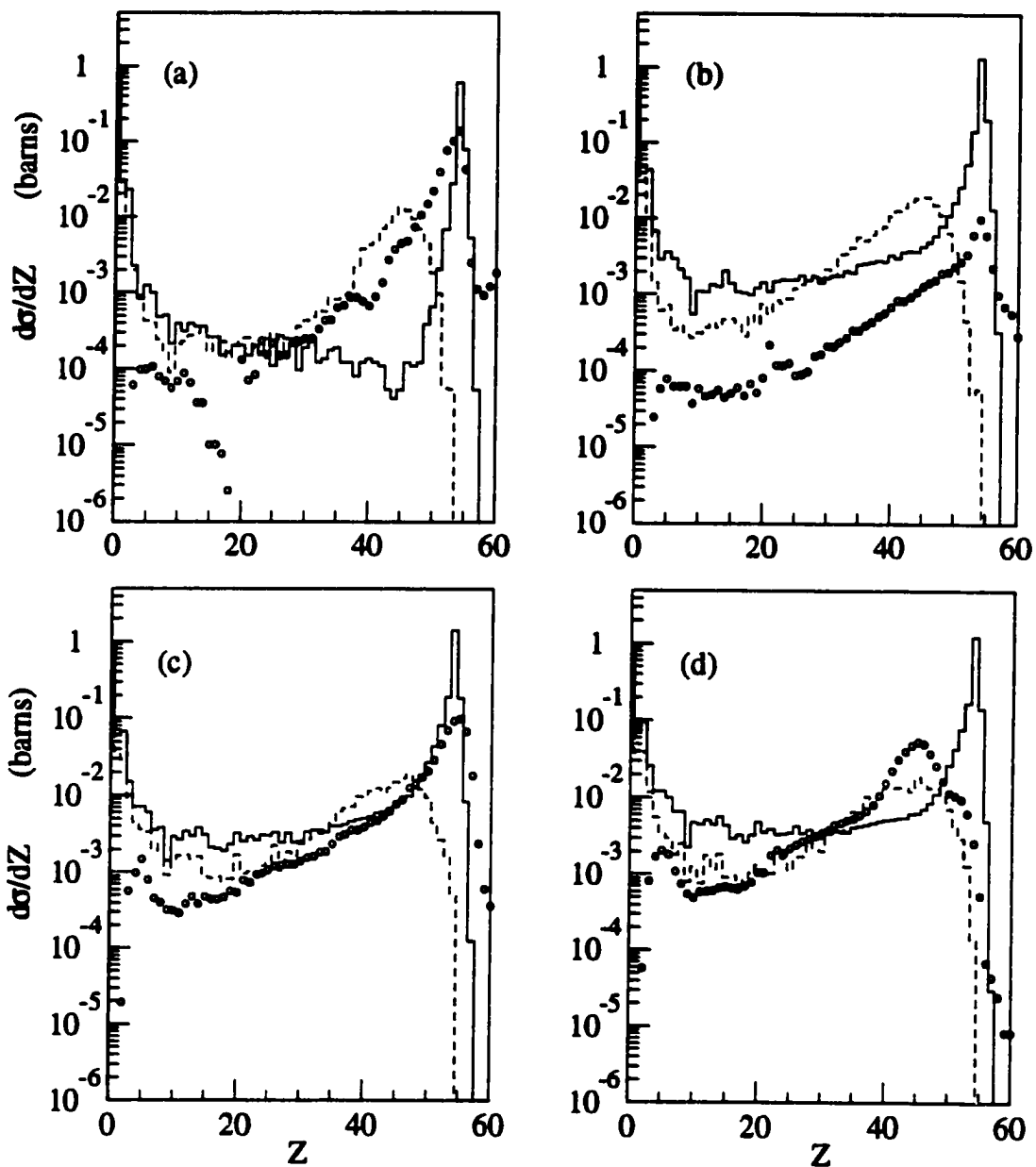
produce a quasi-elastic peak; however, with either afterburner it does a good job at predicting fragments in the region from Z = 10 to Z = 45. At E/A = 60 MeV, the experimental elastic peak falls inside the inner radius of the detector, but calculated quasi-elastic events which should be removed by the filter are not, because the TG model fails to properly calculate the scattering angle, as seen the model deflection functions shown in Figs. IV.8 - IV.11. The BUU model reproduces the charge distribution from around Z = 10 to around Z = 40, but still underpredicts the higher Z component.

The inclusive charge distributions for Xe + Sc at E/A = 30, 40, 50, and 60 MeV, along with the TG+GEM and BUU+GEM calculated distributions, are shown in Fig. V.3(a)-(d). A comparison of the data with the TG+SMM and BUU+SMM is shown in Fig. V.4(a)-(d). The dots represent the data, and the solid and dashed lines represent the TG and BUU model distributions with the appropriate afterburners, respectively. There are several notable differences between the Xe + Cu and Xe + Sc systems. The BUU model with either afterburner does a good job of predicting the cross section in the E/A = 30 and 40 MeV Xe + Sc; however, in the Xe + Cu system it overpredicts the cross section. In the E/A = 50 and 60 MeV Xe + Sc system, BUU underpredicts the cross section in the Xe + Sc, but in the Xe + Cu system it does fine.

V.A.2 Inclusive Energy Distributions

The energy distributions for the Xe + Cu system at E/A = 30, 40, 50, and 60 MeV are shown in Fig. V.5(a)-(d), along with the TG+GEM and BUU+GEM model calculations, and in Fig. V.6(a)-(d), along with the TG+SMM and BUU+SMM model calculations. The dots are the data and the solid and dashed lines are the TG and BUU models, respectively.

In the E/A = 30 MeV Xe + Cu system, the TG+GEM model reproduces the data from the quasi-elastic region down to around where the fission peak starts at

171

Figure V.3 A comparison of the inclusive charge distributions for the data (dots) and TG+GEM (solid lines) and BUU+GEM (dashed lines) model calculations for the Xe + Sc system at (a) E/A = 30 MeV, (b) E/A = 40 MeV (c) E/A = 50 MeV, and (d) E/A = 60 MeV.

173
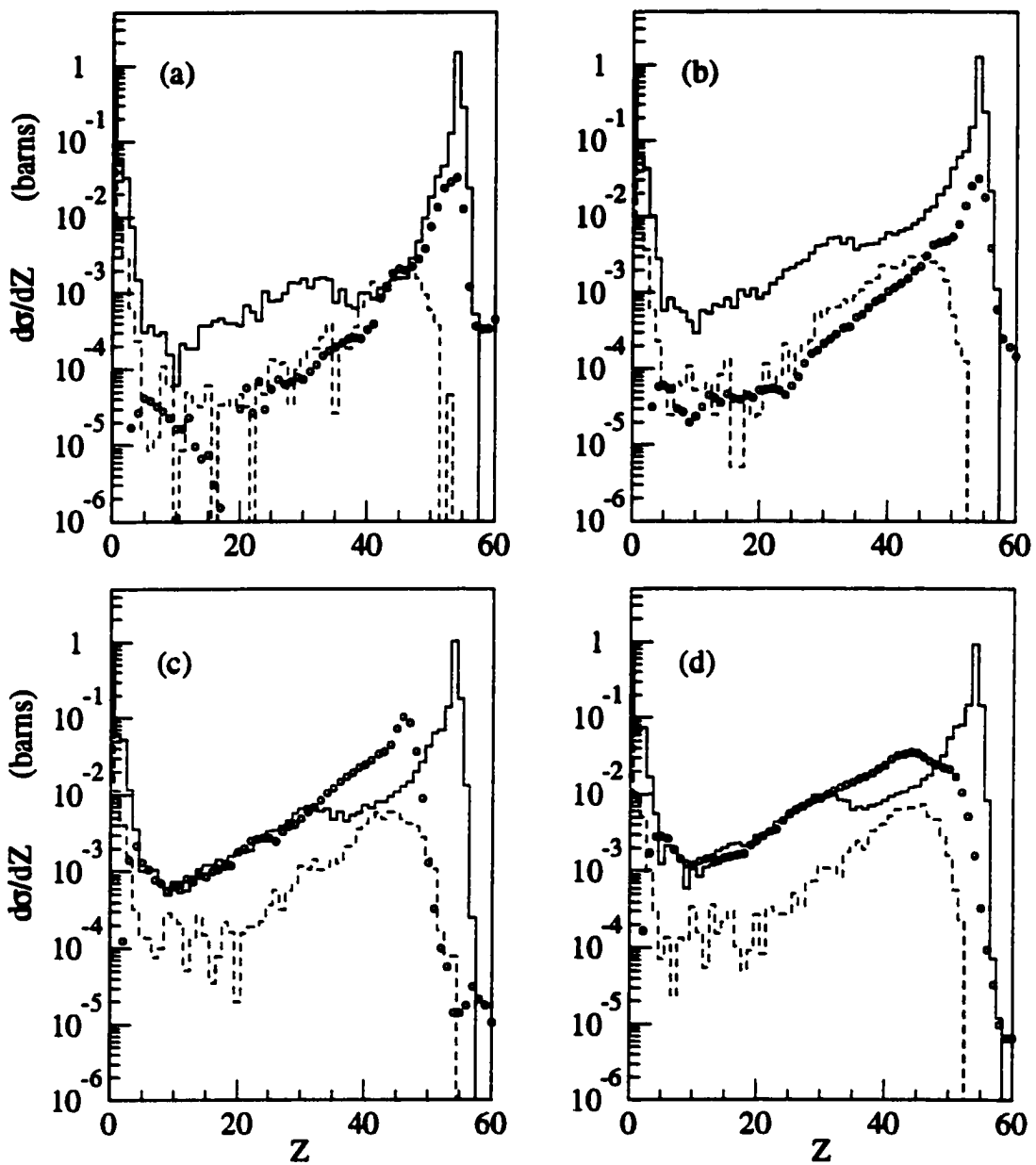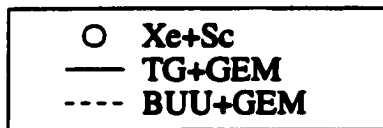
Figure V.4 A comparison of the inclusive charge distributions for the data (dots) and

TG+SMM (solid lines) and BUU+SMM (dashed lines) model calculations for the Xe

+ Sc system at (a) E/A = 30 MeV, (b) E/A = 40 MeV (c) E/A = 50 MeV, and (d) E/A

= 60 MeV.

174

175
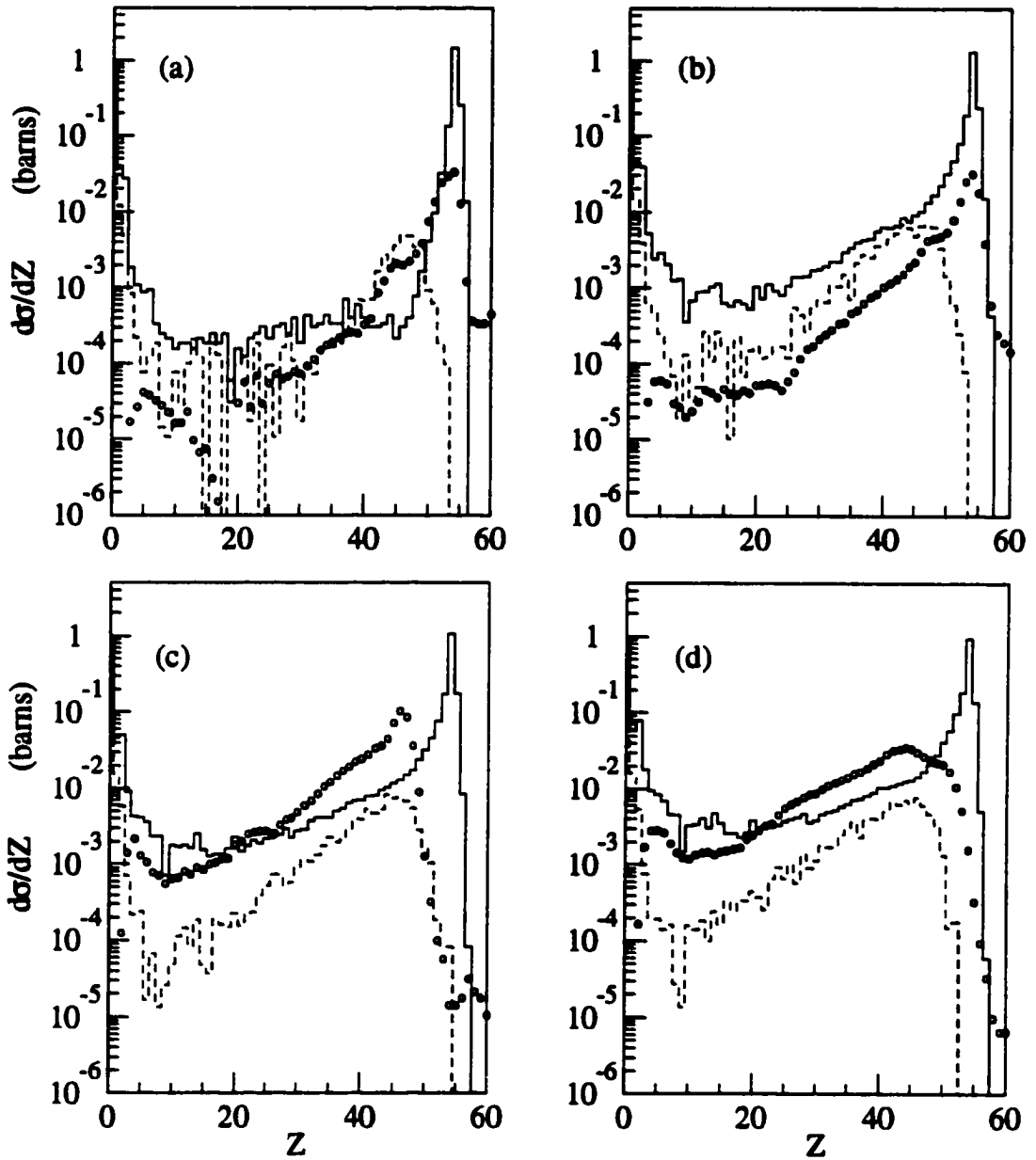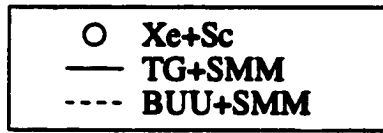
Figure V.5 A comparison of the inclusive energy distributions for the data (dots) and TG+GEM (solid lines) and BUU+GEM (dashed lines) model calculations for the Xe + Cu system at (a) E/A = 30 MeV, (b) E/A = 40 MeV (c) E/A = 50 MeV, and (d) E/A = 60 MeV.

176

177
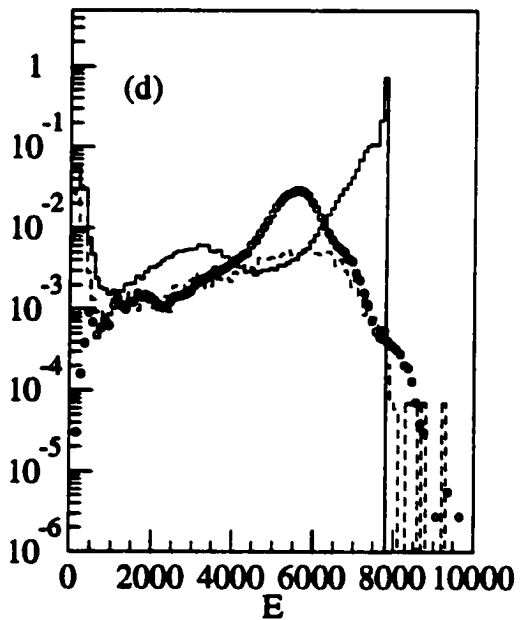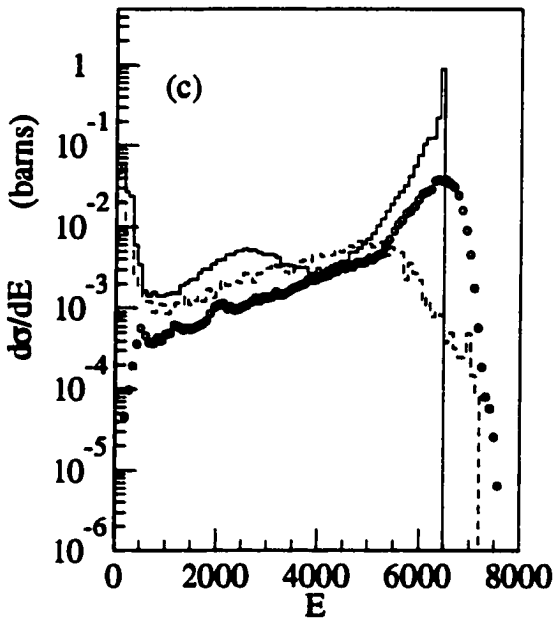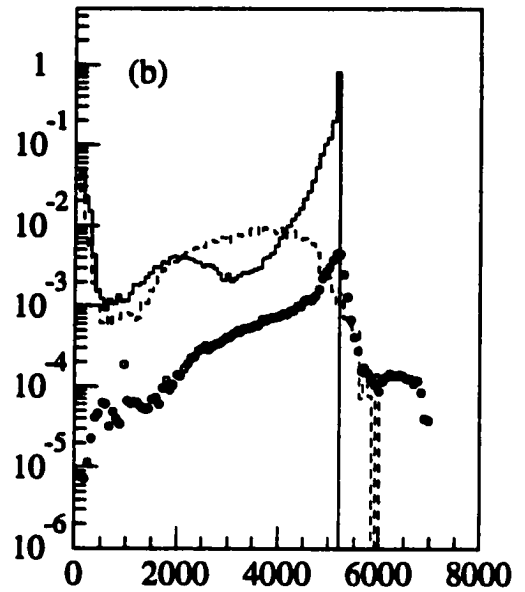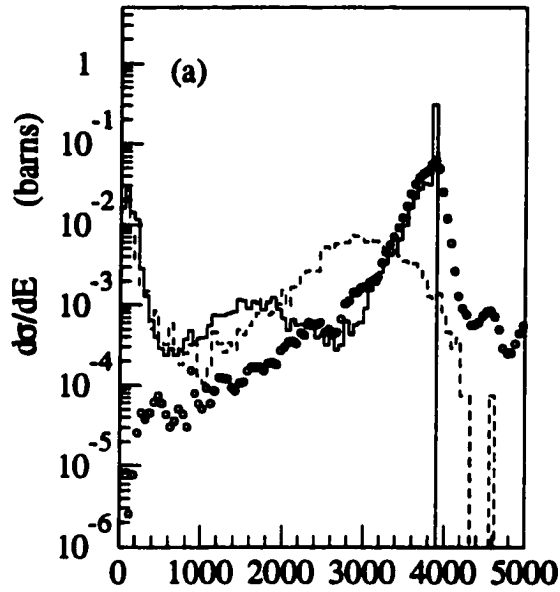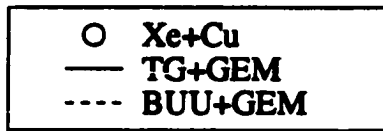
Figure V.6 A comparison of the inclusive energy distributions for the data (dots) and

TG+SMM (solid lines) and BUU+SMM (dashed lines) model calculations for the Xe

+ Cu system at (a) E/A = 30 MeV, (b) E/A = 40 MeV (c) E/A = 50 MeV, and (d) E/A

= 60 MeV.

179
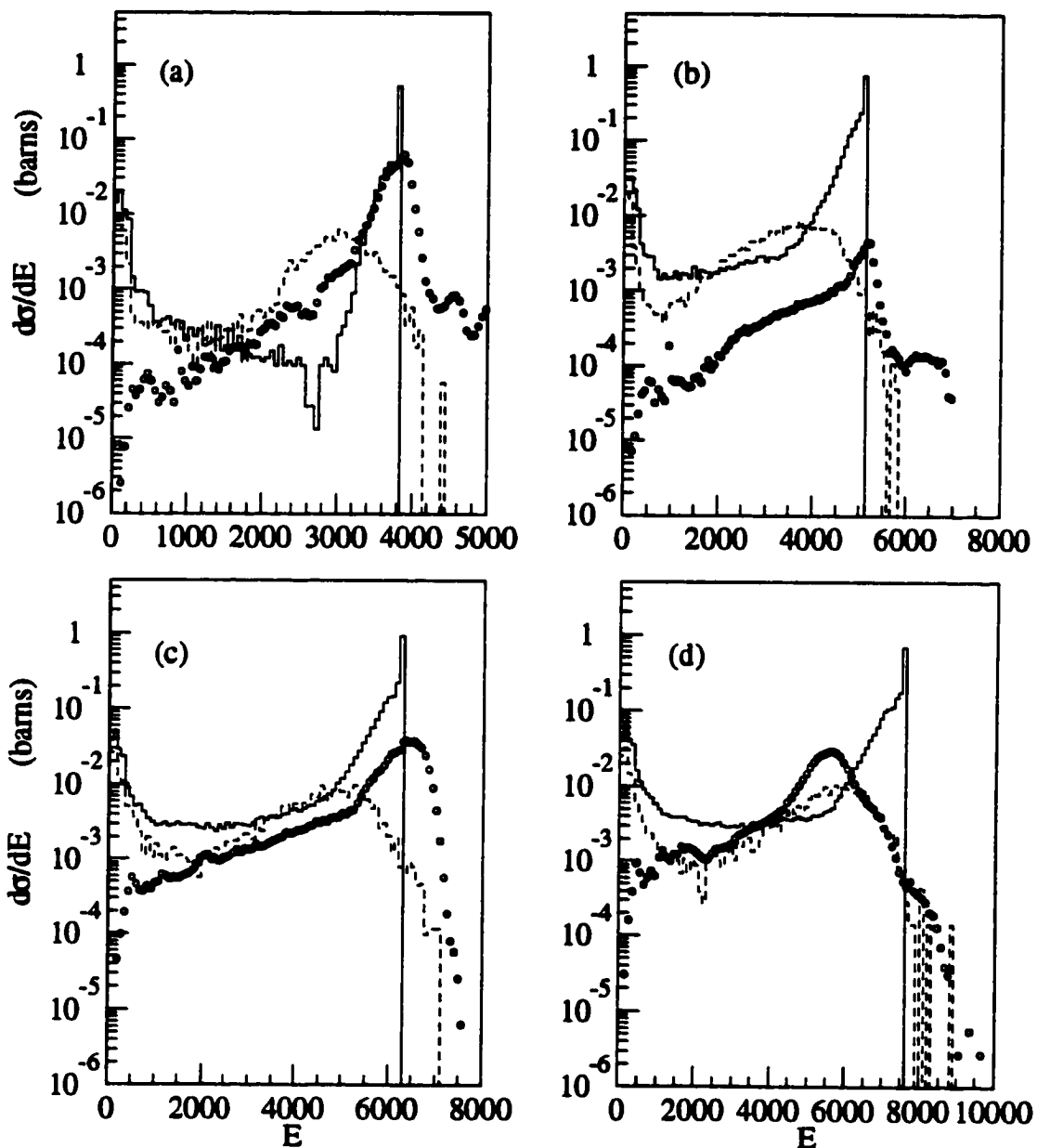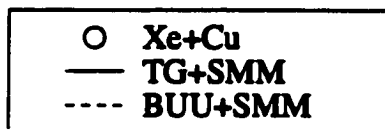
~2500 MeV. The TG+SMM reproduces the data down to about 3500 MeV, but underpredicts the intermediate energy fragments. At 40 MeV, the TG model overpredicts the cross section over all fragment kinetic energies.

The BUU overpredicts the cross section everywhere at $E/A = 30$ and 40 MeV. At $E/A = 40$ MeV, the BUU model with either afterburner reproduces the trends of the data for the region 2000 MeV $< E <$ 4000 MeV, but not the much lower magnitude. At $E/A = 50$ MeV, the energy distribution is well reproduced by the TG+SMM model for $E > 2500$ MeV. The BUU+SMM calculation also reproduces the energy distribution, except for the quasi-elastic region. At $E/A = 60$ MeV, the failure of the TG model to properly calculate the scattering angle allows elastic events to pass through the MFA filter even through they should be filtered out. The BUU model results reproduce the data for 500 MeV $< E <$ 5000 MeV.

For the Xe + Sc system, the energy distributions at $E/A = 30, 40, 50$, and 60 MeV are shown in Fig. V.7(a)-(d), along with the TG+GEM and BUU+GEM model calculations, and in Fig. V.8(a)-(d), along with the TG+SMM and BUU+SMM model calculations. The dots are the data and the solid and dashed lines are the TG and BUU models, respectively. At 30 MeV, neither the TG+GEM or TG+SMM fit the quasi-elastic peak. The BUU model does a good job fitting the distribution, except for the quasi-elastic region. At $E/A = 40$ MeV, the shape of the overall distribution is reproduced by the TG+SMM down to about 1000 MeV, however the overall cross section is about 10 times too high. The BUU model reproduces the data from around 500 MeV to 4000 MeV. At $E/A = 50$ MeV and 60 MeV, the BUU is much too low throughout the energy range. Quasi-elastic scattering is not seen in the data, but due to incorrect angular behavior it is predicted by the TG calculations.

180

Figure V.7 A comparison of the inclusive energy distributions for the data (dots) and

TG+GEM (solid lines) and BUU+GEM (dashed lines) model calculations for the Xe

+ Sc system at (a) E/A = 30 MeV, (b) E/A = 40 MeV (c) E/A = 50 MeV, and (d) E/A

= 60 MeV.

Legend:
- O Xe+Sc
- TG+GEM
- BUU+GEM

(a), (b), (c), (d)

Axis labels: dσ/dE (barns), E

182
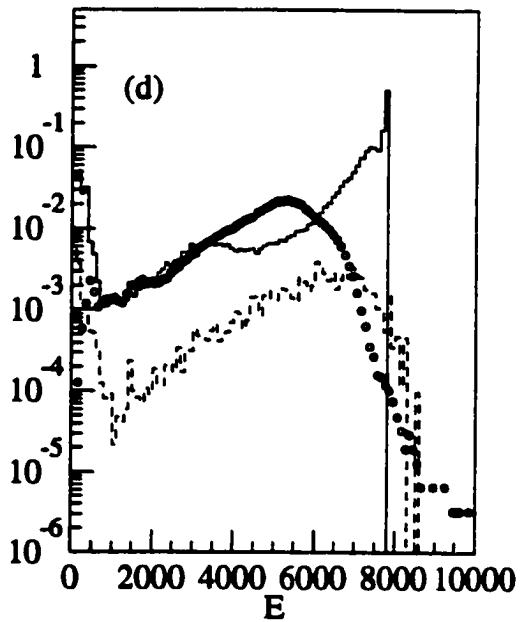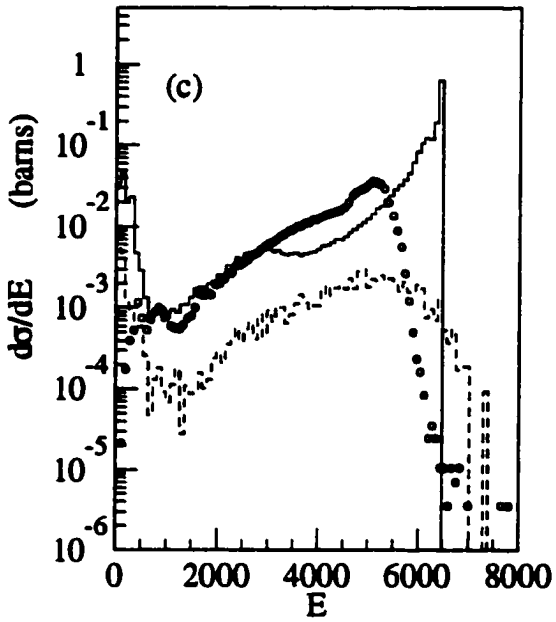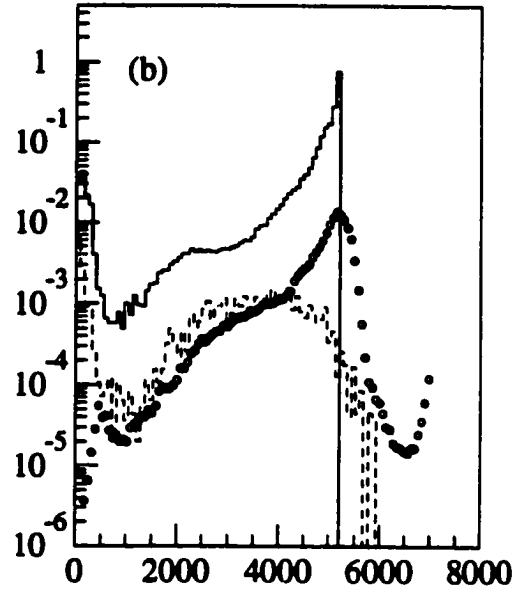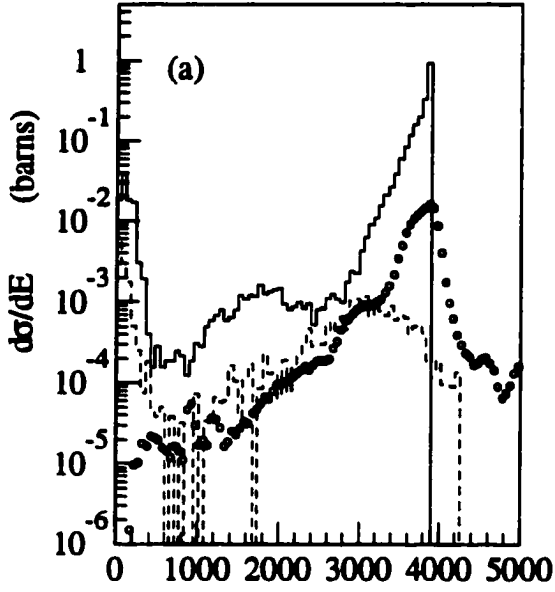
Figure V.8 A comparison of the inclusive energy distributions for the data (dots) and TG+SMM (solid lines) and BUU+SMM (dashed lines) model calculations for the Xe + Sc system at (a) E/A = 30 MeV, (b) E/A = 40 MeV (c) E/A = 50 MeV, and (d) E/A = 60 MeV.

Legend:
- O Xe+Sc
- —— TG+SMM
- ---- BUU+SMM

(a) (b) (c) (d)

Vertical axis: $d\sigma/dE$ (barns)

Horizontal axis: E

184
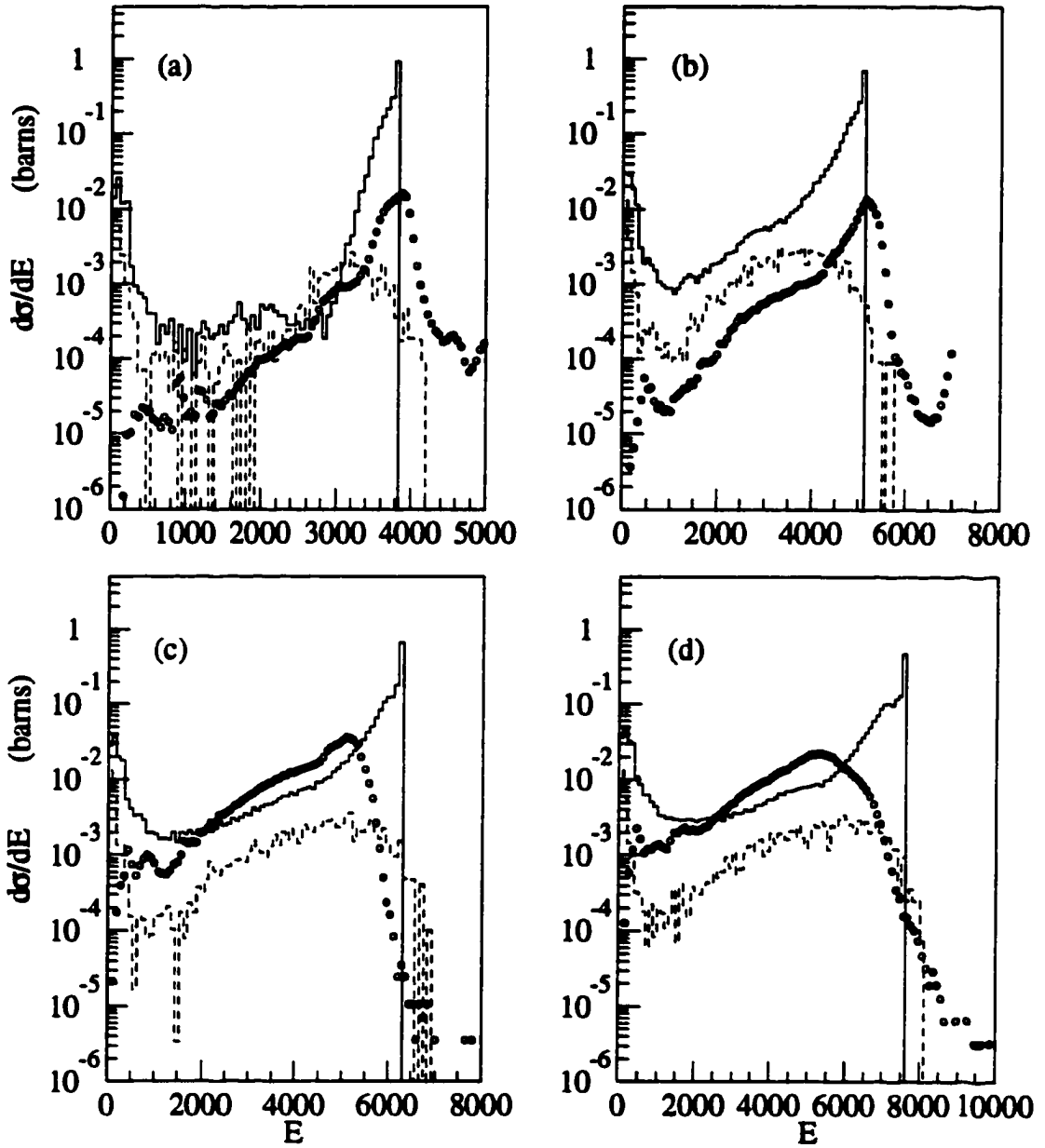
Figure V.9 A comparison of the inclusive velocity distributions for the data (dots) and

TG+GEM (solid lines) and BUU+GEM (dashed lines) model calculations for the Xe

+ Cu system at (a) E/A = 30 MeV, (b) E/A = 40 MeV (c) E/A = 50 MeV, and (d) E/A

= 60 MeV.

Legend:
- ○ Xe+Cu
- —— TG+GEM
- ---- BUU+GEM

(a), (b), (c), (d): $d\sigma/dV$ (barns) vs V/V_{beam}

186
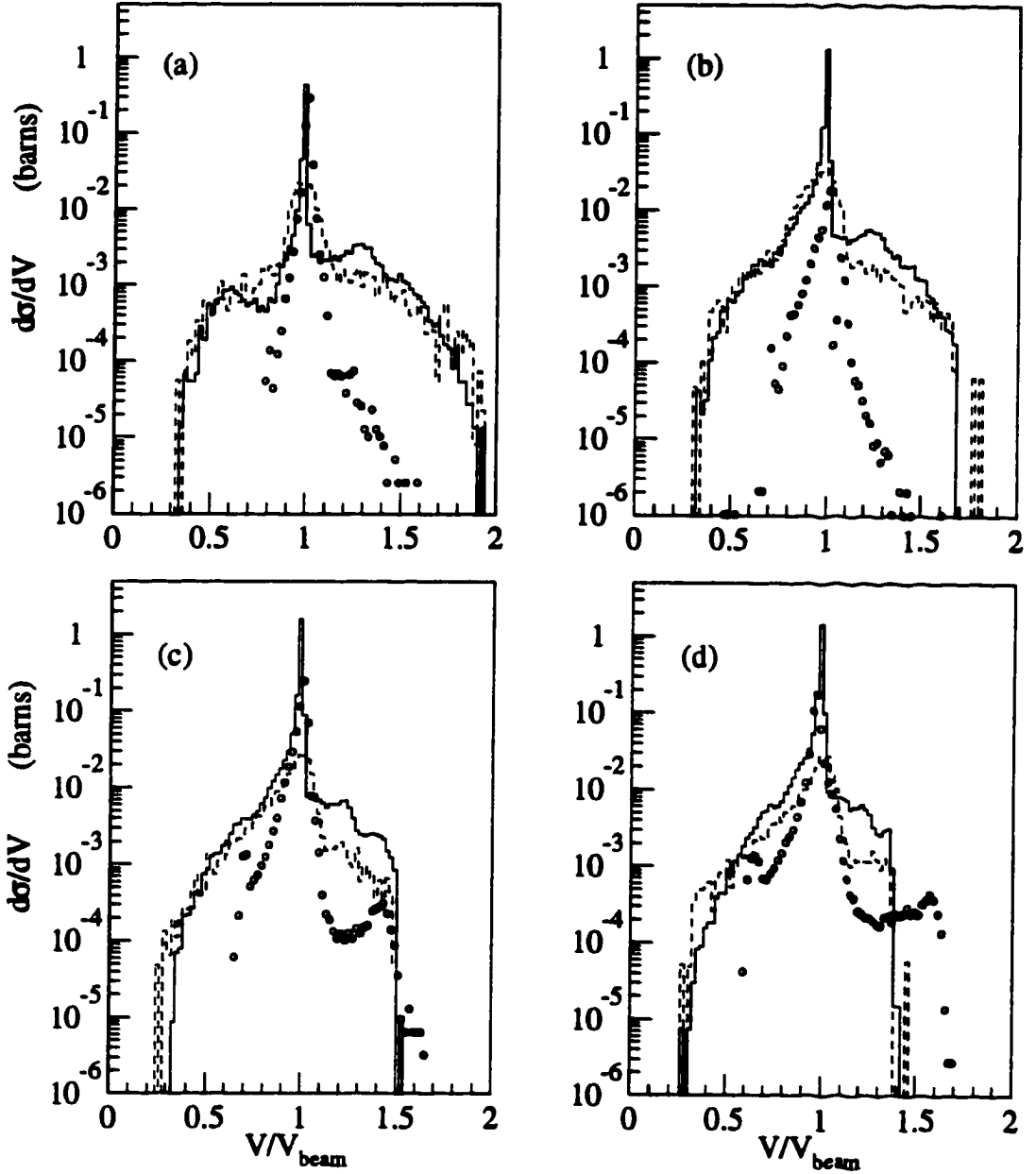
V.A.3 Inclusive Velocity Distributions

The velocity distributions for the Xe + Cu system at E/A = 30, 40, 50, and 60 MeV are shown in Fig. V.9(a)-(d), along with the TG+GEM and BUU+GEM model calculations. The data along with the TG+SMM and BUU+SMM model calculations are shown in Fig. V.10(a)-(d). The Xe + Sc velocity distributions are shown in Fig. V.11(a)-(d), along with the TG+GEM and BUU+GEM model calculations, and in Fig. V.12(a)-(d), along with the TG+SMM and BUU+SMM model calculations. The dots are the data and the solid and dashed lines are the TG and BUU models, respectively.

While all the calculations reproduce the data around the beam velocity, all variations produce distributions which are much too wide at E/A = 30 and 40 MeV. The distributions are still too wide at E/A= 50 and 60 MeV for Cu target, but are reasonable for the Sc target.

V.B Energy Dependence of the Charge Distributions

Unlike the inclusive data, the means and widths are not sensitive to the overall cross section. In a deep-inelastic mechanism, they have been shown to be independent of angle, so they are insensitive to the geometric filter. The means and widths of the distributions have been extracted using Gaussian fits.

V.B.1 Mean Charge

The means of the charge distributions for the Xe + Cu system at E/A = 30, 40, 50, and 60 MeV are shown in Fig. V.13(a)-(d), along with the TG+GEM and BUU+GEM model calculations. Figure V.14(a)-(d) shows the means of the charge distributions for the Xe + Cu system with the TG+SMM and the BUU+SMM model calculations. The dots represent the data and the solid and dashed lines represent the TG and BUU models, respectively. In general, the TG model does a good job

187

Figure V.10 A comparison of the inclusive velocity distributions for the data (dots) and TG+SMM (solid lines) and BUU+SMM (dashed lines) model calculations for the Xe + Cu system at (a) E/A = 30 MeV, (b) E/A = 40 MeV (c) E/A = 50 MeV, and (d) E/A = 60 MeV.

.

188

Legend:
- ○ Xe+Cu
- — TG+SMM
- ---- BUU+SMM

(a) (b) (c) (d)

Axes: $d\sigma/dV$ (barns) versus V/V_{beam}

189
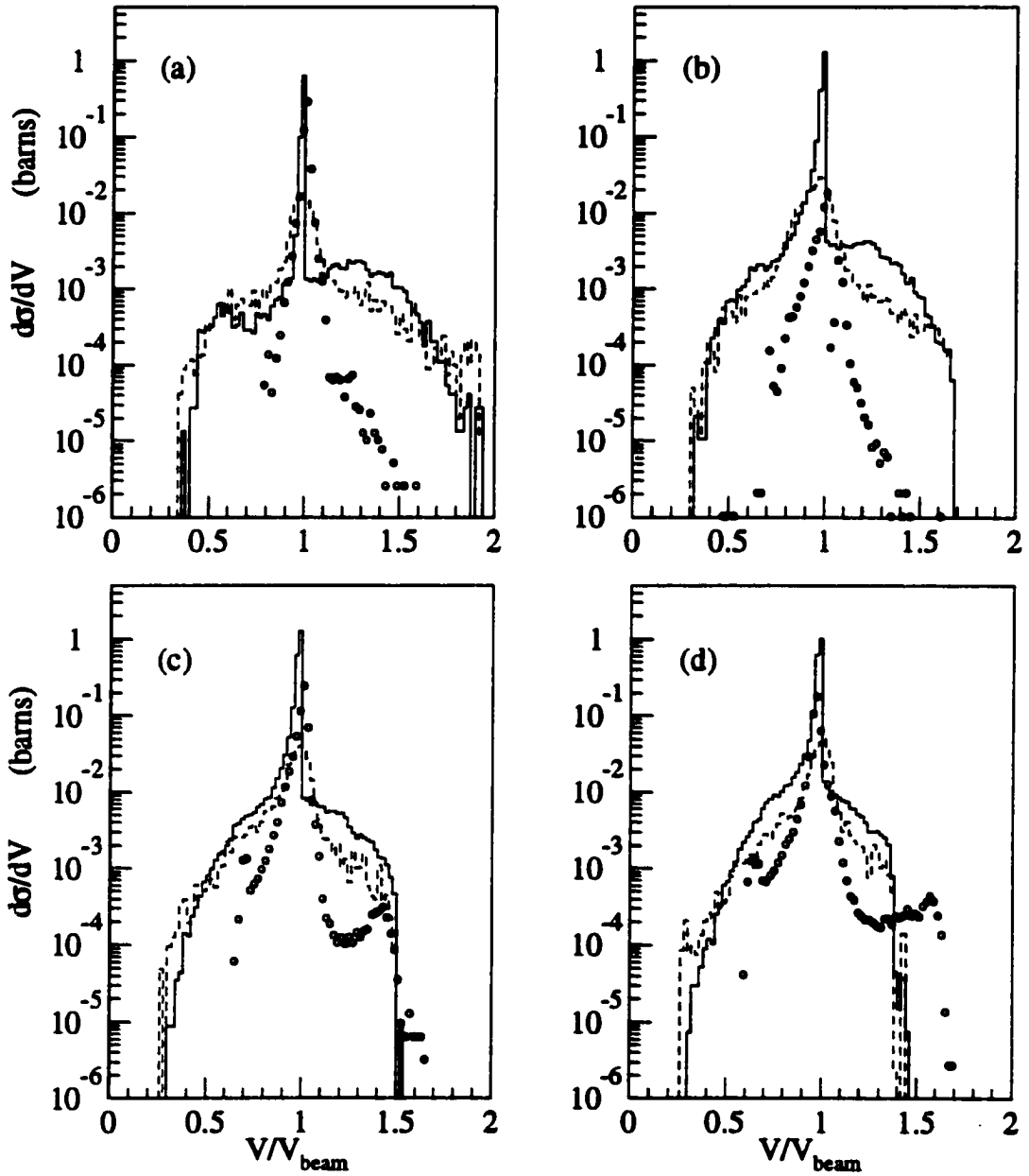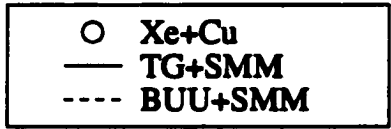
Figure V.11 A comparison of the inclusive velocity distributions for the data (dots)

and TG+GEM (solid lines) and BUU+GEM (dashed lines) model calculations for the

Xe + Sc system at (a) E/A = 30 MeV, (b) E/A = 40 MeV (c) E/A = 50 MeV, and (d)

E/A = 60 MeV.

190

191
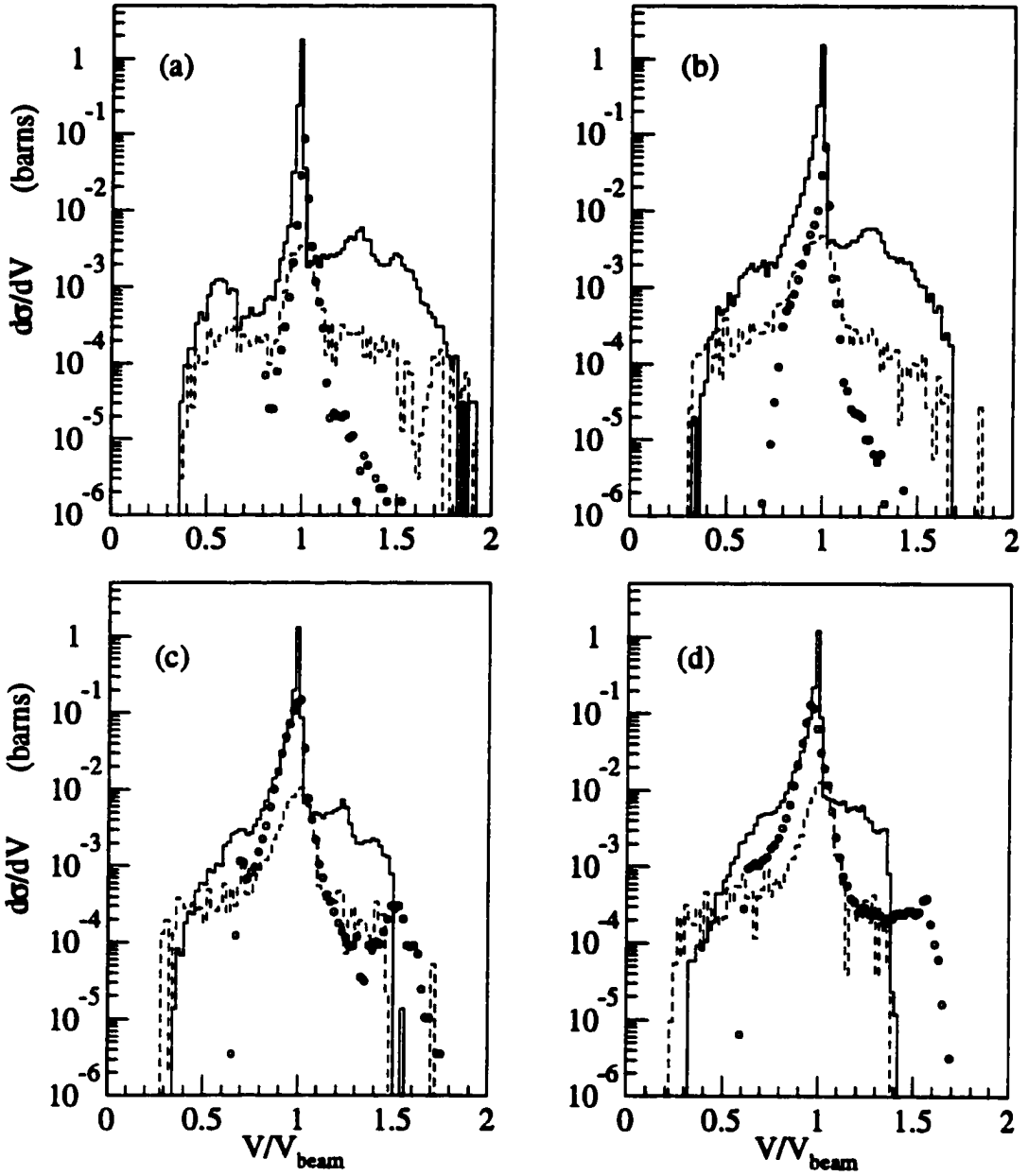
Figure V.12 A comparison of the inclusive velocity distributions for the data (dots) and TG+SMM (solid lines) and BUU+SMM (dashed lines) model calculations for the Xe + Sc system at (a) E/A = 30 MeV, (b) E/A = 40 MeV (c) E/A = 50 MeV, and (d) E/A = 60 MeV.

192

Figure showing $d\sigma/dV$ (barns) versus V/V_{beam} for panels (a), (b), (c), and (d). Legend: Xe+Sc (open circles), TG+SMM (solid line), BUU+SMM (dashed line).

193
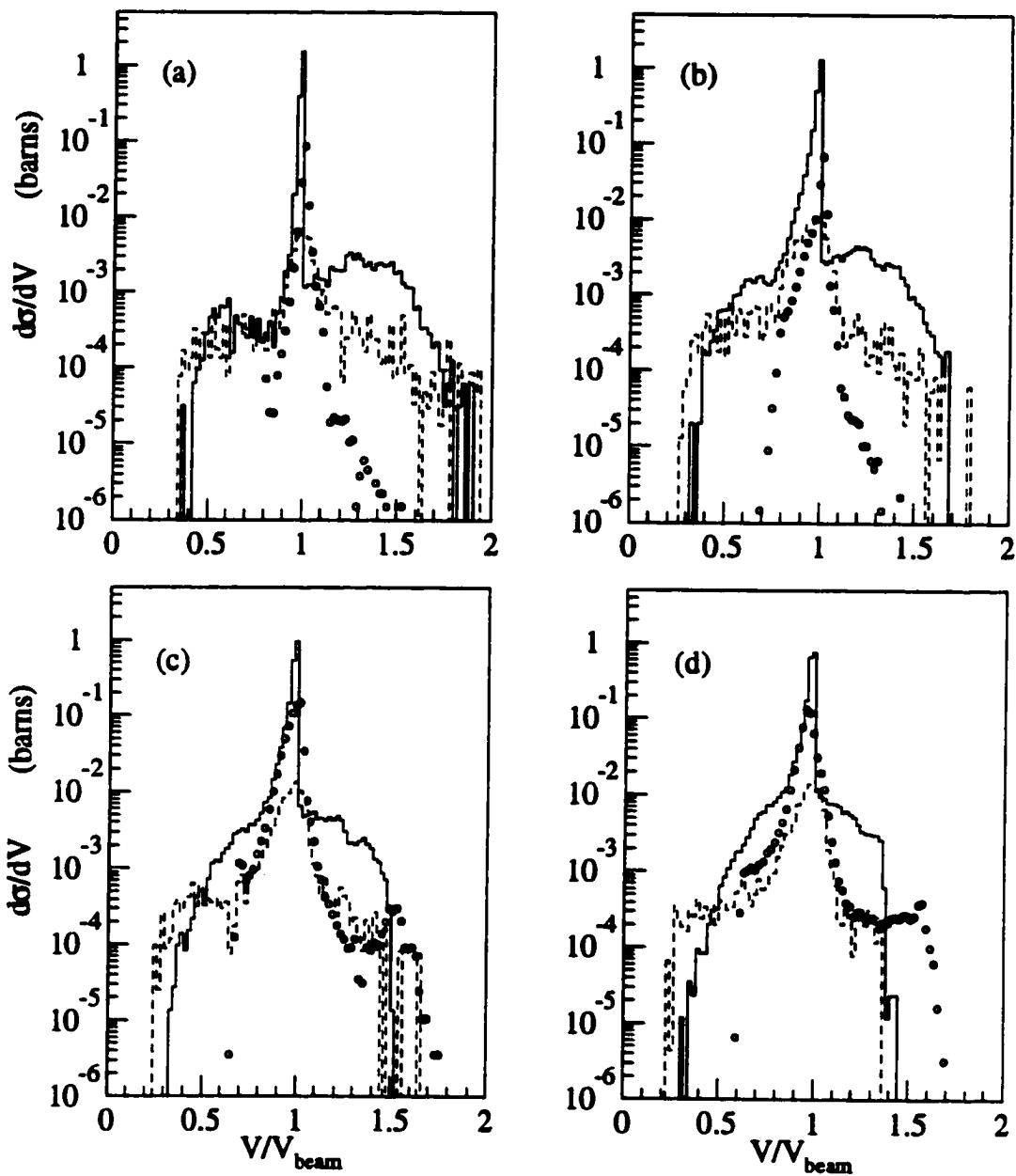
Figure V.13 A comparison of the mean charges as a function of laboratory kinetic energy for the data (dots) and TG+GEM (solid lines) and BUU+GEM (dashed lines) model calculations for the Xe + Cu system at (a) E/A = 30 MeV, (b) E/A = 40 MeV (c) E/A = 50 MeV, and (d) E/A = 60 MeV.

194

195
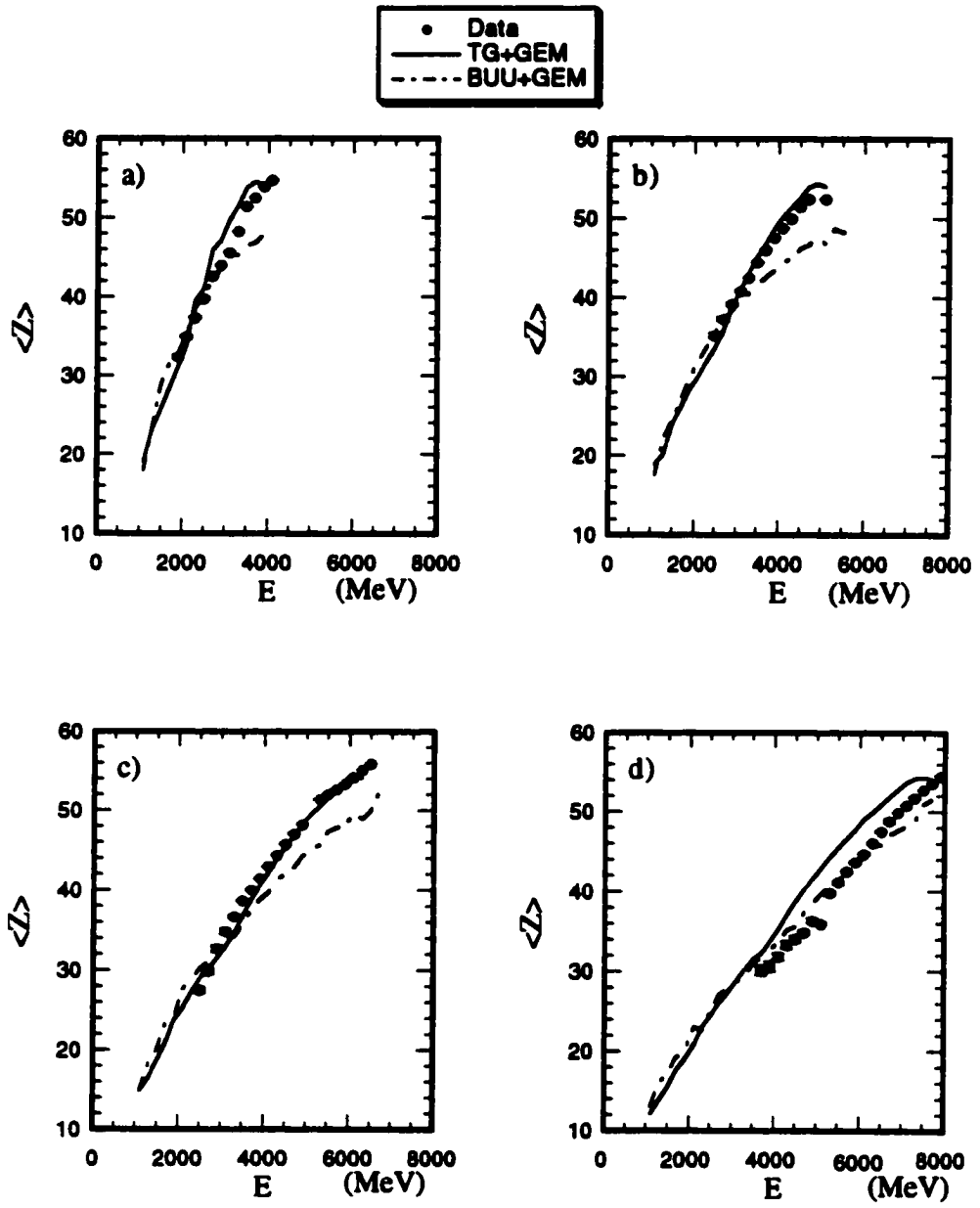
Figure V.14 A comparison of the mean charges as a function of laboratory kinetic

energy for the data (dots) and TG+SMM (solid lines) and BUU+SMM (dashed lines)

model calculations for the Xe + Cu system at (a) E/A = 30 MeV, (b) E/A = 40 MeV

(c) E/A = 50 MeV, and (d) E/A = 60 MeV.

197
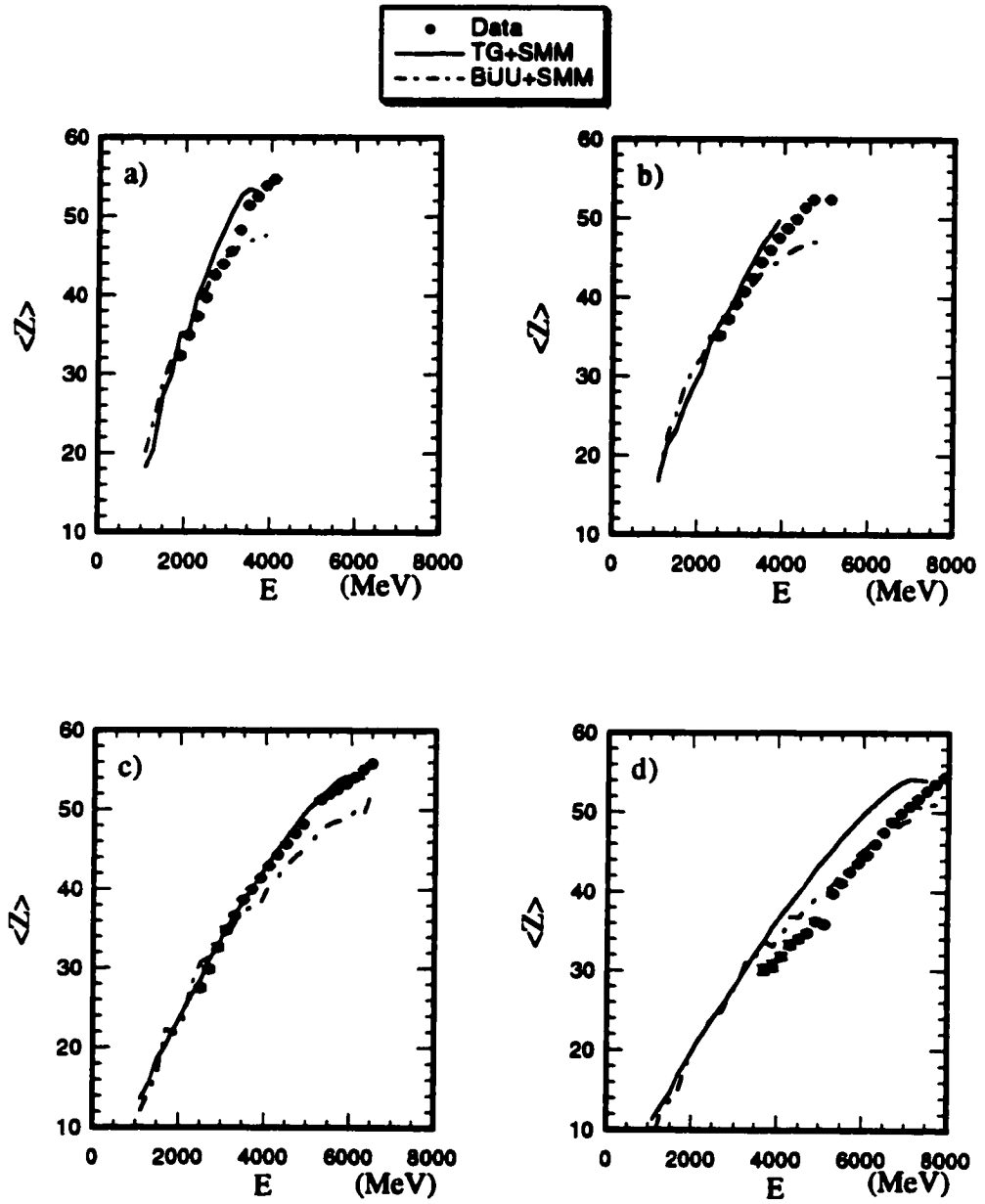
Figure V.15 A comparison of the mean charges as a function of laboratory kinetic energy for the data (dots) and TG+GEM (solid lines) and BUU+GEM (dashed lines) model calculations for the Xe + Sc system at (a) E/A = 30 MeV, (b) E/A = 40 MeV (c) E/A = 50 MeV, and (d) E/A = 60 MeV.

198

199
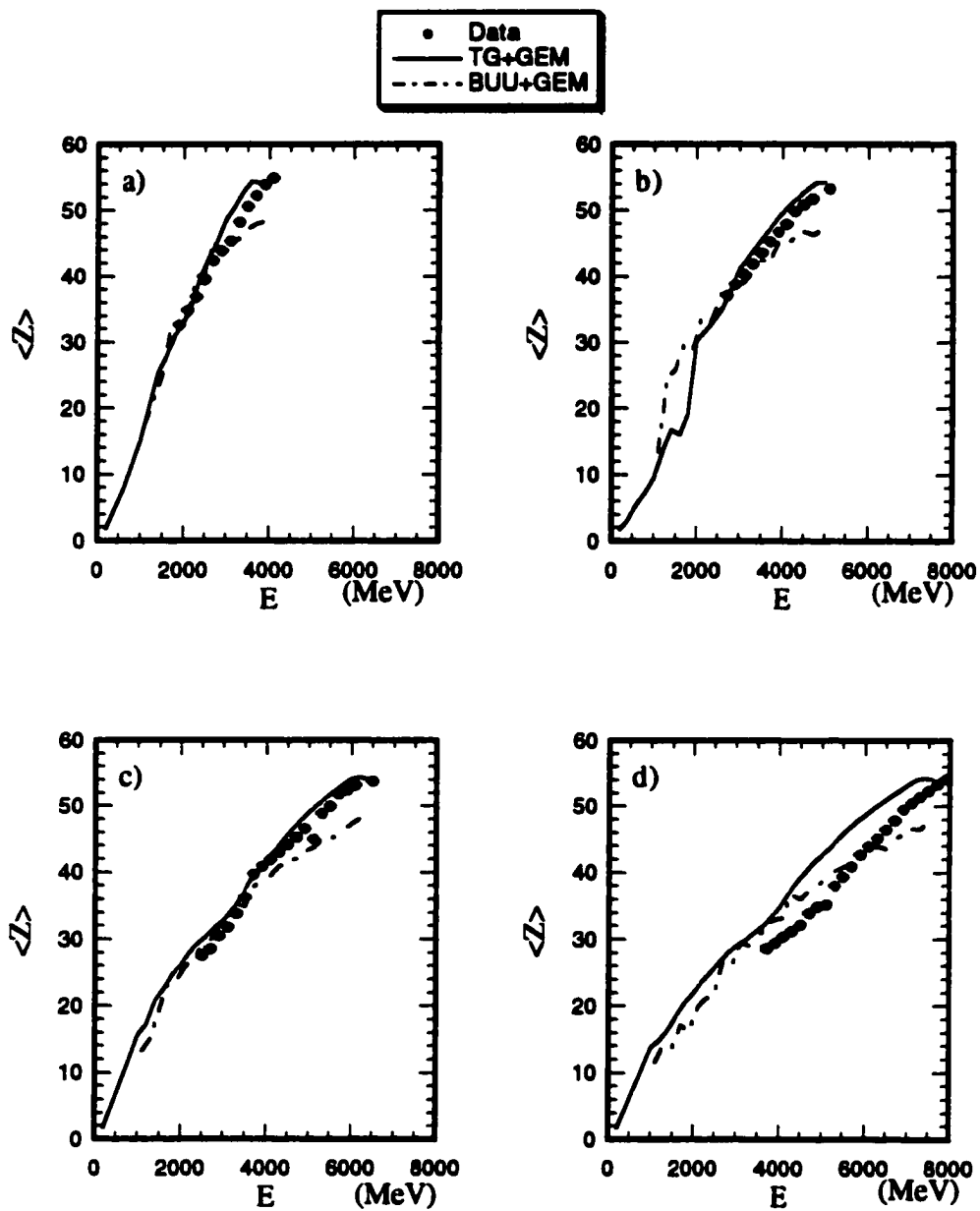
describing the data, except for at E/A = 60 MeV. The BUU model fails to reproduce the means for high energy bins, but does a reasonable job for lower energy bins.

The means of the charge distributions for the Xe + Sc system at E/A = 30, 40, 50, and 60 MeV are shown in Fig. V.15(a)-(d), along with the TG+GEM and BUU+GEM model calculations. Figure V.16(a)-(d) shows the means of the charge distributions for the Xe + Sc system with the TG+SMM and the BUU+SMM model calculations. The dots represent the data and the solid and dashed lines represent the TG and BUU models, respectively. The TG model with both afterburners predicts too large a mean charge at E/A = 60 MeV, and the TG+SMM is slightly high at the other energies. The BUU with either afterburner fails to reproduce the high energy bins, but for intermediate energies it does a good job for E/A = 30, 40 and 50 MeV.

V.B.2 Charge Widths

The widths of the charge distributions for the Xe + Cu system at E/A = 30, 40, 50, and 60 MeV are shown in Fig. V.17(a)-(d), along with the TG+GEM and BUU+GEM model calculations. The data with the TG+SMM and BUU+SMM model calculations are shown in Fig. V.18.(a)-(d) The dots represent the data, and the solid and dashed lines represent the TG and BUU calculations with the appropriate afterburner. The sharp peaks in the figures are associated with the fact that widths are very sensitive to the shape of the charge distributions. Ignoring the peaks, the general trend is reproduced at E/A = 30 and 40 MeV, and for the higher energy bins at 50 MeV. The E/A = 40 MeV TG+SMM model results appear to be shifted to lower energy bins. For all energies, the BUU model is flatter than the TG or the data. In the E/A = 60 MeV system, neither model can reproduce the large widths of the data.

The charge widths for the Xe + Sc system at E/A = 30, 40, 50, and 60 are shown in Fig. V.19(a)-(d) for the data along with TG+GEM and BUU+GEM model calculations and in Fig. V.20(a)-(d) for the data along with the TG+SMM and

200

Figure V.16 A comparison of the mean charges as a function of laboratory kinetic energy for the data (dots) and TG+SMM (solid lines) and BUU+SMM (dashed lines) model calculations for the Xe + Sc system at (a) E/A = 30 MeV, (b) E/A = 40 MeV (c) E/A = 50 MeV, and (d) E/A = 60 MeV.

202
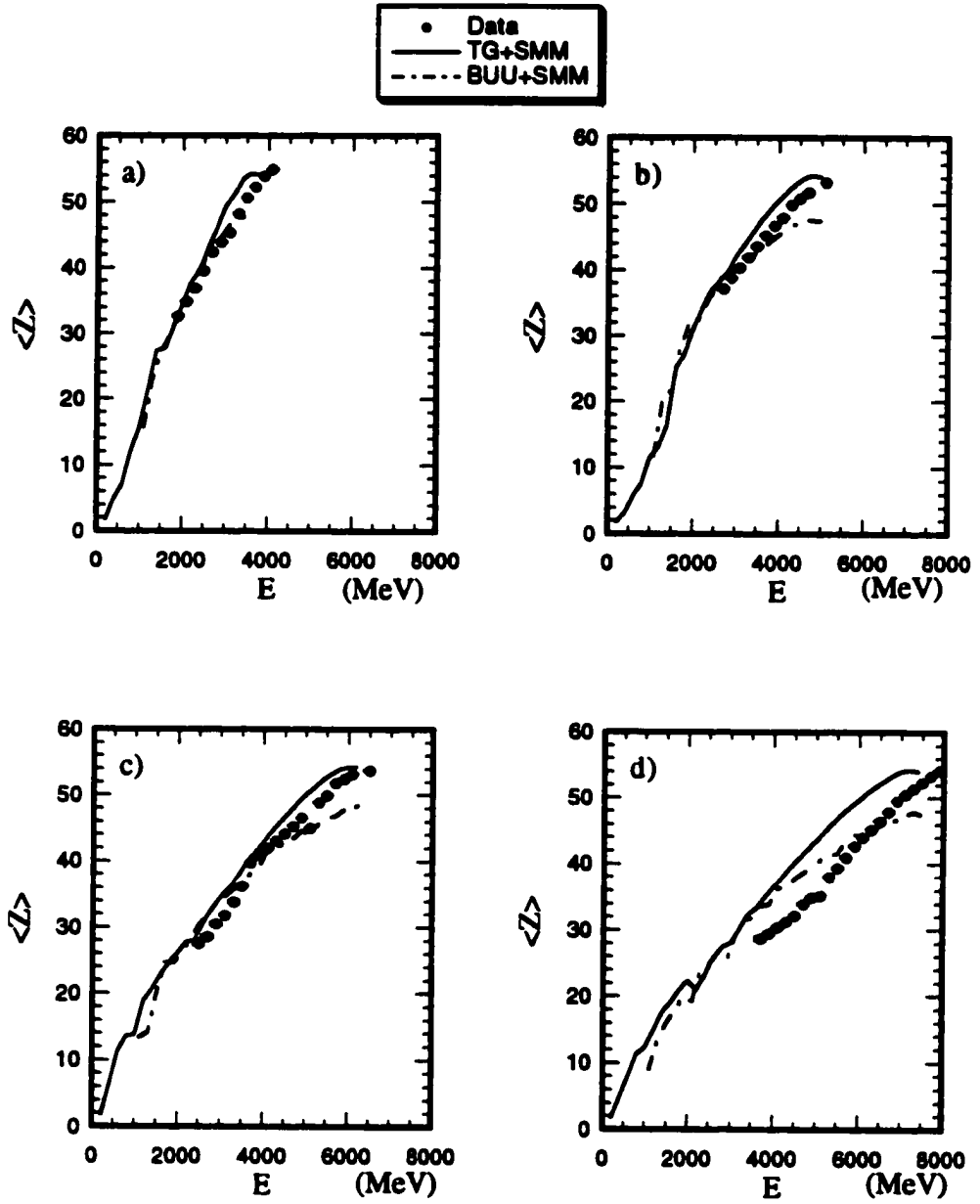
Figure V.17 A comparison of the charge widths as a function of laboratory kinetic energy for the data (dots) and TG+GEM (solid lines) and BUU+GEM (dashed lines) model calculations for the Xe + Cu system at (a) E/A = 30 MeV, (b) E/A = 40 MeV (c) E/A = 50 MeV, and (d) E/A = 60 MeV.

203

204
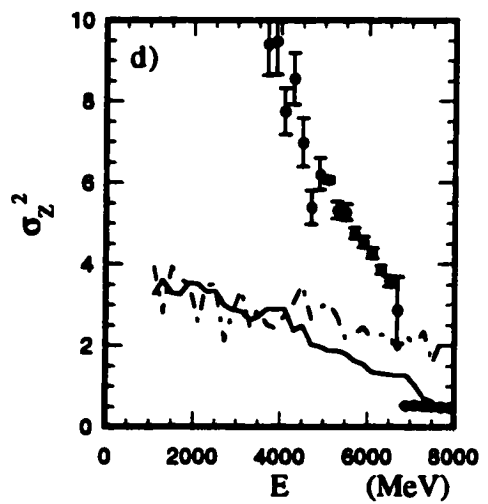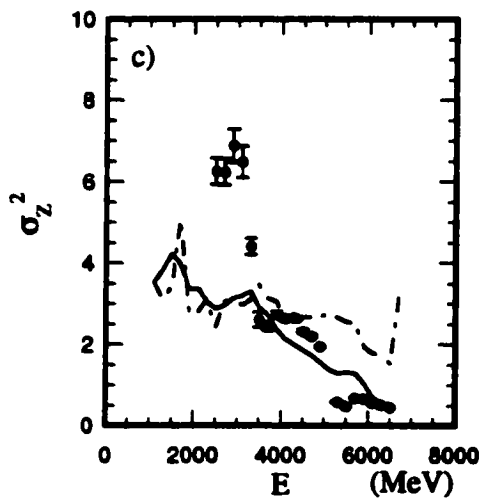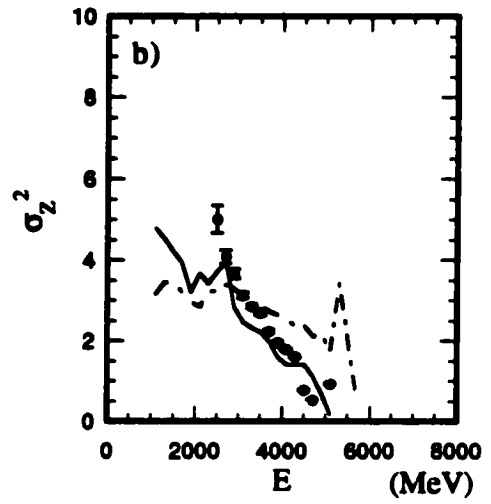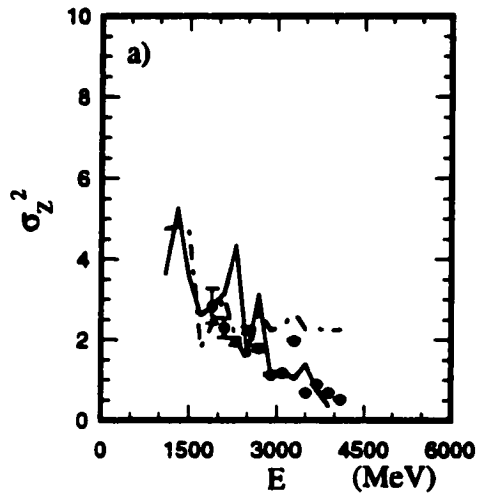
Figure V.18 A comparison of the charge widths as a function of laboratory kinetic

energy for the data (dots) and TG+SMM (solid lines) and BUU+SMM (dashed lines)

model calculations for the Xe + Cu system at (a) E/A = 30 MeV, (b) E/A = 40 MeV

(c) E/A = 50 MeV, and (d) E/A = 60 MeV.

206
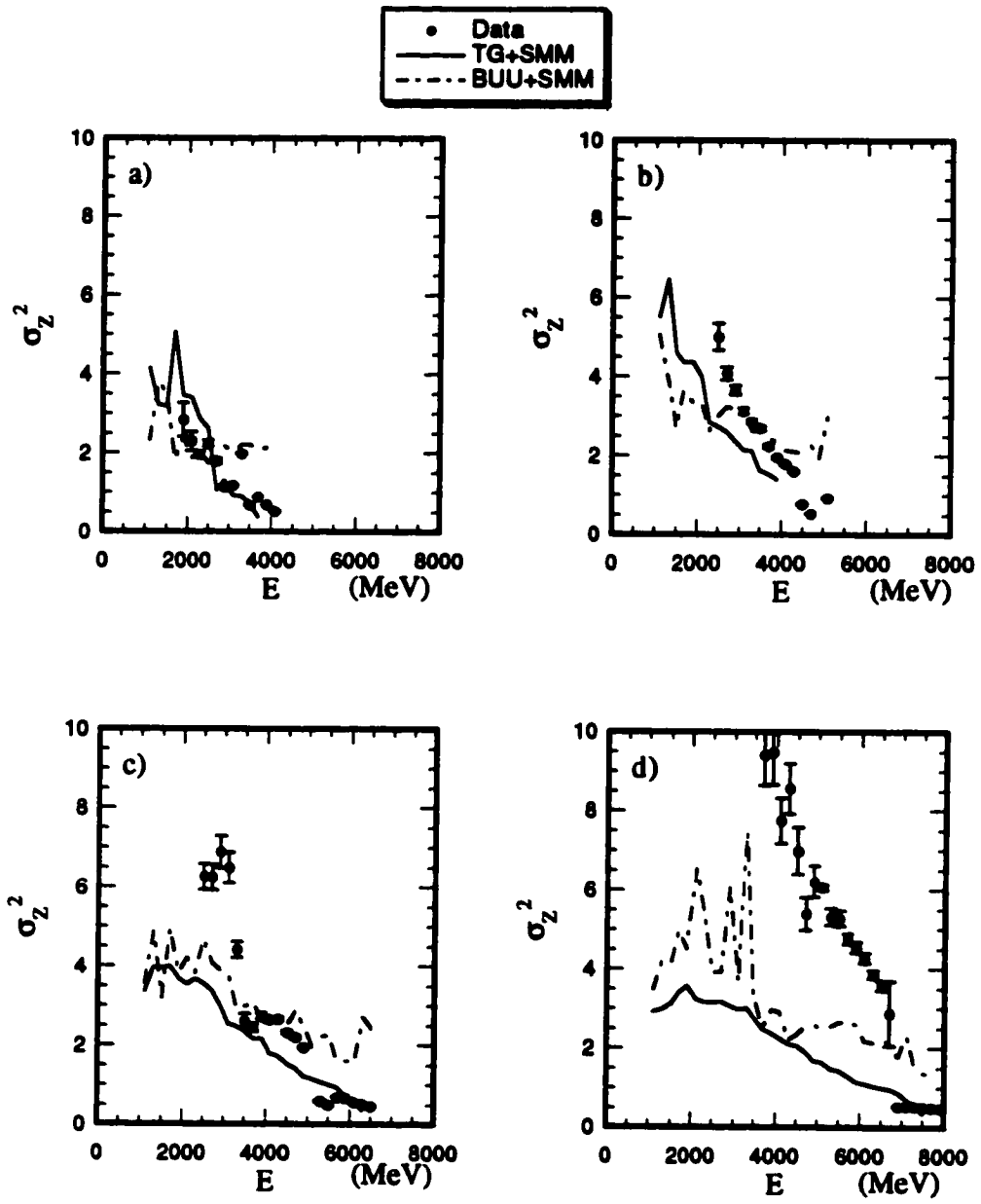
Figure V.19 A comparison of the charge widths as a function of laboratory kinetic energy for the data (dots) and TG+GEM (solid lines) and BUU+GEM (dashed lines) model calculations for the Xe + Sc system at (a) E/A = 30 MeV, (b) E/A = 40 MeV (c) E/A = 50 MeV, and (d) E/A = 60 MeV.

207

208
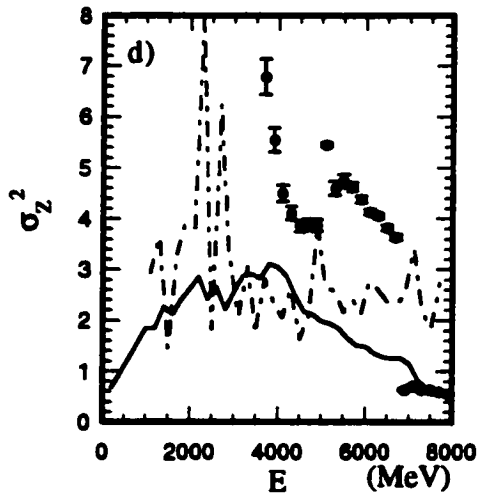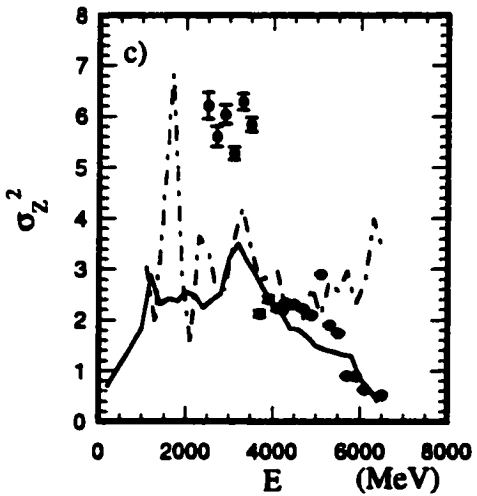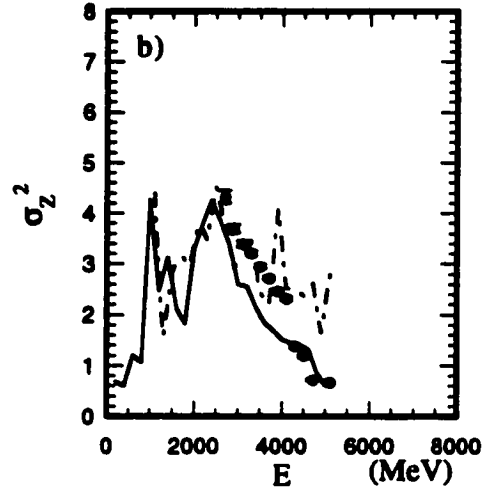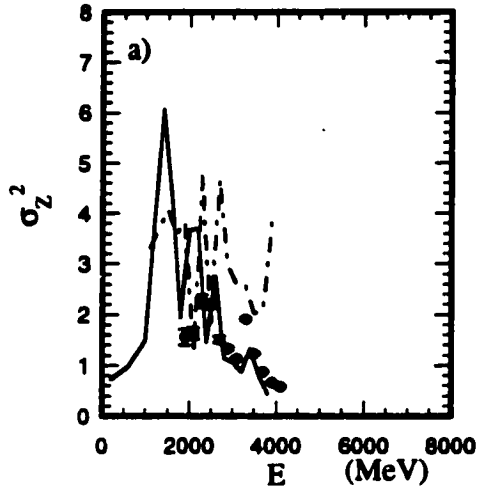
Figure V.20 A comparison of the charge widths as a function of laboratory kinetic energy for the data (dots) and TG+SMM (solid lines) and BUU+SMM (dashed lines) model calculations for the Xe + Sc system at (a) E/A = 30 MeV, (b) E/A = 40 MeV (c) E/A = 50 MeV, and (d) E/A = 60 MeV.

209

210
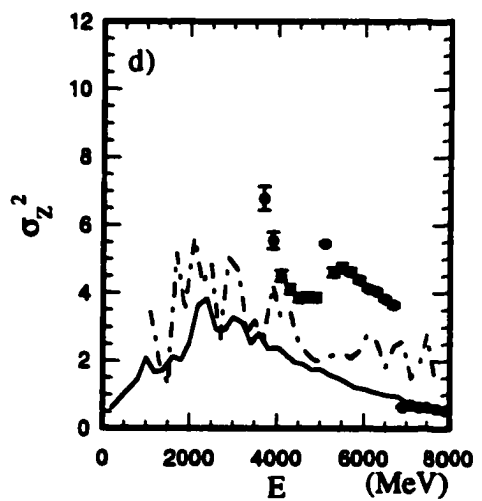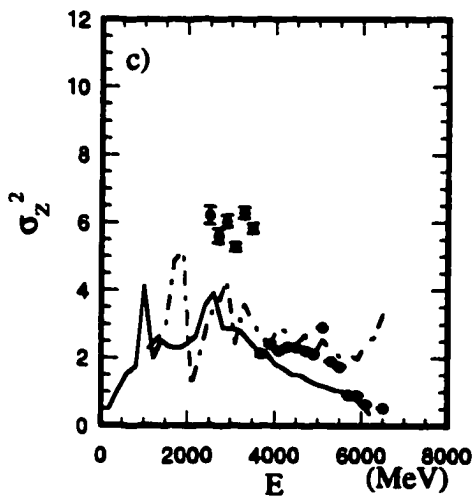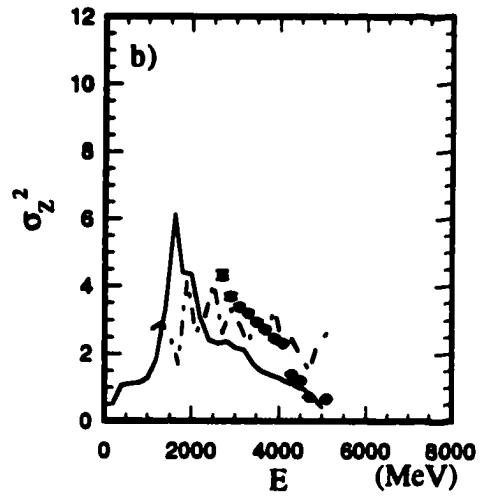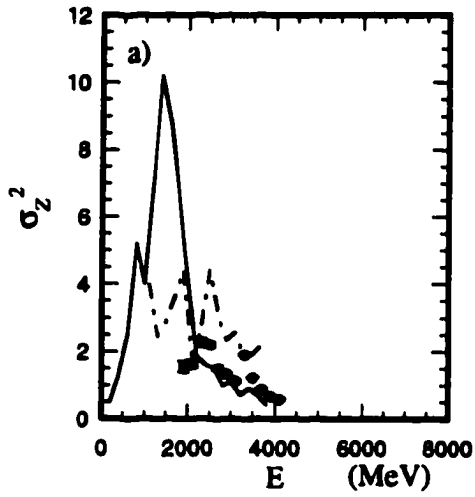
BUU+SMM model calculation. The dots represent the data and the solid and dashed lines represent the TG and BUU model calculations, respectively. The Xe + Sc system has larger fluctuations in the calculations than in the Xe + Cu system. Ignoring the fluctuations and focusing on the general trends, the TG model reproduces the trends at E/A = 30 and 40 MeV, and for the highest energy bins at 50 and 60 MeV. At all energies, The BUU is too flat.

V.C Charge Dependence of the Velocity Distribution

The charge dependence of the mean velocity is shown in Fig. V.21(a) for Xe + Cu at E/A = 30, 40, 50, and 60 MeV and for the Xe + Sc at E/A = 30, 40, 50, and 60 MeV in Fig V.21(b). The dots represent E/A = 30 MeV, the squares represent E/A = 40 MeV, the crosses represent E/A= 50 MeV, and the x's represent E/A = 60 MeV. There appear to be three different slopes seen: the first slope is the E/A = 30 data, the second for the E/A = 40 and 50 MeV data, and the last is for the E/A = 60 MeV data.

The mean velocities for the Xe + Cu system at E/A = 30, 40, 50, and 60 MeV are shown in Fig. V.22(a)-(d) along with the TG+GEM and BUU+GEM model calculations. The data along with the TG+SMM and BUU+SMM model calculations are shown in Fig. V.23(a)-(d). The dots are the data and the solid and dashed lines are the TG and BUU models, respectively. For Z >20 at E/A = 30 MeV, both the BUU and TG model can predict the charge dependence data. At E/A = 40 and 50 MeV, the TG model does a good job predicting the means. Neither model works well at E/A = 60 MeV.

The mean velocities for the Xe + Sc system at E/A = 30, 40, 50, and 60 MeV are shown in Fig. V.24(a)-(d), along with the TG+GEM and BUU+GEM model calculations. The data along with the TG+SMM and BUU+SMM model calculations are shown in Fig. V.25(a)-(d). The dots are the data and the solid and dashed lines are the TG and BUU models, respectively. The calculated mean velocity distributions

211

for the Xe + Sc system look similar to the Xe + Cu system for Z > 20, with the exception being that the Xe + Sc TG+SMM at E/A = 30 MeV is lower that the Xe + Cu and the data.

212

Figure V.21 A comparison of the mean of the velocity distributions as a function of laboratory kinetic energy for the (a) Xe + Cu and (b) Xe + Sc at E/A =30 (dots), 40 (squares), 50 (crosses), and 60 (x's).

(a) Legend: Xe + Cu E/A = 30 MeV, Xe + Cu E/A = 40 MeV, Xe + Cu E/A = 50 MeV, Xe + Cu E/A = 60 MeV

(b) Legend: Xe + Sc E/A = 30 MeV, Xe + Sc E/A = 40 MeV, Xe + Sc E/A = 50 MeV, Xe + Sc E/A = 60 MeV

214
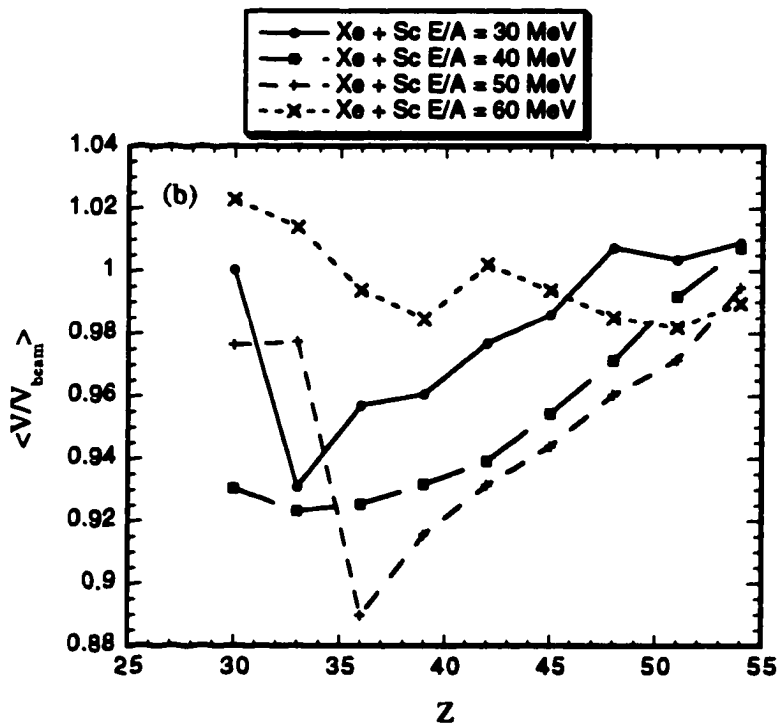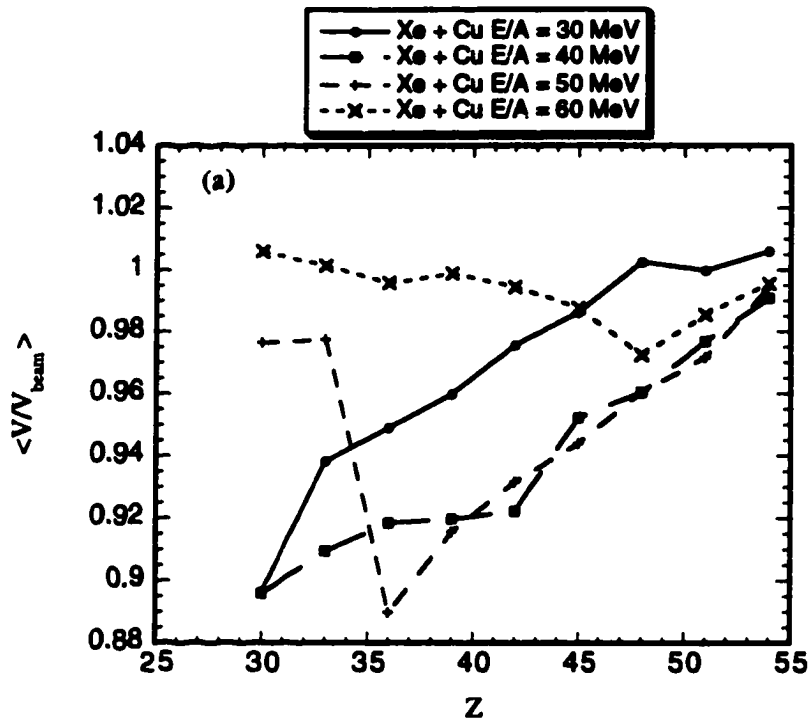
Figure V.22 A comparison of the mean velocities as a function of charge for the data (dots) and TG+GEM (solid lines) and BUU+GEM (dashed lines) model calculations for the Xe + Cu system at (a) E/A = 30 MeV, (b) E/A = 40 MeV (c) E/A = 50 MeV, and (d) E/A = 60 MeV.

215

216
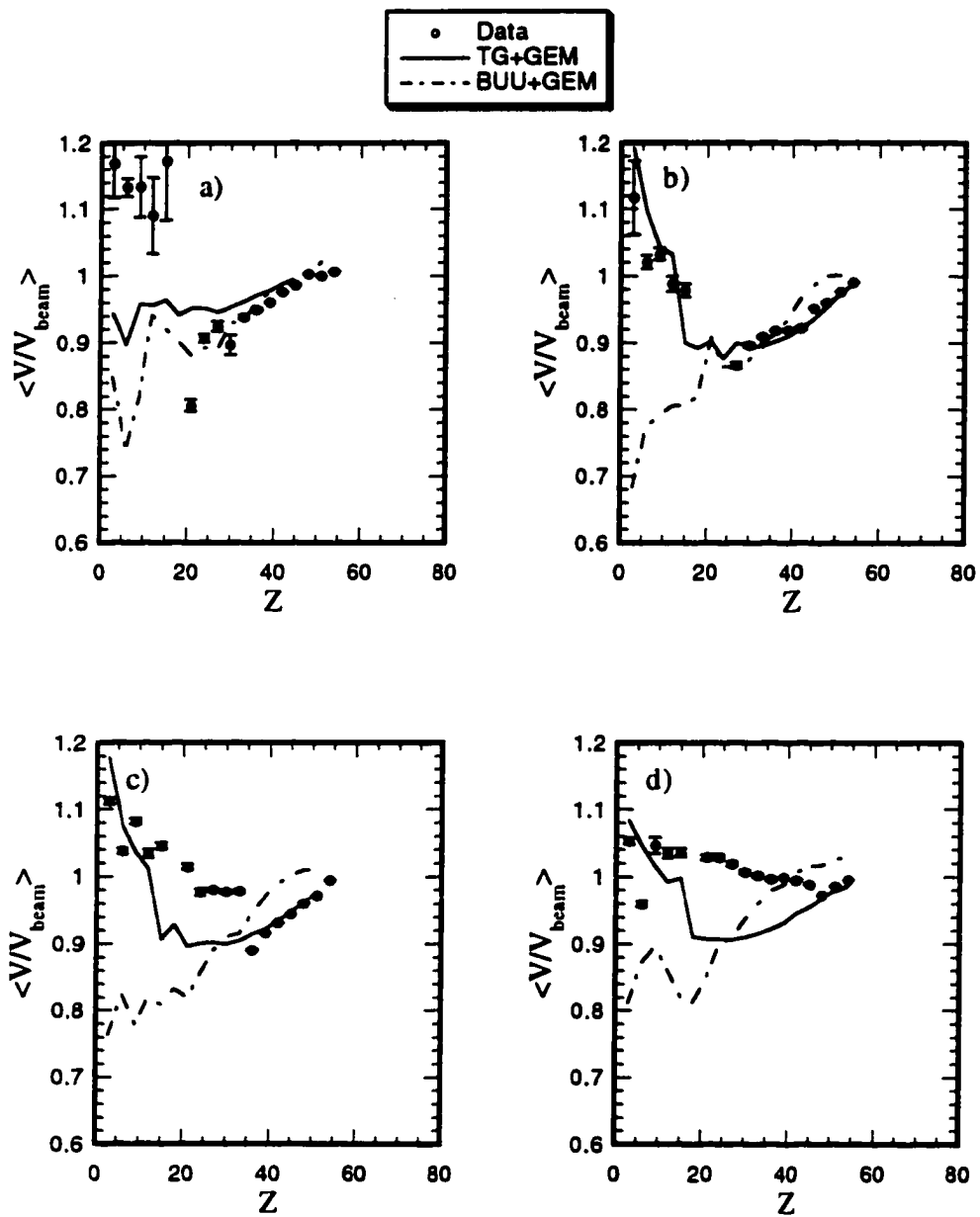
Figure V.23 A comparison of the mean velocities as a function of charge for the data (dots) and TG+SMM (solid lines) and BUU+SMM (dashed lines) model calculations for the Xe + Cu system at (a) E/A = 30 MeV, (b) E/A = 40 MeV (c) E/A = 50 MeV, and (d) E/A = 60 MeV.

217

218
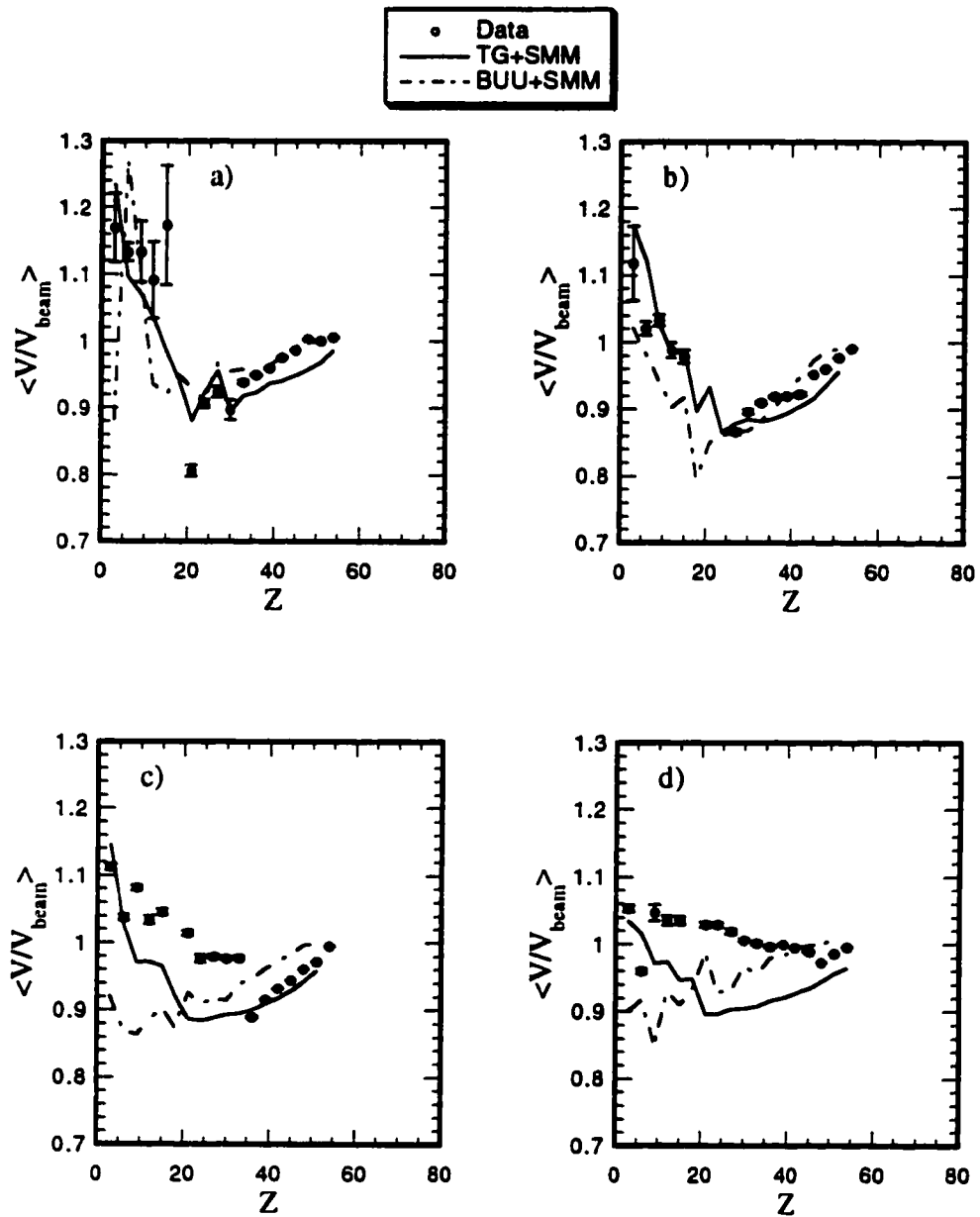
Figure V.24 A comparison of the mean velocities as a function of charge for the data (dots) and TG+GEM (solid lines) and BUU+GEM (dashed lines) model calculations for the Xe + Sc system at (a) E/A = 30 MeV, (b) E/A = 40 MeV (c) E/A = 50 MeV, and (d) E/A = 60 MeV.

219

220
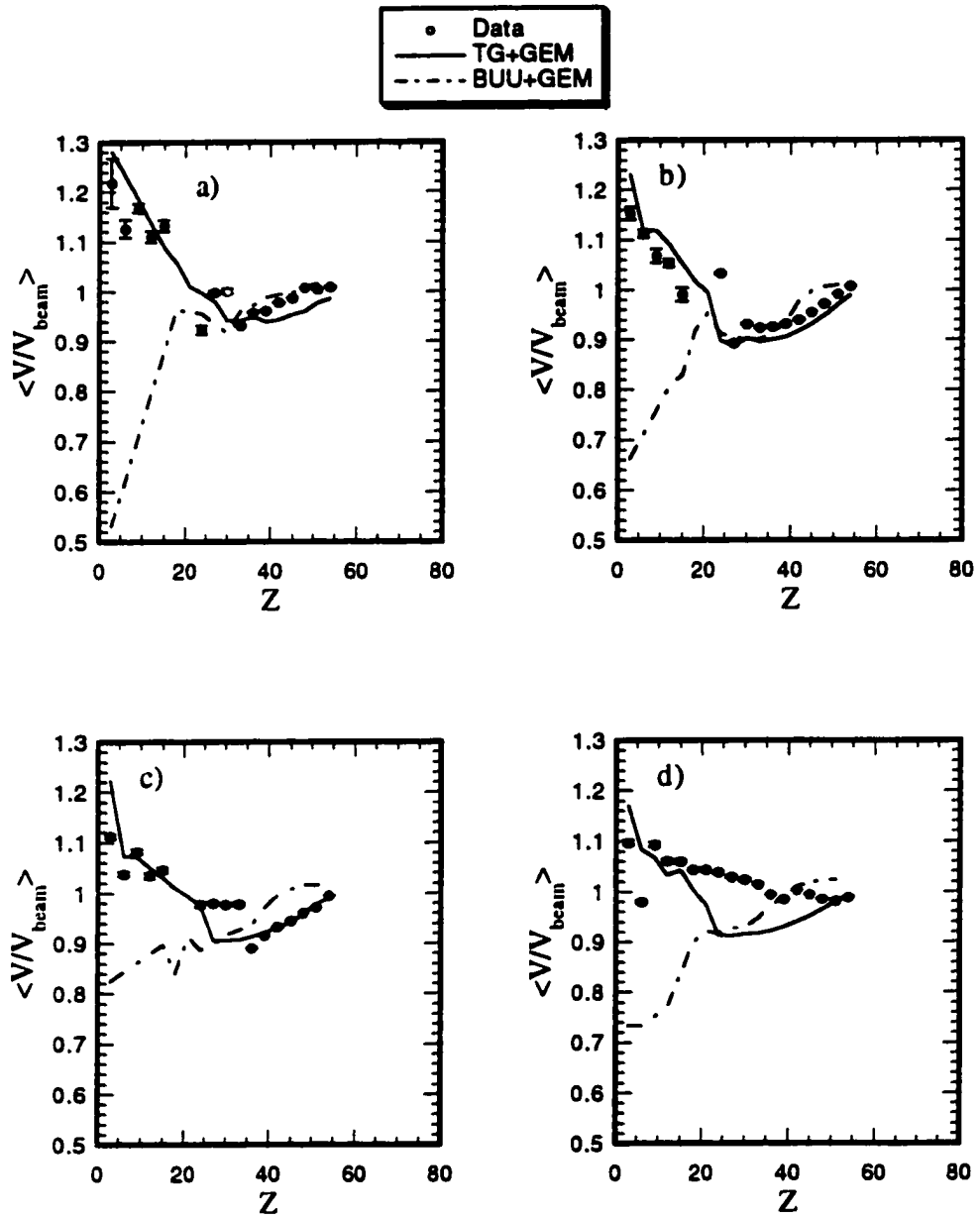
Figure V.25 A comparison of the mean velocities as a function of charge for the data (dots) and TG+SMM (solid lines) and BUU+SMM (dashed lines) model calculations for the Xe + Sc system at (a) E/A = 30 MeV, (b) E/A = 40 MeV (c) E/A = 50 MeV, and (d) E/A = 60 MeV.

221

222
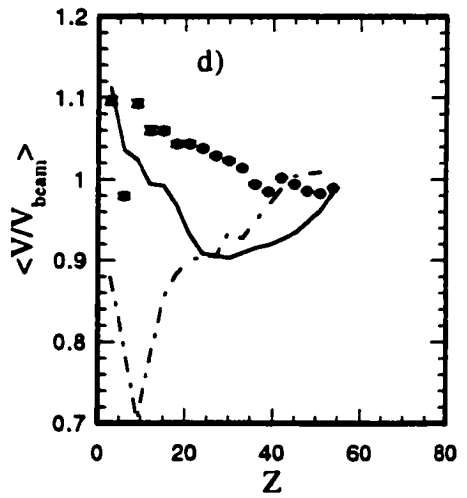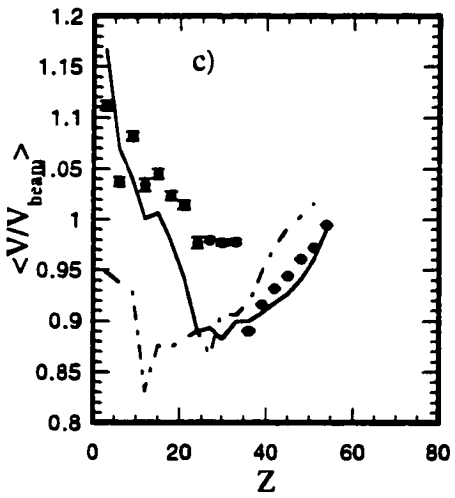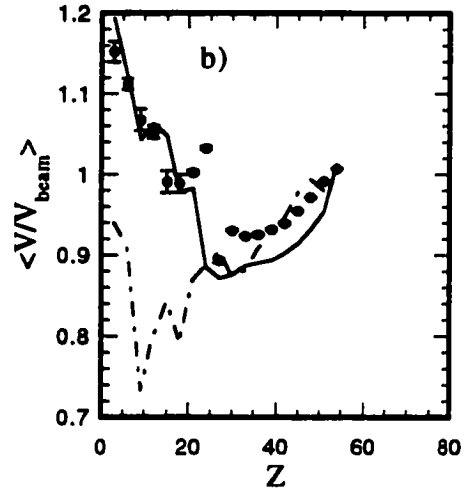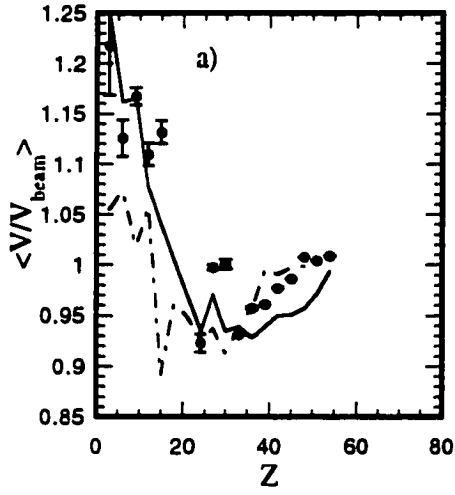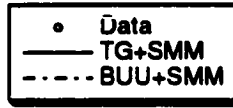
Chapter VI Conclusions

In this experiment, the heavy-ion reactions ^{129}Xe + ^{nat}Cu and ^{nat}Sc at E/A = 30, 40, 50, and 60 MeV were studied to see if deep-elastic reactions are responsible for the production of PLF's within the intermediate energy regime. A new detector, the MFA, was designed and used to identify fragments that go from 1.5° to 2.9° and to measure their energies. In retrospect, the fact that the beam position was offset from the detector's center was lucky. It allowed a larger angular range than if the detector had been centered. Experimental results were compared to BUU and TG model calculations each performed with two different afterburners. An interesting aside is that for all of the systems studied, the differences between the SMM and the GEMINI afterburners are remarkably small. It is serendipitous that this should occur; this study is not focusing on the decay of the hot system (although that is another interesting topic), but rather on the mechanisms forming the hot system

Evidence of rotation is seen in the experimental deflection functions for Xe + Cu at E/A = 30, 40, and 50 MeV. The ability of the TG model to reproduce the shapes, if not always the magnitude, of the inclusive charge, inclusive kinetic energy, inclusive velocity, mean charge, charge width, and mean velocity distributions for PLF's is strong evidence supporting the persistence of the deep-inelastic mechanism up to at least E/A = 50 MeV. The discrepancies in the model distributions in the lower energy and charge bins are less important, because the model does not take into account reactions with $\ell > \ell_{crit}$. Adding a fusion-like component for central collisions may create a better overall fit to the inclusive distributions. It's quite remarkable the TG model fits the lower Z's and E's as well as it does. However, it may be focused nature of the acceptance that makes the fits as good as they are. Unlike at lower beam energies, at E/A = 60 MeV the mean velocity distribution for the Xe + Cu system stays around V/V_{beam} = 1, and the TG model does a poor job fitting almost all of the

223

distributions presented at E/A = 60 MeV. A transition in the reaction mechanism may be occurring between E/A = 50 and 60 MeV in the Xe + Cu system.

The Xe + Sc data looks very similar to the Xe + Cu. The target independence of Xe-induced reactions has been seen previously at E/A = 50 MeV [MAD94, MAD96], so the similarity between the two systems is not unexpected. The Xe + Cu system has more available energy for the reaction (larger E_{cm}), but otherwise the systems behave similarly. The TG model has a weak target dependence, but in the BUU model changing the target has very pronounced effets.

The BUU model does a very good job of predicting the distributions away from the quasi-elastic region. For the E/A = 50 and 60 MeV Xe + Cu, the BUU model shows evidence of a projectile spectator. In addition, the Xe + Sc BUU calculations at E/A = 60 MeV looks similar to the Xe + Cu calculations at 40 E/A = MeV. This may be attributed available energy (E/A = 60 MeV Xe + Sc E_{cm} = 2000.27 MeV, E/A = 40 MeV Xe + Cu E_{cm} = 1702.96 MeV). It appears that the primary BUU mechanism for Xe + Sc will undergo a transition to a participant-spectator mechanism at slightly higher beam energies.

The attractive nuclear potential in the BUU may be too weak. Increasing the strength of the attractive mean field would increase the energy where the transition from deep-inelastic reactions to a different mechanism occurs. In addition, a stronger mean field may hold the nucleus together forming a quasi-elastic peak in the charge distributions. Additionally, it would interesting to measure the balance energy for the Xe + Cu system and see if it falls between E/A = 50 and 60 MeV. This may be extracted from the data set if the MSU 4π main ball detectors are analyzed. In reality, neither model predicts the data and there is no good comprehensive model for the intermediate energy regime.

224

Appendix

Table A.1: Values for calibration constants used for the MFA to calculate the light output by the scintillating plastic using Eqs. II-7 and II-8.

Det	a_1	b_1	c_1	a_2	b_2	c_2
1	4.9724	0.51395	0.599	0.085232	-0.73359	1.46
2	14.393	0.37846	0.523	0.65455	-0.77003	1.238
3	11.483	-0.21224	0.799	0.42955	-0.63434	1.214
4	5.5188	-0.078772	0.819	0.31049	-0.6709	1.239
5	4.7471	-0.95357	1.364	3.8822	-0.2205	0.756
6	13.748	-0.2536	0.802	0.73399	-0.754	1.196
7	7.0906	-0.16706	0.83	0.26856	-0.73584	1.297
8	7.016	-0.21593	0.85	0.2842	-0.70441	1.263
9	9.0096	0.062529	0.71	0.3299	-0.74226	1.3
10	17.748	-0.27213	0.774	1.1687	-0.70706	1.134
11	19.784	-0.14506	0.71	0.96786	-0.73464	1.17
12	14.859	0.12051	0.652	1.5586	-0.65343	1.073
13	8.8123	0.26522	0.629	0.26824	-0.69898	1.308
14	12.104	0.3926	0.515	0.28635	-0.72938	1.313
15	16.371	0.50237	0.449	0.54686	-0.70322	1.233
16	11.621	0.53188	0.463	0.22181	-0.69341	1.348

225

Table A.2: Values for calibration constants used for the MFA in calculating the PID when the particle stops in the slow plastic from Eqs. II-10.

Det	s_{10}	s_{11}	s_{12}	s_{20}	s_{21}	s_{22}
1	6.4009e+05	-1.4492e+05	8875.0	24.525	39.300	0.29095
2	2.5066e+05	-55655	7800.4	147.35	55.642	0.11939
3	1.3681e+05	-31474	3646.9	26.184	22.180	0.25891
4	1.4969e+05	-34496	2836.5	20.558	17.091	0.18561
5	4.6774e+05	-97609	6030.3	-31.013	4.5514	0.23497
6	57187	-11136	3143.3	60.051	23.057	0.16681
7	1.2072e+05	-28671	2884.9	23.790	19.413	0.18085
8	1.0257e+05	-24217	2443.7	18.878	16.316	0.16949
9	2.0070e+05	-47607	4836.5	57.372	30.672	0.22300
10	43453	-4522.5	3386.2	75.920	26.626	0.20597
11	48982	-5473.5	4026.9	102.05	31.014	0.20111
12	2.3673e+05	-48453	6401.1	119.71	31.955	0.23660
13	3.4007e+05	-79138	6580.9	61.202	36.376	0.27139
14	2.6027e+05	-61047	6644.0	122.85	49.190	0.24464
15	3.6710e+05	-81592	9780.5	222.57	62.117	0.27200
16	4.8828e+05	-1.1428e+05	10051	121.91	66.114	0.35878

226

Table A.3: Values for calibration constants used for the MFA in calculating the PID when the particle stops in the fast plastic from Eq. II-11.

Det	f_{10}	f_{11}	f_{12}	f_{20}	f_{21}	f_{22}
1	2.7840e+06	-3.3508e+05	12188	-82.043	58.200	0.97469
2	2.4069e+06	-2.8939e+05	10291	-266.46	50.130	0.75188
3	1.4877e+06	-1.8566e+05	7722.1	-251.65	59.144	0.30557
4	1.5482e+06	-1.8935e+05	7296.1	-135.32	44.334	0.44815
5	1.1348e+06	-1.4712e+05	10721	572.23	120.92	-0.032498
6	2.0779e+06	-2.5397e+05	9731.6	-202.42	58.826	0.59650
7	1.9410e+06	-2.3264e+05	8257.5	-105.41	37.247	0.67326
8	1.7006e+06	-2.0438e+05	7335.8	-95.008	34.590	0.58007
9	2.6122e+06	-3.0917e+05	10441	-116.38	37.029	0.97146
10	1.2973e+06	-1.6573e+05	7800.2	-227.20	72.740	0.15375
11	1.4215e+06	-1.8040e+05	8286.3	-196.75	73.278	0.21845
12	1.5170e+06	-1.9400e+05	9225.1	-248.16	86.687	0.17587
13	1.5869e+06	-1.9780e+05	8416.6	-118.94	63.004	0.37611
14	1.3306e+06	-1.6868e+05	7618.8	-225.67	66.886	0.20141
15	2.1396e+06	-2.6235e+05	10118	-282.99	64.118	0.56784
16	1.7521e+06	-2.1654e+05	8659.7	-239.11	59.899	0.42785

227

Table A.4: Values of constants used to calculate the Kinetic energy of a particle. For particles stopping in the fast plastic, $KE(\Delta L) = n_2 \Delta L^2 + n_1 \Delta L + n_0$, where

$n_0 = n_{02} Z^2 + n_{01} Z + n_{00}$, and $n_1 = n_{15} Z^5 \, n_{14} Z^4 \, n_{13} Z^3 \, n_{12} Z^2 + n_{11} Z + n_{10}$, and

$n_1 = n_{24} Z^4 \, n_{23} Z^3 \, n_{22} Z^2 + n_{21} Z + n_{20}$. Table (a) contains the value needed to calculate n_0, Table (b) contains the value needed to calculate n_1, and Table (c) contains the value needed to calculate n_2

a)

Det	n_{00}	n_{01}	n_{02}
1	-275.48	48.105	0.40267
2	-283.03	48.887	0.37314
3	-283.03	48.887	0.37314
4	-281.08	48.497	0.38578
5	-276.56	48.165	0.39980
6	-281.73	48.570	0.38312
7	-279.00	48.323	0.39271
8	-279.00	48.323	0.39271
9	-279.00	48.323	0.39271
10	-283.00	48.809	0.37542
11	-282.52	48.686	0.37918
12	-282.84	48.764	0.37671
13	-280.34	48.429	0.38847
14	-283.00	48.809	0.37542
15	-283.00	48.809	0.37542
16	-282.84	48.764	0.37671

b)

Det	n_{10}	n_{11}	n_{12}	n_{13}	n_{14}	n_{15}
1	0.36916	-0.024720	0.0014937	-2.9016e-05	2.1030e-07	-9.4280e-11
2	0.54138	-0.062199	0.0036862	-9.3188e-05	1.1306e-06	-5.2520e-09
3	0.43342	-0.049728	0.0030298	-7.3884e-05	8.6696e-07	-3.8466e-09
4	0.55618	-0.051108	0.0030939	-7.0218e-05	7.3363e-07	-2.6895e-09
5	0.08555	-0.003846	0.0003348	-1.2280e-07	-1.0777e-07	1.1825e-09
6	0.43080	-0.041556	0.0025051	-5.8274e-05	6.3340e-07	-2.4978e-09
7	0.65528	-0.055109	0.0032427	-7.2866e-05	7.3835e-07	-2.5379e-09
8	0.70177	-0.058611	0.0034670	-7.7257e-05	7.7214e-07	-2.5748e-09
9	0.65949	-0.057399	0.0033012	-7.6905e-05	8.2545e-07	-3.1800e-09
10	0.31986	-0.035248	0.0021952	-5.1248e-05	5.7503e-07	-2.3858e-09
11	0.31130	-0.031899	0.0019971	-4.5272e-05	4.8530e-07	-1.8659e-09
12	0.26353	-0.028386	0.0017760	-4.0931e-05	4.5165e-07	-1.8241e-09
13	0.34616	-0.029417	0.0018517	-3.8554e-05	3.4995e-07	-9.0436e-10
14	0.35780	-0.039367	0.0024374	-5.7412e-05	6.4902e-07	-2.7256e-09
15	0.41315	-0.045410	0.0027331	-6.6847e-05	7.8205e-07	-3.4591e-09
16	0.43050	-0.046273	0.0028080	-6.7511e-05	7.7444e-07	-3.3291e-09

229

c)

Det	n_{20}	n_{21}	n_{22}	n_{23}	n_{24}
1	8.4741e-06	1.0493e-05	-6.1770e-07	1.2838e-08	-9.1758e-11
2	0.00028975	-5.6620e-07	-4.1596e-07	1.1469e-08	-9.1486e-11
3	7.8971e-05	1.8192e-05	-1.0049e-06	2.0240e-08	-1.4223e-10
4	7.6432e-05	2.4798e-05	-1.4443e-06	2.9668e-08	-2.1035e-10
5	-1.7872e-05	3.9149e-06	-1.6742e-07	3.1171e-09	-2.1519e-11
6	6.2496e-05	1.3232e-05	-7.9895e-07	1.6584e-08	-1.1815e-10
7	0.00014075	1.8953e-05	-1.3209e-06	2.8754e-08	-2.0968e-10
8	0.00014625	2.5016e-05	-1.6625e-06	3.5706e-08	-2.5876e-10
9	0.00019691	6.8743e-06	-7.7128e-07	1.8543e-08	-1.4119e-10
10	-5.8698e-06	1.6689e-05	-7.9192e-07	1.5143e-08	-1.0390e-10
11	-1.0505e-05	1.5554e-05	-7.4867e-07	1.4377e-08	-9.8798e-11
12	-8.8113e-06	1.1812e-05	-5.5581e-07	1.0595e-08	-7.2586e-11
13	-1.6005e-05	1.7347e-05	-8.7790e-07	1.7175e-08	-1.1906e-10
14	8.0218e-06	1.8465e-05	-9.0650e-07	1.7538e-08	-1.2094e-10
15	9.8612e-05	9.8980e-06	-6.5258e-07	1.3859e-08	-9.9774e-11
16	7.5193e-05	1.5271e-05	-8.8520e-07	1.8106e-08	-1.2810e-10

230

Table A.5: Values of constants used to calculate the Kinetic energy of a particle. For particles stopping in the slow plastic, $KE(L) = m_2 L^2 + m_1 L + m_0$, where $m_0 = m_{01} Z + m_{00}$, and $m_1 = m_{15} Z^5 \ m_{14} Z^4 \ m_{13} Z^3 \ m_{12} Z^2 + m_{11} Z + m_{10}$, and $m_1 = m_{24} Z^4 \ m_{23} Z^3 \ m_{22} Z^2 + m_{21} Z + m_{20}$. Table (a) contains the value needed to calculate m_0, Table (b) contains the value needed to calculate m_1, and Table (c) contains the value needed to calculate m_2

a)

Det	m_{00}	m_{01}
1	16.723	1.5240
2	15.946	1.5349
3	15.902	1.5355
4	15.969	1.5345
5	16.894	1.5196
6	15.858	1.5361
7	21.103	1.4565
8	16.038	1.5336
9	16.151	1.5320
10	15.727	1.5379
11	15.799	1.5369
12	15.646	1.5390
13	16.177	1.5316
14	16.193	1.5314
15	15.953	1.5348
16	16.311	1.5297

231

b)

Det	m_{10}	m_{11}	m_{12}	m_{13}	m_{14}	m_{15}
1	1.37220	0.112560	-0.0109520	0.00044452	-7.9395e-06	5.2899e-08
2	0.53714	0.099939	-0.0076828	0.00029822	-5.2829e-06	3.5438e-08
3	0.97155	0.082898	-0.0072736	0.00028736	-5.0277e-06	3.3116e-08
4	1.17230	0.122160	-0.0103100	0.00040188	-7.0017e-06	4.6036e-08
5	1.03290	-0.12037	0.0053433	-0.0001080	1.0806e-06	-3.775e-09
6	0.60138	0.106190	-0.0077980	0.00029003	-4.9178e-06	3.1876e-08
7	0.98878	0.135010	-0.0109550	0.00042133	-7.3266e-06	4.8226e-08
8	1.12180	0.137290	-0.0112780	0.00043556	-7.5681e-06	4.9715e-08
9	0.78993	0.111690	-0.0090258	0.00034663	-6.0192e-06	3.9550e-08
10	0.53195	0.077471	-0.0057323	0.00021369	-3.5979e-06	2.3167e-08
11	0.52647	0.086352	-0.0063514	0.00023630	-3.9949e-06	2.5826e-08
12	0.55892	0.060989	-0.0046639	0.00017612	-2.9490e-06	1.8853e-08
13	0.94640	0.101220	-0.0087443	0.00034314	-6.0202e-06	3.9756e-08
14	0.85619	0.109180	-0.0090711	0.00035148	-6.1324e-06	4.0390e-08
15	0.68020	0.087252	-0.0069951	0.00026802	-4.6294e-06	3.0303e-08
16	0.93564	0.085998	-0.0078347	0.00031248	-5.5305e-06	3.6693e-08

232

c)

Det	m_{20}	m_{21}	m_{22}	m_{23}	m_{24}
1	-0.00190380	0.00028486	-1.4676e-05	3.1573e-07	-2.4408e-09
2	-0.00034422	8.9339e-05	-4.3142e-06	9.0310e-08	-7.0195e-10
3	-0.00065669	0.00018284	-9.5671e-06	2.0594e-07	-1.5913e-09
4	-0.00109850	0.00027768	-1.4228e-05	3.0326e-07	-2.3394e-09
5	0.00137950	0.00028351	-1.7718e-05	4.0195e-07	-3.1326e-09
6	-0.00039186	0.00011896	-5.4599e-06	1.1083e-07	-8.4879e-10
7	-0.00097595	0.00020142	-9.9550e-06	2.0815e-07	-1.6013e-09
8	-0.00113280	0.00026261	-1.3195e-05	2.7857e-07	-2.1470e-09
9	-0.00063759	0.00013038	-6.4239e-06	1.3428e-07	-1.0349e-09
10	-0.00025590	0.00010195	-4.7265e-06	9.6457e-08	-7.3367e-10
11	-0.00027974	9.4829e-05	-4.3713e-06	8.8953e-08	-6.7925e-10
12	-0.00021912	0.00011934	-5.6209e-06	1.1545e-07	-8.7347e-10
13	-0.00080581	0.00016115	-8.2436e-06	1.7571e-07	-1.3571e-09
14	-0.00072115	0.00014180	-7.0952e-06	1.4949e-07	-1.1529e-09
15	-0.00041126	0.00010689	-5.3102e-06	1.1152e-07	-8.5803e-10
16	-0.00078758	0.00014217	-7.3609e-06	1.5812e-07	-1.2230e-09

233

Table A.6 Velocity data for Xe + Cu a) at E/A = 30 and 40 MeV and b) E/A = 50 and 60 MeV

a)

Z	<V> (30)	+/-	<V> (40)	+/-
3.0000	1.1689	0.051724	1.1172	0.055425
6.0000	1.1324	0.013409	1.0204	0.0098446
9.0000	1.1334	0.045721	1.0325	0.0084016
12.000	1.0906	0.057190	0.98805	0.011087
15.000	1.1723	0.089544	0.97831	0.0095580
18.000	1.2100	1.1900	1.0053	0.0027122
21.000	0.80525	0.0086561		
24.000	0.90620	0.0058588		
27.000	0.92388	0.0075362	0.86628	0.0040105
30.000	0.89636	0.014654	0.89589	0.0031756
33.000	0.93817	0.0025724	0.90948	0.0020559
36.000	0.94891	0.0014369	0.91838	0.0015045
39.000	0.95973	0.0010084	0.91968	0.0016124
42.000	0.97558	0.00066363	0.92220	0.0020474
45.000	0.98622	0.00040463	0.95212	0.00099627
48.000	1.0025	0.00017850	0.96035	0.00044854
51.000	0.99982	6.2065e-05	0.97680	0.00010540
54.000	1.0059	3.6365e-05	0.99086	8.7578e-05

234

b)

Z	$\langle V \rangle$ (50)	+/-	$\langle V \rangle$ (60)	+/-
3.0000	1.1116	0.0042936	1.0524	0.0046797
6.0000	1.0372	0.0043157	0.95950	0.0041059
9.0000	1.0814	0.0040351	1.0461	0.012060
12.000	1.0337	0.0057274	1.0347	0.0067500
15.000	1.0449	0.0045877	1.0349	0.0059876
18.000	1.0229	0.0040313	1.0270	0.0034266
21.000	1.0140	0.0037929	1.0288	0.0037815
24.000	0.97615	0.0052235	1.0283	0.0034115
27.000	0.97923	0.0022460	1.0184	0.0034010
30.000	0.97642	0.0024564	1.0061	0.0024819
33.000	0.97741	0.0022023	1.0013	0.0021055
36.000	0.88976	0.00061413	0.99572	0.0015321
39.000	0.91554	0.00054697	0.99875	0.0012210
42.000	0.93151	0.00028950	0.99433	0.0010740
45.000	0.94406	0.00022130	0.98767	0.00097903
48.000	0.96050	0.00028635	0.97238	0.00011190
51.000	0.97155	0.00017668	0.98547	4.7866e-05
54.000	0.99459	4.2841e-05	0.99535	3.3565e-05

235

Table A.7 Velocity data for Xe + Sc a) at E/A = 30 and 40 MeV and b) E/A = 50 and 60 MeV

a)

Z	<Vel> (30)	+/-	<Vel> (40)	+/-
3.0000	1.2176	0.049479	1.1521	0.012671
6.0000	1.1257	0.018106	1.1115	0.0070482
9.0000	1.1671	0.0087314	1.0673	0.013615
12.000	1.1091	0.011284	1.0524	0.0077041
15.000	1.1316	0.011646	0.99045	0.013666
18.000			0.98819	0.011236
21.000			1.0028	0.0023076
24.000	0.92236	0.0090410	1.0327	0.0016074
27.000	0.99712	0.0027085	0.89278	0.0028949
30.000	1.0003	0.0045331	0.93042	0.0012718
33.000	0.93106	0.00094064	0.92328	0.00094310
36.000	0.95705	0.0012324	0.92551	0.0012792
39.000	0.96062	0.0014692	0.93187	0.00093445
42.000	0.97702	0.00047592	0.93931	0.0012999
45.000	0.98600	0.00016378	0.95437	0.00076248
48.000	1.0074	0.00017502	0.97133	0.00033395
51.000	1.0036	3.7502e-05	0.99182	9.6553e-05
54.000	1.0090	1.7524e-05	1.0071	2.2098e-05

236

b)

Z	<Vel> (50)	+/-	<Vel> (60)	+/-
3.0000	1.1116	0.0042936	1.0960	0.0044235
6.0000	1.0372	0.0043157	0.97925	0.0030944
9.0000	1.0814	0.0040351	1.0924	0.0040376
12.000	1.0337	0.0057274	1.0597	0.0043624
15.000	1.0449	0.0045877	1.0593	0.0031217
18.000	1.0229	0.0040313	1.0428	0.0027780
21.000	1.0140	0.0037929	1.0433	0.0025610
24.000	0.97615	0.0052235	1.0374	0.0018333
27.000	0.97923	0.0022460	1.0286	0.0017963
30.000	0.97642	0.0024564	1.0227	0.0015583
33.000	0.97741	0.0022023	1.0139	0.0013900
36.000	0.88976	0.00061413	0.99381	0.0012585
39.000	0.91554	0.00054697	0.98460	0.00090796
42.000	0.93151	0.00028950	1.0019	0.00064006
45.000	0.94406	0.00022130	0.99373	0.00062238
48.000	0.96050	0.00028635	0.98504	0.00042842
51.000	0.97155	0.00017668	0.98203	0.00019141
54.000	0.99459	4.2841e-05	0.98933	0.00018458

237

Table A.8 Mean charge and charge width data for Xe + Cu at (a) E/A = 30 MeV, (b) E/A= 40 MeV, (c) E/A = 50 MeV, and (d) E/A = 60 MeV.

a)

E	<Z>	+/-	σ_z	+/-
1900.0	32.326	0.25244	2.8347	0.43180
2100.0	34.901	0.14793	2.2890	0.24264
2300.0	37.320	0.089318	1.9482	0.082666
2500.0	39.728	0.097627	2.2206	0.085214
2700.0	42.526	0.062405	1.7840	0.064675
2900.0	43.938	0.021636	1.1310	0.026692
3100.0	45.578	0.013005	1.1715	0.021025
3300.0	48.239	0.018162	1.9751	0.019903
3500.0	51.412	0.0058649	0.68050	0.0093689
3700.0	52.466	0.0052026	0.87868	0.0037588
3900.0	53.871	0.0048925	0.68010	0.0037639
4100.0	54.702	0.0045832	0.51350	0.011138

238

b)

E	$\langle Z \rangle$	+/-	σ_z	+/-
2500.0	35.201	0.24675	5.0045	0.34147
2700.0	37.268	0.16305	4.0728	0.16131
2900.0	39.164	0.13782	3.6519	0.11663
3100.0	40.797	0.098672	3.1279	0.080123
3300.0	42.489	0.079774	2.8522	0.057536
3500.0	44.425	0.071482	2.6897	0.052894
3700.0	46.038	0.058521	2.2343	0.042473
3900.0	47.574	0.034044	1.9506	0.035387
4100.0	48.778	0.026245	1.7792	0.027982
4300.0	49.956	0.023271	1.5935	0.029308
4500.0	51.387	0.0053919	0.77487	0.013670
4700.0	52.383	0.0053004	0.52772	0.0055857
4900.0				
5100.0	52.418	0.0077785	0.92296	0.014523

239

c)

E	<Z>	+/-	σ_z	+/-
2500.0	27.438	0.28905	6.2448	0.32238
2700.0	29.833	0.28605	6.2352	0.32020
2900.0	32.601	0.34449	6.8703	0.40878
3100.0	34.769	0.31014	6.4794	0.38822
3300.0	36.641	0.15763	4.4051	0.19814
3500.0	38.638	0.080097	2.6010	0.17656
3700.0	40.000	0.067645	2.4446	0.10047
3900.0	41.356	0.068158	2.7282	0.075765
4100.0	42.894	0.061541	2.6311	0.055379
4300.0	44.339	0.057551	2.6493	0.047471
4500.0	45.716	0.051046	2.3120	0.039237
4700.0	47.016	0.034604	2.1910	0.034463
4900.0	48.194	0.029813	1.9395	0.030046
5100.0				
5300.0	51.311	0.0061240	0.58646	0.010519
5500.0	52.018	0.0044177	0.48299	0.0065293
5700.0	52.597	0.0093964	0.68421	0.012421
5900.0	53.282	0.0034664	0.65833	0.0063347
6100.0	54.179	0.0023675	0.55947	0.0038762
6300.0	55.064	0.0015522	0.51602	0.0038774
6500.0	55.886	0.0033678	0.45439	0.0036795

240

d)

E	$\langle Z \rangle$	+/-	σ_z	+/-
3700.0	30.103	0.53135	9.4029	0.76650
3900.0	30.550	0.57549	9.4769	0.82530
4100.0	31.782	0.38590	7.7336	0.56989
4300.0	33.269	0.42557	8.5510	0.64200
4500.0	33.990	0.31475	6.9742	0.59537
4700.0	34.740	0.23153	5.3810	0.41568
4900.0	36.276	0.24682	6.2066	0.39122
5100.0	35.889	0.084315	6.0563	0.076274
5300.0	39.744	0.17443	5.3144	0.21191
5500.0	41.049	0.15891	5.2643	0.19232
5700.0	42.457	0.12963	4.7430	0.13287
5900.0	43.605	0.11907	4.5300	0.13568
6100.0	44.634	0.10421	4.2631	0.11910
6300.0	46.021	0.086106	3.8561	0.093989
6500.0	47.496	0.084912	3.5688	0.11939
6700.0	48.759	0.24846	2.8626	0.81713
6900.0	49.828	0.0071498	0.52936	0.0069153
7100.0	50.792	0.0040412	0.53208	0.0057242
7300.0	51.736	0.0053478	0.51813	0.0043849
7500.0	52.664	0.0047551	0.50500	0.0043080
7700.0	53.566	0.0043770	0.48840	0.0039219
7900.0	54.443	0.0017123	0.47103	0.0044123

241

Table A.9 Mean charge and charge width data for Xe + Sc at (a) E/A = 30 MeV, (b) E/A= 40 MeV, (c) E/A = 50 MeV, and (d) E/A = 60 MeV.

a)

E	$<Z>$	+/-	σ_Z	+/-
1900.0	32.619	0.11919	1.5483	0.15306
2100.0	34.788	0.096106	1.6253	0.11528
2300.0	36.858	0.097408	2.2602	0.10952
2500.0	39.498	0.086180	2.1976	0.081386
2700.0	42.344	0.042780	1.5012	0.056466
2900.0	43.887	0.016684	1.3248	0.028570
3100.0	45.331	0.010524	1.1276	0.031876
3300.0	48.221	0.025427	1.9097	0.020450
3500.0	50.611	0.0033037	1.2295	0.0088065
3700.0	52.256	0.0035801	0.87479	0.0030916
3900.0	53.872	0.0027475	0.66233	0.0020389
4100.0	54.948	0.0085913	0.57936	0.0087950

242

b)

E	<Z>	+/-	σ_Z	+/-
2700.0	37.164	0.14167	4.3180	0.12555
2900.0	38.800	0.099125	3.6860	0.076904
3100.0	40.378	0.078357	3.3845	0.057351
3300.0	41.911	0.068288	3.2001	0.049850
3500.0	43.577	0.056600	2.9406	0.039563
3700.0	45.273	0.047734	2.7144	0.033204
3900.0	46.717	0.031208	2.4622	0.032459
4100.0	47.933	0.025614	2.3145	0.033327
4300.0	49.844	0.031360	1.3792	0.036592
4500.0	50.851	0.015905	1.1920	0.029540
4700.0	51.799	0.0025234	0.71691	0.012236
4900.0				
5100.0	53.256	0.0053045	0.66023	0.0045380

243

c)

E	$\langle Z \rangle$	+/-	σ_Z	+/-
2500.0	27.473	0.21051	6.2047	0.26250
2700.0	28.538	0.17551	5.5999	0.20058
2900.0	30.440	0.18483	6.0291	0.18415
3100.0	31.776	0.13458	5.2701	0.12531
3300.0	33.804	0.18631	6.2780	0.16192
3500.0	36.234	0.15629	5.8332	0.13902
3700.0	39.730	0.039446	2.1195	0.061215
3900.0	40.900	0.056309	2.4008	0.063777
4100.0	41.890	0.044860	2.2246	0.041216
4300.0	43.031	0.036709	2.3309	0.032932
4500.0	44.113	0.032955	2.3008	0.026803
4700.0	45.276	0.029388	2.2154	0.021389
4900.0	46.505	0.026210	2.0982	0.017145
5100.0	44.948	0.012337	2.8939	0.010274
5300.0	48.824	0.013509	1.8960	0.015204
5500.0	49.948	0.015111	1.7396	0.015111
5700.0	51.802	0.0079699	0.89804	0.017002
5900.0	52.432	0.0069170	0.88475	0.013511
6100.0	53.146	0.0040207	0.62505	0.0090112
6500.0	53.752	0.0023956	0.51818	0.0059711

244

d)

E	<Z>	+/-	σ_Z	+/-
3700.0	28.620	0.26484	6.7712	0.35043
3900.0	29.450	0.19719	5.5425	0.23448
4100.0	30.368	0.14016	4.4915	0.15569
4300.0	31.187	0.12114	4.1028	0.13202
4500.0	32.125	0.10761	3.8474	0.10735
4700.0	33.849	0.095526	3.8795	0.10262
4900.0	34.902	0.094407	3.8624	0.11026
5100.0	35.192	0.050490	5.4436	0.037782
5300.0	37.951	0.11988	4.5962	0.13582
5500.0	39.352	0.11582	4.7394	0.12209
5700.0	40.869	0.094740	4.6162	0.084535
5900.0	42.689	0.073001	4.3695	0.057738
6100.0	43.946	0.066239	4.1247	0.050021
6300.0	45.165	0.061291	4.0462	0.046887
6500.0	46.465	0.061112	3.8159	0.047391
6700.0	47.824	0.059377	3.6316	0.046034
6900.0	49.511	0.010208	0.63260	0.018735
7100.0	50.508	0.010267	0.71059	0.017835
7300.0	51.411	0.0080320	0.62879	0.013956
7500.0	52.386	0.0078043	0.63363	0.012430
7700.0	53.315	0.014045	0.59230	0.014909
7900.0	54.182	0.0056604	0.54554	0.017225

245

References

BAL95   S.P. Baldwin, B. Lott, B.M. Szabo, B.M. Quednau, W. U. Schröder, J. Töke, L.G. Sobatka, J. Barreto, R.J. Charity, L.Gallamore, D.G. Sarantites, D.W. Stacener, and R.T. deSouza, *Phys. Rev. Lett.* **74** 1299 (1995).

BAR87   H.W. Barz, J.P. Bondorf, and H. Schulz, *Nucl. Phys.* **A462**, 742 (1987).

BER88   G.F. Bertsch and S. DasGupta, *Phys. Reports* **160**,189 (1988).

BIR79   J.R. Birkelund, L.E. Tubbs, J.R. Huizenga, J.N. De, D. Sperber, *Phys. Reports,* **156**, 107 (1979).

BIR89   J.R. Bird and J.S. Williams, *Ion Beams for Material Analysis*, Academic, Sydney, Australia, 1989.

BON85a   J.P. Bondorf, R. Donangelo, I.N. Mishustin, C.J. Pethick, H. Schulz, and K. Sneppen, *Nucl. Phys.* **A443**, 321 (1985).

BON85b   J.P. Bondorf, R. Donangelo, I.N. Mishustin, and H. Schulz, *Nucl. Phys.* **A444**, 460 (1985).

BOW91   D.R. Bowman, G.F. Peaslee, R.T. deSouza, N. Carlin, C.K. Gelbke, W.G. Gong, Y.D. Kim, M.A. Lisa, W.G. Lynch, L. Phair, M.B. Tsang, C. Williams, N. Collona, K. Hanold, M.A. McMahan, G.J. Wozniak, L.G. Moretto, and W.A. Friedman, *Phys. Rev. Lett.* **67** 1527 (1991).

BOW92   D.R. Bowman, C.M. Mader, G.F. Peaslee, W.Bauer, N. Carlin, R.T. deSouza, C.K. Gelbke, W.G. Gong, Y.D. Kim, M.A. Lisa, W.G. Lynch, L. Phair, M.B. Tsang, C. Williams, N. Collona, K. Hanold, M.A. McMahan, G.J. Wozniak, L.G. Moretto, *Phys. Rev. C* **46** 1834 (1992).

BOW93   D.R. Bowman, G.F. Peaslee, N. Carlin, R.T. deSouza, C.K. Gelbke, W.G. Gong, Y.D. Kim, M.A. Lisa, W.G. Lynch, L. Phair, M.B. Tsang, C. Williams, N. Collona, K. Hanold, M.A. McMahan, G.J. Wozniak, L.G. Moretto, *Phys. Rev. Lett.* **70** 3534 (1993).

BRE83   Herbert Breuer, Neil R. Yoder, Alice C. Mignerey, Victor E. Viola, Krzysztof Kwiatkowski, and Kevin L. Wolf, *Nucl. Instr. and Meth.* **204** 419 (1983).

CEB89   D. Cebra, J. Karn, C.A. Ogilve, A. Van der Molen, G.D. Westfall, J. Winfield, and E. Norbeck, *Luser's Guide to the MSU 4π Array*, (1989)

CEB92   D.A. Cebra, W.K. Wilson, A. Vander Molen, and G.D. Westfall, *Nucl. Instr. and Meth..* **A313** 367 (1992).

CHA88   R.J. Charity, *Nucl. Phys.* **A483**, 371 (1988).

CHA90   R.J. Charity, *Nucl. Phys.* **A511**, 59 (1990).

CHA96   R.J. Charity, *Phys. Rev.* C **53**, 512 (1996).

DAY86   R. Dayras, *Nucl. Phys.* **A460**, 299 (1986).

GAR96   E.J. Garcia-Solis and A.C. Mignerey, *Phys. Rev.* C **54**, 276 (1996).

HAG94   K. Hagel, M. Gonin, R. Wada, J.B. Natowitz, F. Haddad, Y. Lou, M. Gui, D. Utley, B. Xiaó, J. Li, G. Nebba, D. Fabris, G. Prete, J. Ruiz, D. Drain, B. Chambon, B. Cheynis, D. Guinet, X. C. Hu, A. Demeyer, C. Pastor, A. Giorni, A. Lleres, P. Stassi, J. B. Viano, and P. Gonthier, *Phys. Rev.* C **50**, 2017(1994).

HAN95   K.A. Hanhold, D. Bazin, M.F. Mohar, L.G. Moretto, D.J. Morissey, N.A. Orr, B.M. Sherrill, J.A. Winger, G.J. Wozniak, and S.J. Yennello, *Phys. Rev.* C **51**, 2562 (1995).

HEU94   D. Heuer, A. Chabane, M. E. Brandan, M. Charvet, A. J. Cole, P. Désesquelles, A. Giorni, A. Lleres, A. Menchaha-Rocha, and J. B. Viano, *Phys. Rev.* C **50**, 1943 (1994).

KEH92   W.L. Kehoe, A.C. Mignerey, A. Moroni, I. Iori, G.F. Peaslee, N. Colonna,
K. Hanold, D.R. Bowman, L.G. Moretto, M.A. McMahan, J.T. Walton, and
G.J. Wozniak, *Nucl. Instr. and Meth.* **A311** 258 (1992).

LEE97   S.J. Lee and A.Z. Mekjian, *Phys. Rev. C* **56**, 2621 (1997).

LES95   J.P. Lestone, *Phys. Rev. C* **52**, 1118 (1995).

LLE94   A. Lleres, A. J. Cole, P. Désesquelles, A. Giorni, D. Heuer, J. B. Viano, B.
Chambon, B. Cheynis, D. Drain, and C. Pastor, *Phys. Rev. C* **50**, 1973
(1994).

LOT92   B. Lott, S.P. Baldwin, B.M. Szabo, B.M. Quednau, W. U. Schröder, J.
Töke, L.G. Sobatka, J. Barreto, R.J. Charity, L.Gallamore, D.G. Sarantites,
D.W. Stacener, and R.T. deSouza, *Phys. Rev. Lett.* **68** 3141 (1992).

LUK97   J. Lukasik, J. Benlliure, B. Métivier, E. Plagnol, B. Tamain, M. Assenard, G.
Auger, Ch. O. Bacri, E. Bisquer, B. Bordie, R. Bougault, R. Brou, Ph.
Buchet, J.L. Charvet, A. Chbihi, J. Colin, D. Cussol, R. Dayras, A. Demeyer,
D. Doré, D. Durand, E. Gerlic, D. Gourio, D. Guinet, P. Lautesse, J.L.
Laville, J.F. Lecolley, A. Le Fèvre, T. Lefort, R. Legrain, O. Lopez, M.
Louvel, N. Marie, L. Nalpas, M. Parlog, J. Péter, O. Politi. A. Rahmani, T.
Reposeur, M.F. Rivet, E. Rosato, F. Saint-Laurent, M. Squalli, J.C.
Steckmeyer, M.Stern, L. Tassan-Got, E. Vient, C. Volant, J.P. Wieleczko, M.
Collona, F. Haddad, Ph. Eudes, T. Sami, and F. Sebille, *Phys. Rev. C* **55**,
1906 (1997).

MAD92   H. Madani, Ph.D. Thesis. University of Maryland (1992).

MAD94   H. Madani, A.C. Mignerey, D.E. Russ, J.Y. Shea, G. Westfall, W.J. Llope,
        D. Craig, E. Gualtieri, S. Hannuscke, R. Pak, T. Li, A. Vandermolen, J. Yee,
        E. Norbeck, and R. Pedroni, *Proceedings of the 10th Winter Workshop on
        Nuclear Dynamics Advances in Nuclear Dynamics*, Snowbird Utah (USA), Ed.
        J. Harris, A. Mignerey, and Wolfgang Bauer, World Scientific, New York,
        1994.

MAD95   H. Madani, A.C. Mignerey, A.A. Marchetti, A.P. Weston-Dawkes, W.L.
        Kehoe, and F. Obershain, *Phys. Rev. C* **51**, 2562 (1995).

MAD96   H. Madani, A.C. Mignerey, D.E. Russ, J.Y. Shea, G. Westfall, W.J. Llope,
        D. Craig, E. Gualtieri, S. Hannuscke, R. Pak, T. Li, A. Vandermolen, J. Yee,
        E. Norbeck, and R. Pedroni, *Advances in Nuclear Dynamics*, Ed. Wolfgang
        Bauer and Alice Mignerey, Plenum Press, New York, 1996.

MOR93   L.G. Moretto and G.J. Wozniak, *Annu. Rev. Nucl. Part. Sci.* **43** 379 (1993).

MOU78   J.B. Moulton, J.E. Sephenson, R.P. Schmitt, and G.J. Wozniak, *Nucl. Instr.
        and Meth..* **157** 325 (1978).

PHA92   L. Phair, W. Bauer, D.R. Bowman, N. Carlin, R.T. deSouza, C.K. Gelbke,
        W.G. Gong, Y.D. Kim, M.A. Lisa, W.G. Lynch, G.F. Peaslee, M.B. Tsang,
        C. Williams, F. Zhu, N. Collona, K. Hanold, M.A. McMahan, G.J. Wozniak,
        and L.G. Moretto, *Phys. Lett.* **B285** 10 (1992).

RUS97   D.E. Russ, A.C. Mignerey, E.J. Garcia-Solis, H. Madani, J.Y. Shea, P.J.
        Stanskas, O. Bjarki, D. Craig, E.E. Gualtieri, S.A. Hannuschke, T. Li, W.J.
        Llope, R. Pak, N.T.B. Stone, A. Vandermolen, G.D. Westfall, J. Yee, E.
        Norbeck, and R. Pedroni, *Annual Progress Report 1997*, Appendix B,
        DOE/ER/40802-6 (1997)

SCH84   W.U. Schröder and J.R. Huizenga, *Treatise on Heavy-Ion Science*, Vol 2, Ed.
        by D.A. Bromely, Plenum, New York, 1984; Chapter 3.

249

SIW76   K. Siwek-Wilcynska and J. Wilczynski, *Nucl. Phys.* **A264** 115 (1976).

SOB97   L.G. Sobotka, J.F. Dempsey, R.J. Charity, and P. Danielewicz,*Phys. Rev. C* **55**, 2109 (1997).

TAS9i   L. Tassan-Got, and C. Stéphan, *Nucl. Phys.* **A524**, 121 (1991).

TOK92   J. Töke, and W. U. Schröder, *Annu. Rev. Nucl. Part. Sci.* **42** 401 (1992).

WES85   G.D. Westfall, J.E. Yurkon, J. Van Der Plicht, Z.M. Koenig, B.V. Jacak, R.Fox, G.M. Crawley, M.R. Maier, B.E. Hasselquist, R.S. Tickle, and D. Horn, *Nucl. Instr. And Meth.* **A238** 347 (1985).

WIL80   W.W. Wilke, J.R. Birkelund, H.J. Wollersheim, A.D. Hoover, J.R. Huizenga, W. U. Schröder, and L.E. Tubbs, *Atomic Data and Nuclear Data Tables* **25**, 389 (1980).

WON90   Samuel A.M. Wong, *Introductory Nuclear Physics*, Prentice Hall, Englewood Cliffs NJ, 1990.

ZIE80   J.F. Ziegler, *Handbook of stopping cross-sections for energetic ions in all elements*, Pergamon Press, New York, 1980

250